Publikationsbasierte Dissertation

Gold at the Nanoscale

Plasmon - Exciton Coupling and Optical Heating

Felix Stete

Universität Potsdam

Mathematisch-Naturwissenschaftliche Fakultät
Institut für Physik & Astronomie

Publikationsbasierte Dissertation

Gold at the Nanoscale

Plasmon - Exciton Coupling and Optical Heating

Felix Stete

zur Erlangung des akademischen Grades
doctor rerum naturalium (Dr. rer. nat.)
in der Wissenschaftsdisziplin: Experimentalphysik

Gutachter: Prof. Dr. Matias Bargheer
Prof. Dr. Oliver Benson
Prof. Dr. Bert Hecht

Eingereicht am: 17.06.2020
Disputation am: 09.12.2020

Universität Potsdam

Mathematisch-Naturwissenschaftliche Fakultät
Institut für Physik & Astronomie

Published online on the
Publication Server of the University of Potsdam:
https://doi.org/10.25932/publishup-49605
https://nbn-resolving.org/urn:nbn:de:kobv:517-opus4-496055

Abstract

In this cumulative dissertation, I want to present my contributions to the field of plasmonic nanoparticle science. Plasmonic nanoparticles are characterised by resonances of the free electron gas around the spectral range of visible light. In recent years, they have evolved as promising components for light based nanocircuits, light harvesting, nanosensors, cancer therapies, and many more.

This work exhibits the articles I authored or co-authored in my time as PhD student at the University of Potsdam. The main focus lies on the coupling between localised plasmons and excitons in organic dyes. Plasmon–exciton coupling brings light–matter coupling to the nanoscale. This size reduction is accompanied by strong enhancements of the light field which can, among others, be utilised to enhance the spectroscopic footprint of molecules down to single molecule detection, improve the efficiency of solar cells, or establish lasing on the nanoscale. When the coupling exceeds all decay channels, the system enters the strong coupling regime. In this case, hybrid light–matter modes emerge utilisable as optical switches, in quantum networks, or as thresholdless lasers. The present work investigates plasmon–exciton coupling in gold–dye core–shell geometries and contains both fundamental insights and technical novelties. It presents a technique which reveals the anticrossing in coupled systems without manipulating the particles themselves. The method is used to investigate the relation between coupling strength and particle size. Additionally, the work demonstrates that pure extinction measurements can be insufficient when trying to assess the coupling regime. Moreover, the fundamental quantum electrodynamic effect of vacuum induced saturation is introduced. This effect causes the vacuum fluctuations to diminish the polarisability of molecules and has not yet been considered in the plasmonic context.

The work additionally discusses the reaction of gold nanoparticles to optical heating. Such knowledge is of great importance for all potential optical applications utilising plasmonic nanoparticles since optical excitation always generates heat. This heat can induce a change in the optical properties, but also mechanical changes up to melting can occur. Here, the change of spectra in coupled plasmon–exciton particles is discussed and explained with a precise model. Moreover, the work discusses the behaviour of gold nanotriangles exposed to optical heating. In a pump–probe measurement, X-ray probe pulses directly monitored the particles' breathing modes. In another experiment, the triangles were exposed to cw laser radiation with varying intensities and illumination areas. X-ray diffraction directly measured the particles' temperature. Particle melting was investigated with surface enhanced Raman spectroscopy and SEM imaging demonstrating that larger illumination areas can cause melting at lower intensities.

An elaborate methodological and theoretical introduction precedes the articles. This way, also readers without specialist's knowledge get a concise and detailed overview of the theory and methods used in the articles. I introduce localised plasmons in metal nanoparticles of different shapes. For this work, the plasmons were mostly coupled to excitons in J-aggregates. Therefore, I discuss these aggregates of organic dyes with sharp and intense resonances and establish an understanding of the coupling between the two systems. For *ab initio* simulations of the coupled systems, models for the systems' permittivites are presented, too. Moreover, the route to the sample fabrication – the dye coating of gold nanoparticles, their subsequent deposition on substrates, and the covering with polyelectrolytes – is presented together with the measurement methods that were used for the articles.

Kurzdarstellung

In der vorliegenden publikationsbasierten Dissertation möchte ich meinen Beitrag aus meiner Zeit als Doktorand an der Universität Potsdam zum Forschungsgebiet plasmonischer Nanopartikel vorstellen. Letztere zeichnen sich durch Resonanzen des freien Elektronengases im Spektralbereich sichtbaren Lichts aus mit vielversprechenden Anwenungsgebieten, unter anderem in Bereichen der Nanosensorik, lichtbasierter Nanoschaltkreise oder auch der Krebstherapie.

Die Arbeit beinhaltet die von mir mitverfassten wissenschaftlichen Artikel, mit dem Hauptaugenmerk auf der Kopplung zwischen lokalisierten Plasmonen in Gold-Nanopartikeln und Exzitonen in organischen Farbstoffen. Plasmonen konzentrieren Lichtfelder auf kleinstem Raum. Dadurch verstärkt sich die Licht–Materie-Wechselwirkung, welche es etwa ermöglicht, die Effizienz von Solarzellen zu erhöhen, die Spektren weniger bis einzelner Moleküle aufzunehmen oder auch Laser auf der Nanoskala zu entwickeln. Überschreitet die Wechselwirkung zwischen Plasmonen und Exzitonen alle anderen Dissipationskanäle, spricht man vom Regime der starken Kopplung. In diesem Regime entstehen neue untrennbare Licht–Materie-Hybridzustände aus denen ultraschnelle optische Schalter, Quantennetzwerke oder pumpschwellenfreie Laser konstruiert werden können. Die Artikel bieten dabei sowohl Erkenntnisse der Grundlageforschung als auch neue technische Verfahren. So wird unter anderem eine Methode zur Sichtbarmachung der vermiedenen Kreuzung gekoppelter Resonanzen vorgestellt, in der die Partikel selber nicht verändert werden. Die Technik wird hier beispielsweise verwendet, um den Zusammenhang zwischen Kopplungsstärke und Partikelgröße zu untersuchen. Zusätzlich zeigt die Arbeit, dass das alleinige Betrachten von Extinktionsspektren unzureichend für die Beurteilung des Kopplungsregimes sein kann. Desweiteren wird die Sättigung durch Vakuumfelder vorgestellt, ein Effekt der Quantenelektrodynamik, der im Zusammenhang mit Plasmonen bisher unbekannt war.

Die Reaktion von Gold-Nanopartikeln auf optische Erwärmung stellt den zweiten Themenbereich der Arbeit dar. Da durch optische Anregung grundsätzlich auch Wärme entsteht, ist die Kenntnis über diese Reaktion für alle Anwendungen plasmonischer Nanopartikel von Bedeutung. Zum einen wird hier die spektrale Änderung nach der Anregung gekoppelter Gold–Farbstoff-Partikel untersucht und quantitativ modelliert, zum anderen betrachtet die Arbeit Gold-Nanodreiecke bei optischer Anregung. In zeitaufgelösten Messungen wurde die Ausdehnung des Kristallgitters direkt mit Röntgen-Pulsen aufgenommen. Mit Hilfe von kontinuierlicher Röntgenstrahlung wurde außerdem die Temperatur der Teilchen bei konstanter Beleuchtung von Laserlicht gemessen, wobei die Größe der beleuchteten Fläche und die Lichtintensität variierten. Durch oberflächenverstärkte Raman-Spektren und REM-Bilder ließ sich indes das Schmelzen der Teilchen beobachten.

Den Artikeln steht eine ausführliche Einleitung voran, die eine detaillierte Übersicht sowohl über die theoretischen Grundlagen als auch über die experimentelle Methodik bietet. Sie führt lokalisierte Plasmonen auf unterschiedlich geformten Teilchen ein. Für diese Arbeit wurden die Teilchen mit J-Aggregaten ummantelt. Folglich werden diese speziellen Aggregate organischer Farbstoffe mit ihren intensiven und scharfen Resonanzen vorgestellt und die Kopplung ihrer Anregungen mit Plasmonen diskutiert. Für Ab-initio-Simulationen der gekoppelten Spektren werden Modelle für Permittivität der beiden Komponenten besprochen. Abschließend werden die Herstellung der Proben sowie alle in den Artikeln verwendeten Messmethoden eingeführt.

Contents

1 | Introduction

The history of light manipulation via metal nanoparticles reaches back to the ancient Romans. The 4th-century Lycurgus cup belongs to the oldest known examples of dichroic glass. Colloidal gold–silver alloy nanoparticles give rise to a colour variarion from red to green depending on whether light is transmitted or reflected by the cup [1]. Later, in the Middle Ages, metal nanoparticles were used to stain glass in various colours [2]. Gold nanoparticles also found application as pigments in the very early days of photography [3]. However, the roots of the effects and even the mere occurrence of nanoparticles remained unknown until Michael Faraday presented his studies on metal aerosols and their influence on light [4] in 1857. He was the first to attribute the colours to the occurrence extremely fine metal particles.

In 1908, Gustav Mie [5] provided a detailed explanation of the scattering and absorption behaviour of spherical nanoparticles explaining the colours by resonant oscillations of the free electrons. Today, we refer to these collective oscillations as *localised plasmons*. The Mie model predicted correctly that metal nanoparticles can absorb but also strongly scatter light explaining the pronounced colour effects exhibited by the stained glass types produced in the centuries before. In 1912, Richard Gans expanded the Mie model to the description of ellipsoidal nanoparticles to account for possible non-spherical shapes [6]. His theory showed that the plasmon resonance could be tuned over the hole visible spectrum by changing the shape of the nanoparticles.

Besides the strong scattering and absorption, Mie and Gans showed that the electromagnetic energy of light illuminating a nanoparticle is concentrated in the particle's inside and vicinity. This concentration to a volume much smaller than the light's wavelength causes a strong enhancement of the electric field. However, by their time, Mie's and Gans' theories were no more than interesting insights into an intriguing physical phenomenon. Possible applications for metal nanoparticles based on these findings were hardly discussed.

In the last decades, this attitude has changed dramatically thanks to the improvements in nanoparticle fabrication. Both wet chemical processes and etching techniques allow the production of particles of arbitrary size and shape. Additionally, in contrast to the early 1900s, electron microscopes or AFMs allow precise control over the particles. These developments have paved the way for a plethora of application ideas utilising the features of plasmonic nanoparticles as light antennas, absorbers and scatterers at tunable wavelengths.

The strong and tunable absoprtion is for example applied to remotely generate heat in a strongly confined region [7]. This heat can be harvested for cancer therapies [8], for nanosurgery [9], but also for other uses like 3D printing [10]. A further scope of applications for plasmonic nanoparticles is sensing [11]. The change of their optical properties under aggregation, the high sensitivity to the chemical environment or their ability to enhance the fluorescence of adjacent chromophores makes metal nanoparticles promising

sensors with a sensitivity down to the single molecule limit [12]. Moreover, plasmonic nanoparticles have proven to serve as pigments for sub-diffraction image printing [13]. Another wide field that utilises a wide range of plasmonic properties – the local heat around nanoparticles combined with the electric field enhancement and the generation of nonthermal electrons – is plasmon assisted photochemistry [14]. Here, plasmonic nanoparticles are used as catalisers for chemical reactions like water splitting [15] or CO_2 reduction [16]. These presented concepts constitute only a small fraction of the various ideas how plasmonic nanoparticle might shape future technologies.

One of the most promising areas of application is yet to be mentioned as it plays a major role in this work: The coupling of localised plasmons to electric excitations in atoms, molecules or semiconductors. The enhanced electric fields in vicinity of plasmonic nanoparticles are used to increase the efficiency of solar cells [17], to establish lasing at the nanoscale [18], or to enhance infrared [19] and optical absorption [20]. Surface enhaced Raman spectroscopy (SERS) [21] makes use of the high electric fields with which the Raman scattering signal even of single molecules can be investigated [22]. These applications have in common that this light–matter coupling is excelled by other energy decay channels. The situation is called the *weak coupling* regime. When the coupling exceeds all decay channels a new and intriguing regime arises: the *strong coupling* regime. In this regime, new light–matter hybrid states emerge. These hybrid states possess both light and matter like properties and possibly even new features diverging from those of the original subsystems. Such hybrid systems have been proposed to faciltate the realisation of quantum networks [23], to serve as optical switches [24], to enable coherent control over chemical landscapes [25], to allow for thresholdless lasing [26] and much more.

This cumulative dissertation presents the articles I authored or co-authored during my time as PhD student in the group of ultrafast dynamics of condensed matter (UDKM) at the University of Potsdam. The work's main focus lies on the articles to which I contributed as main author. These discuss the coupling between plasmons in gold nanoparticles and excitons in an organic dye in terms of strong coupling, its detection and the consequences of the coupling in general. The systems under investigation are core–shell nanoparticles with a gold core and a shell of the J-aggregate forming dye TDBC. Such J-aggregates possess very high transition dipole moments which enable strong light–matter couplings. The articles present a method to tune the plasmon resonance by manipulating the particles' environment. This way, the coupling strength of particles with various sizes can be determined. The work also shows that the wide spread way of measuring the extinction spectrum of the nanoparticles can lead to erroneous conclusions and that indeed, scattering and absorption should rather be recorded individually. Additionally, this work discusses that vacuum fluctuations can saturate the dye. Taking this effect into account enables a precise simulation of spectra of coupled core–shell systems.

Other articles in this thesis investigate the reaction of gold nanoparticles to optical heating. In all potential applications utilising localised plasmons, nanoparticles are exposed to radiation and will change temperature due to absorption. Consequently, all applications require precise knowledge about the influence of heat on the particles. This might address changes of the optical properties, heat diffusion within the particles and their surroundings up to possible melting of the particles. The change of the optical properties is discussed for the coupled core–shell nanoparticles. Moreover, this work investigates bare nanotriangles under optical excitation. The temporal behaviour in the first picoseconds after excitation is directly observed with pulsed X-rays. Moreover, the work discusses the melting of the

particles under continuous optical heating. This melting process can start earlier for larger illuminated areas despite lower excitation intensities.

This dissertation is organised as follows: Chapter 2 gives a short overview of the articles, their respective scientific novelties and my personal contributions to their development. Chapter 3 introduces the theoretical foundations of these articles. Addressing readers without specialist's knowledge in the field as well as graduate and undergraduate students, mainly my successors in the UDKM, I decided to give a thorough and concise introduction. It includes detailed derivations and elaborate discussions about the topics of interest for this work. Here, the main focus is the knowledge that is required for a full understanding of the articles discussing plasmon–exciton coupling. The theoretical part is followed by an introduction into the methodology of this work in Chapter 4. Having my successors in mind again, I give a detailed introduction into the sample fabrication and measurement set-ups. The articles are then presented in Chapter 5. This chapter forms the scientific core of this dissertation. The articles are preceded by a short introduction presenting the links between the articles and each article's role in its respective scientific context. Eventually, Chapter 6 will conclude the work and give an outlook to possible development in the near future based on the presented articles.

2 | List of Articles

The following articles constitute the scientific core of this dissertation. They were planned, drafted and completed in my time as doctoral researcher at the University of Potsdam financed by the DFG via the graduate school *School of Analytical Sciences Adlershof* (SALSA). All articles discuss plasmonic gold nanoparticles and can be apportioned to two topics: plasmon–exciton coupling and optical heating. The first four articles discuss the coupling between localised plasmons on gold nanoparticles to the excitons in shells formed of an organic dye. Articles I and II focus on the regime of strong coupling, the third shows that already the vacuum plasmon field can saturate the excitonic transition in the shell. The fourth article forms the bridge between the two topics as it discusses the reaction of optical heating in coupled plasmon–exciton nanoparticles. The last two articles present transient (Article V) and static (Article VI) measurements of excited gold nanotriangles. All articles are listed below together with a specification of the scientific novelties they present, as well as with a description of my contribution to the respective article.

Felix Stete, Wouter Koopman, and Matias Bargheer, *ACS Photonics* 4, 7 (2017)

This article serves with three main contributions to the scientific field of strong plasmon–exciton coupling: First, the technique of layer-by-layer deposition of polyelectrolytes has not been used in this field before. This technique enables a tuning of the plasmon resonance in nanoparticles without changing the particles' sizes or shapes. This enables a completely new way of engineering the optical response of a composite system and facilitates an assessment of the coupling strength. As a second key point, the article gave experimental evidence that the simple measurement of the extinction can result in erroneous results when trying to assess the coupling regime. Scattering and absorption spectra need to be recorded independently. As a third topic, the article introduces a simple model system of two coupled oscillators with which the differences between scattering, absorption and extinction can be exemplified.

I developed the technique for sample manufacturing, I conducted all experiments, evaluated the data, created the graphical content and substantially contributed to writing the manuscript.

II **Size-Dependent Coupling of Hybrid Core–Shell Nanorods: Toward Single-Emitter Strong-Coupling** **123**

Felix Stete, Phillip Schoßau, Wouter Koopman, and Matias Bargheer, *The Journal of Physical Chemistry C* 122, 31 (2018)

This article presents a discussion about the connection between size and coupling strength in core-shell nanoparticles. Until this point this had only been done theoretically. The article confirms the theoretical prediction of increasing coupling strength with decreasing particle size and even provides a quantitative explanation. Additionally, the possibility of single emitter strong coupling is predicted with a simple gold nanoparticle as cavity - a system much less complex than other suggested geometries.

I supervised a bachelor student who conducted one measurement series and I conducted the other measurements myself. I evaluated the data, created the graphical content and substantially contributed to writing the manuscript.

III **Vacuum Induced Saturation in Plasmonic Nanoparticles** **133**

Felix Stete, Wouter Koopman, Günter Kewes, Carsten Henkel, Oliver Benson, and Matias Bargheer, *submitted* , (2020)

This article introduces the intriguing effect of vacuum induced saturation on plasmonic nanoparticles. It argues that the vacuum fluctuations in electromagnetic cavities can decrease the probability of photon absorption. Such an effect has been observed in traditional cavity quantum electrodynamics, but not yet in the plasmonic context. Besides the fundamental insight, the article provides a modified expression for the susceptibility of two-level systems in plasmonic cavities. This new expression for the susceptibility allows the accurate simulation of the extinction spectra of the core–shell particles. Previously published theoretical models predicted an electromagnetic mode that could never be observed in measurements. Taking the effect of vacuum induced saturation into account, allows the reconciliation between theory and experiment.

I conducted the experiments, I evaluated the data and provided the analytical simulations, created the graphical content and substantially contributed to writing the manuscript.

IV **Optical Non-Linearities in Plasmon–Exciton Core–Shell Systems: The Role of Heat** . . **143**

Felix Stete, Wouter Koopman, and Matias Bargheer, *submitted* , (2020)

This article presents simulations of transient spectra of coupled core–shell nanoparticles. Such spectra could previously only be explained phenomenologically. The article combines two methods: a well-established method of simulating the behaviour of pure nanoparticles and the simulation of static coupled spectra developed in Article III. The

article confirms that transient features on a picosecond timescale mainly stem from the heating of the gold.

I constructed the measurement set-up and conducted the experiments. I evaluated and simulated the data, created the graphical content and substantially contributed to writing the manuscript.

V **Watching the Vibration and Cooling of Ultrathin Gold Nanotriangles by Ultrafast X-ray Diffraction** **153**

Alexander von Reppert, Radwan M. Sarhan, **Felix Stete**, Jan Pudell, Natalia Del Fatti, Aurelién Crut, Joachim Koetz, Ferenc Liebig, Claudia Prietzel and Matias Bargheer, *The Journal of Physical Chemistry C* 120, 50 (2016)

This article presents a study of the dynamics of gold nanotriangles after optical excitation. It is the first study that is based on a laser-driven femtosecond X-ray source. This enabled a direct observation of the out-of-plane strain of the particles. Previous studies were either experimentally challenging since a free electron laser was mandatory or they could only indirectly assess the strain via optical probing techniques. In addition to the experimental novelties, a simple 1D simulation reproduced the measurement results nicely.

I recorded the SEM images, provided parts of the graphical content and commented on the manuscript.

VI **Scaling-Up Nano-Plasmon Catalysis: The Role of Heat Dissipation** **161**

Radwan M. Sarhan, Wouter Koopman, Jan Pudell, **Felix Stete**, Matthias Rössle, Marc Herzog, Clemens Schmitt, Ferenc Liebig, Joachim Koetz, and Matias Bargheer, *The Journal of Physical Chemistry C* 123, 14 (2019)

This article examines the consequences of macroscopic illumination of nanoparticles on a substrate. Usually, studies on nanoparticles as for example utilised in SERS or plasmon assisted photochemistry employ strongly focussed laser beams. This article shows that simply scaling up the illuminated area using the same or even lower intensity can cause the particles to melt. It presents simulations that show that the particle cooling shifts from 3D to 1D heat transport. This effect had not been investigated previously but needs to be taken into account in large scale nanoparticle experiments.

I constructed a Raman microscope for preliminary measurements to assess the settings used in the actual experiments. I also recorded the SEM images, designed the graphical content and commented on the manuscript.

3 | Theoretical Background

This dissertation mainly discusses the coupling between plasmons on gold nanoparticles and excitons in organic emitters in Articles I – IV. Additionally, Articles IV – VI examine gold nanoparticles exposed to optical heating. Also there, plasmons play a crucial role. This chapter shall establish the theoretical background of the main concepts discussed in the research articles that will later be presented in Chapter 5.

Plasmons describe resonances of the free electrons in a metal. In the case of gold and silver nanoparticles, these resonances, referred to as localised plasmons, lie in the visible range. They come along with strong electric fields on the particle surface which can affect emitters in the particle's vicinity. This impact works in both directions and the excitons can also influence the plasmons. If the interaction exceeds all other channels for energy dissipation, the regime is called the *strong coupling* regime. The main ingredients for understanding this process will be introduced as follows:

We will start with a very short roundup of the main features of the permittivity. The permittivity is the fundemental material properity behind all optical processes and determines the conditions for the occurrence of plasmons. It shall therefore receive a short introduction on Section 3.1.

Localised plasmons on metal nanoparticles are the topic of Section 3.2. The main tool for investigating plasmons is optical spectroscopy. Therefore, this section introduces the optical response of metal nanoparticles. In its first part, this response is derived in detail for nanospheres. Subsequently, we will discuss the optical properties of metal ellipsoids. Their shape is a good approximation to nanorods which represent one of the main systems investigated in this dissertation. For most of the articles, the particles were covered with a thin film of an organic dye. Therefore, we will later take a look at the optical properties of core–shell ellipsoids. The presented concepts for spheres, ellipsoids and core–shell particles are strictly valid only for particles that are much smaller than the wavelength of visible light. This assumption is not always true for the particles used for the articles. This is taken into account in the last part of the section where the theory is expanded to larger particles.

The subsequent Section 3.3 discusses the phenomenon of J-aggregates, a special type of clusters that can be formed by some organic dyes. These aggregates feature very sharp and intense resonances, strongly enhancing the coupling to plasmons in comparison to monomer dyes or quantum dots. We will discuss the basic concept of direct dipole-dipole interaction within an aggregate which explains the main features of J-aggregates.

The optical properties of bare metal nanoparticles as well as of core–shell systems mainly depend on the permittivity of the involved materials. Therefore, Section 3.4 shall establish a profound understanding of the permittivity of gold and two-level systems as foundation for the detailed simulations that are presented in the Articles III and IV. Simple models – the approximation of gold as a Drude metal and of an emitter as Lorentz oscillator – are extended to models with higher precision. Interband transitions are

incorporated into the permittivity of gold via the joint density of states and the permittivity of a two-level system is derived from the semi-classical optical Bloch equations enabling accurate simulations of the core–shell nanoparticle systems.

At the end of the chapter, Section 3.5 will be dealing with the general concept of coupling between electromagnetic cavities and quantum emitters. The energy transfer between the two systems can be so strong that it exceeds all other decay channels. This situation is described by the strong coupling regime, a regime where the original systems hybridise and states with both light and matter properties emerge. The coupling is first discussed within the framework of a full quantum treatment and subsequently generalised to the system of two coupled classical oscillators. These oscillators eventually help to assess the regime of strong coupling.

3.1 Permittivity

This work discusses plasmonic nanoparticles, mainly their interaction with excitations in organic emitters but also their reaction to optical heating. Plasmons are resonant oscillations of the free electrons in a metal nanostructure which can occur under radiation of an external electric field. The conditions for the occurrence of resonances are determined by the permittivity ε of the structure's material and of the environment. The permittivity determines not only the occurrence of plasmons but generally the response of a substance to an external electric field as it connects the electric field with the polarisation within the material. This work mostly discusses the features of gold nanoparticles investigated by optical spectroscopy. The permittivity is therefore at the foundation of the theory presented in this chapter and this first section gives a short roundup of its main features.

When a material is exposed to an external electric field $\mathbf{E}$, its charge carriers get displaced and a polarisation $\mathbf{P}$ builds up. This polarisation is the sum of all microscopic dipoles per unit volume. The electric field and the polarisation define the dielectric displacement field $\mathbf{D}$ via

$$\mathbf{D} = \varepsilon_0 \mathbf{E} + \mathbf{P} \,. \tag{3.1}$$

Here, ε_0 represents the vacuum permittivity.

On the other hand, the dielectric displacement field and the electric field are directly connected by the permittivity since

$$\mathbf{D} = \varepsilon_0 \varepsilon \mathbf{E} \,. \tag{3.2}$$

The polarisation and the permittivity are thus directly related as

$$\mathbf{P} = \varepsilon_0 (\varepsilon - 1) \mathbf{E} = \varepsilon_0 \chi \mathbf{E} \,. \tag{3.3}$$

The factor χ is the susceptibility and also often used to describe the material's reaction to an external

field. This means, the permittivity and susceptibility are measures of the reaction of a material to an electric field. A larger ε (and consequently a larger χ) indicates a stronger polarisation for the same electric field. Note that this work uses ε and the term permittivity always as relative value to the vacuum.

In a metal, a part of the electrons can move freely in an external field. This means that for a static field, a part of the charge carriers can theoretically be infinitely displaced and consequently $\varepsilon = \infty$. In contrast, for dielectric materials without free electrons, the permittivity for constant fields is finite.

In case of an oscillating external field, for example an incoming wave, also the polarisation undergoes oscillations. Like in the case of a classical driven oscillator, their amplitude depends on the frequency of the exciting field. Also, polarisation and external field do not need to oscillate in phase. This reflects in a non-vanishing imaginary part of $\varepsilon(\omega) = \varepsilon'(\omega) + i\varepsilon''(\omega)$. The imaginary part accounts for the absorption of electric energy whereas the absolute $|\varepsilon|$ accounts for the polarisability's amplitude. ε' and ε'' are connected via the Kramers–Kronig relations that means they are not independent and the knowledge of one of the two directly enables the determination of the other. We will use this in Section 3.4 where we will calculate the permittivity of gold.

All optical properties of a material are determined by its permittivity since it defines the reaction of all charge carriers to an electric field. Consequently, the (complex) refractive index $n = n' + i\kappa$ is directly connected to ε via

$$n = \sqrt{\varepsilon}\,. \tag{3.4}$$

Let us take a look at the influence of the permittivity on an electromagnetic wave. The dispersion relation for the wavevector $k = k' + ik''$ is given by

$$k = n\frac{\omega}{c}\,. \tag{3.5}$$

An electromagnetic wave propagating in the z-direction inside the material of interest writes as

$$E = E_0 e^{i(kz-\omega t)} + c.c. = E_0 e^{-k''z}\left(e^{i(k'z-\omega t)} + c.c.\right) = E_0 e^{-\kappa\frac{\omega}{c}z}\left(e^{i(n'\frac{\omega}{c}z-\omega t)} + c.c.\right)\,. \tag{3.6}$$

This means that κ accounts for the attenuation of the wave. For small susceptibilities, the refractive index can be approximated from a Taylor series to $n \approx (1+\varepsilon')/2 + i\varepsilon''/2$. This is the case for optically thin media like gases or dielectrics far away from resonances. Hence, the attenuation of a wave is directly proportional to the permittivity's imaginary part. For materials with larger permittivities, the situation is more complex. But the relation $\kappa = \varepsilon''/2n'$ (which is directly retrieved from equating the coefficients in Equation 3.4) indicates that also here, ε'' mainly accounts for the attenuation of a wave inside the material.

This short overture should reestablish our knowledge about the permittivity as direct measure for the polarisation that arises due to an external electric field. We will meet this material feature throughout this work starting with the description of localised plasmons in the next section.

3.2 Localised Plasmons

Plasmons are resonant collective oscillations of the free electrons in a material. The effect can be be distinguished in three different manifestations: *Bulk plasmons* describe longitudinal oscillations of the electron cloud in the whole volume of a bulk metal. *Surface plasmon polaritons* are electron oscillation waves propagating along the metal surface. *Localised plasmons* (also referred to as localised surface plasmons) can be considered as a mixture of the first two kinds as coherent oscillations of the electron cloud in metal nanoparticles, causing charge displacements on the surface. Due to their high spatial confinement, localised plasmons can strongly enhance electric fields. This effect has inspired a plethora of applications suggested in the past years. This includes nanoparticles as chemical or biological sensors [11], in photovoltaics [17], for surface enhanced infrared absorption [19] or Raman scattering [21], for data storage [27], as contrast agents for photoacoustic tomography [28] and many more [29, 30].

Additionally, the enhancement can be employed to achieve strong interactions between the electric fields and emitter excitations, as is discussed in detail in this work (see Articles I – IV). Localised plasmons can also efficiently absorb radiation and can cause strongly localised thermal energy. Articles IV – VI examine consequences of this optical heating process in nanoparticles. To provide a basis for the understanding of these articles, this section introduces the most important theoretical aspects of localised plasmons on metal nanoparticles.

The basic phenomenon is illustrated in Figure 3.1. The cloud of free conduction electrons can be displaced from the ion lattice by an external electric field. This displacement causes an accumulation of negative charges on one side of the particle and of positive charges on the other. The attraction between these charges causes a restoring force on the free electrons. For every system in which a restoring force tries to reestablish an equilibrium state, an eigenfrequency ω_0 can be found at which the system can be driven in resonance by an external force. In case of nanoparticles, these resonances are called localised plasmons. For gold an silver nanoparticles (among others), the resonance frequencies fall into the visible range making them promising systems for light manipulation.

Plasmonic nanoparticles can be seen as cavities for electromagnetic energy. The modes are matter bound and can thus be confined to almost arbitrarily small volumes. Smaller mode volumes generate higher fields enabling tremendous field strengths at the surface of plasmonic nanoparticles [31].

Due to their spectral position and their strong reaction to visible light, plasmons and their influence on external electric fields are best investigated by optical spectroscopy. To establish an understanding of the respective spectra presented in this work's articles, this section discusses the basic theory explaining the optical response of metal nanoparticles. For this, we will examine three example systems: In the first part, the simplest system of nanospheres is introduced. Their optical cross sections shall be derived in detail and key features like the resonance position or the dependence of the resonance on the surrounding medium will be discussed. The theory will thereafter be expanded to ellipsoidal particles. Eventually, as most general case and as best representation of the systems actually used for Articles I – IV, the case of particles consisting of an ellipsoidal core and a thin shell will be discussed. All derivations are made in the quasistatic limit in which electric fields are assumed to be constant in space and vary only in time. This limit demands particle dimensions that are much smaller than the wavelength. To expand the theory to larger particles, the last part of this section will introduce a correction to the quasistatic approach.

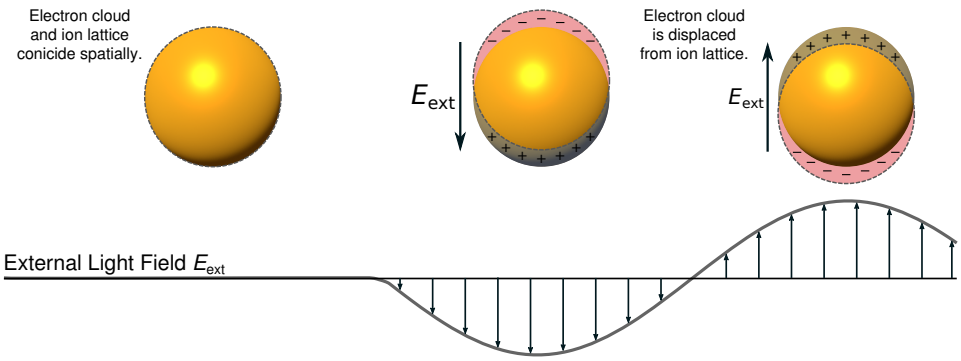

Figure 3.1: Phenemonological illustration of a localised plasmon. The cloud of free electrons and the ion lattice of a metal nanoparticle are in the same position until an external electric field E_{ext} is applied. In that case, the electron cloud is displaced from the immobile lattice. The displacement induces a charge separation which causes a restoring force on the electrons.

3.2.1 Spherical Particles

The theoretical analysis of the optical response of nanospheres is nowadays strongly connected to Gustav Mie and in his honour often called Mie theory. He wanted to understand the scattering and absoprtion behaviour of small particles of gold suspended in water. In 1908, he developed a theory which is not only valid for gold spheres but for spheres of any material embedded in a homogeneous medium. Mie theory describes the exact analytical solution to the question how a spherical particle reacts to an incoming external light wave [5]. It does not require any approximations or assumptions to the electric field or the particle size. The solution is based on a multipole extension of the fields and the result is a rather complex expression consisting of an infinite series of the Riccarti–Bessel functions, from which physical insight is hard to gain.

For particles that are small compared to the wavelength of the incoming light, a simpler and more instructive approach is sufficient to describe the optical response. It will eventually show that a small particle can be treated as point dipole with a polarisability α. This polarisability determines all optical features of the dipole and consequently of the particle. In the following, we want to derive this insight in detail.

In case of a small particle, the electric field of an incoming plane wave can be regarded as constant at all points of the particle volume. The time dependence can be added later when the static field is known. Without temporal dependence, the problem reduces to the Laplace equation for the electric potential Φ, that means

$$\Delta\Phi = 0\,. \tag{3.7}$$

This equation is to be solved under the boundary conditions dictated by the respective particle geometry. From the resulting potential Φ, we directly obtain the electric field at all positions inside and outside of the particle.

Polarisability of a nanosphere: The following section roughly reproduces the arguments given by

Maier in his book on plasmonics [32] to find the solution of to the Laplace equation for a metal nanosphere with radius a in a constant external electric field E_0. Its goal is a detailed derivation of the sphere's polarisability α. For simplicity, the coordinates are chosen such that the origin falls into the sphere's centre and the electric field points in the z-direction. Inside the sphere, the (frequency dependent) permittivity is given by ε_{sph}, outside by ε_{med}. Figure 3.2 depicts an illustration of the geometry.

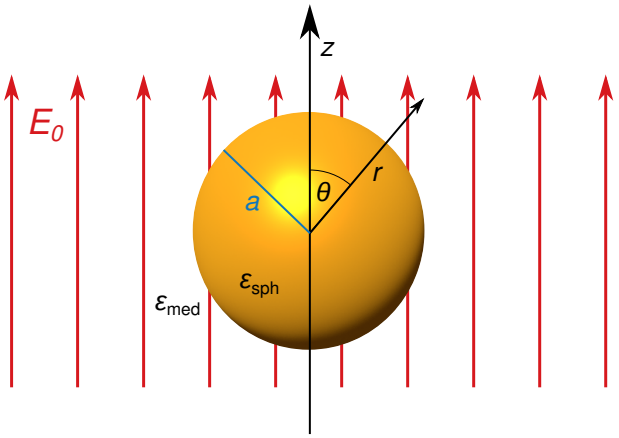

Figure 3.2: Gold nanosphere with radius a illuminated by an external light field E_0. The permittivities are ε_{sph} inside the particle and ε_{med} in the area surrounding the particle.

Due to the system's spherical symmetry, a treatment of the problem in spherical coordinates (r as radial distance, θ as polar angle, ϕ as azimuthal angle) seems convenient and the Laplace equation reads as

$$\frac{1}{r^2 \sin\theta}\left[\sin\theta\frac{\partial}{\partial r}\left(r^2\frac{\partial}{\partial r}\right)+\frac{\partial}{\partial\theta}\left(\sin\theta\frac{\partial}{\partial\theta}\right)+\frac{1}{\sin\theta}\frac{\partial^2}{\partial\varphi^2}\right]\Phi(r,\theta,\varphi)=0\,. \tag{3.8}$$

We can find the solution for two regions: Φ_{I} inside the sphere and Φ_{II} outside of the sphere. The potential outside can be expressed as the potential of the unaffected eletric field E_0 added to the potential of the scattered field $\Phi_{\text{II}} = \Phi_0 + \Phi_{\text{scatt}}$. Φ_{I} and Φ_{II} are connected to an overall potential via the boundary conditions at the surface: On a metal surface the tangential component of the electric field E needs to be continuous as well as the normal component of the dielectric displacement field D. In the case of a metal sphere in spherical coordinates, these conditions read as [32]

$$\left.\frac{\partial\Phi_{\text{I}}}{\partial\theta}\right|_{r=a}=\left.\frac{\partial\Phi_{\text{II}}}{\partial\theta}\right|_{r=a} \quad \text{and} \quad \left.\varepsilon_{\text{sph}}\frac{\partial\Phi_{\text{I}}}{\partial r}\right|_{r=a}=\left.\varepsilon_{\text{med}}\frac{\partial\Phi_{\text{II}}}{\partial r}\right|_{r=a}. \tag{3.9}$$

As further boundary condition the potential needs to be finite at the origin. That means

$$\Phi_{\text{I}}(r=0)<\infty\,. \tag{3.10}$$

This is due to the absence of residual charges in the sphere's centre. Furthermore, the sphere's influence on the external field E_0 should be negligible at positions far away from the sphere, that is

$$\Phi_{\mathrm{II}} \xrightarrow{r\to\infty} \Phi_0 = -E_0 z = -E_0 r\cos\theta\,. \tag{3.11}$$

Solving the Laplace equation is simplified by the choice of the coordinate system: The system is symmetric in φ. Thus, Φ does not depend on φ and the last term in the Laplace equation gives zero. The resulting differential equation has a general solution and for the two regions it reads [33]:

$$\Phi_{\mathrm{I}} = \sum_{k=0}^{\infty} [A_k r^k + B_k r^{-(k+1)}] P_k(\cos\theta)\,, \tag{3.12a}$$

$$\Phi_{\mathrm{II}} = \sum_{k=0}^{\infty} [C_k r^k + D_k r^{-(k+1)}] P_k(\cos\theta)\,. \tag{3.12b}$$

Here, $P_k(x)$ represents the Legendre polynomial of the k-th order and A_k, B_k, C_k and D_k are constants that are to be found in the following section.

The requirement of a finite field at the point of origin results in the necessity of all B_k being zero since otherwise their respective terms would diverge for $r \to 0$. The fact that the sphere should not have influence far away form the point of origin requires that

$$\sum_{k=0}^{\infty} C_k r^k P_k(\cos\theta) = \Phi_0 = -E_0 r\cos\theta\,. \tag{3.13}$$

Legendre polynomials form a orthonormal basis. This means that there is only one distinct representation of $\cos(\theta)$ as a combination of Legendre polynomials. Since $P_1(\cos\theta) = \cos\theta$ already, all C_k need to be zero for $k \neq 1$ and $C_1 = 1$.

We now find the potentials inside and outside of the sphere as

$$\Phi_{\mathrm{I}} = \sum_{k=0}^{\infty} A_k r^k P_k(\cos\theta)\,, \tag{3.14a}$$

$$\Phi_{\mathrm{II}} = \Phi_0 + \sum_{k=0}^{\infty} D_k r^{-(k+1)} P_k(\cos\theta)\,. \tag{3.14b}$$

These two equations still need to fulfil the two boundary conditions at the particle surface. The condition of a continuous normal displacement field (right side of Equation 3.9) demands

$$\sum_{k=0}^{\infty} \left[\varepsilon_{\mathrm{sph}} A_k k a^{k-1} + \varepsilon_{\mathrm{med}} D_k (k+1) a^{-(k+2)}\right] P_k(\cos\theta) = -\varepsilon_{\mathrm{med}} E_0 \cos\theta\,. \tag{3.15}$$

Again, the orthogonality of the Legendre polynomials requires each prefactor $k \neq 1$ to vanish independently. That is

$$\varepsilon_{\text{sph}} A_k k a^{(k-1)} + \varepsilon_{\text{med}} D_k (k+1) a^{-(k+2)} = 0\,. \tag{3.16}$$

For $k = 1$, the the prefactors on both sides need to be equal, namely

$$\varepsilon_{\text{sph}} A_1 + 2\varepsilon_{\text{med}} D_1 a^{-3} = -E_0 \varepsilon_{\text{med}}\,. \tag{3.17}$$

Plugging Equations 3.14 into the condition of continuous tangential electric fields (left side of Equation 3.9), we obtain

$$\sum_{k=0}^{\infty} \left[A_k a^k - D_k a^{-(k+1)} \right] \frac{\partial}{\partial \theta} P_k(\cos\theta) = -E_0 a \frac{\partial}{\partial \theta} \cos\theta\,. \tag{3.18}$$

Since also the derivations of the Legendre polynomials are orthogonal [33], the same arguments as above are valid and for $k \neq 1$, A_k and B_k have to fulfil

$$A_k a^k - D_k a^{-(k+1)} = 0 \tag{3.19}$$

and for $k = 1$,

$$A_1 + D_1 a^{-3} = E_0\,. \tag{3.20}$$

For all $k \neq 1$, only $A_k = D_k = 0$ can satisfy Equations 3.16 and 3.19 simultaneously whereas the system of equations for $k = 1$ is solved by

$$A_1 = -\frac{3\varepsilon_{\text{med}}}{\varepsilon_{\text{sph}} + 2\varepsilon_{\text{med}}} E_0\,, \tag{3.21a}$$

$$D_1 = \frac{\varepsilon_{\text{sph}} - \varepsilon_{\text{med}}}{\varepsilon_{\text{sph}} + 2\varepsilon_{\text{med}}} a^3 E_0\,. \tag{3.21b}$$

The findings for the A_k ad D_k can be plugged into Equations 3.14 and we find the static potential inside and outside of the sphere to be

$$\Phi_{\text{I}} = -\frac{3\varepsilon_{med}}{\varepsilon_{sph} + 2\varepsilon_{med}} E_0 r \cos\theta\,, \tag{3.22a}$$

$$\Phi_{\text{II}} = \Phi_0 + \frac{\varepsilon_{sph} - \varepsilon_{med}}{\varepsilon_{sph} + 2\varepsilon_{med}} E_0 a^3 \frac{\cos\theta}{r^2}\,. \tag{3.22b}$$

The potential inside the sphere describes an electric field parallel to the external field E_0. The potential outside is the superposition of the external potential and that of an electric dipole at the point of origin with a dipole moment

$$\mathbf{p} = 4\pi\varepsilon_0\varepsilon_{\text{med}}a^3\frac{\varepsilon_{\text{sph}}-\varepsilon_{\text{med}}}{\varepsilon_{\text{sph}}+2\varepsilon_{\text{med}}}\mathbf{E}_0\,. \tag{3.23}$$

That means, the potential outside reads as

$$\Phi_{\text{II}} = \Phi_0 + \frac{1}{4\pi\varepsilon_0\varepsilon_{\text{med}}}\frac{\mathbf{p}\cdot\mathbf{r}}{r^3}\,. \tag{3.24}$$

The dipole moment is proportional to the external electric field. This is usually the case for dipoles with movable charges for which then a polarisability α can be defined via $\mathbf{p} = \varepsilon_{\text{med}}\alpha\mathbf{E}_0$. The polarisability determines the strength of the dipole moment in a given electric field. It is a fundamental feature of a point dipole and from it, all optical properties, like absorption or scattering can be deduced. In our case, the polarisability of a small sphere directly results from equation 3.23 to be

$$\alpha = 4\pi\varepsilon_0 a^3\frac{\varepsilon_{\text{sph}}-\varepsilon_{\text{med}}}{\varepsilon_{\text{sph}}+2\varepsilon_{\text{med}}}\,. \tag{3.25}$$

This expression for the polarisability of a small nanosphere is the main insight of the previous section. It is the starting point for the calculation of the sphere's optical properties. We will find expressions for the polarisability of ellipsoids and core–shell particles later in this work. Note that, for spheres, it is of the same form as the Clausius-Mossotti relation. This is, in fact, not very surprising since also that relation describes the polarisability of a sphere depending on its permittivity [33].

We obtain the electric field around the particle from $\mathbf{E} = -\nabla\Phi$. With $\mathbf{e}_{\text{r}}$ as unit vector in direction of $\mathbf{r}$, it writes as

$$\mathbf{E}_{\text{I}} = \frac{3\varepsilon_{\text{med}}}{\varepsilon_{\text{sph}}+2\varepsilon_{\text{med}}}\mathbf{E}_0\,, \tag{3.26a}$$

$$\mathbf{E}_{\text{II}} = \mathbf{E}_0 + \frac{\alpha}{4\pi\varepsilon_0}\frac{3\mathbf{e}_{\text{r}}(\mathbf{e}_{\text{r}}\cdot\mathbf{E}_0)-\mathbf{E}_0}{r^3}\,. \tag{3.26b}$$

Up to this point, we assumed the electric field to be constant in time and space. To investigate a nanoparticle's reaction to light, the electric field must be allowed to vary in time. We worked in the quasistatic limit in which the external field can be assumed constant in space. We saw that, in this case, the particle can be treated as a point dipole. In the quasistatic limit, fields can change in time and a light field can be written as a plane wave with $\mathbf{E}(\mathbf{r},t) = \mathbf{E}_0(\mathbf{r})e^{i\omega t}$. In this chapter's first section, we discussed the frequency dependence of the permittivity. Consequently, α, too, is frequency dependent. It can therefore show resonances whenever the denominator in Equation 3.25 becomes minimal. The sphere's permittivity may have a non-vanishing imaginary part and writes as $\varepsilon_{\text{sph}}(\omega) = \varepsilon'_{\text{sph}}(\omega) + i\varepsilon''_{\text{sph}}(\omega)$. For a dielectric medium, the permittivity's imaginary part can usually be neglected. In the case of a small or

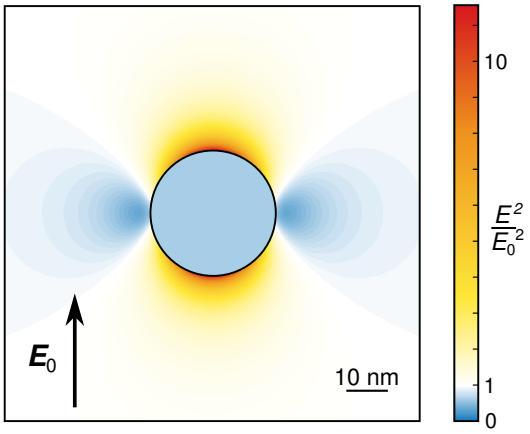

Figure 3.3: Square value of the electric field around a sphere excited by an external field E_0. The field is calculated from Equation 3.26, the sphere's diameter is 30 nm, $\varepsilon_{\text{sph}} = 2 + 3.7i$ and $\varepsilon_{\text{med}} = 1$.

weakly dispersive $\varepsilon''_{\text{sph}}(\omega)$, the polarisability becomes resonant for

$$\varepsilon'_{\text{sph}} = -2\varepsilon_{\text{med}} \,. \tag{3.27}$$

This relation is known as the *Fröhlich condition* [34]. It describes the state where the free electrons oscillate in resonance with the external light field. Exactly these modes are the *localised plasmons* this section is meant to introduce. For gold and silver, the Frölich condition is fulfilled for visible frequencies making both metals suitable materials for plasmonic applications.

Note that if the imaginary part is strongly dispersive or not negligibly small, the maximum position of α can slightly deviate from the position predicted by the Fröhlich condition. Moreover, a metal particle in a dielctric medium is not the only system that can fulfil this condition. The inverse case of dieletric particles or simple voids inside a metal film is also a valid system to obtian resonances [35]. This situation will however not be treated further since the articles of this work only discuss metal nanoparticles.

In plasmonic nanoparticles, the induced dipole moment $\mathbf{p} = \varepsilon_{\text{med}} \alpha \mathbf{E}_0 e^{i\omega t}$ can reach high values causing strong electric fields. Thus, the local field can be higher than the incoming field E_0, an effect that is usually referred to as *field enhancement*. The effect is illustrated in Figure 3.3 which depicts the field enhancement around a metal nanosphere with $a = 15\,\text{nm}$ by plotting Equation 3.26 for $\varepsilon_{\text{sph}} = 2 + 3.7i$ – a realistic value for gold – and $\varepsilon_{\text{med}} = 1$. In direct vicinity of the particle, the field is strongly enhanced. This field enhancement at plasmon resonance is the basis for many application ideas amongst which this work will later focus on the coupling to excitons.

Scattering cross section: We can now take a look at the characteristic optical features of plasmonic nanospheres. An incident light field can interact with a plasmonic nanoparticle in three ways: The wave can pass the particle unaffectedly, it can be scattered by the particle and it can be absorbed while the energy is dissipated in the particle. The quantities describing the amount of scattered and absorbed light

are the optical cross sections. To derive the optical cross sections, we can make use of the approximation of the particle as a point dipole and the quantity defining the cross sections is the polarisability α.

The scattering cross section σ_{scatt} of a nanoparticle is calculated by dividing the radiated power by the energy density of the incoming plane wave [36]. The former is obtained via the Pointing vector $\mathbf{S} = \mathbf{E} \times \mathbf{H}$. The electric field of a point dipole is given by [33]

$$\mathbf{E} = \frac{1}{4\pi\varepsilon_0\varepsilon_{\text{med}}} \left[k^2(\mathbf{e}_\text{r} \times \mathbf{p}) \times \mathbf{e}_\text{r} \frac{e^{ikr}}{r} + [3\mathbf{e}_\text{r}(\mathbf{e}_\text{r} \cdot \mathbf{p}) - \mathbf{p}] \left(\frac{1}{r^3} - \frac{ik}{r^2} \right) e^{ikr} \right] \tag{3.28}$$

and the respective magnetic field is given by [33]

$$\mathbf{H} = \frac{ck^2}{4\pi}(\mathbf{e}_\text{r} \times \mathbf{p}) \frac{e^{ikr}}{r} (1 - \frac{1}{ikr}) \,. \tag{3.29}$$

Here, $k = \lambda/2\pi$ is the light's angular wavenumber with λ as the light's wavelength. Note that the previously derived static electric field given by Equation 3.26 is recovered in the vicinity of the particle, i.e. for $kr \ll 1$.

We find the total power P radiated by the dipole via integration of the Pointing vector on a closed surface around the particle and averaging over time. With c denoting the speed of light and n as the refractive index in the medium, this results in [36]

$$P = \frac{1}{4\pi\varepsilon_0\varepsilon_{\text{med}}} \frac{ck^4}{3n} |\mathbf{p}|^2 = \frac{ck^4}{12\pi\varepsilon_0 n} |\alpha|^2 |E_0|^2 \,. \tag{3.30}$$

Now, dividing this power by external field's energy density

$$S_{\text{inc}} = \frac{\varepsilon_0 c}{2n} E_0^2 \tag{3.31}$$

leads to an expression for the scattering cross section of

$$\sigma_{\text{scatt}} = \frac{k^4}{6\pi\varepsilon_0^2} |\alpha|^2 = \frac{8\pi}{3} k^4 a^6 \left| \frac{\varepsilon_{\text{sph}} - \varepsilon_{\text{med}}}{\varepsilon_{\text{sph}} + 2\varepsilon_{\text{med}}} \right|^2 . \tag{3.32}$$

This shows that the scattering becomes resonant at frequencies where α is resonant and thus, when plasmons occur. The scattering cross section can be measured directly with optical spectroscopy. This makes it an important feature for assessing plasmon resonances in nanoparticles.

As an illustration, Figure 3.4 presents the simulation of the scattering cross sections of gold and silver spheres in different media, obtained from Equation 3.32. Three examples were chosen: $\varepsilon_{\text{med}} = 1$ to resemble air, $\varepsilon_{\text{med}} = 1.7$ to resemble water, and $\varepsilon_{\text{med}} = 2.3$ to resemble glass. The lower part of the figure shows plots of the real and imaginary parts of the permittivities that were used from Reference 37.

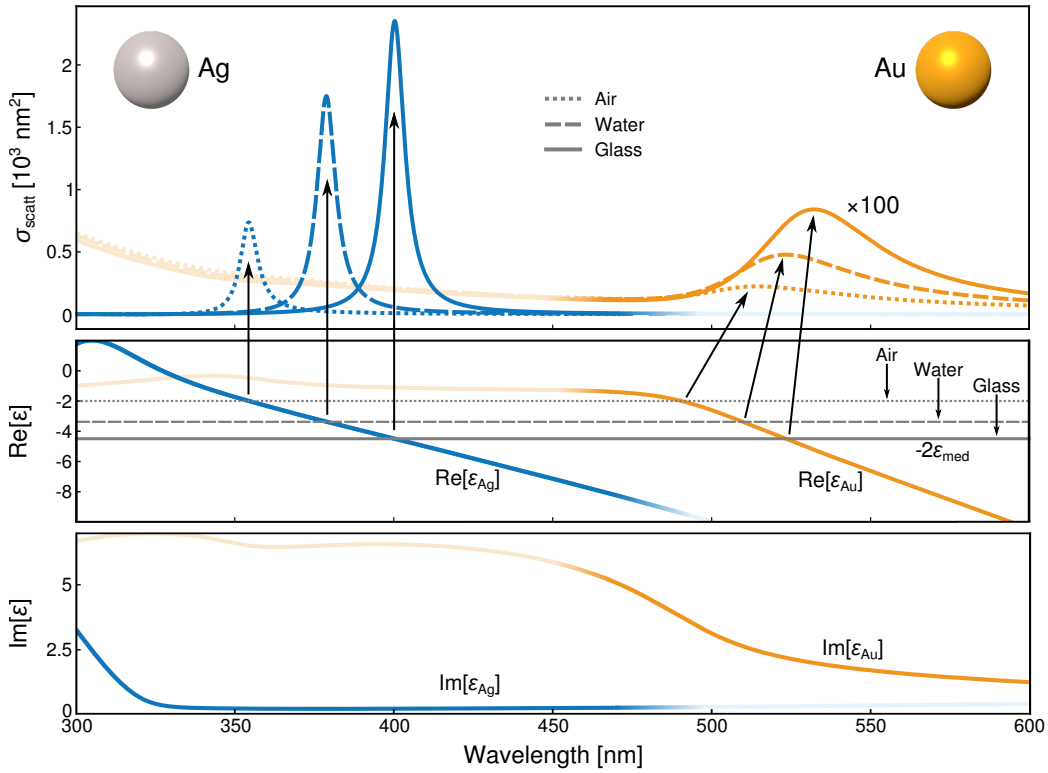

Figure 3.4: Scattering cross sections of silver (blue lines) and gold (orange lines) nanospheres with a diameter of 25 nm in different media. The permittivities are chosen to be $\varepsilon_{med} = 1$ (air, dotted lines), $\varepsilon_{med} = 1.7$ (water, dashed lines) and $\varepsilon_{med} = 2.3$ (glass, solid lines). The central plot illustrates the Fröhlich condition: The real parts of ε_{sph} for gold and silver are plotted with $-2\varepsilon_{med}$ for the respective media. The respective crossing points indicate the spectral position where the Fröhlich condition is met. To understand the amplitudes of the scattering cross section, the imagnary parts of ε_{sph} for gold and silver are shown in the lowest plot. The data for the permittivities of gold and silver were taken from Reference 37.

The real parts are plotted together with $-2\varepsilon_{med}$ for the different media to illustrate the Fröhlich condition. Silver particles were not actually used for the articles in Chapter 5 but they give another instructive example for the properties of localised plasmons.

A few features of metal nanospheres become apparent from this plot. First, resonances occur which lie in the visible range. The Fröhlich condition gives a good approximation for the spectral position of the scattering maxima. It explains for example the blue-shift for silver nanoparticles in comparison to gold. The real part of silver's permittivity simply fulfils the condition $\varepsilon'_{sph} = -2\varepsilon_{med}$ for higher frequencies than in the case of gold. For silver, the Fröhlich condition even predicts the resonance positions almost perfectly since for silver ε''_{sph} is small. For gold on the other hand, the permittivity's imaginary part is larger and more dispersive in the region, where the condition is met. Therefore, it has a stronger influence on the resonance position which is not only defined by ε'_{sph}. The different positions of the scattering maxima make the particle appear in different colours. By the choice of material and also shape of the particle, the colour can be varied arbitrariliy. This effect has already been utilised for centruries

for example in coloured glass [2], although the source of the phenomenon was not yet understood.

Since the particle polarisability depends on ε_{med}, the resonance position is shifted for different environments. Due to the monotonicity of $\varepsilon'_{\text{sph}}$ for both metals in the visible region, an increase of the environment's permittivity implies a red-shift of the resonance wavelength. We can understand this red-shift also in the picture of a displaced electron cloud: The plasmon induces an electric field in the vicinity of the particle. In this field, the medium gets polarised. The induced polarisation charges cause the net charge at the particle surface to decrease [34]. This results in a weakening of the restoring force on the electron cloud and consequently in a lowering of the resonance frequency i.e. a red-shift of the resonance. As seen in the beginning of this chapter, a higher permittivity in the medium leads to a stronger polarisation and consequently to a stronger red-shift of the resonance position. The strong connection between plasmon resonance and surrounding medium makes nanoparticles excellent sensors for changes in refractive index. The effect was employed for Articles I and II where the deposition of thin polymer layers on top of gold nanoparticles caused a change in the environment's refractive index and consequently induced a red-shift in the plasmon resonance.

The height of the peaks can be understood by looking at the scattering cross section when the Fröhlich condition is met. In this case $\varepsilon'_{\text{sph}} = -2\varepsilon_{\text{med}}$ and

$$\sigma_{\text{scatt}} \propto \lambda^{-4} \left[1 + \left(\frac{\varepsilon_{\text{med}}}{\varepsilon''_{\text{sph}}} \right)^2 \right] . \tag{3.33}$$

Thus, the difference of two orders of magnitude between the amplitudes of silver and gold can mainly be ascribed to the λ^{-4}-dependence. But also the larger imaginary part of gold's permittivity contributes to the difference.

Within one material, a red-shift comes along with a larger scattering amplitude, as well. For silver, the imaginary part can be considered as constant over the region of the resonances. But the change in ε_{med} makes up for the increasing λ and causes an increase of σ_{scatt} at the resonance position. In case of gold, this effect is enhanced by the decreasing $\varepsilon''_{\text{sph}}$ resulting in an even larger difference between scattering peaks in different media. Note that the decrease in $\varepsilon''_{\text{sph}}$ also leads to a better fit of the Fröhlich condition for the red-shifted resonances in gold.

Absorption cross section: Since the permittivities of metals are never purely real, the polarisability always has an imaginary component. As a result, the incoming light is not only scattered but also absorbed. The property describing this effect is the absorption cross section σ_{abs}. It is defined in analogy to σ_{scatt}. This time it is the total dissipated power that is set in relation to the incoming energy density. For a point dipole the dissipated power can be retrieved by the Pointing theorem and is given by [36]

$$P_{\text{abs}} = \frac{kc}{2n} \operatorname{Im}[\mathbf{p} \cdot \mathbf{E}_0^*] . \tag{3.34}$$

Here, $\mathbf{E}_0^*$ represents the incoming field's complex conjugated amplitude. Assuming a purely real

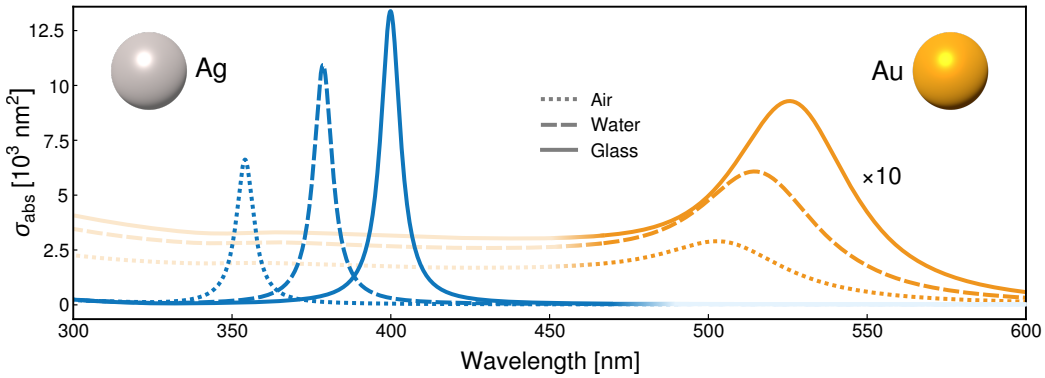

Figure 3.5: Absorption cross sections of silver (blue lines) and gold (red lines) nanospheres with a diameter of 25 nm in different media. The permittivities are chosen to be $\varepsilon_{\text{med}} = 1$ (air, dotted lines), $\varepsilon_{\text{med}} = 1.7$ (water, dashed lines) and $\varepsilon_{\text{med}} = 2.3$ (glass, solid lines). The data for the permittivities of gold and silver were taken from Reference 37.

permittivity of the medium and using the previous expression of the dipole moment $\mathbf{p} = \varepsilon_{\text{med}}\alpha\mathbf{E}_0$, leads to

$$P_{\text{abs}} = \frac{kc}{2n}\varepsilon_{\text{med}}E_0^2\,\text{Im}[\alpha]\,. \tag{3.35}$$

We can now divide this expression for the total dissipated power by the energy density of the incoming light obtaining the absorption cross section as

$$\sigma_{\text{abs}} = \frac{k}{\varepsilon_0}\text{Im}[\alpha] = 4\pi k a^3 \text{Im}\left[\frac{\varepsilon_{sph} - \varepsilon_{\text{med}}}{\varepsilon_{sph} + 2\varepsilon_{\text{med}}}\right]. \tag{3.36}$$

Also the absorption can be directly measured and is thus an as important feature as the scattering. In the quasistatic approximation, the absorption cross section behaves qualitatively very similar to the scattering cross section. This can be seen in Figure 3.5. The peak positions as well as the peak heights and widths look comparable to those in Figure 3.4. The differences in the amplitudes can again be explained by at the cross section for $\varepsilon'_{\text{sph}} = -2\varepsilon_{\text{med}}$. It is then

$$\sigma_{\text{abs}} \propto \lambda^{-1}\frac{\varepsilon_{\text{med}}}{\varepsilon''_{\text{sph}}}\,. \tag{3.37}$$

Within one material, the reasons for the changes in amplitude accompanying a red-shift are similar to those we discussed for the scattering cross section: A change of ε_{med} is stronger than a change in λ and thus the amplitudes raise for a red-shift in silver. In gold, the decrease in $\varepsilon''_{\text{sph}}$ enhances this effect.

The difference between the materials is not as strong as for the scattering. It is now dominated by the difference of $\varepsilon''_{\text{sph}}$, which is almost zero for silver in the region of interest and notably greater than one for gold in its respective resonance region. This non-negligible imaginary part of gold is caused by interband transitions which shall be discussed in more detail in Section 3.4. These transitions create electron-hole pairs whose energy is subsequently lost to the phonon bath [34]. For silver, interband

transitions start to play a role for wavelengths below 320 nm [38]. Thus, they don't really have an impact on the plasmon resonance in silver nanoparticles. Interband transitions in gold become relevant already in the visible region (this is the root of the yellowish colour of bulk gold in contrast to "white" silver). Therefore, they influence the plasmon resonance in gold nanospheres. Due to the energy loss, interband transitions damp the amplitude of the free electron oscillations. This damping lowers the polarisability α and also results in a shorter lifetime of the excitations. Spectrally, this is reflected in a wider linewidth the gold nanoparticles in comparison to silver [39].

Extinction cross section: Due to its simplicity, a transmission spectrometer is the device that is most often used for spectroscopic analysis of nanoparticles. It detects the light that is transmitted through a sample. The part of the light, that is absorbed or scattered by the particles does not reach the detector. But the spectrometer cannot differentiate if the light's extinction is caused by one or the other. For this case, a third cross section, the extinction cross section σ_{ext} is defined as

$$\sigma_{\text{ext}} = \sigma_{\text{scatt}} + \sigma_{\text{abs}} \,. \tag{3.38}$$

A graphical comparison of the three different cross sections is depicted in Figure 3.6 for gold nanospheres with a diameter of 25 nm (left) and 100 nm (right). The medium is chosen to be water ($\varepsilon_{\text{med}} = 1.7$). For small spheres, the extinction is completely dominated by absorption. Due to the a^6-dependence of the scattering cross section, the scattering becomes more relevant for increasing particle sizes. For the 100 nm spheres, both scattering and absorption contribute notably. Moreover, the maximum positions for the different cross section don't coincide exactly. This is rooted in the different dependence on α as well as the different dependence on the wavelength. The λ^{-4}-dependence causes the scattering maximum to be red-shifted in comparison to the maximum in absorption which only shows a λ^{-1}-dependence.

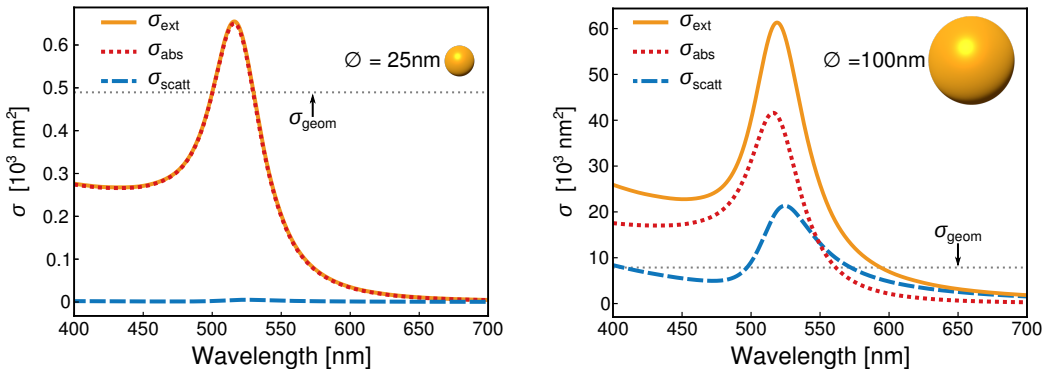

Figure 3.6: Scattering (dashed blue line), absorption (dotted red line) and extinction (orange solid line) cross sections of gold nano spheres with a diameter of 25 nm in the left panel and 100 nm on the right side. For small particles, scattering can be neglected and absorption completely dominates the extinction. For larger particles, scattering becomes more relevant and notably contributes to the extinction, as well. As comparison, the dotted grey lines mark the geometrical cross sections of the two particles. The data for the permittivities of gold and silver were taken from Reference 37.

Strictly speaking, the quasistatic approximation is no more valid for particles as large as 100 nm in diameter, but it gives a good impression of how both scattering and absorption contribute notably to the extinction. Particles of that size were used for Article I which discusses the difference between their scattering and absorption which cannot be revealed by extinction measurements. The article underlines the importance of differentiating between the three effects showing strong differences between them.

As an additional comparison, Figure 3.6 also shows the geometrical cross sections for the two particle sizes. In the case of the smaller particles, the absorption and the extinction cross section exceed the geometrical cross section at resonance. For the larger particles, also the scattering cross section is larger. For silver nanoparticles, this effect is even more pronounced since both absorption and scattering are even stronger. This indicates, that indeed plasmonic nanoparticles can be used as efficient absorbers or scatterers.

The previous part established the basic concepts for describing localised plasmons in metal nanoparticles. We derived the polarisability of spheres that are small compared to the wavelength. From this polarisability, we deduced the optical cross sections by which we could identify the basic phenomena concerning localised plasmons: (i) The plasmon resonances of gold and silver fall into the visible part of the electromagnetic spectrum, (ii) at the resonance positions strong field enhancements occur and (iii) the resonances strongly depend on the environment. These phenomena provide the foundation of the articles constituting this dissertation.

Only gold nanoparticles were actually examined for the articles. Silver was not used. The previous discussion included silver purely for instructive reasons since the comparison with gold provides an even deeper understanding of localised plasmons. Article I investigated nanospheres. Another kind of nanoparticles under investigation in this article are gold nanorods. Those also play the major role in Articles II – IV. Therefore, the next section expands the previously introduced concepts to a more general theory of nanoellipsoids in the next section. Ellipsoids are a good approximation to rods and thus, the properties of localised plasmons in metal nanorods can be deduced and understood from such an extended Mie theory.

3.2.2 Ellipsoidal Particles

In 1912, Richard Gans expanded Mie theory to general spheroidal particles that are small against the wavelength [6]. He presented a quasistatic solution claiming it could easily be generalised to non-spheroidal ellipsoids. Today, the model describing the optical properties of ellipsoids with an electrostatic approach is often referred to as Mie–Gans theory. This theory is the main topic of the following section.

The quasistatic case requires a solution to the Laplace equation. The boundary conditions dictate the exact form of the potential. With this in mind, it should be possible to predict the scattering and absorption behaviour for particles with arbitrary shapes as long as they are small in comparison to the wavelength. However, finding an analytical solution is usually not possible. It requires an adequate set of coordinates in which the problem is symmetric. In case of the sphere discussed above,

spherical coordinates were the obvious choice. But we can also find a solution for the more general system of an ellipsoid. Articles I – IV discuss the features of gold nanorods. Ellipsoids represent a reasonable approximation to nanorods and the main features of nanorods can be explained by those of nanoellipsoids. Therefore, the following section shall give a short wrap up of the derivation of the polarisability in case of a nanoellipsoid. It will reproduce the main arguments given in the book by Bohren and Huffman [40], where also a more detailed discussion can be found. Eventually, we will again find the solution of the Laplace equation to be a sum of the external potential and a potential that is generated by a point dipole in the particle centre. This point dipole possesses a polarisability α with resonances that determine the occurrence of localised plasmons and from which all optical features can be derived.

An ellipsoid is mathematically defined by its semiaxes a, b and c. In Cartesian coordinates, they obey the equation

$$\frac{x^2}{a^2}+\frac{y^2}{b^2}+\frac{z^2}{c^2}=1\,. \tag{3.39}$$

Without loss of generality, a is here assumed to be the longest semiaxis, while c is shortest. The ellipsoid, consisting of a material with permittivity ε_{sph}, is again placed in a medium with permittivity ε_{med}. The ellipsoid is surrounded by a constant electric field. A general ellipsoid exhibits a lower degree of symmetry in comparison to the special case of a sphere. Thus, the solution to the Laplace equation and consequently the optical features of a nanoellipsoid depend on the polarisation of the external electric field in regard to the particle. The problem therefore requires three different solutions, each one with a field polarisation along one semiaxis. The general solution can then be composed of these three cases. We will begin here with an electric field pointing in the direction of the semiaxis c, that means a field with a component only in the z-direction. A sketch of the situation is presented in Figure 3.7.

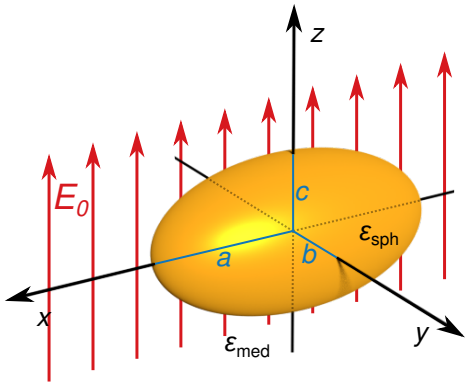

Figure 3.7: Nanoellipsoid in an electric field E_0 in direction of the semiaxis c, which is parallel to the z-direction. The other semiaxes are a and b along the x- and y-direction, respectively. The permittivity is ε_{sph} inside the particle and ε_{med} in the surrounding medium.

The boundary conditions are the same as in the case of the sphere (Equations 3.9 – 3.11): The potential should be finite at the point of origin and unaffected by the particle far away from it. At the particle

surface, the tangential component of the electric field should be continuous as well as the normal component of the dielectric displacement field. Only the surface differs from that of a sphere.

Now, ellipsoidal coordinates ξ, η and ζ are the system of choice to describe the problem. They are defined as

$$\frac{x^2}{a^2+\xi}+\frac{y^2}{b^2+\xi}+\frac{z^2}{c^2+\xi}=1\,, \tag{3.40a}$$

$$\frac{x^2}{a^2+\eta}+\frac{y^2}{b^2+\eta}+\frac{z^2}{c^2+\eta}=1\,, \tag{3.40b}$$

$$\frac{x^2}{a^2+\zeta}+\frac{y^2}{b^2+\zeta}+\frac{z^2}{c^2+\zeta}=1\,. \tag{3.40c}$$

The values are restricted to $-c^2<\xi<\infty$, $-b^2<\eta<-c^2$ and $-a^2<\zeta<-b^2$. Due to the power of 2 for each coordinate, there is no isomorphism between (ξ, η, ζ) and (x, y, z). This means that although for every tuple of Cartesian coordinates, there is exactly one tuple of ellipsoidal coordinates representing the same point, the inverse direction is not unique. A tuple (ξ, η, ζ) only defines a unique point within each octant of the coordinate system. That means eight symmetrical points (x, y, z) can be attributed to each (ξ, η, ζ). This ambiguity in the coordinates resolves later thanks to the problem's symmetry.

With $f(q)=\left[(q+a^2)(q+b^2)(q+c^2)\right]^{\frac{1}{2}}$, we can express the Laplace equation in the new coordinates in the clear form

$$\begin{aligned}\Delta\Phi=(\eta-\zeta)f(\xi)\frac{\partial}{\partial\xi}\left[f(\xi)\frac{\partial\Phi}{\partial\xi}\right]+(\zeta-\xi)f(\eta)\frac{\partial}{\partial\eta}\left[f(\eta)\frac{\partial\Phi}{\partial\eta}\right]\\ +(\xi-\eta)f(\zeta)\frac{\partial}{\partial\zeta}\left[f(\zeta)\frac{\partial\Phi}{\partial\zeta}\right]=0\,.\end{aligned} \tag{3.41}$$

Applying the boundary conditions yields an expression for the potential inside and outside of the particle.

$$\Phi_{\mathrm{I}}=\Phi_0\frac{1}{1+\dfrac{L_{\mathrm{c}}(\varepsilon_{\mathrm{sph}}-\varepsilon_{\mathrm{med}})}{\varepsilon_{\mathrm{med}}}}\,, \tag{3.42a}$$

$$\Phi_{\mathrm{II}}=\Phi_0+\Phi_0\frac{\dfrac{abc}{2}\displaystyle\int_\xi^\infty\frac{dq}{(q+c^2)f(q)}}{1+\dfrac{L_{\mathrm{c}}(\varepsilon_{\mathrm{sph}}-\varepsilon_{\mathrm{med}})}{\varepsilon_{\mathrm{med}}}}\,. \tag{3.42b}$$

Here,

$$L_{\mathrm{c}}=\frac{abc}{2}\int_0^\infty\frac{dq}{(q+c^2)f(q)} \tag{3.43}$$

represents the *geometrical factor*. Details of the derivation of the potentials are discussed by Bohren

and Huffman [40].

For large distances r from the origin, the integral in Φ_{II} reduces to

$$\int_{\xi}^{\infty} \frac{dq}{(q+c^2)f(q)} \approx \int_{\xi}^{\infty} \frac{dq}{q^{5/2}} = \frac{2}{3}\xi^{-3/2}\,. \tag{3.44}$$

This means that far away from the ellipsoid the potential reads as

$$\Phi_{\mathrm{II}} = \Phi_0 + \frac{E_0\cos(\theta)}{r^2}\frac{\frac{abc}{3}\frac{\varepsilon_{\mathrm{sph}}-\varepsilon_{\mathrm{med}}}{\varepsilon_{\mathrm{med}}}}{1+\frac{L_{\mathrm{c}}(\varepsilon_{\mathrm{sph}}-\varepsilon_{\mathrm{med}})}{\varepsilon_{\mathrm{med}}}}\,. \tag{3.45}$$

This potential can again be identified as the potential of a point dipole located at the origin with the dipole moment $\mathbf{p} = \varepsilon_{\mathrm{med}}\alpha\mathbf{E}_0$ with

$$\alpha_{\mathrm{c}} = 4\pi\varepsilon_0 abc\frac{\varepsilon_{\mathrm{sph}}-\varepsilon_{\mathrm{med}}}{3\varepsilon_{\mathrm{med}}+3L_{\mathrm{c}}(\varepsilon_{\mathrm{sph}}-\varepsilon_{\mathrm{med}})}\,. \tag{3.46}$$

We now found an expression for the polarisability along the semiaxis c. From this polarisability we can again retrieve all optical properties like scattering and absorption in the same way as elaborated for nanopsheres, only with the constraint that the light needs to be polarised along the semiaxis c. The dependence of α_{c} on L_{c} confirms that the situation with an electric field along another semiaxis will yield a different solution and polarisability. A general solution requires also the polarisabilities along the semiaxes a and b. Looking at the previous derivation of α_{c}, we find that the solution for the situation with an electric field along the other two axes would be completely analogous and c would only have to be replaced by a or b, respectively. Thus, a general expression for the polarisability along the ellipsoid's main axes is

$$\alpha_i = 4\pi\varepsilon_0 abc\frac{\varepsilon_{\mathrm{sph}}-\varepsilon_{\mathrm{med}}}{3\varepsilon_{\mathrm{med}}+3L_i(\varepsilon_{\mathrm{sph}}-\varepsilon_{\mathrm{med}})} \tag{3.47}$$

with

$$L_i = \frac{abc}{2}\int_0^{\infty} \frac{dq}{(q+s_i^2)f(q)}\,. \tag{3.48}$$

The index i denotes the direction a, b or c and s_i the semiaxis in the respective direction.

This is the general result of the polarisability of an ellipsoid. Since a sphere is just an ellipsoid with $a = b = c$, its polarisability should be contained within Expression 3.47. This is indeed the case, since then $f(q) = (q+a^2)^{3/2}$ and thus, the geometrical factor of all axes is

$$L_i = \frac{a^3}{2}\int_0^{\infty} \frac{dq}{(q+a^2)^{5/2}} = \frac{1}{3}\,. \tag{3.49}$$

Hence, Equation 3.47 becomes Equation 3.25.

The nanoparticles mainly used for Articles I - IV were gold nanorods. The shape of a rod can be approximated by a prolate spheroid, a special ellipsoid with $a > b = c$. In this case, we can find explicit expressions for the geometrical factors and consequently directly calculate the polarisabilities. First, the L_i are not independent. Since

$$\frac{d}{dq}f(q) = \frac{1}{2}\left[\frac{f(q)}{(q+a^2)} + \frac{f(q)}{(q+b^2)} + \frac{f(q)}{(q+c^2)}\right], \tag{3.50}$$

the sum of the geometrical factors is

$$\begin{aligned}\sum_\mathrm{i} L_\mathrm{i} &= \frac{abc}{2}\int_0^\infty \frac{1}{f(q)^2}\frac{f(q)}{(q+a^2)} + \frac{f(q)}{(q+b^2)} + \frac{f(q)}{(q+c^2)}dq \\ &= -abc\int_0^\infty \frac{d}{dq}\frac{1}{f(q)}dq = -abc\left[\frac{1}{f(q)}\right]_0^\infty = 1\,.\end{aligned} \tag{3.51}$$

Therefore, a general ellipsoid has only two independent geometrical factors. In the case of a spheroid, the associated equality of the short axes leaves only one independent L_i. For the long axis, the integral can be solved and we can express the geometrical factor in terms of the *eccentricity* $e = (1 - b^2/a^2)^{1/2}$ as [40]

$$L_\mathrm{a} = \frac{1-e^2}{e^2}\left[\frac{1}{2e}\ln\left(\frac{1+e}{1-e}\right) - 1\right]. \tag{3.52}$$

Equation 3.51 then yields the other two factors $L_\mathrm{b,c}$ as

$$L_\mathrm{b,c} = \frac{1-L_\mathrm{a}}{2}\,. \tag{3.53}$$

Plugging these expressions for the geometrical factors into Equation 3.47, we obtain a direct expression for the general polarisability of an ellipsoid along its main axes. We can again identify resonances determining the occurrence of localised plasmons. For the spectral position of the resonances, we can generalise the Fröhlich condition to

$$\mathrm{Re}(\varepsilon_\mathrm{sph}) = \left(1 - \frac{1}{L_\mathrm{i}}\right)\varepsilon_\mathrm{med}\,. \tag{3.54}$$

Of course, the result for a sphere is recovered with $L_\mathrm{i} = 1/3$. For a general spheroid, the geometrical factors are not equal but different for the long and the short axes. Hence, a spheroid possesses two different resonance positions, one for a polarisation along the long axis, called *longitudinal* resonance and one along the short axis, referred to as *transverse* resonance. The geometrical factor of the long axis

is always smaller than $1/3$. Consequently, it is always smaller than the geometrical factor of the short axis. Due to the monotonous real part of the permittivity in the region of interest for gold and silver, the longitudinal resonance is always red-shifted in respect to the transverse resonance.

Since the sphereoid is described as a point dipole with polarisability α, the optical cross sections are obtained just as in the case of spheres, i.e. $\sigma_{\mathrm{abs,i}} = k^4/6\pi\varepsilon_0^2|\alpha_\mathrm{i}|^2$, $\sigma_{\mathrm{abs,i}} = k/\varepsilon_0 \mathrm{Im}[\alpha_\mathrm{i}]$ and $\sigma_{\mathrm{ext,i}} = \sigma_{\mathrm{abs,i}} + \sigma_{\mathrm{scatt,i}}$. But now, we need to consider the different contributions from transverse and longitudinal resonances. These contributions vary for different situations: In the case of polarised light illuminating a single rod (or an ensemble of equally oriented rods), the contribution of each semiaxis is found by weighting the cross section along this semiaxis with the cosine of the angle between semiaxis and light polarisation. If the particles are randomly oriented (e.g. when suspensed in water), all main axes contribute equally and the average cross section is obtained by summing over all axes, each weighted with a factor $1/3$ [40]. This means, in case of a prolate spheroid, the short axis is weighted with $2/3$ and the long axis with $1/3$. For normal light incidence on particles lying flat (but randomly oriented) on a substrate, only one of the transverse resonances can be excited. In this case the short axis and the long axis are both weighted with $1/2$. These considerations on the different contributions always need to be kept in mind when modelling experimental spectra of plasmonic nanospheroids.

Figure 3.8 illustrates a few of the features that result from the mathematical form of the polarisability for prolate ellipsoids and that can therefore be observed for plasmonic nanorods. The first panel presents the absorption spectrum for a prolate gold spheroid randomly oriented in water. The particle dimensions were chosen to be 10 nm and 20 nm for the short and long axis diameter, respectively. We can identify two peaks in the spectrum. These two peaks can be attributed to the longitudinal and the transverse resonances. The two parts are once more plotted separately. The transverse absorption cross section shows a resonance around 507 nm. This value is close to that for spheres. This is always the case for gold nanospheroids of any size as we will see later in the other plots of the Figure. The longitudinal contribution is resonant around 574 nm. This means, it is, as predicted, red-shifted in regard to the transverse resonance. Moreover, the longitudinal resonance is notably higher than the transverse resonance. Again, we can identify the reason by looking at the absorption cross section for the case when the resonance condition 3.54 is fulfilled. It is then

$$\sigma_{\mathrm{abs}} \propto \frac{abc}{\lambda} \frac{\varepsilon_{\mathrm{med}}}{L_\mathrm{i}^2 \mathrm{Im}[\varepsilon_{\mathrm{sph}}]} \,. \tag{3.55}$$

The long axis has a smaller geometrical factor L_i. Also, the imaginary part of gold's permittivity is smaller at the longitudinal resonance position. The difference of these two factors exceeds the difference of wavelength between transverse and longitudinal resonance and explains the different amplitudes of the two contributions.

The resonance positions of both axes depend on the aspect ratio, that is the relation between long and short axis. It is the only variable in the eccentricity and consequently in the geometrical factors. The relation between resonances and aspect ratio is illustrated in Figure 3.8b which shows the absorption cross sections of gold nanospheroids with identical short axis diameter but varying aspect ratios randomly oriented in water. The transverse resonance is only slightly affected showing a blue-shift

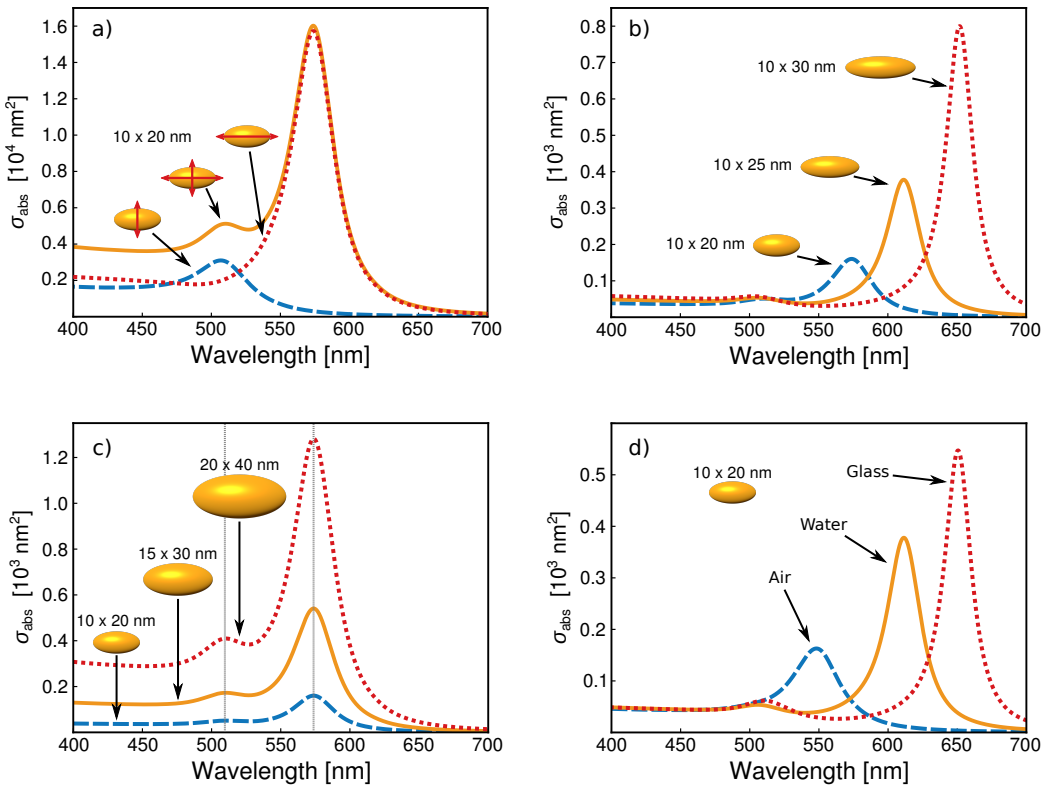

Figure 3.8: Absorption cross sections for gold spheroids. Panel a illustrates a general spectrum for a gold particle in water (solid orange line) illustrating the contributions of transverse (dashed blue line) and longitudinal (dotted red line) polarisation. The dependence on the aspect ratio is illustrated in panel b. Different aspect ratios are realised by a changing the long axis (20 nm, blue dashed line, 25 nm, orange solid line and 30 nm red dotted line while the short axis diameter is kept constant at 10 nm. The resonance positions are independent of the volume if the aspect ratio is kept constant. This is shown in panel c, where absorption cross sections for spheroids with an aspect ratio of 2:1 are presented with a short axis diameter of 10 nm (dashed blue line), 15 nm (solid orange line) and 20 nm (dotted red line). Panel d illustrates the dependence on the surrounding medium. Increasing permittivities were chosen to be $\varepsilon_{\text{med}} = 1$, representing air (blue dashed line), $\varepsilon_{\text{med}} = 1.7$, representing water (solid orange line) and $\varepsilon_{\text{med}} = 2.3$ representing glass (dotted red line). The data for the permittivities of gold and silver were taken from Reference 37.

for increasing aspect ratios. The longitudinal resonances on the other hand show a strong red-shift. The different directions of the shifts are rooted in the fact that a larger geometrical factor for the one axis implies a smaller geometrical factor for the other one to fulfil Equation 3.51. The difference in the shifts' magnitudes is rooted in a difference in the change of the Fröhlich condition for the two polarisations. We can understand this with the following example: When the aspect ratio changes from 2:1 to 2.5:1, the geometrical factor of the short axis changes from 0.41 to 0.42 resulting in a shift of the resonance condition from $\text{Re}[\varepsilon_{\text{sph}}] = -1.4\varepsilon_{\text{med}}$ to $\text{Re}[\varepsilon_{\text{sph}}] = -1.3\varepsilon_{\text{med}}$. For the long axis, this difference is much stronger since the geometrical factor changes from 0.17 to 0.14 and consequently the resonance condition from $\text{Re}[\varepsilon_{\text{sph}}] = -4.8\varepsilon_{\text{med}}$ to $\text{Re}[\varepsilon_{\text{sph}}] = -6.4\varepsilon_{\text{med}}$. This implies a stronger spectral shift for the longitudinal resonance in comparison to the transverse contribution. The difference in the

peak heights for varying aspect ratio is again explained from Equation 3.55: Increasing the long axis diameter a also results in an increase of L_i. In the case of gold this is accompanied by a decrease of the permittivity's imaginary part. Thus, three factors cause an increase in the amplitude which cannot be prevented by an increase in the wavelength. This plot is a nice illustration of the tunability of plasmon resonances in nanoparticles. By smart particle design, any resonance in the visible or infrared can be created explaining the large amount of potential applications for plasmonic nanoparticles.

To underline that the resonance positions only depend on the aspect ratio and not on the particle size, Figure 3.8c presents the absorption cross sections of gold spheroids with different sizes but identical aspect ratios, again randomly oriented in water. The resonance positions are identical for both longitudinal and transverse resonance. We can explain the difference in the spectra simply by the proportionality of α_abs to the particle volume. The largest particle discussed in the figure has an eight times larger particle volume than the smallest particle. Thus, multiplying the absorption spectrum of the smallest particle with a factor eight completely recovers the spectrum of the largest particle. The possibility of changing the particle size without changing the resonance position was utilised for Articles II and III which investigate the influence of the particle volume on the field electric enhancement.

Not only a change in particle shape can shift the resonances but also a change in the surrounding medium. The effect is the same as discussed above for the case of spheres: A changing ε_med will change the resonance condition which consequently demands another value of ε_sph. Figure 3.8d illustrates this effect. Here, σ_abs is plotted for a gold spheroid like in Panel a, only with changing surrounding media. Again, $\varepsilon_\mathrm{med} = 1$, $\varepsilon_\mathrm{med} = 1.7$, and $\varepsilon_\mathrm{med} = 2.3$ were chosen to represent air, water and glass, respectively. A red-shift for both resonances becomes apparent for increasing ε_med. The shift is much stronger for the longitudinal resonance. This is a consequence of the different prefactors in the resonance conditions for different polarisations. As mentioned above, for the resonance condition for the transverse peak is $\mathrm{Re}[\varepsilon_\mathrm{sph}] = -1.4\varepsilon_\mathrm{med}$. For the longitudinal peak, it is $\mathrm{Re}[\varepsilon_\mathrm{sph}] = -4.8\varepsilon_\mathrm{med}$. Thus, a change in the surrounding medium affects the longitudinal peak position much stronger. The change in amplitude is this time explained by a raise in ε_med and a decrease in $\mathrm{Im}[\varepsilon_\mathrm{sph}]$ having a stronger effect on the amplitude than the change of the wavelength. This sensitivity to the surrounding medium is the basis for resonance tuning of gold nanoparticles utilised for Articles I and II.

This section presented a derivation of the polarisability of ellipsoids that are small compared to the wavelength and gave an overview over the optical features of prolate nanospheroids. These features can be observed in the spectra of plasmonic nanorods which were used for Articles I – IV. The articles investigate the coupling of the plasmon resonances to excitations inside an emitter shell that was coated around the nanoparticles. In the following, section we shall therefore take a look at the systems of core–shell spheroids.

3.2.3 Core–Shell Particles

Articles I – IV discuss the coupling of excitons in organic emitters to plasmons in gold nanoparticles. The coupling is maximised by minimising the distance between emitters and particles. This is realised in a core–shell geometry where a layer of an organic dye forms a coating around a gold nanoparticle. Such a system can be approximated by a core–shell spheroid. If the spheroid is small compared to the wavelength of visible light, we can again apply the concepts introduced in the previous sections to deduce its optical properties. The solution of the Laplace equation will again be formed by the external potential and that of a point dipole with a polarisability α for which we can find an analytical expression. The result shall be presented in this section.

Figure 3.9 illustrates the necessary parameters for describing a prolate core–shell spheroid. We can regard the system to consist of two spheroids, an inner one with the long semiaxis $a^{(1)}$ and the short semiaxis $b^{(1)}$ surrounded by an outer one with long semiaxis $a^{(2)}$ and short semiaxis $b^{(2)}$. The permittivities are $\varepsilon_{\text{core}}$ in the core, $\varepsilon_{\text{shell}}$ in the region between the surfaces of the inner and outer spheroid and ε_{med} outside of the particle.

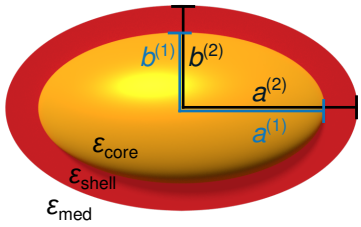

Figure 3.9: Prolate core–shell spheroid. The system is composed by an inner spheroid with semiaxes $a^{(1)}$ and $b^{(1)}$ and an outer spheroid with semiaxes $a^{(2)}$ and $b^{(2)}$. The permittivities are $\varepsilon_{\text{core}}$ in the core, $\varepsilon_{\text{shell}}$ in the region between the surfaces of the inner and outer spheroid and ε_{med} outside of the particle.

Like in the case of bare spheroids, the polarisability varies for different light polarisations in respect to the particle orientation. We can again solve the problem for light polarised along the main axes and subsequently deduce the general expression. The polarisability α_i along axis s_i (where i represents the long or the short axis) is given by [40]

$$\alpha_i = V\varepsilon_0 \frac{(\varepsilon_{\text{shell}}-\varepsilon_{\text{med}})[\varepsilon_{\text{shell}}+(\varepsilon_{\text{core}}-\varepsilon_{\text{shell}})(L_i^{(1)}-gL_i^{(2)})]+g\varepsilon_{\text{shell}}(\varepsilon_{\text{core}}-\varepsilon_{\text{shell}})}{[\varepsilon_{\text{shell}}+(\varepsilon_{\text{core}}-\varepsilon_{\text{shell}})(L_i^{(1)}-gL_i^{(2)})][\varepsilon_{\text{med}}+(\varepsilon_{\text{shell}}-\varepsilon_{\text{med}})L_i^{(2)}]+gL_i^{(2)}\varepsilon_{\text{shell}}(\varepsilon_{\text{core}}-\varepsilon_{\text{shell}})}. \tag{3.56}$$

Here, V represents the volume of the outer spheroid and $L_i^{(k)}$ the geometrical factor of the inner ($k=1$) and outer ($k=2$) spheroid along axis i. Furthermore, g describes the inner spheroid's fraction of the whole particle, that is $g = a^{(1)}b^{(1)}b^{(1)}/a^{(2)}b^{(2)}b^{(2)}$.

Note that this expression for the polarisability is generally valid for all core–shell ellipsoids and not only for prolate spheroids. This theoretical introduction only discusses the latter in detail due to their similarity to rods which were used for this work's articles. Like in the case of uncoated prolate spheroids,

we can write the geometrical factors in the analytical form of

$$L_{\mathrm{a}}^{(k)} = \frac{1-e_{(k)}^2}{e_{(k)}^2}\left[\frac{1}{2e_{(k)}}\ln\left(\frac{1+e_{(k)}}{1-e_{(k)}}\right)-1\right] \tag{3.57}$$

and

$$L_{\mathrm{b,c}}^{(k)} = \frac{1-L_{\mathrm{a}}^{(k)}}{2}\,. \tag{3.58}$$

The form of the polarisability given in Expression 3.56 contains the expression for an uncoated spheroid (and thus the uncoated sphere) as a special case. This becomes clear when setting $\varepsilon_{\mathrm{shell}} = \varepsilon_{\mathrm{med}}$ or equalising the dimensions of inner and outer ellipsoid (i.e. reducing the shell thickness to zero). In both cases, Equation 3.56 becomes identical to Equation 3.47.

With a metal as core material, the material of the shell can be chosen quite freely and plasmon resonances would still occur. This expands the variability of plasmonic nanoparticles even further. Many examples of core–shell nanoparticles have been studied. Silica shells are for example often utilised to increase the stability of gold and silver cores [41, 42]. But also the inverted version of such systems, namely particles with a silica core and a gold or silver shell show plasmon resonances, which are widely tunable [43, 44]. Also combinations of metals as both core and shell material have been fabricated [45, 46].

As an example, Figure 3.10a shows spectra for gold spheroids with a silica shell of varying thickness. The silica shell has a similar effect on the plasmon resonance as a dielectric medium. A thicker shell implies more polarisation charges in the metal's vicinity and thus a lowered resonance frequency. This means that, besides working as chemical stabiliser, a silica shell can be used to tune the plasmon resonance. The influence of an additional shell thickness decreases for thicker shells. That means the difference in resonance position between a 25 nm and a 40 nm shell is not as large as that between a 0.5 nm and a 2 nm shell. This is due to the fact that for thicker shells, the additional compensation dipoles in the silica are located at a greater distance from the metal surface. Hence, they only feel a weaker electric field enhancement and are therefore less excited. Additionally, their influence on the restoring force of the free electron cloud is also smaller than that of compensation dipoles close to the metal surface. Consequently, further away from the metal core, more compensation dipoles and more silica are needed to generate the same red-shift as the silica in direct vicinity of the metal. Eventually, the red-shift saturates for shell thicknesses on the order of the particle size. At such distances, the core's influence on the electric field can be neglected [47]. This effect is similar to that of thin polymer layers covering a particle on a substrate. This effect has been previously utilised to tune the plasmon resonance [47, 48] and also plays a central role in Articles I and II.

As mentioned, for this work, I fabricated particles with a gold core and an organic dye shell. This system is quite different to that of a metal–silica particle since the dye possesses an additional resonance frequency. But also this case can be described in the framework of the presented quasistatic theory. In case of weak oscillator strengths in the dye, we can model the permittivity as a Lorentz oscillator [26]. The resulting absorption cross section for a gold core with 15 nm short and 30 nm long axis diameter is plotted in Figure 3.10b. The shell strongly modifies the spectrum around its resonance and a new

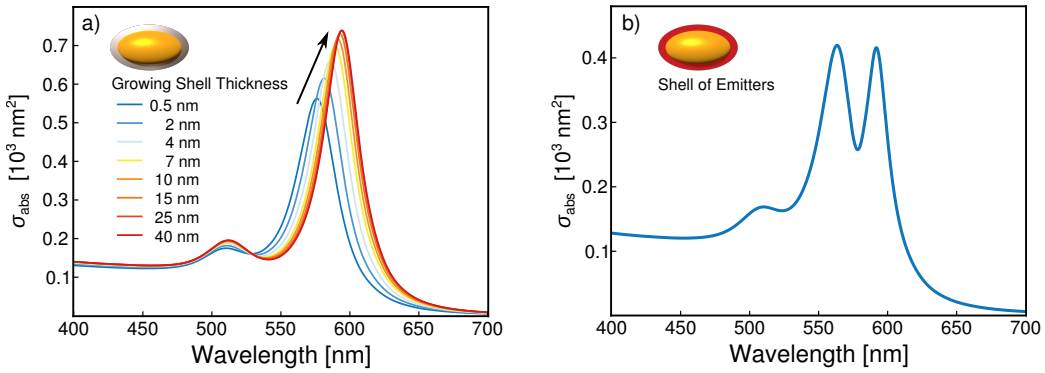

Figure 3.10: Absorption cross sections for core–shell spheroids with a gold core with 15 nm short axis and 30 nm and long axis diameter. The left panel presents spectra with silica shells of varying thickness between 0.5 and 40 nm. The plasmon resonances are similar to those of pure gold spheroids, only showing a red-shift for increasing shell thickness. This red-shift saturates for thicknesses on the order of the core-diameter. The right panel presents σ_{abs} for a Lorentz emitter as shell. A new peak can be seen indicating new features of the compound. Details will be discussed later in this work.

peak appears. This shows that core–shell particles can contain completely new features. Details of this system shall be discussed in later sections and in Article III, which will also show that Equation 3.56 is a good basis to describe the optical properties of coupled plasmon–exciton systems when a correct description of the emitter is applied.

The previous section presented the optical properties of the general case of core–shell spheroids which contains the special cases of uncoated spheroids and spheres. Beyond ellipsoids, a variety of other shapes of nanoparticles has been presented in recent years. The precise design of nanoparticles enables a high control over the electric nearfield. For example, the lightning-rod-effect can be used to achieve even stronger field enhancements than for ellipsoidal particles. In this sense nanocubes [49], nanostars [50], nanocones [51], nanotriangles [52] and other shapes have been employed to harvest the high fields at the sharp tips and corners. An analytical description as presented above is however not always possible and numerical methods have to be applied.

Bringing metal structures close together can lead to even stronger field enhancements than in the vicinity of sharp tips. In the space between two structures, *hot spots* can arise and the electric field is mainly concentrated in the gap. This effect is employed for example in *tip enhanced Raman spectroscopy* [53]. Bowtie structures with tiny gaps between two metal nanotriangles have been designed for achieving single emitter strong coupling [54] and single molecules have been investigated in the nm wide gap between a gold nanosphere and a gold film [55, 56]. Layers of gold nanotriangles were used for Articles V and VI. The field enhancements at the hot spots at plasmonic resonances in these structures can be utilised for effective photocatalysis and surface enhanced Raman spectroscopy.

In the previous sections, we have established an understanding for the properties of plasmonic nanoparticles within the framework of the quasistatic approximation. We found that in this approximation, a

metal particle can be described as as a point dipole with polarisability α. This polarisability enables the modelling of the particle's optical features. However, the model loses its precision for particles where the electric field can no more be assumed to be constant. In this case, we need to consider retardation effects and scattering losses. The next section shall discuss an approach to extend the applicability of the quasistatic model to larger particles.

3.2.4 Corrections to the Quasistatic Solution

If the external electric field can no more be considered constant over the whole particle volume, the quasistatic solution must be extended. In the quasistatic approximation, the particle could be considered as a dipole, since charges were all displaced in the same direction. If the field is no more constant over the whole particle volume, this is not the case anymore and contributions from higher multipole moments become relevant. The full solution for the optical cross sections of spheres as given by Mie is therefore a series of multipole oscillations with [57]

$$\sigma_{\text{ext}} = \frac{2\pi}{k^2} \sum_{l=1}^{\infty} (2l+1)\,\text{Re}[a_l + b_l] \tag{3.59}$$

and

$$\sigma_{\text{scatt}} = \frac{2\pi}{k^2} \sum_{l=1}^{\infty} (2l+1)\,|a_l|^2 + |b_l|^2\,. \tag{3.60}$$

σ_{abs} is then given by the difference of σ_{ext} and σ_{scatt}.

The terms a_l and and b_l are composed of the Riccarti-Bessel functions ψ_l and η_l via [57]

$$a_l = \frac{m\psi_l(mx)\psi_l'(x) - \psi_l(x)\psi_l'(mx)}{m\psi_l(mx)\eta_l'(x) - \eta_l(x)\psi_l'(mx)} \tag{3.61a}$$

and

$$b_l = \frac{\psi_l(mx)\psi_l'(x) - m\psi_l(x)\psi_l'(mx)}{\psi_l(mx)\eta_l'(x) - m\eta_l(x)\psi_l'(mx)}\,. \tag{3.61b}$$

They depend on the relative refractive index $m = n_{\text{sph}}/n_{\text{med}}$ and the size parameter $x = ka$ (a again denotes the particle radius and k the absolute value of the wave vector). The single elements of the series represent different multipole moments. The first $l = 1$ element can be identified as the dipole contribution retrived from the quasistatic solution [39]. This contribution dominates for small particles and quadrupole, octupole and higher moments play a minor role.

The complete expressions are rather complicated and cannot be applied for ellipsoidal particles. For Article III and IV, another approach was applied to account for deviations from the quasistatical solution. Phenomenologically, we can comprehend this approach as follows: If the external electric field is not constant over the whole particle volume, not all free electrons oscillate in phase. This reduces the charge accumulations at the surface resulting in a reduced restoring force. Thus, we can expect a red-shift for increasing particle sizes. Additionally, increasing particle sizes come along with increasing scattering contributions which again result in a loss of energy. This radiation damping becomes more relevant for increasing particle sizes. These two effects can be regarded as the lowest order corrections to the quasistatic model [34] and we can combine them to a correction factor.

This correction is often referred to as *modified long wavelength approximation* (MLWA) [58]. The basis is a modified expression for the electric field $\mathbf{E}_{\mathrm{loc}}$ at the centre of the particle, the position of the assumed point dipole. It is not identical with the external field $\mathbf{E}_0$ but more correctly written as [58, 59]

$$\mathbf{E}_{\mathrm{loc}} = \mathbf{E}_0 + \mathbf{E}_{\mathrm{rad}} + \mathbf{E}_{\mathrm{dep}} \,. \tag{3.62}$$

Here, $\mathbf{E}_{\mathrm{rad}}$ accounts for the radiative losses of the dipole and writes as [58, 60]

$$\mathbf{E}_{\mathrm{rad}} = i\frac{1}{6\pi\varepsilon_0\varepsilon_{\mathrm{med}}}k^3\mathbf{p} \tag{3.63}$$

where k represents the wave vector in the medium and $\mathbf{p}$ describes the dipole moment. $\mathbf{E}_{\mathrm{dep}}$ is the local depolarisation field and is given by [58, 59]

$$\mathbf{E}_{\mathrm{dep}} = \frac{1}{4\pi\varepsilon_0\varepsilon_{\mathrm{med}}}\frac{k^2}{s_i}\mathbf{p} \tag{3.64}$$

where s_i denotes the spheroid's long or short semiaxis [61].

In the previous sections, we ignored these modifications and assumed the electric field to be equal to the external field. Locally, the derived polarisability α_0 still describes the reaction of the dipole, but now on the modified field, that is

$$\mathbf{p} = \varepsilon_{\mathrm{med}}\alpha_0\mathbf{E}_{\mathrm{loc}} \,. \tag{3.65}$$

The idea is to find a modified polarisability α^{M} that again directly describes the connection between dipole moment and external electric field by

$$\mathbf{p} = \varepsilon_{\mathrm{med}}\alpha^{\mathrm{M}}\mathbf{E}_0 \,. \tag{3.66}$$

Inserting the expression for $\mathbf{E}_{\mathrm{loc}}$ into Equation 3.65 and comparing with Equation 3.66 results in an

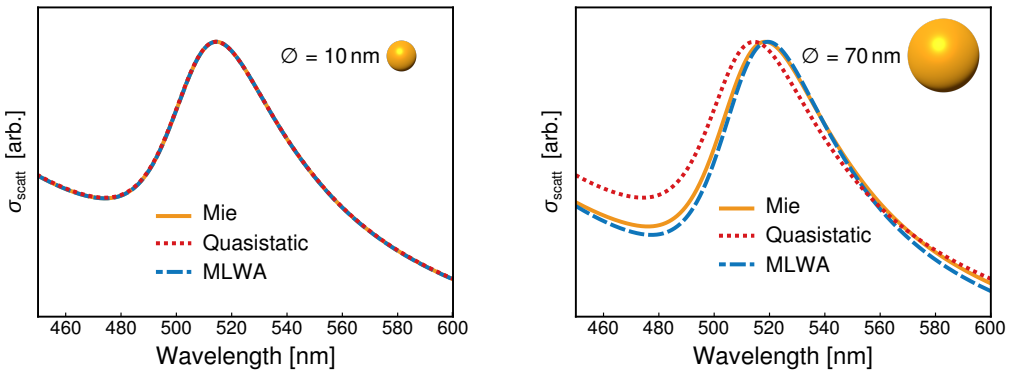

Figure 3.11: Comparison between the full Mie solution (solid orange line), the quasistatic model (dotted red line) and the MLWA (dashed blue line) for the simulation of the scattering cross section of gold nanospheres. The left panel depicts the result for a sphere with 10 nm diameter. All three models yield the same spectrum. The right panel depicts the result for a sphere with 70 nm diameter. Here, the quasistatic solution deviates from the correct Mie solution. This deviation can be corrected by the MLWA.

expression for the modified polarisability as

$$\alpha^{\mathrm{M}} = \alpha_0 \left(1 - i\frac{\alpha_0}{6\pi\varepsilon_0}k^3 - \frac{\alpha_0}{4\pi\varepsilon_0}\frac{k^2}{s_i} \right)^{-1} . \tag{3.67}$$

With this modified polarisability, we can again calculate the optical cross sections as introduced for the quasistatic case. The MLWA provides an explicit analytical expression for the polarisability that is not only applicable for spheres but also for general ellipsoids. It accounts for the polarisation losses and retardation effects. Figure 3.11 illustrates the influence of the modification. It depicts the spectra of gold spheres retrieved from the exact Mie solution, from the quasistatic approach and from the MLWA. The left panel depicts the results for particles with a diameter of 10 nm showing that in this case, the quasistatic approach nicely reproduces the exact solution. In the right panel, the quasistatic approach can no more perfectly describe the Mie result for particles with a diameter of 70 nm. The MLWA still gives a good approximation and nicely reproduces the red-shift caused by scattering losses and retardation effects.

The previous discussion about the MLWA closes this section about localised plasmons. We discussed the basic concepts: Gold and silver particles that are small compared to the wavelength can be approximated by a point dipole and its resonances fall into the range of visible light. We looked at the polarisablity of spheres, ellipsoids and core–shell spheroids and discussed their scattering, absorption and extinction cross section. Plasmon resonances are easily influenced by the particle environment and in case of spheroids strongly depend on the aspect ratio. In the end, the modified long wavelength approximation was introduced to expand the quasistatic theory to larger particles. Localised plasmons are the fundamental phenomenon utilised in the articles of this dissertation. Articles I – IV discuss the

coupling of the localised plasmon in gold nanospheres and rods to excitons in emitters forming a shell around the dye. The emitter material in all cases was a J-aggregate forming organic dye. The following section shall therefore give an overview over the properties of such J-aggregates.

3.3 J-aggregates

The coupling strength between plasmons and excitons in an emitter is proportional to the emitter's transition dipole moment and the electric field at its position. As presented in the previous section, the electric field on the surface of nanoparticles can reach very high values making them promising canditates for applications requiring high coupling strengths. On the emitter side, a variety of materials can be utlilised. Among the materials with the highest transition dipole moments, J-aggregate forming dyes rank in a top position [62]. They are supermolecular clusters of organic dyes held together by van der Waals forces [63]. The coupling of monomer excitations over the whole aggregate induce strong transition dipole moments, very sharp resonances and almost completely remove Stokes shifts [64]. J-aggregates are therefore versatile materials for light emitting diodes [65], optical sensitisers [66], solar cells [67], fluorescent tags and more. For this work, they were utilised in Articles I – IV discussing plasmon–exciton coupling in general and strong coupling in particular. Therefore, this section will give an overview over the properties of J-aggregates, starting with the model of dimers from which the red-shift, the enhancement of the oscillator strength can already be understood. We will then discuss the model for larger aggregates for which the peak-sharpness and the lack of Stokes shift can be argued.

J-aggregates were discovered independently by Edwin E. Jelley [68, 69] and Günter Scheibe [70, 71] in the 1930s. The cyanine dye PIC developed a new peak in both absorption and fluorescence for high concentrations contradicting the Beer-Lambert law. This process was reversible and the new feature disappeared again after dilution. The new peak emerged also when the solvent was changed. Scheibe et al. correctly attributed this behaviour to polymerisation of the molecules that could dissolve into monomers again. The J in J-aggregates stands for Jelley and sometimes these structures are also refered to as Scheibe aggregates [72].

Due to the high polarisability of the π-electrons along the polymethine group, cyanine dye molecules feel strong reciprocal van der Waals forces facilitating the formation of aggregates [73]. Additionally, the thiol groups enforce an in-plane shift between two adjacent molecules (we will later discuss the influence of this shift). Therefore, cyanine dyes are found among the most common J-aggregate forming dyes. For this work's articles, the dye TDBC was used. The molecule and the aggregation process are schematically shown in Figure 3.12. We can regard the monomers (i.e. single molecules) as plain two dimensional structures that form brick wall like clusters with one row always transversally shifted from the neighbouring rows [74, 75]. This aggregation occurs at sufficiently high concentrations or in appropriate chemical environments like on surfaces. The interaction between the transition dipoles of neighbouring monomers modifies the optical properties of the aggregate. The transition dipole moment of each molecule is oriented in the molecular plane along the π-orbitals. Therefore, the dipole moments of the clusters are parallel and mutually shifted causing a strong red-shifted absorption and emission line with remarkably narrow bandwidth. The model of Frenkel excitons [76] has proven to be a valid

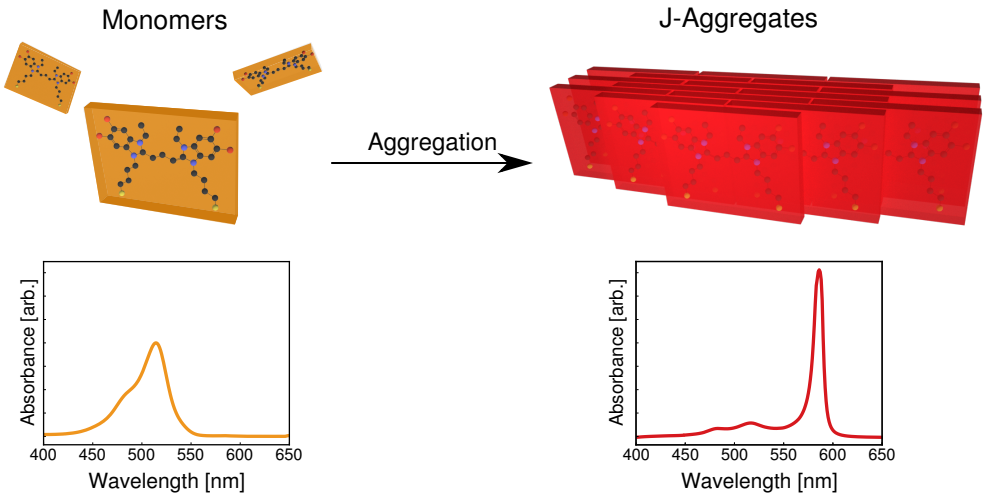

Figure 3.12: Schematic representation of the aggregation of TDBC monomers to J-aggregates. TDBC molecules are flat quasi two dimensional plates that form a brick like structure under aggregation. The spectrum of the J-aggregates exhibits a very sharp red-shifted peak that is not visible in pure monomer spectra.

concept for describing the energy structure in J-aggregates [63].

A Frenkel exciton describes an electron-hole pair delocalised over a crystal or, in this case, an aggregate of molecules. Electron and hole are bound to each other so that no charge is transferred. An electron-hole pair arises when an electron from the highest occupied molecule orbital (HOMO) is exited to the lowest unoccupied molecule orbital (LUMO). The molecule's wave function then changes from $|\mathrm{g}\rangle$ to $|\mathrm{e}\rangle$. Both are eigenfunctions of single molecule Hamilton operator H^0 with energies $E^{\mathrm{g}} = 0$ and $E^{\mathrm{e}} = \varepsilon$. In an aggregate consisting of N molecules without intermolecular coupling, the Hamiltonian reads as

$$H^0 = \sum_{i=1}^{N} H_i^0 \tag{3.68}$$

and the ground state with energy zero is written as

$$\Psi^{\mathrm{g}} = \bigotimes_{i=1}^{N} |\mathrm{g}\rangle_i \,. \tag{3.69}$$

If now an electron on the j-th molecule is excited, the new state ϕ_j^{e} writes as

$$\phi_j^{\mathrm{e}} = |\mathrm{e}\rangle_j \bigotimes_{i \neq j}^{N} |\mathrm{g}\rangle_i \,. \tag{3.70}$$

This is an eigenstate of the Hamiltonian and it is N-fold degenerated. If however interaction between

closest neighbours is introduced, Ψ_j^{e} is no more an eigenstate of the Hamiltonian but new eigenstates have to be found from linear combinations of all Ψ_j^{e}. That means that the excitation is not localised on one molecule, but distributed over the whole aggregate.

We can understand most physical properties of J-aggregates by the model of a dimer as for example discussed by Kasha et al. [77]. Their main arguments shall be reproduced in the following. A dimer is an aggregate consisting of only two molecules. In that case, the Hamiltonian is

$$H = H_1^0 + H_2^0 + V \tag{3.71}$$

where V accounts for the interaction between the two molecules. The ground state writes as $|\mathrm{g}\rangle_1 \otimes |\mathrm{g}\rangle_2 = |\mathrm{g,g}\rangle$ and its energy is different to the uncoupled case due to the interaction. It is found as

$$E^{\mathrm{g}} = \langle \mathrm{g},\mathrm{g}|H|\mathrm{g},\mathrm{g}\rangle = \langle \mathrm{g},\mathrm{g}|V|\mathrm{g},\mathrm{g}\rangle \ . \tag{3.72}$$

Note that the ground state energy of the single molecules was set to equal zero. $\langle \mathrm{g},\mathrm{g}|V|\mathrm{g},\mathrm{g}\rangle$ represents the ground state van der Waals interaction energy between the molecular ground states [77].

We recognise the interesting optical features caused by the interaction when calculating the one excitation states and the respective energies. In general, a state with one excitation, i.e. with one exciton, writes as

$$\Psi^{\mathrm{e}} = c_{\mathrm{a}} |\mathrm{e},\mathrm{g}\rangle + c_{\mathrm{b}} |\mathrm{g},\mathrm{e}\rangle \ . \tag{3.73}$$

The exact values of the prefactors $c_{\mathrm{a,b}}$ and the energy of the excited states is found by solving the stationary Schrödinger equation

$$H(c_{\mathrm{a}} |\mathrm{e},\mathrm{g}\rangle + c_{\mathrm{b}} |\mathrm{g},\mathrm{e}\rangle) = E^{\mathrm{e}}(c_{\mathrm{a}} |\mathrm{e},\mathrm{g}\rangle + c_{\mathrm{b}} |\mathrm{g},\mathrm{e}\rangle) \, . \tag{3.74}$$

With

$$H_{1,1} = \langle \mathrm{e},\mathrm{g}|H|\mathrm{e},\mathrm{g}\rangle = H_{2,2} \tag{3.75a}$$

and

$$H_{1,2} = \langle \mathrm{e},\mathrm{g}|H|\mathrm{g},\mathrm{e}\rangle = H_{2,1} \, , \tag{3.75b}$$

we can find a solution via the characteristic polynomial and the energies with the respective eigenstates

are

$$E_+^{\mathrm{e}} = H_{1,1} + H_{1,2} \quad \text{with} \quad \Psi_+^{\mathrm{e}} = \frac{1}{\sqrt{2}} \left(|\mathrm{e,g}\rangle + |\mathrm{g,e}\rangle \right) \tag{3.76a}$$

and

$$E_-^{\mathrm{e}} = H_{1,1} - H_{1,2} \quad \text{with} \quad \Psi_-^{\mathrm{e}} = \frac{1}{\sqrt{2}} \left(|\mathrm{e,g}\rangle - |\mathrm{g,e}\rangle \right) . \tag{3.76b}$$

This means that the exciton is evenly delocalised on the whole dimer without any charge transfer taking place between the molecules. We obtain the exact energies $E_\pm^{\mathrm{e}}$ from inserting the Hamiltonian resulting in

$$E_\pm^{\mathrm{e}} = \varepsilon + \langle \mathrm{e,g}|V|\mathrm{e,g}\rangle \pm \langle \mathrm{e,g}|V|\mathrm{g,e}\rangle \ . \tag{3.77}$$

Here, ε is again the excited energy of an isolated molecule. The second term represents van der Waals forces between an excited molecule and a molecule in the ground state [77]. The last term gives the energy splitting of the two eigenstates and is the reason for a red-shift of resonances in J-aggregates. In the first approximation, this term is determined by dipole–dipole interaction of two point dipoles [63].

$$W = \langle \mathrm{e,g}|V|\mathrm{g,e}\rangle = \frac{1}{4\pi\varepsilon_0} \frac{\boldsymbol{\mu}_1 \cdot \boldsymbol{\mu}_2}{r^3} - \frac{3\,(\boldsymbol{\mu}_1 \cdot \mathbf{r})\,(\boldsymbol{\mu}_2 \cdot \mathbf{r})}{r^5} . \tag{3.78}$$

In this expression, $\mathbf{r}$ describes the position vector of molecule 2 (with transition dipole moment $\boldsymbol{\mu}_2$) with molecule 1 (with transition dipole moment $\boldsymbol{\mu}_1$) positioned at the point of origin and accordingly, r describes the distance between the two. The absolute values of the transition dipole moments are $\mu_1 = \mu_2 = \mu$.

The excited energy of a dimer is then given by

$$E_\pm^{\mathrm{e}} - E^{\mathrm{g}} = \varepsilon + \Delta D \pm W \, . \tag{3.79}$$

Here, $\Delta D = \langle \mathrm{e,g}|V|\mathrm{e,g}\rangle - \langle \mathrm{g,g}|V|\mathrm{g,g}\rangle$ accounts for the differences in the van der Vaals attraction between excited state and ground state. ΔD is dominated by the interaction between excited state and ground state as the van der Waals interaction merely affects the ground state [77].

The mutual orientation of the two transition dipoles determines if W is positive or negative. This shall be illustrated in Figure 3.13 which depicts the energy diagrams for three different cases. First, the case where the dipoles lie parallel to each other, second, the case where the dipoles lie in line and third, the case where the dipoles are parallel but shifted along the dipole direction. In all cases, the molecule centres are separated by the distance a. Due to its small impact, the van der Waals interaction between the ground states is omitted in the scheme [77].

In the first case, the energy splitting between the two states, found by inserting Equation 3.78 into

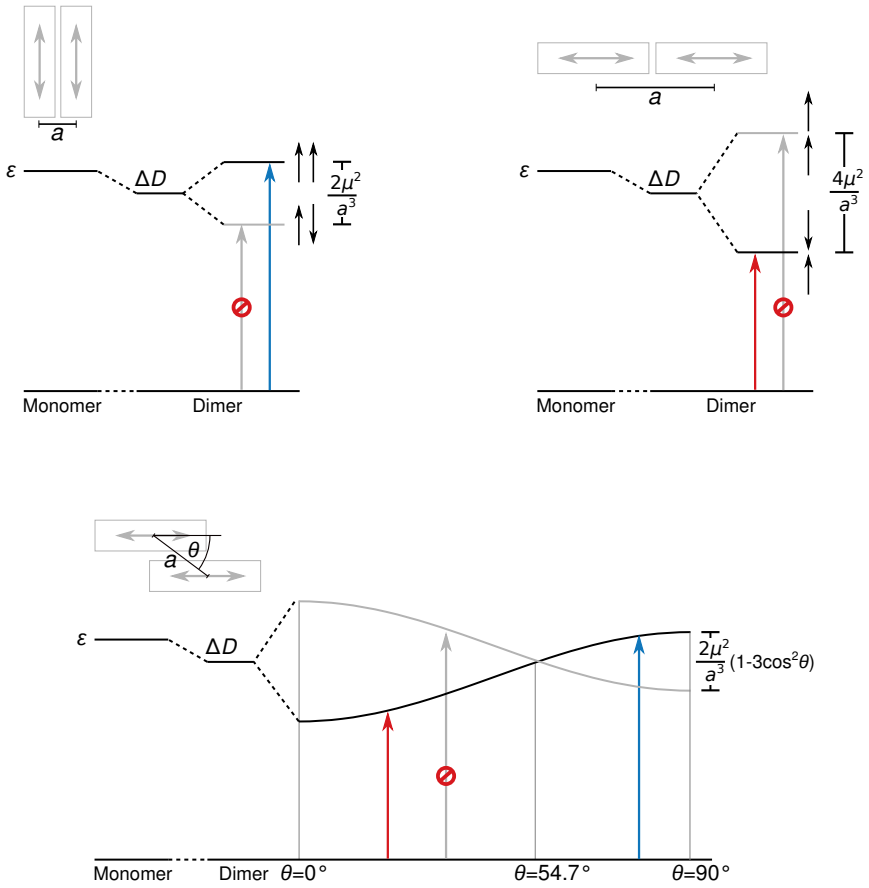

Figure 3.13: Energy splitting in dimers due to transition dipole interaction. Upper left: For parallel dipoles, the interaction energy is positive for dipoles pointing in the same direction and negative for the opposite case. Only the transition to the upper state is optically allowed. The upper right panel illustrates the case for in-line oriented dipoles. Here, in-phase dipoles have a lower energy and only this state is optically active. The case of parallel but shifted dipole moments is presented in the lower panel. The interaction energy depends on the relative angle between dipole moments and the connecting vector. For angles smaller than 54.7°, the optically allowed transition is red-shifted in regard to the uncoupled case. Modified from Reference 77.

Equation 3.79, is $\Delta W = 2\mu^2/a^3$. Due to repulsion, transition dipoles pointing in the same direction, described by Ψ^{e}_{+}, have a higher energy in regard to the uncoupled case. Due to attraction, the energy of antiparallel dipoles as in Ψ^{e}_{-} is lowered. Since the dimer's size is negligible in comparison to the wavelength of light in the resonance region, we can assume the electric field of an exciting light wave to be constant. This means that the transition from ground state to Ψ^{e}_{-} can't be excited by external light. A more rigid argument for this missing coupling to the far field is that the transition dipole moment of the dimer is given by $\boldsymbol{\mu}_{\mathrm{tot}} = (\boldsymbol{\mu}_1 \pm \boldsymbol{\mu}_2)/\sqrt{2}$, where $\boldsymbol{\mu}_{\mathrm{i}}$ describes the transition dipole moment of the respective molecule [78]. This means that for the antiparallel case, the transition dipole moment is zero and therefore, a transition to the corresponding energy level is dipole forbidden. The transition to the higher level is allowed with a transition dipole moment of $\mu_{\mathrm{tot}} = \sqrt{2}\mu$. Thus, the only excitable

resonance is blue-shifted against the uncoupled resonance. Such kind of dimers or aggregates are called hypsochromic aggregates or short H-aggregates. In H-aggregates, the fluorescence is usually very weak since the excited states tend to decay non-radiatively to the lower state [79] whose fluorescent decay to the ground state is dipole forbidden. Note, that for very weak dipole coupling, the excitable resonance might only be blue-shifted against the van der Waals-shifted energy level and slightly red-shifted to the monomer case. Often however, ΔW is large enough to cause a blue-shift [64].

The upper right panel in Figure 3.13 illustrates the situation when the transition dipole moments lie in a line. The energy splitting is calculated to be $\Delta W = 4\mu^2/a^3$. Now, an antiparallel dipole orientation Ψ^{e}_{-} has a higher energy than the uncoupled case, whereas the Ψ^{e}_{+} shows a red-shift. Also here, external light can only excite Ψ^{e}_{+} and therefore, the absorption is red-shifted in relation to the monomers. This is the effect in J-aggregates.

Often, the orientation of molecules within an aggregate is more complex than the two previous cases. To account for the structure of TDBC J-aggregates, the lower panel of Figure 3.13 depicts the situation of coplanar but shifted transition dipoles. The structure is defined via the distance a between the molecule centres and the angle θ between the transition dipole moments and the vector connecting the molecule centres. In this case the energy shift can be calculated to be

$$\Delta W = 2\frac{\mu^2}{a^3}\left(1 - 3\cos^2\theta\right) . \tag{3.80}$$

Note that the first two cases are included in this model with relative angles $\theta = 90°$ and $\theta = 0°$, respectively. For $\theta = 54.7°$ the energy splitting between the states becomes zero. Again, only dipole moments in the same directions can be excited. Thus, dimers with $\theta > 54.7°$ show a blue-shift and can be counted among the group of H-aggregates. For dimers with $\theta < 54.7°$ the energy shift is negative and they can be counted among the group of J-aggregates. This is the case for TDBC since molecule extension in the direction of the transition dipole moment is much larger than the thickness of a molecular sheet. This can also be seen in Figure 3.12.

A few features of J-aggregates can already be explained with the dimer case. The exciton is delocalised on the dimer and equally distributed between the moleucles. The resonance of J-aggregates is red-shifted (H-aggregates show a blue-shift) and the transition dipole moment is $\sqrt{2}$-fold enhanced in comparison to the monomer. The oscillator strength f which is proportional to the total absorption of the resonance is also proportional to the squared transition dipole moment [78] and therefore, $f_{\mathrm{tot}} = 2f_0$ with f_{tot} and f_0 describing dimer's and monomer's oscillator strength, respectively.

The principle of describing clusters with more than two molecules is basically the same as above. The real structure of J-aggregates is often complicated to assess and the process of understanding the strucure of the first discovered and thoroughly studied dye PIC lasted a few decades [80]. Various shapes of aggregates can arise depending on the molecular structure. A great feature of TDBC is its simplicity, both spectrally and structurally [80]. Its aggregation structure was found to be a brickstone arrangement [74, 75] as schematically shown in Figure 3.12. The interaction between neighbouring molecules is attractive for transition dipoles in phase and the orientation of the dipoles to each other is as for the

mutually shifted dimer with $\theta < 54.7°$. Thus, the state with the strongest transition dipole moment is red-shifted, defining the structure as a J-aggregate. For this 'in phase' case, the exciton is evenly delocalised over the whole aggregate and the total transition dipole moment is $\mu_{\text{tot}} = \sqrt{N}\mu_0$.

This concentration of oscillator strength is one of the main features of molecular aggregates [79]. It leads to a reduced life time of the excited state of $\tau_{\text{agg}} = \tau_0/N$ where τ_0 is the monomer life time [79]. The effect is referred to as *superradiance* [79, 81]. Phenomenologically, one could explain this life time reduction from the fact that $f_{\text{tot}} = Nf_0$. This means the oscillator strength and thus the absorption of N independent monomers is now governed by only one state. Strickler and Berg showed that the life time of an excited state is inversly proportional to its absorption [82]. Thus, an N-fold enhanced oscillator strength directly implies an N-fold reduction of the life time. This reduction can also be shown more rigidly [81].

Besides the red-shift and superradiance, an important feature of J-aggregates is the sharpness of the resonance peak. This is rooted in the weak coupling to vibrational states in comparison to the strong intermolecular coupling by exciton delocalisation. This delocalisation hinders the formation of a well defined vibrational eigenstate [83]. In a classical picture, this can be understood as follows: The excitation on one molecule jumps to a neighbouring molecule before vibrational relaxation can occur [64]. Frank Spano provided also a better-founded quantum mechanical explanation for this phenomenon showing that the absorption is almost purely defined by the 0–0 vibronic transition [64]. In the same report, he also showed that the fluorescence essentially describes the 0–0 vibronic transition explaining the lack of Stokes shift in J-aggregates.

Above, we assumed an aggregate to consist of N monomers. But an exciton can potentially be hindered to spread over the whole cluster due to static and dynamical disorder and the aggregate's physical size can be much bigger. Therefore, N rather describes the coherence length, that is the number of monomers over which the exciton is delocalised. This coherence length strongly dependes on the temperature and the chemical environment. It can be deduced from the transtions between the one-exciton band and the two-exciton band in pump-probe experiments. For TDBC, coherence lengths of up to 45 monomers were reported at 1.5 K [84] and of around 15 monomers at room temperature [85].

The previous section presented the properties of J-aggregates in general and of TDBC in particular. TDBC was used to investigate the coupling of excitons to plasmons on nanoparticles in Articles I – IV. TDBC is a great emitter system to study the coupling thanks to the concentration of oscillator strength, the extremely sharp resonance and the almost fully absent Stokes shift. These features were explained above together with the red-shift accompanying aggregation. The following section will discuss the modelling of the permittivity of such an excitonic system, as well as of the permittivity of gold.

3.4 Permittivity of Core and Shell

As discussed in Section 3.2, a nanoparticle's reaction to electric fields is mainly determined by the particle shape and the permittivity of the involved materials. Above, we have discussed the shapes's

influence while taking the values for the permittivity from literature. However, it is often desired to base such simulations on purely theoretical models, either to gain a deeper understanding of a system or to investigate the influences of parameters such as temperature. Moreover, changes in the chemical environment can cause changes in the permittivity, as is for example the case in organic emitters [86]. In this case, experimental permittivity data in water are of no help when the emitters' permittivity on gold nanoparticles is required.

Gold nanoparticles form the basis of all articles constituting this dissertation. Additionally, Article IV directly simulates the influence of heat on the core–shell nanoparticles via the temperature dependence of the permittivity of gold. A deeper understanding of gold's permittivity would therefore be beneficial or is even necessary for Article IV. This shall be established in the first part of this section starting with an explanation of the contribution of free electrons to the permittivity. Transitions between energy bands will be introduced afterwards, first, using a simple harmonic oscillator approximation and subsequently with a more precise model employing the joint density of states. This last model was directly used for Article IV to model the influence of heat on the optical properties of core–shell particles.

For Articles I – IV, the gold nanoparticles were coated with a layer of the J-aggregate forming dye TDBC presented in the previous section. Such an excitonic emitter can be modelled by a two-level system. We can describe the permittivity of such a two-level system in different ways. As a first approximation, we can model the system as a Lorentz oscillator. In this model, the two-level nature of the system is ignored delivering satisfying results for emitters exposed to weak electric fields. Article III shows that in plasmonic nanoparticles, even vacuum fields can reach values where this model is no more sufficient and a quantum mechanical approach is necessary. This approach was also utilised in Article IV and shall be discussed in the second part of this section.

3.4.1 Gold

Evidently, gold is a metal. It's optical properties at electromagnetic frequencies in the long wavelength range are therefore determined by the electrons in the conduction band. The contributions of the conduction electrons to the permittivity are referred to as Drude part and will be discussed in the beginning of this section. At higher frequencies, transitions between electronic bands can be excited. These so-called interband transitions strongly influence the permittivity. They can be approximated as Lorentz oscillatiors. A more physical and precise approach was introduced by Renzo Rosei [87–90] taking into account the actual shape of the electronic bands and their occupation probability. With this approach, the influence of temperature on the permittivity can be modelled as was done for Article IV. After the introduction of the Drude part, we will discuss both approaches, the oscillator approximation and the more precise model.

From this chapter's first section, we know that the permittivity ε and the susceptibility χ connect the polarisation $\mathbf{P}$ in a material and the electric field $\mathbf{E}$ via

$$\varepsilon = 1 + \chi = 1 + \frac{\mathbf{P}}{\varepsilon_0 \mathbf{E}}\,. \tag{3.81}$$

An electric field causes a displacement of each charge carrier. Often, this displacement can be determined via Newton's law. The polarisation can be derived via the sum of dipole moments per unit volume induced by charge displacements. Knowing this polarisation and the electric field eventually allows for finding an expression for the permittivity of a material.

Contribution of free electrons: The contribition of the conduction electrons to the permittivity is described by the Drude-Sommerfeld model. In this model, the electrons can move freely with an effective mass $m_{\mathrm{e,con}}$. This free motion is only disturbed by scattering events at unspecified collision centres. These collision centres can for example be lattice ions, other electrons, defects in the lattice [91]. The effect of the scattering events can be expressed by a friction or damping Γ as a material constant.

We can describe an external light field as $\mathbf{E} = \mathbf{E}_0 e^{i\omega t}$ with ω as the light's frequency. For a conduction electron at position $\mathbf{r}$ that is exposed to this field, the equation of motion writes as

$$m_{\mathrm{e,con}} \frac{\partial^2 \mathbf{r}}{\partial t^2} + m_{\mathrm{e,con}} \Gamma \frac{\partial \mathbf{r}}{\partial t} = q_{\mathrm{e}} \mathbf{E}_0 \mathrm{e}^{-i\omega t} \,. \tag{3.82}$$

Here, q_e describes the elementary charge of an electron. With the ansatz $\mathbf{r} = \mathbf{r}_0 e^{i\omega t}$, we obtain an expression for the dipole moment $\mathbf{p} = q_e \mathbf{r}$. Assuming an isotropic metal, the electric field affects all electrons in the same way. With the electron density n, the polarisation then reads as

$$\mathbf{P} = n\mathbf{p} = -\frac{n e^2 \mathbf{E}_0}{m_{\mathrm{e,con}}(\omega^2 + i\Gamma\omega)} \,. \tag{3.83}$$

In a bulk metal, surface effects are neglected. This also means that a displaced electron cloud in principle is still in a stable state. Thus, in contrast to the metal nanoparticles discussed previously, the electron cloud does not feel a restoring force. In that sense, we can regard the free electron contribution to the polarisation as an oscillation with resonance at $\omega_0 = 0$.

Plugging the expression of the polarisation into Equation 3.81 gives the Drude contribution to the permittivity:

$$\varepsilon_{\mathrm{Drude}}(\omega) = 1 - \frac{\omega_{\mathrm{p}}^2}{\omega^2 + i\Gamma\omega} \,. \tag{3.84}$$

Here, the definition of the volume plasma frequency $\omega_{\mathrm{p}} = \sqrt{n e^2/(m_{e,con}\varepsilon_0)}$ is used. The permittivity's real and imaginary parts are often expressed separately as $\varepsilon = \varepsilon' + i\varepsilon''$. For the Drude permittivity, this means

$$\varepsilon'_{\mathrm{Drude}}(\omega) = 1 - \frac{\omega_{\mathrm{p}}^2}{\omega^2 + \Gamma^2} \,, \tag{3.85a}$$

$$\varepsilon''_{\mathrm{Drude}}(\omega) = \frac{\Gamma\omega_{\mathrm{p}}^2}{\omega(\omega^2 + \Gamma^2)} \,. \tag{3.85b}$$

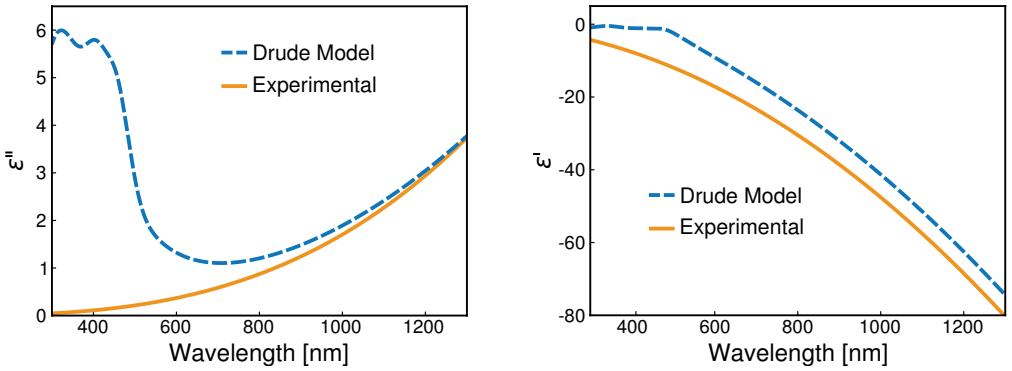

Figure 3.14: Measured (dashed blue line) and simulated (solid orange line) permittivity of gold. The left panel depicts the imaginary part ε'' while the right panel depicts the real part ε'. The simulation is the Drude model given by Equation 3.85 and fitted to the experimental data [92].

To compare the presented model with reality, Figure 3.14 presents experimental data [92] and the model from Equations 3.85. The parameters ω_p and Γ were adjusted to fit best to the measured data. For low frequencies and thus high wavelengths, the imaginary parts show an acceptable agreement. The real part of the model reproduces the form of the experimental values quite nicely, too. There is just a small offset that will be discussed later.

For wavelengths below 800 nm, however, the model fails to recreate the measured ε''. This discrepancy is rooted in the fact that not only the free electrons contribute to the permittivity. An electric field can also excite transitions between two electronic bands. These transitions are called interband transitions and are not taken into account in the Drude model. Metals like silver where interband transitions begin to have an influence on the permittivity only in the UV-region are often well described as a Drude metal in the visible. Therefore, simulations of the plasmon resonances of silver often only take into account contributions of the conduction electrons [93, 94]. In gold however, transitions between electronic bands are already excited by light in the visible. We therefore need to incorporate them into the model of the permittivity.

Interband transitions as Lorentz oscillators: A transition between two bands can occur when three conditions are met: A state in a lower energy band must be occupied while the state with the same k-vector in a band with higher energy is unoccupied. Additionally, the light energy $\hbar\omega$ must coincide with the energy difference of the two involved states. Such interband transitions can be desribed via the joint density of states between two energy bands [87]. We will do this later in this section. First, we will discuss an approximation in the following referred to as the Drude–Lorentz model. This model utilises the fact that the transition between two electronic states can be approximated by classical harmonic oscillations of the involved electrons [95]. In that case, we can again formulate an equation of motion to

$$m_{\mathrm{e,int}}\frac{\partial^2\mathbf{r}}{\partial t^2} + m_{\mathrm{e,int}}\gamma\frac{\partial\mathbf{r}}{\partial t} + \alpha\mathbf{r} = q_\mathrm{e}\mathbf{E}_0\mathrm{e}^{-i\omega t}\,. \tag{3.86}$$

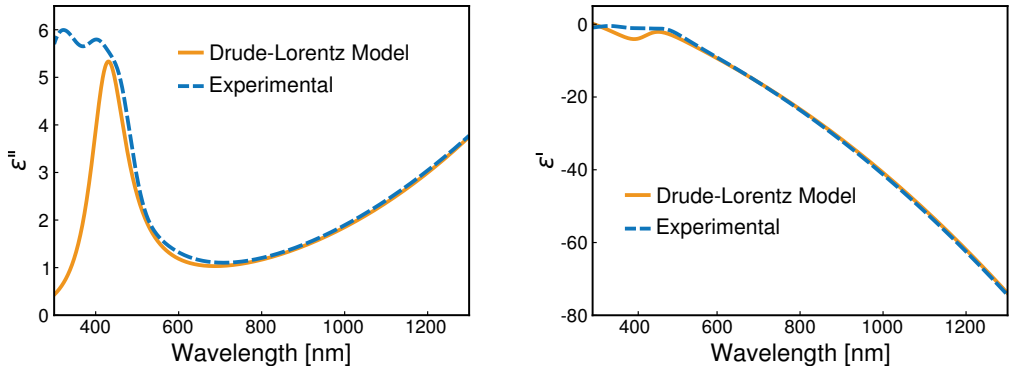

Figure 3.15: Measured (dashed blue line) and simulated (solid orange line) permittivity of gold. The left panel depicts the imaginary part ε'' while the right panel depicts the real part ε'. The simulation is the Drude–Lorentz model given by Equation 3.88 and fitted to the experimental data [92].

The effective mass of the electrons making the transition is represented by $m_{\mathrm{e,int}}$, the damping by γ. In contrast to the conduction electrons, the electrons in lower lying bands are bound to the atom cores. Thus, a restoring force of $\alpha\mathbf{r}$ acts on the displaced electrons. For each interband transition, an extra equation with different constants needs to be formulated. In analogy to the treatment of the conduction electrons, we can solve the equation of motion and subsequently calculate a contribution to the polarisation. For one interband transition, we can find the contribution to the susceptibility $\chi = \mathbf{P}/\varepsilon_0\mathbf{E}$ as

$$\chi(\omega) = \frac{\tilde{\omega}_\mathrm{p}^2}{(\omega_0^2 - \omega^2) - i\gamma\omega}\,. \tag{3.87}$$

Here, $\omega_0 = \sqrt{\alpha/m_{\mathrm{e,int}}}$ describes the resonance frequency of the transition while $\tilde{\omega}_\mathrm{p} = \sqrt{\tilde{n}e^2/(m_{e,int}\varepsilon_0)}$ represents a parameter analogous to the plasma frequency of the conduction electrons. $\tilde{n}$ in this case describes the density of electrons making the transition.

In reality, numerous interband transitions may occur also with resonances far away from the region of interest. Evidently, not all of them can be incorporated into the model, but we still need to consider their impact on the permittivity: An oscillator that is driven by an external force with a frequency far below the resonance frequency can directly follow this force without a phase difference. Therefore, this oscillation is loss free and only contributes to the real part of the polarisability. This is reflected in Expression 3.87 which becomes $(\tilde{\omega}_\mathrm{p}/\omega_0)^2$ for $\omega \to 0$. For frequencies far above the resonance, the oscillator can no more follow the external force and both real and imaginary part become zero. We also see this in the fact that $\chi \to 0$ for large frequencies. This means that interband transitions with resonance frequency far above the region of interest contribute to the permittivity with a constant real value ε_∞. If there are any transitions with resonances on the red side of the region of interest, they do not contribute to the permittivity. Note that in the case of gold, there are no interband transitions with frequencies below the region of visible light.

The total polarisation is composed by the polarisation of the conduction electrons and that of the electrons making the interband transition to $\mathbf{P}_\mathrm{tot} = \mathbf{P}_\mathrm{Drude} + \mathbf{P}_\mathrm{inter}$. Taking one interband transition into

account, all previous considerations lead to an expression for the permittivity $\varepsilon_{\text{Drude–Lorentz}}$ of gold, as

$$\varepsilon_{\text{Drude–Lorentz}}(\omega) = \varepsilon_\infty - \frac{\omega_\text{p}^2}{\omega^2 + i\Gamma\omega} + \frac{\tilde{\omega}_\text{p}^2}{(\omega_0^2 - \omega^2) - i\gamma\omega}\,. \tag{3.88}$$

The results of the interband correction with a single oscillation are presented in Figure 3.15 with parameters fitted to the experimental data and again divided into real and imaginary part.

This model is already an acceptable extension to the pure Drude approach and expands the range at which the permittivity can be described analytically to lower wavelengths of around 450 nm. However, it is a purely phenomenological model. It does not take into account the actual shape of the electron bands that usually does not lead to one sharp resonance. It can for example cause a resonance of the form of a step function with an onset at the position of minimal distance (of occupied and unoccupied states) between the bands. Additionally, changes in the parameters like the temperature cannot be incorporated in a reasonable fashion.

Interband transitions via the joint density of states: Renzo Rosei introduced a more physical way to model the permittivity of gold [87–90]. His approach calculates the transition probability of a certain interband transition. Multiplied with the oscillator strength, this probability is directly proportional to the imaginary part of the permittivity [87]. Considering the interband transitions at optical photon energies together with the Drude contribution, the imaginary part of the permittivity can be fitted to experimental values. The real part can then be calculated from the imaginary part via the Kramers-Kronig relation.

We can identify the interband transitions with the lowest energies from the band structure of gold which is depicted in Figure 3.16. In the visible region, three transitions can be excited [96]: The transition from the *d* band to the *p* band at the X point of the Brillouin zone and the transitions from the *d* band to the *p* band and from the *p* band to the *s* band at the L point of the Brillouin zone. Magnifications of the regions of interest at those two points are presented at the sides of Figure 3.16.

The probability that an incoming photon with energy $\hbar\omega$ can excite an interband transition is found via the joint density of states (JDOS). It takes the number of pairs of points on the two involved bands that are separated by the energy $\hbar\omega$ with each pair weighted by the probability that the lower state is occupied and the higher one is not.

The procedure shall be explained at the transition at the X point of the Brillouin zone. We obtain the contributions of the other transitions similarly. For an analytical expression, we need to calculate the energy of the two bands in the region of interest. Assuming, the energy depends quadratically on the distance from X and assuming that from X to Γ, the energy only depends on the absolute value of $k_\parallel$ (i.e. assuming rotational symmtetry around Δ), the energy $\hbar\omega_\text{d}$ of the *d* band yields directly from Figure 3.16 as [89]

$$\hbar\omega_\text{d} = -\hbar\omega_\text{f} - \frac{\hbar^2}{2m_{\text{d}\perp}}k_\perp^2 - \frac{\hbar^2}{2m_{\text{d}\parallel}}k_\parallel^2\,. \tag{3.89}$$

The masses $m_{\text{d}\parallel}$ and $m_{\text{d}\perp}$ describe the effective masses in the different directions in *k*-space. Note that

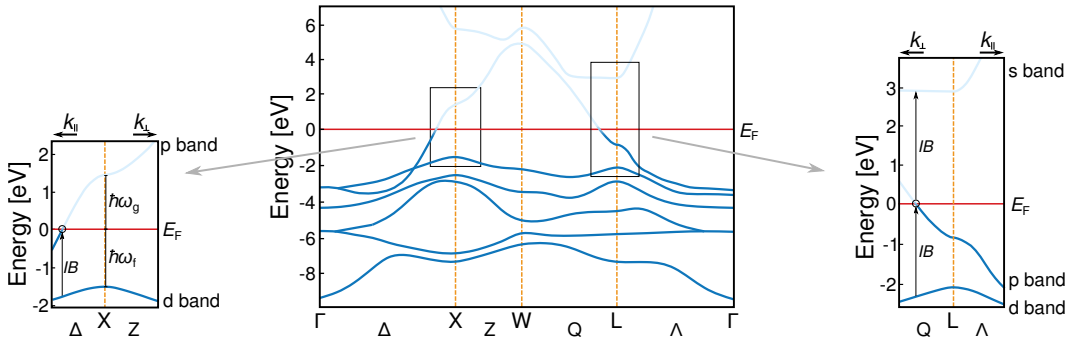

Figure 3.16: The central panel shows the band structure of gold, modified from Reference 97. The plots on the sides are zooms into the regions of interest, that is the X point (left) and the L point (right). At the X point, interband transitions in the visible occur from the *d* band to the *p* band at the crossing of the Fermi edge. At the L point, visible transitions occur from the *d* band to the *p* band and from the *p* band to the *s* band.

the energy offset was chosen to set the Fermi energy to zero while the X point marks the zero of the k-vector.

The energy of the p band around the X point reads similarly as

$$\hbar\omega_\mathrm{p} = \hbar\omega_\mathrm{g} + \frac{\hbar^2}{2m_{\mathrm{p}\perp}}k_\perp^2 - \frac{\hbar^2}{2m_{\mathrm{p}\parallel}}k_\parallel^2 . \tag{3.90}$$

A photon with energy $\hbar\omega$ that induces a transition between the two bands does not change $\mathbf{k}$ of the state due to the negligible k of visible light. In k-space, transitions are therefore restricted to a surface with $\Omega_{\mathrm{d,p}}(\mathbf{k}) = \hbar\omega_\mathrm{p} - \hbar\omega_\mathrm{d} - \hbar\omega = 0$.

If the Fermi edge was sharp (at temperature $T = 0\,\mathrm{K}$), we could retrieve the number of possible transitions $J_{\mathrm{d}\to\mathrm{p}}(\hbar\omega)$ from the d to the p band from an integration [98]

$$J_{\mathrm{d}\to\mathrm{p}}(\hbar\omega) = \frac{1}{(2\pi)^3}\int \delta\left(\Omega_{\mathrm{d,p}}(\mathbf{k})\right)\mathrm{d}^3k \tag{3.91}$$

where the integration is limited to k-vectors for which $\hbar\omega_\mathrm{d} < 0 < \hbar\omega_\mathrm{p}$. This integral can be solved using the definition of $\Omega_{\mathrm{d,p}}(\mathbf{k})$ and the expressions for the respective energies.

At finite temperature, the occupation probability around the Fermi energy smears out. To account for this varying occupation probability, we need to apply the concept of the energy distribution of the joint density of states (EDJDOS) [87]. The EDJDOS $D_{\mathrm{d}\to\mathrm{p}}(\hbar\omega, E)$ describes the number of transitions from the d band to the p band with energy $\hbar\omega$ where the initial states on the d band possess the energy E. To find all pairs of states that fulfil this condition, the integral in k-space is expanded by another δ-function to [87]

$$D_{\mathrm{d}\to\mathrm{p}}(\hbar\omega, E) = \frac{1}{(2\pi)^3}\int \delta\left(\Omega_{\mathrm{d,p}}(\mathbf{k})\right)\delta\left(E - \hbar\omega_\mathrm{d}\right)\mathrm{d}^3k . \tag{3.92}$$

The δ functions force the integral to a line in k-space where $\hbar\omega_\mathrm{d} = E$ and $\Omega_\mathrm{d,p}(\mathbf{k}) = 0$ which here means $\hbar\omega_\mathrm{p} = E + \hbar\omega$. This integral can be rewritten to [99]

$$D_{\mathrm{d}\to\mathrm{p}}(\hbar\omega, E) = \frac{1}{(2\pi)^3} \int \frac{dl_\mathrm{d,p}}{|\nabla_k(\hbar\omega_\mathrm{p}) \times \nabla_k(\hbar\omega_\mathrm{d})|} \,. \tag{3.93}$$

Here, the $dl_\mathrm{d,p}$ are increments of the described line. Again, we can solve this integral analytically. Expressions 3.89 and 3.90 yield

$$|\nabla_k(\hbar\omega_\mathrm{p}) \times \nabla_k(\hbar\omega_\mathrm{d})| = \hbar^4 F_{\mathrm{d}\to\mathrm{p}}^{-1} k_\parallel k_\perp \tag{3.94}$$

with

$$F_{\mathrm{d}\to\mathrm{p}} = \frac{m_{\mathrm{d},\perp} m_{\mathrm{p},\parallel} + m_{\mathrm{d},\parallel} m_{\mathrm{p},\perp}}{m_{\mathrm{d},\perp} m_{\mathrm{p},\parallel} m_{\mathrm{d},\parallel} m_{\mathrm{p},\perp}} \,. \tag{3.95}$$

We can make use of the cylindrical symmetry of the problem: Both constant energy surfaces, $\hbar\omega_d = E$ and $\hbar\omega_p = E + \hbar\omega$, possess cylinidrcal symmetry around $k_\parallel$. Thus, the intersection of the two forms a circle [88]. Therefore, we can rewrite $dl_\mathrm{d,p} = k_\perp d\theta$ and

$$D_{\mathrm{d}\to\mathrm{p}}(\hbar\omega, E) = \frac{1}{(2\pi)^3} \int_0^{2\pi} \frac{d\theta}{\hbar^4 F k_\parallel} \,. \tag{3.96}$$

We retrieve $k_\parallel$ directly from Expressions 3.89 and 3.90 and consequently, the EDJDOS reads as

$$D_{\mathrm{d}\to\mathrm{p}}(\hbar\omega, E) = \frac{1}{8\pi^2\hbar^2} F_{\mathrm{d}\to\mathrm{p}}^{-1/2} \left(\frac{\hbar^2}{2m_{\mathrm{d},\perp}} \left(\hbar\omega_\mathrm{g} - E - \hbar\omega\right) - \frac{\hbar^2}{2m_{\mathrm{p},\perp}} \left(E + \hbar\omega_\mathrm{f}\right) \right)^{-1/2} \tag{3.97}$$

To obtain the eventual JDOS for finite temperature, we have to weight each $D_{\mathrm{d}\to\mathrm{p}}(\hbar\omega, E)$ with the probability that the initial state (with energy E) is occupied and the final state (with energy $E + \hbar\omega$) is not. The occupation probability follows the Fermi–Dirac distribution $f(E,T)$. Then all possible E need to be included via integration. That means

$$J_{\mathrm{d}\to\mathrm{p}}(\hbar\omega) = \int_{E_\mathrm{min}}^{E_\mathrm{max}} D_{\mathrm{d}\to\mathrm{p}}(\hbar\omega, E) \left[f(E,T) \left(1 - f(E + \hbar\omega, T)\right) \right] dE \,. \tag{3.98}$$

The upper integration limit is chosen such that all possible transitions from the d band to the p band are included but that the integral can still be solved. This means that the upper limit is defined by the term within the square root of $D_{\mathrm{d}\to\mathrm{p}}(\hbar\omega, E)$ being zero [87]. The lower limit can be chosen to be negative infinity.

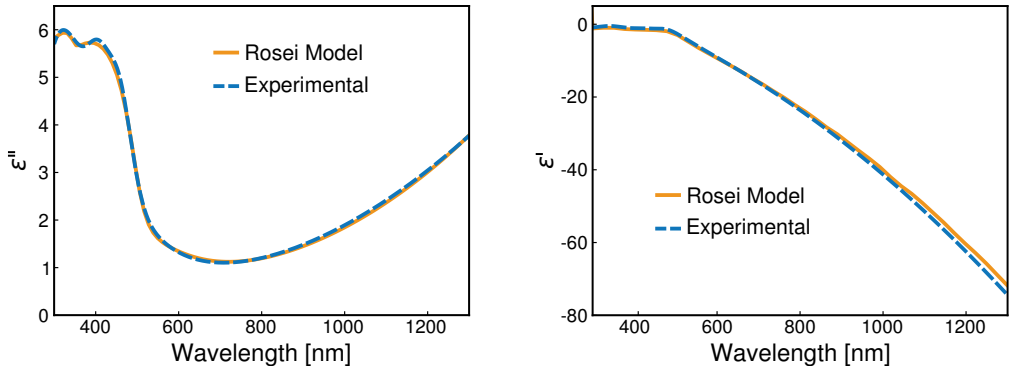

Figure 3.17: Measured (dashed blue line) and simulated (solid orange line) permittivity of gold. The left panel depicts the imaginary part ε'' while the right panel depicts the real part ε'. The simulation is the Rosei model: Equation 3.99 is fitted to the measured ε'' [92]. Subsequently, Equation 3.100 yields the simulated ε'.

An interband transition contributes to the permittivity via [87, 96]

$$\varepsilon''_{\mathrm{IB}} = \frac{4\pi^2 q_\mathrm{e}^2}{\varepsilon_0 m_\mathrm{e}^2 \omega^2} \left|P_{\mathrm{d}\to\mathrm{p}}\right|^2 J_{\mathrm{d}\to\mathrm{p}}\left(\hbar\omega\right) . \tag{3.99}$$

The total imaginary part of the permittivity is then the sum of all contributing interband transitions added to the Drude contribution. In the visible range, the three interband transitions that were presented in Figure 3.16 can be observed and thus

$$\varepsilon''_{\mathrm{tot}}\left(\omega\right) = \varepsilon''_{\mathrm{Drude}}\left(\omega\right) + \frac{4\pi^2 q_\mathrm{e}^2}{\varepsilon_0 m_\mathrm{e}^2 \omega^2} \left(\left|P^{\mathrm{X}}_{\mathrm{d}\to\mathrm{p}}\right|^2 J^{\mathrm{X}}_{\mathrm{d}\to\mathrm{p}}\left(\omega\right) + \left|P^{\mathrm{L}}_{\mathrm{d}\to\mathrm{p}}\right|^2 J^{\mathrm{L}}_{\mathrm{d}\to\mathrm{p}}\left(\omega\right) + \left|P^{\mathrm{L}}_{\mathrm{p}\to\mathrm{s}}\right|^2 J^{\mathrm{L}}_{\mathrm{p}\to\mathrm{s}}\left(\omega\right)\right) . \tag{3.100}$$

The calculations for the JDOS of the two transitions at the L point of the Brillouin zone work the same way as the one presented here for the X point. [87, 88]. The necessary parameters for a direct caluculation can be extracted from the band structure [96] and the missing parameters like the transition strength can be fitted to the measured data of ε.

The temperature dependece of the Fermi–Dirac distribution reflects the temperature dependence of the permittivity. Interestingly, the best fit for data at room temperature is obtained for a temperature of 600 K used in the Fermi–Dirac distribution. The temperature that is thus used in this model can be regarded as effective temperature that also incorporates other smearing effects at the Fermi surface [90]. The left panel of Figure 3.17 presents the best fit. The Rosei model completely reproduces the measurement data of the permittivity's imaginary part.

The real part of the permittivity arises directly from the Kramers–Kronig relation as [100]

$$\varepsilon'_{\mathrm{tot}}(\omega) = \frac{2}{\pi} \int_{\delta'}^{\omega-\delta} \frac{\omega' \varepsilon''_{\mathrm{tot}}(\omega')}{\omega'^2 - \omega^2} \mathrm{d}\omega' + \frac{2}{\pi} \int_{\omega-\delta}^{\infty} \frac{\omega' \varepsilon''_{\mathrm{tot}}(\omega')}{\omega'^2 - \omega^2} \mathrm{d}\omega' \tag{3.101}$$

with $\delta, \delta' \to 0$. This yields the contributions of the incorporated interband transitions to ε'. In analogy to the discussion of the Drude–Lorentz model, interband transitions of higher energy that have not been taken into account for ε'' can be included via a constant ε_∞. The result for the real part is plotted on in the right panel of Figure 3.17. We see that the Rosei model also reproduces the permittivity's real part accurately. It is obviously the most precise of the three presented approaches.

Additionally, the Rosei model allows an investigation of the permittivity's temperature dependence. Article IV makes use of this feature and discusses the change in the spectrum of core–shell nanoparticles induced by heat. The temperature influences both the Drude contribution and the interband transitions, yet in two different manners. The motion of the free electrons is damped by electron–phonon scattering as well by electron–electron scattering. While the latter becomes relevant only for very high temperatures [101], the former is linear in the temperature of the lattice [102]. Hence, the temperature dependent damping in the Drude part can be written as

$$\Gamma(T) = \Gamma_0 + \Gamma_0 \frac{T - T_0}{T_0} \,. \tag{3.102}$$

Here, T_0 represents a reference temperature and Γ_0 its respective damping. Strictly speaking, T describes the phonon temperature here. It can be different from the temperature of the electron gas, in particular right after the absorption of photons. The latter influences the interband transitions via the Fermi distribution in the integral of the JDOS. Knowing both temperatures allows for a direct determination of the permittivity. For static measurements, the ion lattice and the electrons are in thermal equilibrium and thus, both temperatures are identical. In pump–probe measurements on the other hand, this is not necessarily the case. In the first few picoseconds after excitation, the metal is not thermalised and different subsystems can possess different temperatures. For a complete description of the permittivity, a two-temperature model is then required. Details to this procedure are given in Article IV.

The previous part introduced a precise analytical description of the permittivity of gold. A complete ab initio model for the optical properties of core–shell particles with a gold core and an excitonic shell requires also a possibility to determine the shell's permittivity. Articles III and IV utilised a model to describe the permittivity of the emitters which will be discussed in the next section.

3.4.2 Two-Level Systems

An excitonic system can often be described as a two-level system with a ground state and an excited state. Absorption takes place when the system makes a transition from the ground state and light is emitted when the transition works in the other direction. Therefore, these systems are often referred to as *quantum emitters* or *quantum absorbers*. Following the literature on plasmon–exciton coupling [26, 62, 103], this section will mostly refer to excitonic systems as emitters.

Classical approach: Often, such a system is described by the the dynamics of a bound classical electron in an external electric field [26] as shown in Figure 3.18. This electron motion determines the system's

dipole moment from which then the permittivity can be derived in analogy to the case of gold. With the emitter irradiated by a plane wave with $E = E_0 \exp(i\omega t)$ with a wavelength much larger than the emitter dimensions, the equation of motion is

$$\frac{\partial^2}{\partial t^2} r + \Gamma \frac{\partial}{\partial t} r + \omega_0^2 r = \frac{q_e}{m} E_0 e^{i\omega t} \,. \tag{3.103}$$

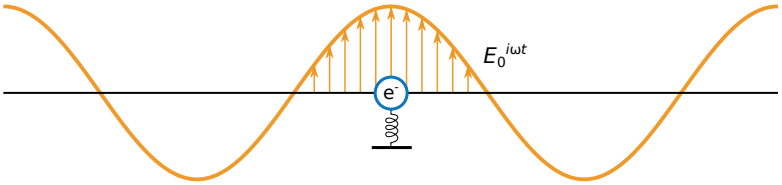

Figure 3.18: Sketch of the classical analogon to a two-level emitter exposed to light. An electron is described as oscillator bound to a rest position leading to a resonance frequency ω_0. The electron can oscillate in the classical electric light field.

With the ansatz $r = r_0 \exp(i\omega t)$, we can calculate the emitter's dipole moment to be

$$p = -q_e r = \frac{q_e^2}{m} \frac{1}{\omega_0^2 - \omega^2 - i\Gamma\omega} E \,. \tag{3.104}$$

For an ensemble of emitters with density N/V, the polarisation is $P = N/V\, p$ yielding the ensemble's susceptibility as

$$\chi_{\text{Lorentz}} = \frac{N q_e^2}{V \varepsilon_0 m} \frac{1}{\omega_0^2 - \omega^2 - i\Gamma\omega} \,. \tag{3.105}$$

A real quantum two-level system is not simply a bound electron. For example, the probability of a transmission between the two levels depends on the transition dipole moment. We saw this for example in the introduction of J-aggegates. This variation of transition probability is not respected in Equation 3.105. To make the Lorentz model applicable, an additional material constant f_0 is simply multiplied to the prefactor of the permittivity, that means [26]

$$\frac{N q_e^2}{V \varepsilon_0 m} \to f_0 \frac{N q_e^2}{V \varepsilon_0 m} \,. \tag{3.106}$$

In the Lorentz model, f_0 is simply a phenomenological factor which is fitted to the data. Its connection to the transition dipole moment and its calculability will become clear later in this section in the discussion of a quantised two-level system. Often the dimensionless oscillator strength f is defined as [93]

$$f = \frac{f_0}{\omega_0^2} \frac{N q_e^2}{V \varepsilon_0 m} \,. \tag{3.107}$$

It includes all material dependent prefactors reducing the expression of χ to only three parameters: the oscillator strength itself, the resonance frequency ω_0 and the linewidth Γ.

The permittivity $\varepsilon_{\text{Lorentz}}$ is directly calculated from Equation 3.81. A real emitter does not only possess one electron with two possible energy states. This means other resonances than that under consideration exist with an impact on the permittivity. This impact is the same as that discussed for interband transitions beyond the region of interest. Those with higher frequencies contribute to the permittivity with a real constant ε_∞. Including this constant and the oscillator strength, the permittivity of a two-level system that is approximated by a Lorentz oscillator reads as [93]

$$\varepsilon_{\text{Lorentz}} = \varepsilon_\infty + \frac{f\omega_0^2}{\omega_0^2 - \omega^2 - \mathrm{i}\Gamma\omega} = \varepsilon_\infty + f\omega_0^2 \frac{(\omega_0^2 - \omega^2) + i\Gamma\omega}{(\omega_0^2 - \omega^2)^2 + \Gamma^2\omega^2}\,. \tag{3.108}$$

This is the wide-spread expression for the permittivity of a system of emitters with an optical transition at ω_0 with a bandwidth Γ and an emitter density N/V. For electric fields that are not too strong, it provides a rather accurate description of reality. However, it does not really take into account the quantum mechanical two-level nature of the system. The electrons here may oscillate with arbitrary amplitudes. In contrast, a real two-level system can only be in the state "excited" or "not excited" or a linear combination of the two. Different values for the amplitudes in the classical approach represent different probabilities to be in the excited state in the two-level system, but in a real system, this probability is limited.

Semi-classical approach: When the electric field grows so strong that the classical amplitude would become too large, a more accurate description of the permittivity of two-levels systems is necessary. We can achieve this by respecting the quantum nature of the matter while we may still describe the electric field classically. This approach is usually referred to as the semi-classical approach. It can be found in various books on quantum optics. The following discussion roughly follows the argumentation given by Grynberg et al. [104]. A sketch of the situation is illustrated by Figure 3.19.

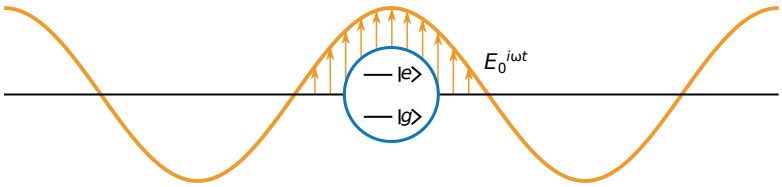

Figure 3.19: Sketch illustrating the semi-classical approach for describing an emitter exposed to a light field. The emitter is represented by a quantum mechanical two-level system with ground state $|g\rangle$ and excited state $|e\rangle$. The light field is described by a classical electric field.

The ground state and the excited state of a two-level system are described by $|g\rangle$ and $|e\rangle$, respectively. Any linear combination of the two, $|\psi\rangle = c_g\,|g\rangle + c_e\,|e\rangle$, represents a possible state of the system. The

density matrix of a state writes as

$$\rho = |\psi\rangle \langle\psi| = \begin{pmatrix} \rho_{gg} & \rho_{ge} \\ \rho_{eg} & \rho_{ee} \end{pmatrix} . \tag{3.109}$$

Here, the matrix elements are not independent. ρ_{nn} can be regarded as the probability to find the system in state $|n\rangle$ and thus, $\mathrm{tr}(\rho) = \rho_{aa} + \rho_{ee} = 1$. The density matrix also needs to be Hermitian and therefore, $\rho_{eg} = \rho_{eq}^{*}$. These off-diagonal elements describe the coherences between ground and excited state.

The Hamiltonian for a two-level system interacting with an electric field E is given by

$$H = H_0 - \mu E(t) . \tag{3.110}$$

H_0 represents the Hamiltonian of the system without an electric field for which $|g\rangle$ and $|e\rangle$ are the eigenvalues. We can understand the interaction term $-\mu E(t)$ as the potential energy of the transition dipole with moment μ in the electric field. The idea of this approach is now, to find the density matrix for this system from which for the polarisability can be derived. From this polarisability, the permittivity is obtained analogous to the previous situations.

In the basis of H_0 ($|g\rangle$ and $|e\rangle$), the Hamiltonian writes as

$$H = \begin{pmatrix} E_g & -\mu E(t) \\ -\mu E(t) & E_e \end{pmatrix} . \tag{3.111}$$

Here, E_g and E_e represent the energies of the ground state and excited state, respectively.

The time evolution of a state ρ in the Schrödinger picture is given by

$$\frac{d}{dt}\rho = -\frac{i}{\hbar}[H, \rho] . \tag{3.112}$$

In the Liouville formalism, the equation is formed for each single matrix element, that means

$$\frac{d}{dt}\rho_{nm} = -\frac{i}{\hbar}\sum_{kl} L_{nm,kl}\rho_{kl} \tag{3.113}$$

where, each element $L_{nm,kl}$ is chosen to recreate Equation 3.112.

The advantage of this formalism is that we can easily incorporate damping and dephasing mechanisms phenomenologically. In case of a closed two-level system (no transitions to other states than $|g\rangle$ and $|e\rangle$) two damping mechanisms arise: spontaneous decay Γ_{sp} from the excited state to the ground state and the dephasing of the off-diagonal elements γ. Adding these to the time evolution and assuming an oscillating electric field $E = E_0 \cos(\omega t)$, we obtain a differential equation for each matrix element of ρ

as

$$\frac{\mathrm{d}}{\mathrm{d}t}\rho_{\mathrm{gg}} = -\frac{i\Omega}{2}(\rho_{\mathrm{eg}} - \rho_{\mathrm{ge}})(e^{i\omega t} + e^{-i\omega t}) + \Gamma_{\mathrm{sp}}\rho_{\mathrm{ee}}\,, \tag{3.114a}$$

$$\frac{\mathrm{d}}{\mathrm{d}t}\rho_{\mathrm{ee}} = \frac{i\Omega}{2}(\rho_{\mathrm{eg}} - \rho_{\mathrm{ge}})(e^{i\omega t} + e^{-i\omega t}) - \Gamma_{\mathrm{sp}}\rho_{\mathrm{ee}}\,, \tag{3.114b}$$

$$\frac{\mathrm{d}}{\mathrm{d}t}\rho_{\mathrm{ge}} = i\omega_0\rho_{\mathrm{ge}} - \frac{i\Omega}{2}(\rho_{\mathrm{ee}} - \rho_{\mathrm{gg}})(e^{i\omega t} + e^{-i\omega t}) - \gamma\rho_{\mathrm{ge}}\,, \tag{3.114c}$$

$$\frac{\mathrm{d}}{\mathrm{d}t}\rho_{\mathrm{eg}} = -i\omega_0\rho_{\mathrm{eg}} + \frac{i\Omega}{2}(\rho_{\mathrm{ee}} - \rho_{\mathrm{gg}})(e^{i\omega t} + e^{-i\omega t}) - \gamma\rho_{\mathrm{eg}}\,. \tag{3.114d}$$

Here, $\hbar\Omega = -\mu E_0$ and $\hbar\omega_0 = E_{\mathrm{e}} - E_{\mathrm{g}}$. These equations are usually referred to as the *optical Bloch equations*. The common way to solve these equation is, to transfer the system to the *rotating frame* of the exciting field. This transformation means

$$\tilde{\rho}_{ge} = \rho_{ge}\mathrm{e}^{-\mathrm{i}\omega t}\,, \tag{3.115a}$$

$$\tilde{\rho}_{eg} = \rho_{eg}\mathrm{e}^{\mathrm{i}\omega t}\,, \tag{3.115b}$$

$$\tilde{\rho}_{gg} = \rho_{gg}\,, \tag{3.115c}$$

$$\tilde{\rho}_{ee} = \rho_{ee}\,. \tag{3.115d}$$

Substituting the new $\tilde{\rho}$ into the Bloch equations yields

$$\frac{\mathrm{d}}{\mathrm{d}t}\tilde{\rho}_{\mathrm{gg}} = -\frac{i\Omega}{2}\left[\tilde{\rho}_{\mathrm{eg}}\left(1 + e^{-i2\omega t}\right) - \tilde{\rho}_{\mathrm{ge}}\left(1 + e^{i2\omega t}\right)\right] + \Gamma_{\mathrm{sp}}\tilde{\rho}_{\mathrm{ee}}\,, \tag{3.116a}$$

$$\frac{\mathrm{d}}{\mathrm{d}t}\tilde{\rho}_{\mathrm{ee}} = \frac{i\Omega}{2}\left[\tilde{\rho}_{\mathrm{eg}}\left(1 + e^{-i2\omega t}\right) - \tilde{\rho}_{\mathrm{ge}}\left(1 + e^{i2\omega t}\right)\right] - \Gamma_{\mathrm{sp}}\tilde{\rho}_{\mathrm{ee}}\,, \tag{3.116b}$$

$$\frac{\mathrm{d}}{\mathrm{d}t}\tilde{\rho}_{\mathrm{ge}} = i\left(\omega_0 - \omega\right)\tilde{\rho}_{\mathrm{ge}} - \frac{i\Omega}{2}(\tilde{\rho}_{\mathrm{ee}} - \tilde{\rho}_{\mathrm{gg}})\left(1 + e^{-i2\omega t}\right) - \gamma\tilde{\rho}_{\mathrm{ge}}\,, \tag{3.116c}$$

$$\frac{\mathrm{d}}{\mathrm{d}t}\tilde{\rho}_{\mathrm{ge}} = -i\left(\omega_0 - \omega\right)\tilde{\rho}_{\mathrm{ge}} + \frac{i\Omega}{2}(\tilde{\rho}_{\mathrm{ee}} - \tilde{\rho}_{\mathrm{gg}})\left(1 + e^{i2\omega t}\right) - \gamma\tilde{\rho}_{\mathrm{eg}}\,. \tag{3.116d}$$

There are two kinds of terms in these equations. One that is not oscillating in the rotating frame picture and one that is proportional to $\exp(i2\omega t)$ or $\exp(-i2\omega t)$, oscillating at twice the light frequency. After integration (which is done to obtain mean values of operators), the contribution of the quickly oscillating terms is negligibly small. We can therefore ignore them already in the differential equations. This is the

rotating frame approximation. In this approximation, the differential equations read as

$$\frac{\mathrm{d}}{\mathrm{d}t}\tilde{\rho}_{\mathrm{gg}} = -\frac{i\Omega}{2}(\tilde{\rho}_{\mathrm{eg}} - \tilde{\rho}_{\mathrm{ge}}) + \Gamma_{\mathrm{sp}}\tilde{\rho}_{\mathrm{ee}}\,, \tag{3.117a}$$

$$\frac{\mathrm{d}}{\mathrm{d}t}\tilde{\rho}_{\mathrm{ee}} = \frac{i\Omega}{2}(\tilde{\rho}_{\mathrm{eg}} - \tilde{\rho}_{\mathrm{ge}}) - \Gamma_{\mathrm{sp}}\tilde{\rho}_{\mathrm{ee}}\,, \tag{3.117b}$$

$$\frac{\mathrm{d}}{\mathrm{d}t}\tilde{\rho}_{\mathrm{ge}} = i(\omega_0 - \omega)\tilde{\rho}_{\mathrm{ge}} - \frac{i\Omega}{2}(\tilde{\rho}_{\mathrm{ee}} - \tilde{\rho}_{\mathrm{gg}}) - \gamma\tilde{\rho}_{\mathrm{ge}}\,, \tag{3.117c}$$

$$\frac{\mathrm{d}}{\mathrm{d}t}\tilde{\rho}_{\mathrm{eg}} = -i(\omega_0 - \omega)\tilde{\rho}_{\mathrm{eg}} + \frac{i\Omega}{2}(\tilde{\rho}_{\mathrm{ee}} - \tilde{\rho}_{\mathrm{gg}}) - \gamma\tilde{\rho}_{\mathrm{eg}}\,. \tag{3.117d}$$

The right sides are now all time-independent. The solutions of interest are the steady state solutions in the roatating frame [104]. We can find them by setting the derivatives to zero. This yields

$$\tilde{\rho}_{\mathrm{ee}} = \frac{1}{2}\frac{\Omega^2\frac{\gamma}{\Gamma_{\mathrm{sp}}}}{(\omega_0 - \omega)^2 + \gamma^2 + \Omega^2\frac{\gamma}{\Gamma_{\mathrm{sp}}}}\,, \tag{3.118a}$$

$$\tilde{\rho}_{\mathrm{gg}} = 1 - \tilde{\rho}_{\mathrm{ee}}\,, \tag{3.118b}$$

$$\tilde{\rho}_{\mathrm{ge}} = \frac{i\Omega}{2}\frac{\gamma - i(\omega - \omega_0)}{\gamma^2 + (\omega_0 - \omega)^2 + \Omega^2\frac{\gamma}{\Gamma_{\mathrm{sp}}}}\,, \tag{3.118c}$$

$$\tilde{\rho}_{\mathrm{eg}} = \tilde{\rho}^*_{\mathrm{ge}}\,. \tag{3.118d}$$

A back-transformation from $\tilde{\rho}$ to ρ eventually yields the density matrix of a two-level system in an oscillating electric field. We obtain the expectation value of the dipole moment p from $\langle p\rangle = \langle\psi|p|\psi\rangle = \mathrm{tr}(\rho p)$. The dipole operator only has off-diagonal elements and reads as $p = \mu\,|\mathrm{e}\rangle\langle\mathrm{g}| + \mu\,|\mathrm{g}\rangle\langle\mathrm{e}|$. Consequently, $\langle p\rangle = \mu(\rho_{\mathrm{ge}} + \rho_{\mathrm{eg}})$. With this dipole moment, we obtain the susceptibility of an ensemble of emitters with density N/V analogous to the classical model as

$$\chi_{\text{two-level}} = \frac{N}{V}\frac{\mu^2}{\varepsilon_0\hbar}\frac{\omega_0 - \omega + i\gamma}{(\omega_0 - \omega)^2 + \gamma^2 + \Omega^2\frac{\gamma}{\Gamma_{sp}}}\,. \tag{3.119}$$

This is the general permittivity for an ensemble of two-level systems. In contrast to the classical solution it is the correct solution for all orders of light–matter interactions [26]. It is often justified to assume that decoherence only occurs via spontaneous decay. In that case $\gamma = \Gamma_{\mathrm{sp}}/2 = \Gamma/2$ [104]. In real systems, also higher energy states exist. Transitions to these higher states are incorporated into the model like in the classical case via a constant ε_∞. With these two considerations, the semi-classical permittivity reads as

$$\varepsilon_{\text{two-level}} = \varepsilon_\infty + \frac{N}{V}\frac{\mu^2}{\varepsilon_0\hbar}\frac{\omega_0 - \omega + i\frac{\Gamma}{2}}{(\omega_0 - \omega)^2 + \frac{\Gamma^2}{4} + \frac{\Omega^2}{2}}\,. \tag{3.120}$$

A comparison with the classical result of a Lorentz oscillator (Equation 3.108) leads to the following conclusion: If the oscillator strength in the classical case is defined to fit to the prefactor in the semi-classical case, the forms of the two equations are rather similar. There are only two differences that become apparent: First, in the denominator, the dependence on ω in the semi-classical case is different from the classical case. Second, the term $\Omega^2/2$ does not appear in the classical soltution. The first difference is rooted in the fact that the Schrödinger equation is a first order differential equation whereas the Newton approach uses a second derivative in time. For not too strong damping $\Gamma \ll \omega$ and close to resonance however, we can rewrite the classical expression using the appoximation $(\omega_0^2 - \omega^2) \approx 2\omega_0(\omega_0 - \omega)$ [26], to

$$\varepsilon_{\text{Lorentz}} = \varepsilon_\infty + f\omega_0^2 \frac{(\omega_0^2 - \omega^2) + i\Gamma\omega}{(\omega_0^2 - \omega^2)^2 + \Gamma^2\omega^2} \approx \varepsilon_\infty + \frac{f\omega_0}{2} \frac{\omega_0 - \omega + i\dfrac{\Gamma}{2}}{(\omega_0 - \omega)^2 + \dfrac{\Gamma^2}{4}}\,. \tag{3.121}$$

When setting $f = 2N\mu^2/V\omega_0\varepsilon_0\hbar$, this expression is already much closer to the correct semi-classical solution. Only the dependence on Ω is still missing. This is because this term accounts for the saturation of a two-level system, an effect that is not incorporated in the classical approach since it allows arbitrary amplitudes of the polarisation.

The fact that Ω^2 causes saturation can be seen when defining a saturation parameter

$$s = \frac{\dfrac{\Omega^2}{2}}{(\omega_0 - \omega)^2 + \dfrac{\Gamma_{\text{sp}}^2}{4}}\,. \tag{3.122}$$

With this term, the semi-classical susceptibility can be rewritten as

$$\chi_{\text{two-level}} = \frac{\chi_0}{1+s} \tag{3.123}$$

where χ_0 describes the polarisability without external electric field, i.e. $\Omega = 0$.

For weak electric fields and consequently small $\Omega^2 \ll \Gamma$, the saturation parameter becomes small and the semi-classical and the classical solution approximately coincide. For large Ω however, s becomes larger until, in the extreme case $\chi_{\text{two-level}} \to 0$. This means the emitters can no more interact with the light since they already are fully saturated.

Spectrally, the effect is seen in a lowering of the amplitude and a broadening of the resonance peak. It is therefore also sometimes referred to as *power broadening* [104]. In most light–matter interactions, the electric fields are small enough to neglect saturation. This explains the huge success of the Lorentz oscillator model which is mostly used to describe emitters.

On the other hand, electric fields can be so strong that saturation can no more be negelcted. We can

define a saturation intensity I_{sat} above which saturation needs to be regarded as [36]

$$I_{\mathrm{sat}} = \frac{1}{4} c \varepsilon_0 \frac{\hbar^2 \gamma^2}{\mu^2} \,. \tag{3.124}$$

Emitters in a field of this intensity have a halved susceptibility. Traditionally, these fields are generated by intense laser beams. Article III argues that also the field fluctuations of the vacuum mode in plasmonic nanoparticles can generate intensities in the region of I_{sat}. Thus, a correct description needs to take saturation into account. The article argues that Equation 3.120 is to be used in correct simulations of core–shell nanoparticle spectra. However, in this form, the saturation would be zero for vanishing external fields (since $\Omega \to 0$). Therefore, to account for the vacuum fluctuations, Ω needs to be replaced by the vacuum Rabi frequency which will be introduced in the following section.

The previous examination of two-level systems in strong electric fields marks the end of this section. It established the understanding of the permittivity of gold and of two-level emitters. This can be used to simulate the spectra of plasmon–exciton gold nanoparticles as is done in Articles III and IV. The permittivities are there plugged into the expressions for the optical cross sections of core–shell particles discussed in the first part of this chapter.

The section first discussed the permittivity of gold starting with the contribution of the free electrons, and subsequently including interband transitions. In the second part the permittivity of two-level systems was introduced, first using the model of a bound electron acting as a Lorentz oscillator and afterwards respecting the actual two-level nature of the emitter. The two models together serve with an ab-initio possibility to model the optical properties of plasmon–exciton core–shell particles.

In these particles, plasmons and excitons are directly coupled, in some cases so strongly that the interaction exceeds all other decay channels. The consequences of this coupling is one of the main topics in Articles I – IV. Therefore, this chapter's last section will discuss the coupling between plasmons and excitons.

3.5 Plasmon–Exciton Coupling

Articles I - IV discuss the coupling of excitons in a J-aggregate forming dye with plasmons in gold nanoparticles. The dye can be regarded as an ensemble of quantum emitters, whereas a plasmonic nanoparticle in principle forms an electromagnetic cavity. A cavity can strongly alter an emitter's properties like its absorption and emission in regard to free space. The reason is the coupling, i.e. the interaction between emitter and cavity. It enables an energy transfer from the emitter to the cavity and vice versa.

Energy can also be dissipated from the emitter or the cavity to the environment. In case, the dissipation is stronger than the coupling, the system is in the *weak coupling regime*. This situation is the basis of

effects like the Purcell enhancement of emission and absoprtion [105], enhancement of light harvesting e.g. in solar cells [17], surface enhanced Raman spectroscopy (SERS) [21].

If the coupling exceeds all other energy decay channels, the system is in the *strong coupling regime*. In this case, the two components can no more be regarded as independent but a new hybrid entity emerges with potentially new features. Various applications utilising this effect have been suggested. Examples include ultrafast optical switches [24], thresholdless lasing [26], modifications of chemical landscapes [25] or quantum networks [23], to name a few.

This work's articles investigate core–shell systems that exhibit both strong and weak coupling and this section introduces the general consequences of light–matter coupling. It is structured as follows: The first part will present a full quantum approach to describe the coupling between a quantum two-level system and an electromagnetic cavity. A more general way to describe coupling between two systems is represented by the system of classical harmonic coupled oscillators. This system also offers a more intuitive approach to introduce energy dissipation to the environment. Therefore, we will discuss this more general model and show the analogy to the more special cavity–emitter case. After the inclusion of damping to the model the section will subsequently discuss the two regimes of strong and weak coupling. In the end, the discussion will be generalised to the case of many emitters coupled to one cavity.

Full quantum approach: This part can be regarded as the continuation of the previous section which discussed a two-level system placed in a classical electric field. Now, the system is placed in a cavity and the field is quantised as shown in Figure 3.20. In contrast to the semi-classical discussion above, we will focus on the coupling between the two systems and not on a description of the emitter's susceptibility.

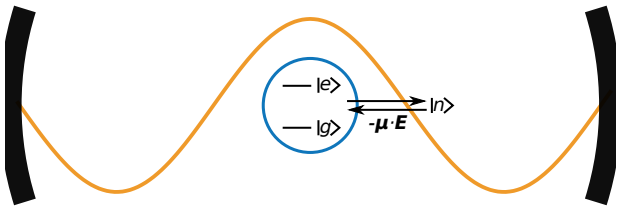

Figure 3.20: Full quantum representation of an emitter in an electromagnetic cavity. The emitter is represented by a two-level system with ground state $|g\rangle$ and excited state $|e\rangle$ while the cavity mode is described by the quantised electric field with photon number state $|n\rangle$. The interaction is mediated by the coupling energy $-\boldsymbol{\mu}\cdot\mathbf{E}$.

The quantised field of a cavity is expressed by the operator $\mathbf{E} = \mathscr{E}(a^\dagger + a)$ [106] with the creation ($a^\dagger$) and annihilation (a) operators of the electromagnetic mode. For simplicity, we only consider one mode with photon energy $\hbar\omega_{\text{cav}}$. Like in the semi-classical case, the interaction between the field and an emitter with resonance energy $\hbar\omega_{\text{em}}$ is given by the energy of the transition dipole with dipole moment $\boldsymbol{\mu} = \mu(|g\rangle\langle e| + |e\rangle\langle g|)$ in the electric field. This is now expressed via the interaction Hamiltonian $H_{\text{int}} = -\boldsymbol{\mu}\cdot\mathbf{E}$.

The Hamiltonian describing the complete coupled system is composed of the undisturbed Hamiltonians of the subsystems and the interaction Hamiltonian, that is $H = H_{\text{cav}} + H_{\text{em}} + H_{\text{int}}$. When including time evolution, $|g\rangle\langle e|$ and a would oscillate in the same direction, as well as $|e\rangle\langle g|$ and $a^\dagger$. Therefore, $|g\rangle\langle e|a$

and $|e\rangle\langle g|a^\dagger$ would oscillate very quickly and average to zero. They can therefore be neglected in H_{int} [106]. This is exactly the rotating wave approximation that we already applied in the semi-classical case. Without losses, the Hamiltonian then writes as [104]

$$H = \hbar\omega_{\text{cav}} a^\dagger a + \hbar\omega_{\text{em}} |e\rangle\langle e| + \hbar\Omega_0 (|g\rangle\langle e| a^\dagger + |e\rangle\langle g| a) \tag{3.125}$$

with the coupling energy $\hbar\Omega_0 = -\mu\mathscr{E}$. Note that the zero of energy was chosen such that it coincides with the energy of the state $|g,0\rangle$. This Hamiltonian is often referred to as the *Jaynes-Cummings Hamiltonian*.

For each value n of the number of photons in the cavity, the interaction couples the states $|g,n+1\rangle$ and $|e,n\rangle$ since only for $\langle e,n|H_{\text{int}}|g,n+1\rangle \neq 0$ (and $\langle g,n+1|H_{\text{int}}|e,n\rangle \neq 0$). We can therefore write H as a sum of Hamiltionians H_n acting only on the manifold $\{|g,n+1\rangle, |e,n\rangle\}$ [106]. In this basis, H_n writes as [104]

$$H_n = \hbar \begin{pmatrix} (n+1)\omega_{\text{cav}} & \sqrt{n+1}\Omega_0 \\ \sqrt{n+1}\Omega_0 & n\omega_{\text{cav}} + \omega_{\text{em}} \end{pmatrix}. \tag{3.126}$$

We are interested in the eigenenergies $\hbar\omega_{n,\pm}$ of this Hamiltionian which can be experimentally recognised as resonances in an optical spectrum. They are found from $\det(H_n - \hbar\omega_{n,\pm}) = 0$ as

$$\omega_{n,\pm} = n\omega_{\text{cav}} + \frac{\omega_{\text{cav}} + \omega_{\text{em}}}{2} \pm \sqrt{\frac{(\omega_{\text{cav}} - \omega_{\text{em}})^2}{4} + (n+1)\Omega_0^2}\,. \tag{3.127}$$

These eigenfrequencies are often referred to as the *normal modes* or *polariton modes* of the system. For the articles of this work that investigate plasmon–exciton coupling, weak non-coherent light sources were used. In this case, at most one excitation is found in the coupled system. Before the arrival of a potentially second external photon, the energy is already decayed. This situation is described by setting $n = 0$ referred to as low excitation limit. We will concentrate on this case. There, the eigenfrequencies are

$$\omega_\pm = \frac{\omega_{\text{cav}} + \omega_{\text{em}}}{2} \pm \sqrt{\frac{(\omega_{\text{cav}} - \omega_{\text{em}})^2}{4} + \Omega_0^2}\,. \tag{3.128}$$

In the absence of coupling ($\Omega_0 = 0$), $\omega_\pm$ are identical to the original resonances of cavity and emitter. For $\Omega_0 \neq 0$, the coupled resonances start to deviate from the original ones. Figure 3.21 illustrates this by plotting the new resonances in respect to the detuning $\delta = \omega_{\text{cav}} - \omega_{\text{em}}$ between the original resonances. The emitter resonance is kept constant at $\hbar\omega_{\text{em}} = 2\,\text{eV}$ while the cavity resonance is tuned. The coupling is set to $\hbar\Omega_0 = 100\,\text{meV}$. The values are chosen to be in the region of realistic values for the plasmon–exciton systems of Articles I – IV. For a strong detuning, the new resonances are similar to ω_{cav} and ω_{em}. For the detuning approaching zero, the deviation between normal modes and original frequencies becomes larger, resulting in an *anticrossing* of the branches and an *energy splitting* of the original resonances. At the position of zero detuning, the distance between ω_+ and ω_- is $2\Omega_0$. This means that the anticrossing of a coupled system directly yields the coupling energy $\hbar\Omega_0$. This was used

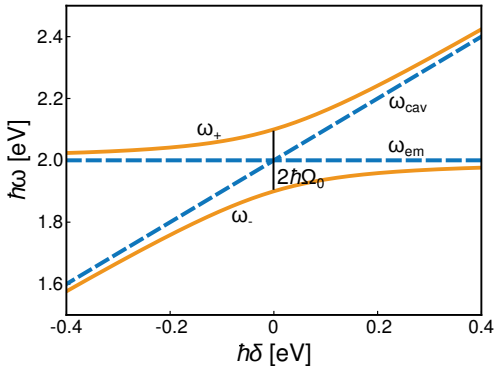

Figure 3.21: Illustration of the anticrossing of the coupled eigenmodes $\omega_{\pm}$. The solid orange lines depict the eigenfrequencies resulting from Equation 3.128. The emitter resonance is fixed at $\hbar\omega_{\mathrm{em}} = 2\,\mathrm{eV}$ while the cavity resonance is tuned. The coupling is $\hbar\Omega_0 = 100\,\mathrm{meV}$. The dashed blue lines represent the original resonances of cavity and emitter.

in Articles I and II which assess the coupling strength of plasmon–exciton core–shell nanoparticles via their anticrossing.

Interestingly, a splitting for $n = 0$ implies that even in the absence of cavity excitations, the modes are split up. The effect is referred to as *vacuum Rabi splitting* [26]. Its occurrence is attributed to the vacuum fluctuations, that is the non-vanishing expectation value of the squared electric field in the vacuum state. This expectation value calculates as

$$\langle 0|\,\mathbf{E}^2\,|0\rangle = \langle 0|\,\mathscr{E}(a^\dagger + a)^2\,|0\rangle = |\mathscr{E}|^2\,. \tag{3.129}$$

These vacuum fluctuations are also the root of other effects like spontaneous emission or the Lamb shift [107]. They can even cause saturation of the emitter as discussed in Article III.

From the expression for the vacuum fluctuations, we see why $\mathscr{E}$ is usually referred to as *vacuum electric field*. We can now also find a quantitative expression for this vacuum field. The vacuum energy is restricted to a volume V. This volume is the so-called mode volume of the cavity. The total energy of the vacuum state is $\hbar\omega_{\mathrm{cav}}/2$. Consequently, the vacuum energy density multiplied with the mode volume needs to match this value. Assuming that both electric and magnetic field contribute equally to the energy, this means [108]

$$\varepsilon\varepsilon_0|\mathscr{E}|^2 V = \frac{\hbar\omega_{\mathrm{cav}}}{2}\,. \tag{3.130}$$

This yields an expression for the vacuum electric field as

$$\mathscr{E} = \sqrt{\frac{\hbar\omega_{\mathrm{cav}}}{2\varepsilon\varepsilon_0 V}}\,. \tag{3.131}$$

Thus, in the low excitation limit, the coupling energy of an emitter coupled to an electromagnetic cavity

is

$$\hbar\Omega_0 = \mu\mathscr{E} = \sqrt{\frac{\hbar\omega_{\mathrm{cav}}\mu^2}{2\varepsilon\varepsilon_0 V}}\,. \tag{3.132}$$

This expression contains another interpretation, why plasmonic nanoparticles represent excellent cavities for light–matter coupling: For a small nanoparticle, the mode volume is on the order of the particle's physical volume [109]. This small mode volume is the root of the high field strengths that were discussed in Section 3.2. Therefore, the interaction between a plasmonic nanoparticle and an emitter can become quite intense.

To gain a deeper understanding of the coupling, we want to investigate the new states that are generated by the coupled Hamiltonian. The eigenstates to the respective eigenmodes of H are found to be

$$|+\rangle = \sin\theta_0\,|g,1\rangle + \cos\theta_0\,|e,0\rangle \tag{3.133a}$$

and

$$|-\rangle = \cos\theta_0\,|g,1\rangle - \sin\theta_0\,|e,0\rangle\ , \tag{3.133b}$$

corresponding to ω_+ and ω_-, respectively [106]. Here,

$$\sin\theta_0 = \frac{2\Omega_0}{\sqrt{(R_0-\delta)^2+4\Omega_0^2}}\,, \tag{3.134a}$$

$$\cos\theta_0 = \frac{R_0-\delta}{\sqrt{(R_0-\delta)^2+4\Omega_0^2}} \tag{3.134b}$$

with $R_0 = \sqrt{\delta^2+4\Omega_0^2}$ were used. Note that we, due to its exclusive relevance for this work, still only discuss the case of $n=0$. In the special case of no detuning ($\delta = 0$), the eigenstates simplify to

$$|+\rangle = \frac{1}{\sqrt{2}}\left(|g,1\rangle + |e,0\rangle\right) \tag{3.135a}$$

and

$$|-\rangle = \frac{1}{\sqrt{2}}\left(|g,1\rangle - |e,0\rangle\right)\,. \tag{3.135b}$$

That means that in the case of no detuning, both subsystems are equally excited, once in phase ($|+\rangle$) and once with a phase difference of π ($|-\rangle$). Like in the case of J-aggregates where the exciton is

delocalised over the whole aggregate, the excitation is here evenly distributed here. It is hence no more possible to treat the systems independently. They form new hybridised states. In the case of J-aggregates, it is easy to see, that the hybridised state shows new features that were not present in the uncoupled subsystems (e.g. a new resonance). Similarly, other hybrid systems can exhibit comparable manifestations of new properties. As an example from a different (light free) context, covalent chemical bonds can be regarded as strong coupling between atoms. The atoms form hybrid states with completely new chemical properties.

Let us now look at the temporal behaviour of a coupled system. In the Schrödinger picture, the temporal evolution is found from $|\psi(t)\rangle = e^{-i\frac{H}{\hbar}t}|\psi(0)\rangle$. Let us assume the emitter to be initially excited and the cavity to be in the ground state. In the coupled eigenstates, this writes as

$$|\psi(0)\rangle = |e,0\rangle = \frac{1}{\sqrt{2}}(|+\rangle - |-\rangle)\,. \tag{3.136}$$

Thus, after time t, the state has evolved to

$$\begin{aligned} |\psi(t)\rangle =& \frac{1}{\sqrt{2}}\left(e^{-i\omega_+ t}|+\rangle - e^{-i\omega_- t}|-\rangle\right) \\ =& e^{-i\omega_0 t}\left(\cos(\Omega_0 t)|e,0\rangle - i\sin(\Omega_0 t)|g,1\rangle\right) \end{aligned} \tag{3.137}$$

with $\omega_0 = \omega_{\text{cav}} = \omega_{\text{em}}$. This time evolution directly yields the probability for the emitter to be in the excited state P_e which is given by [104]

$$P_e(t) = |\langle e,0|\psi(t)\rangle|^2 = \cos^2(\Omega_0 t)\,. \tag{3.138}$$

That means, P_e oscillates between 0 and 1. This oscillation is the famous *Rabi oscillation*.

Analogously, the probability for a photon to be in the cavity (and thus, the emitter to be in the ground state) P_g is

$$P_g(t) = |\langle g,1|\psi(t)\rangle|^2 = \sin^2(\Omega_0 t)\,. \tag{3.139}$$

Figure 3.22 illustrates the situation. It presents the occupation probability of ground and excited state for a system with an uncoupled resonance at $\hbar\omega_0 = 2\,\text{eV}$ coupled with an energy $\hbar\Omega_0 = 100\,\text{meV}$. Both occupation probabilities oscillate with a frequency $2\Omega_0$ and their sum is one. The excitation on the emitter is thus emitted as a photon into the cavity and reabsorbed again. This means, the Rabi oscillations describe a periodic exchange of energy between the emitter and the cavity. This energy exchange occurs at twice the so-called *Rabi frequency* Ω_0 [103].

For plasmonic cavities, the correct quantum mechanical description is conceptually challenging and needs to be conducted within the framework of *quasinormal modes* [110, 111]. Therefore, the coupling between plasmons and emitters is often described by the model system of classical coupled oscillators [25, 54, 61] due to the model's simplicity and intuitivity while at the same time, most features of a

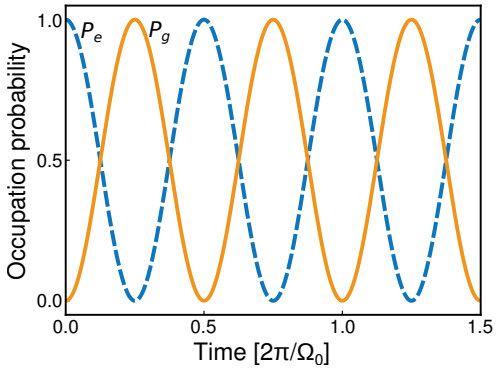

Figure 3.22: Time evolution of the occupation probability P_i of the emitter's ground (solid orange line) and excited (dashed blue line) state. Both probabilities perform Rabi oscillations at a frequency of $2\Omega_0$. P_g is identical to the occupation probability of the one photon state.

coupled light–matter system can be retrieved [112]. Also Article I uses classical harmonic oscillators to explain the scattering and absorption spectra of core–shell nanoparticles.

Furthermore, especially in plasmonic cavities, energy dissipation cannot be neglected. To apprehend the occurrence of weak and strong coupling regimes, we need to take these losses into account. In the presented quantum model, we could do this phenomenologically as we did in the semi-classical case (note, that this only works in the case of $n = 0$ [62]). But also here, classical oscillators already give a good insight into the properties of lossy systems. The following part will therefore introduce the general model of two coupled classical oscillators.

Classical coupled oscillators: First, the model is discussed without damping to show the analogy between the resulting expressions and the quantum model. Afterwards, damping and its consequences for the coupling regime will be introduced. Let us consider two masses (m_A and m_B), each attached to the ground with a spring with constant k_A and k_B and both connected with a spring with constant κ. Figure 3.23 illustrates the situation.

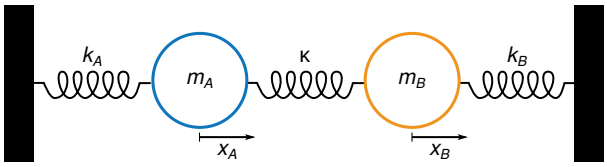

Figure 3.23: Sketch of two classical coupled harmonic oscillators. Two massed m_A and m_B are connected to solid ground via springs with constants k_A and k_B. The two masses are coupled via another spring with constant κ.

The equations of motion for this coupled system are then given by

$$m_A x_A + k_A x_A + \kappa(x_A - x_B) = 0\,, \tag{3.140a}$$

$$m_B x_B + k_B x_B + \kappa(x_B - x_A) = 0\,. \tag{3.140b}$$

The Fourier ansatz with $x_i = x_{0,i}\exp(i\omega t)$ leads to the eigenfrequencies $\omega_\pm$ of the system. With $\omega_i^2 = (k_i + \kappa)/m_i$ and $\kappa/m_i = 2\omega_i\Omega$, the problem can be expressed in matrix form

$$\begin{pmatrix} \omega_A^2 - \omega^2 & 2\omega_A\Omega \\ 2\omega_B\Omega & \omega_B^2 - \omega^2 \end{pmatrix} \begin{pmatrix} x_A \\ x_B \end{pmatrix} = \begin{pmatrix} 0 \\ 0 \end{pmatrix}. \tag{3.141}$$

The definitions of ω_A, ω_B and Ω are chosen to coincide with the values from the full quantum model.

We are are interested in the spectral region around the oscillator resonances that should not be detuned too much. We can therefore assume that $\omega \approx \omega_A \approx \omega_B$. Consequently, $\omega_i^2 - \omega^2 \approx 2\omega_i(\omega_i - \omega)$. With this, the problem simplifies to

$$\begin{pmatrix} \omega_A - \omega & \Omega \\ \Omega & \omega_B - \omega \end{pmatrix} \begin{pmatrix} x_A \\ x_B \end{pmatrix} = \begin{pmatrix} 0 \\ 0 \end{pmatrix}. \tag{3.142}$$

The eigenfrequencies $\omega_\pm$ are found by setting the determinant of the system of equations to zero:

$$\omega_\pm = \frac{\omega_A + \omega_B}{2} \pm \sqrt{\frac{(\omega_A - \omega_B)^2}{4} + \Omega^2}\,. \tag{3.143}$$

A comparison with Equation 3.128 shows that these are exactly the same frequencies as in the full quantum model in the case of $n = 0$. Thus, the anticrossing from Figure 3.21 is directly recovered in both models.

Also the temporal evolution is the same as retrieved from the Jaynes-Cummings Hamiltonian. The general solution is obtained by plugging the new modes into the Fourier ansatz.

$$x_A(t) = X_{A,-}e^{i\omega_- t} + X_{A,+}e^{i\omega_+ t} + c.c\,, \tag{3.144a}$$

$$x_B(t) = X_{A,-}e^{i\omega_- t} - X_{A,+}e^{i\omega_+ t} + c.c\,. \tag{3.144b}$$

When only mode ω_- is excited, both masses oscillate in phase whereas when only the higher value ω_+ is excited, the masses oscillate out of phase. This is exactly the same phase relation as in the quantum case. A slight difference is only that in the oscillator case, the in-phase motion has lower energy, since there, the coupling spring is always in rest position, whereas a dipole oriented parallel to an electric field possesses higher energy and consequently, in the emitter-in-cavity system, the in-phase is attributed to the higher eigenenergy.

The situation of no detuning occurs when both oscillators possess the same resonance frequency ω_0. As an example, oscillator A shall be at rest, but displaced from equilibrium by x_0 and oscillator B at rest at

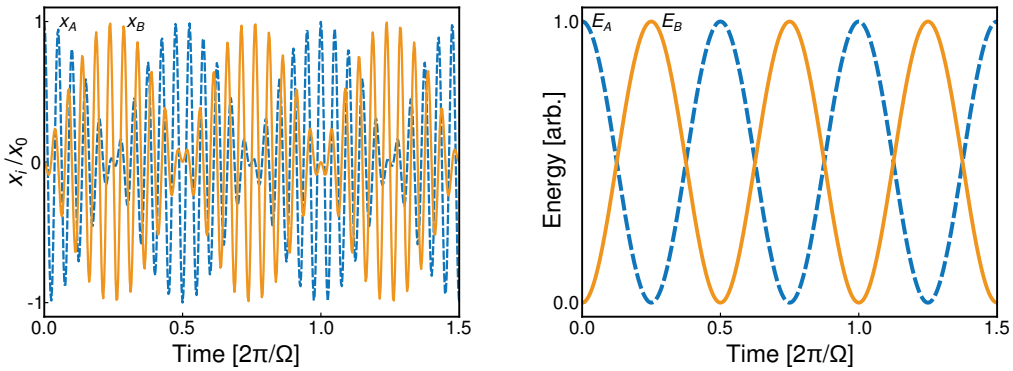

Figure 3.24: Temporal evolution of two identical coupled oscillators with $\hbar\omega_0 = 2\,\mathrm{eV}$ with a coupling energy of $\hbar\Omega = 100\,\mathrm{meV}$. Initially, oscillator A (dashed blue line) is at rest at x_0, while oscillator B (solid orange line) rests at $x = 0$. The left panel depicts the position of the respective oscillator. Both oscillate at a frequency ω_0 multiplied by an envelope $\cos(\Omega t)$ and $\sin(\Omega t)$ for A and B, respectively. The right panel shows the energy of both oscillators. The energy stored each oscillator oscillates at a frequency of 2Ω, with a mutual phase difference of π.

$x_B = 0$. The dynamics is then described as

$$x_A(t) = \frac{x_0}{2}(\cos(\omega_- t) + \cos(\omega_+ t))\,, \tag{3.145a}$$

$$x_B(t) = \frac{x_0}{2}(\cos(\omega_- t) - \cos(\omega_+ t))\,. \tag{3.145b}$$

Figure 3.24a presents the displacements x_i for two oscillators with $\hbar\omega_0 = 2\,\mathrm{eV}$ and $\hbar\Omega = 100\,\mathrm{meV}$. The pattern is the typical beating pattern of two similar oscillation frequencies, in this case ω_+ and ω_-. Already here, an energy exchange becomes visible. At early times, mainly oscillator A is moving at frequency ω_0. This motion is damped while oscillator B begins to oscillate with the same frequency and increasing amplitude. After $t = \pi/2\Omega$, oscillator A is almost completely at rest. Subsequently, its amplitude rises again at the cost of B's amplitude. In other words, the motion of each oscillator is limited by an envelope function $\cos(\Omega t)$ and $\sin(\Omega t)$ for oscillator A and B, respectively.

The analogy to the Rabi oscillations becomes more clear, when looking at the energy of each oscillator. We can write the energy of each subsystem as

$$E_i = E_{\mathrm{kin},i} + E_{\mathrm{pot},i} = \frac{1}{2}m\dot{x_i}^2 + \frac{1}{2}m\omega_0^2 x_i^2\,. \tag{3.146}$$

For oscillator A, this yields

$$E_A = \frac{1}{2}m\omega_0^2 x_0^2\left[\cos^2(\Omega t) + \frac{\Omega}{2\omega_0}\sin(2\omega_0 t)\sin(2\Omega t) + \frac{\Omega^2}{4\omega_0^2}(\sin(\omega_+ t) - \sin(\omega_- t))^2\right]\,. \tag{3.147}$$

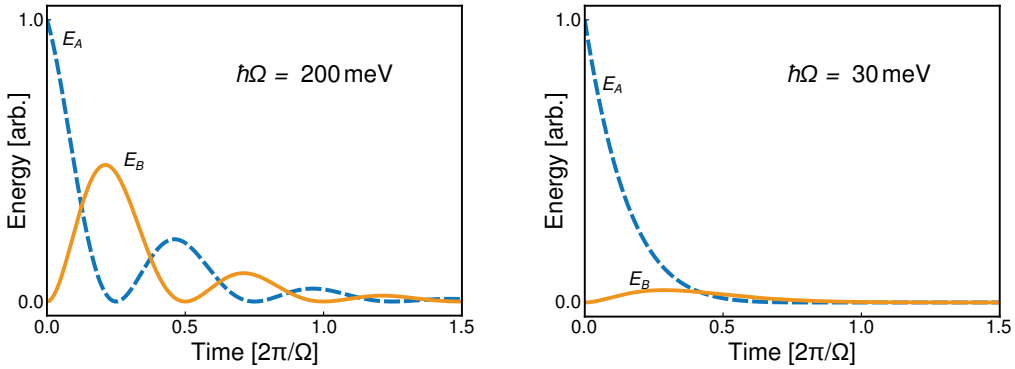

Figure 3.25: Temporal evolution of two identical coupled oscillators with $\hbar\omega_0 = 2\,\text{eV}$ damped by $\hbar\gamma = 60\,\text{meV}$. Initially, oscillator A (dashed blue line) is at rest at x_0, while oscillator B (solid orange line) rests at $x = 0$. The energy oscillations are of the same form as for the uncoupled case. Only now, energy is additionally dissipated. The left panel depicts the situation with $\hbar\Omega = 200\,\text{meV}$, the left panel that with $\hbar\Omega = 30\,\text{meV}$. On the left side, energy can be passed back and forth a few cycles before it is lost, while on the right side, no more energy is transferred back to oscillator A.

For not too high couplings, that means as long as $\omega_0 \gg \Omega$, the first term dominates the energy and consequently

$$E_A = \frac{1}{2} m\omega_0^2 x_0^2 \cos^2(\Omega t)\,. \tag{3.148}$$

Analogously, the energy of oscillator B is

$$E_B = \frac{1}{2} m\omega_0^2 x_0^2 \sin^2(\Omega t)\,. \tag{3.149}$$

Hence, just like in the full quantum case, the energy is passed between the two subsystems with a frequency of 2Ω. Figure 3.24b presents this situation for the same oscillators as used in Panel a.

We saw, that the model of coupled classical oscillators is able to reproduce the main features of the pure quantum model in the low excitation limit ($n = 0$) and for couplings that are not too strong ($\omega_0 \gg \Omega$). The anticrossing, the phase relation and the Rabi oscillations can be derived. This explains the model's success in discussions about coupled plasmon–exciton systems.

Now that the analogy between the two models is established, we can introduce damping to the discussion. This is simply done by adding a friction term $m_i\gamma_i\dot{x}_i$ to Equations 3.140. The coupled resonances are then calculated as above to be

$$\omega_\pm = \frac{\omega_A + \omega_B}{2} - i\frac{\gamma_A + \gamma_B}{4} \pm \sqrt{\left(\frac{\omega_A - \omega_B}{2} - i\frac{\gamma_A - \gamma_B}{4}\right)^2 + \Omega^2}\,. \tag{3.150}$$

The temporal solution for the deflections is then found from inserting these resonances into the general

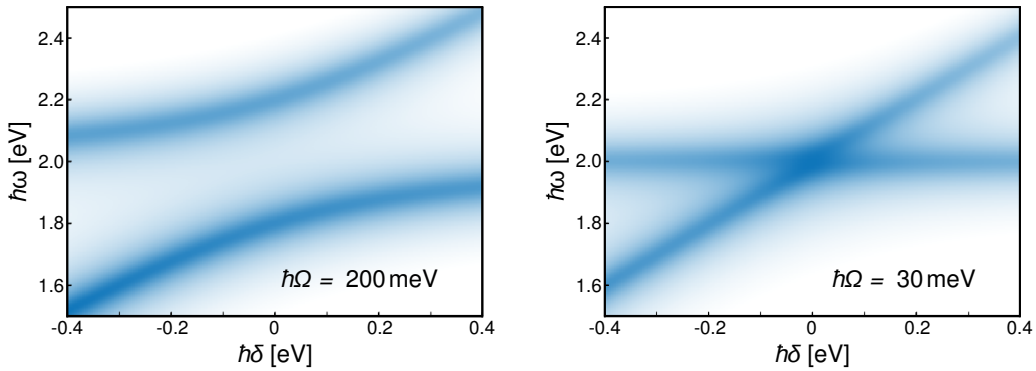

Figure 3.26: Amplitudes of two coupled oscillators damped by $\hbar\gamma = 60\,\mathrm{meV}$. The resonance of oscillator B is kept constant at $\hbar\omega_B = 2\,\mathrm{eV}$ while the resonance of oscillator A is tuned. The plots are found by assuming the coupled modes to be Lorentz peaks with complex resonances $\omega_\pm$. The left panel depicts the situation with $\hbar\Omega = 200\,\mathrm{meV}$, the right panel that with $\hbar\Omega = 30\,\mathrm{meV}$. While on the left side, a clear anticrossing is visible the branches seem to cross in the right panel.

solution given in Equation 3.144. The oscillations are now damped due to the non-vanishing imaginary component in the frequencies $\omega_\pm$. For the case of identical oscillators with $\hbar\omega_0 = 2\,\mathrm{eV}$, this is shown in Figure 3.25. Again, the energies are shown for an initial condition of $x_A(0) = x_0$ and $x_B(0) = 0$ with both oscillators at rest. In both panels, a damping of $\hbar\gamma = 60\,\mathrm{meV}$ is included. For the left panel, the coupling was chosen to be $\hbar\Omega = 200\,\mathrm{meV}$, for the right, $\hbar\Omega = 30\,\mathrm{meV}$.

We can identify two different situations: In the left case, the energy can be passed back and forth before it is lost, whereas in the overdamped case in the right panel, it decays so quickly that it is not retransferred to oscillator A. These two situations are accounted to two regimes: the strong coupling regime on the left and the weak coupling regime on the right.

Another interpretation of the two different regimes is found by looking at the anticrossings in Figure 3.26. The Figure exhibits the coupled resonances for the same situations as the energy oscillations in Figure 3.25. In the presence of damping, the anticrossing is washed out due to the widening of the resonances. If the coupling is too weak as in the right panel, the two branches can no more be differentiated. Only when the splitting is wider than the linewidths, a clear anticrossing can be identified. This can be regarded as another way to differentiate between weak and strong coupling [26].

For both interpretations of the strong coupling regime, the sufficiently wide splitting and the sufficiently fast energy transfer, a good demand to the coupling strength is that

$$2\Omega > \frac{\gamma_A + \gamma_B}{2}. \tag{3.151}$$

This criterion is found to be applicable not only for classical oscillators, but also for light–matter interactions [25, 62, 113] and is also used in Articles I – III.

The model of classical coupled oscillators is widely used for describing plasmon–exciton systems. Here, we discussed the case of a closed system without external forces. An external light field illuminating a

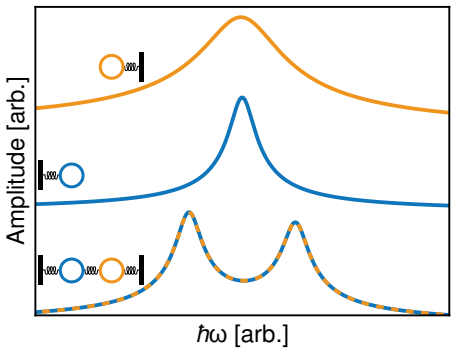

Figure 3.27: Illustration of the effect of coupling. The two upper lines represent the amplitude of two oscillator representing a plasmon (orange line) and an exciton (blue line). The dashed orange–blue line shows the amplitudes that arise when a coupling between the two systems is established.

plasmon–exciton system works like an external driving force on the oscillators. Also for this situation, a coupled oscillator model can be used to describe the main features of the plasmon–exciton system as in Article I.

Before moving on to the situation of many emitters coupled to a cavity, let us have a conclusive look at the typical spectrum of a coupled plasmon–exciton system in comparison to the uncoupled situation. Figure 3.27 shows the frequency dependent amplitudes of two single oscillators, one with a wider linewidth representing the plasmon, one with a narrower linewidth, representing the exciton. As soon as a coupling is established, the original peaks split up and two new resonances, one red-shifted, one blue-shifted, arise. This model gives a good representation of real spectra of plasmon–exciton core-shell particles. Examples will be presented in the next chapter.

Many emitters coupled to one cavity: Until now, we only discussed the coupling between a single emitter and a single mode in a cavity. Articles I–IV all treat the situation of core–shell particles with shells consisting of many emitters. Fortunately, many emitter coupling can be described in terms of the two models presented above.

For the quantum case, the Jaynes-Cummings Hamiltonian needs to be expanded to the situation of many emitters. It then becomes

$$H = \hbar\omega_{\mathrm{cav}} a^{\dagger} a + \sum_{i=1}^{N} \hbar\omega_{\mathrm{em}} |e\rangle_i \langle e|_i + \sum_{i=1}^{N} \hbar\Omega_0 (|g\rangle_i \langle e|_i a^{\dagger} + |e\rangle_i \langle g|_i a) \tag{3.152}$$

where $|g\rangle_i$ and $|e\rangle_i$ describe the ground and excited state of the i-th emitter. This Hamiltonian is often called *Dicke* or *Tavis-Cummings* Hamiltonian [26]. This Hamiltonian can be solved analytically [114] but the solution is rather complicated and does not serve with deeper insights for our purposes. In the case of only a few excitations in the emitter system, the Hamiltonian can be simplified. The emitter

system can then be described as one giant oscillator and

$$H = \hbar\omega_{\mathrm{cav}} a^{\dagger} a + \hbar\omega_{\mathrm{em}} b^{\dagger} b + \hbar\Omega_0 (a^{\dagger} b + a b^{\dagger}) \,. \tag{3.153}$$

Here, $b^{\dagger}$ and b represent the creation and annihilation operators of the giant oscillator system.

In the following, we will again discuss the case of only one excitation in the system as we did in the single emitter case. Several eigenstates can be found for the Hamiltonian, but only two of them couple to external light fields [62]. These *bright states* have the resonance frequencies [115]

$$\omega_{\pm} = \frac{\omega_{\mathrm{cav}} + \omega_{\mathrm{em}}}{2} \pm \sqrt{\frac{(\omega_{\mathrm{cav}} - \omega_{\mathrm{em}})^2}{4} + N\Omega_0^2} \,. \tag{3.154}$$

This is the same anticrossing as for the single emitter case in Equation 3.128, however with a wider splitting with a minimum of $2\sqrt{N}\Omega_0$ at the point of no detuning. Thus, the energy exchange between emitters and cavity can be increased by the number of emitters N and strong coupling for many emitters can be reached also for systems that would not show strong coupling for single emitters. In fact, in the plasmonic context, only very few systems with single emitter strong coupling have been reported [54, 116]. In most other cases, like in this work, strong coupling is achieved by the coupling of several emitters to one plasmonic cavity [117–119]. Note that also the case of N classical oscillators coupled to another classical oscillator is analogous to the findings above [120]. Also in this classical case the difference between the normal modes is proportional to $\sqrt{N}$.

From the Tavis-Cummings Hamiltonian, Equation 3.153, the respective eigenstates to $\omega_{\pm}$ are found to be

$$|\pm\rangle = \frac{1}{\sqrt{2}} [|g,...,g,1\rangle \pm \frac{1}{N} \sum_{i=1}^{N} |e\rangle_i \langle g|_i \, |g,...,g,0\rangle] \,. \tag{3.155}$$

In the excited state, the excitation on the emitters is evenly spread over the whole emitter system. This is the same situation as in the case of J-aggregates. It shows that a J-aggregate consists of N strongly coupled monomers. This analogy is also consistent with the energy splitting above. From Equation 3.154, we would obtain the same splitting for N weak emitters with transition dipole moment μ as for a single strong emitter with $\sqrt{N}$-fold higher transition dipole moment. The latter describes precisely the situation of a J-aggregate of N monomers.

Article III argues that the fact that an ensemble of emitters acts like one giant J-aggregate, allows describing this ensemble as two-level system. Section 3.3 discussed the situation of a single exciton delocalised over an aggregate. Due to Pauli exclusion, a potential second exciton cannot reside on the same monomer as the first one [121]. This causes a blue-shift of the transition between one-exciton state and two-exciton state [85]. Simply speaking, this blue shift is caused by the smaller effective space in which the second exciton can reside [122]. As a consequence, the saturation of the transition from the ground state to the one-exciton state (*ground state bleaching*) and the transition from the one-exciton to the two-exciton state (*excited state absorption*) can be obeserved in pump–probe experiments at different spectral positions [123]. In a monochromatic field, the detuning between the two transitions

allows the descirption of a J-aggregate as two-level system as in Section 3.4.2. Article III argues that this is the case also for a shell of emitters in a core–shell geometry. This assumption is supported by transient measurements of J-aggegate–gold nanoshell complexes [124]. In such geometries, very similar to the core–shell particles utilised for Articles I – IV, both ground state bleaching and a spectrally shifted excited state absorption has been observed. This indicates that the whole shell can be approximated by a two-level system.

Conclusively, this section has established an understanding of plasmon–exciton coupling. It introduced the full quantum description yielding the important anticrossing of the polariton modes and showed Rabi oscillations. Both anticrossing and Rabi oscillations can also be derived in the framework of classical coupled oscillators which we did before discussing energy decay and its influence on the coupling regime. If the losses exceed the coupling, the system is in the weak coupling regime while it exhibits strong coupling when the coupling dominates the losses. We eventually discussed the situation of many emitters coupled to one cavity and how the coupling strength increases with the number of emitters.

This chapter has summarised the theoretical foundations for an understanding of the articles constituting this thesis. We found that localised plasmons can occur on small nanoparticles of various shapes. The plasmons' properties depend on the particle material, the particle shape and the environment. Plasmons can strongly enhance electric fields, a feature that is utilised in this thesis by the coupling of plasmons to excitons on J-aggregates in a core–shell geometry. These aggregates were introduced and their main properties were discussed. For precise simulations, we derived expressions for the permittivity of gold and excitonic emitters with which spectra of core–shell particles can be modelled. At the end of the chapter we took a closer look at plasmon–exciton coupling. We discussed that the coupling causes new resonances to arise and a hybridisation of the subsystems.

The next chapter introduces the methods that were applied for the articles. It will document the route to the sample fabrication and subsequently describe the different experimental set-ups.

4 | Methods

In order to understand the physics that is discussed in the articles, the necessary theoretical background was introduced in the last chapter. The following chapter shall present the methods used for the articles. This includes on one side sample fabrication and characterisation and on the other side the measurement techniques.

The development of sample fabrication techniques was an important task during my time working on this thesis. This development enabled the reproducible fabrication of samples with strongly coupled core–shell nanoparticles on substrates covered with polyelectrolyte layers of various thickness. Due to the simplicity in production and low experimental effort (the particles can be investigated at ambient conditions), this system is a useful example system for fundamental strong coupling research.

The first section of this chapter presents the route from independent components to finished samples that were used in different variations for Articles I – IV. I describe this route in detail to empower succeeding students to fabricate the same or similar samples in the future. The section starts with a characterisation of the bare gold nanoparticles and the J-aggregate forming dye TDBC. Subsequently, the coating process is presented and characterised after which a splitting in the optical response indicates the coupling between the excitonic shell and the plasmonic core. A short interlude presents the coating of gold nanorods with another J-aggregate forming dye with the resonance in the infrared. An important method for both particle deposition on substrates and covering of the particles with polyelectrolytes is the layer-by-layer deposition. A general introduction into this technique is followed by a discussion how particles can be immobilised on a substrate. The successful covering of particles with polyelectrolytes, indicated by a red-shift of the optical resonances, is presented close to the end of the section, followed by a short discussion about the systematic photobleaching of the dye to recover uncoupled plasmon resonances.

Several measurement techniques were utilised for this thesis. These are the topic in this chapter's second section. Linear optical spectroscopy was the main tool used for Articles I – III. Here, one needs to differentiate between extinction, absorption and scattering spectroscopy since the scattering cross section of core–shell nanoparticles can strongly deviate from the absorption cross section as discussed in Article I. Pump–probe spectroscopy is the tool of choice to investigate temporal changes in the spectrum after optical excitation. This was done for Article IV and is the topic subsequent to the linear techniques. A powerful method to measure the temperature of crystals is X-ray diffraction. It was applied to measure the temperature of gold nanotriangles in Article VI. Combining this technique with pump–probe methods enables a direct investigation of the cooling of nanoparticles on a picosecond timescale as was done for Article V. Article VI uses surface enhanced Raman spectroscopy (SERS) to investigate photochemical reactions on the particle surface and relates the spectra to the particle temperature and melting behaviour. This chapter will therefore end with an introduction to SERS.

4.1 Samples

Articles I – IV discuss the features and signatures of plasmon–exciton coupling. As seen in Section 3.5, the coupling strength between a plasmonic cavity and an excitonic emitter is determined by the electric vacuum field E_{vac} of the plasmon and the emitter's transition dipole moment μ. Owing to the small mode volume, strong field enhancements can be obtained in plasmonic cavitites and various geometries supporting strong plasmon–exciton coupling have been presented in the recent years. Examples include dye-covered metal thin films [125], grids [126] or particle arrays [127, 128], as well as semiconductor quantum dots on silver nanoshells [129], nanoparticles on transition metal dichalcogenides [130, 131], organic dyes [119, 132] or quantum dots [54, 116] in hot spots between metallic nanostructures and many more.

This work focusses on the coupling between plasmons in gold nanoparticles and excitons in a J-aggregate forming dye in a core–shell geometry. Such core–shell systems have proven to support high coupling strengths with various core shapes and materials. Amongst others, silver nanorods [61], silver nanotriangles [117], aluminum discs [133], gold nanoflowers [50] have been presented. In each of the mentioned examples, J-aggregate forming dyes were used as shell material. As discussed in the previous chapter, these dyes feature high transition dipole moments and very sharp resonances, two helpful features on the way to achieve strong coupling. Core–shell systems are appealing due to their structural simplicity and high symmetery. The metal that is easiest to handle is gold. In contrast to silver or aluminum, oxidation hardly occurs making gold very stable to the environment. Also the control of the shape seems to be explored better for gold, large-scale and high-quality production for example is still a problem for silver nanorods. Therefore, gold is often the material of choice and coupling to J-aggregates has been shown for gold nanospheres [134] and gold nanorods [118], too.

This section discusses the characteristics and fabrication of the samples used for this works articles. Article I examines both dye-coated gold nanospheres and nanorods deposited on substrates and covered with polyelectrolytes. Article II focusses on dye-coated rods on substrates only. For Articles III and IV, coated gold nanorods were directly investigated in solution. Articles V and VI do not discuss plasmon–exciton coupling, but the reaction of gold nanotriangles to optical excitation. For these two articles, the sample fabrication was developed and conducted by my colleagues Radwan Sarhan and Ferenc Liebig and will therefore not be discussed here.

The first part of this section introduces the components used for the core–shell geometries, that is the cyanine dye *TDBC* and the gold particles that were used. In a next step, the coating process is presented and the influence of various parameters like dye concentration or adsorption time is investigated. Eventually, a procedure to coat gold nanorods with a J-aggregate forming dye whose resonance lies in the infrared is presented.

The section's second part introduces the technique of layer-by-layer deposition of polyelectrolytes. With this process, substrates can be functionalised, so that nanoparticles can be immobilised. The technique additionally enables the covering of the nanoparticles with thin polymer layers. The cover thickness can be tuned with nm-precision providing precise control over the particles' environment. As discussed in the previous chapter, the plasmon resonance is very sensitive to the environment's permittivity and consequently layer-by-layer deposition permits an accurate modulation of the detuning between plasmon

and exciton resonance.

The last part of this section discusses the deposition of the nanoparticles on glass substrates. Subsequently, the influence of polyelectrolyte covers on the plasmon resonance is examined with consequences for coupled and uncoupled systems. To retrieve the original plasmon resonance position of coupled core–shell particles, the dye was photobleached. Different bleaching processes are discussed at the section's end.

4.1.1 Coating Nanoparticles with TDBC

The following section introduces the procedure of coating different gold nanoparticles with the cyanine dye TDBC. First, the pure components will be presented, then the coating process together with the influence of dye concentration, adsorption time and centrifugation speed. The end of the section shortly discusses the coating of gold nanorods with a different cyanine dye with exciton resonance in the infrared.

Pure components: The particles used for the articles were gold nanoparticles of various sizes and shapes. For the coupling investigations, the cyanine dye TDBC was used. Its correct chemical name is *5, 5', 6, 6'-tetrachloro-1-1'-diethyl-3, 3'-di (4-sulfobutyl)-benzimidazolocarbocyanine* and it was purchased from *FEW-Chemicals*. The molecules possess a broad resonance in absorption around 515 nm. At sufficiently high concentrations, the dye forms J-aggregates indicated by the occurrence of a sharp red-shifted resonance. This is exemplified in Figure 4.1. It shows the extinction (left) and fluorescence (right) spectra of TDBC in water at room temperature. At a concentration of $c = 3 \times 10^{-5}$ M, only monomers can be identified in the extinction spectrum, their fluorescence is only very weak around 530 nm. At a concentration of $c = 10^{-4}$ M a new peak emerges in both extinction and fluorescence around 590 nm. It becomes dominant at a concentration of $c = 3 \times 10^{-4}$ M. Note, that the aggregate formation is strongly temperature dependent. Lower temperatures would support the aggregation already at lower concentrations.

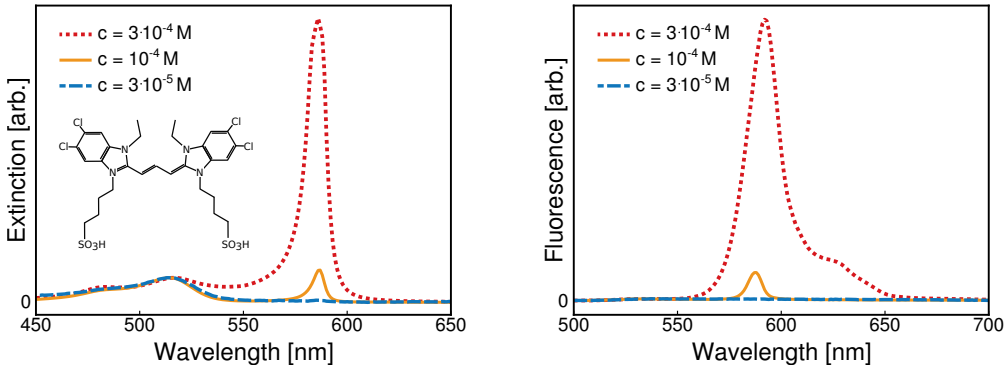

Figure 4.1: Extinction (left) and fluorescence (right) spectrum of TDBC for different concentrations in water at room temperature. For increasing concentrations, J-aggregates emerge with an extinction and emission peak around 590 nm. The inset in the left panel shows the chemical structure of TDBC. The fluorescence spectra were recorded with the spectrometer *Fluorolog* from *Horiba*.

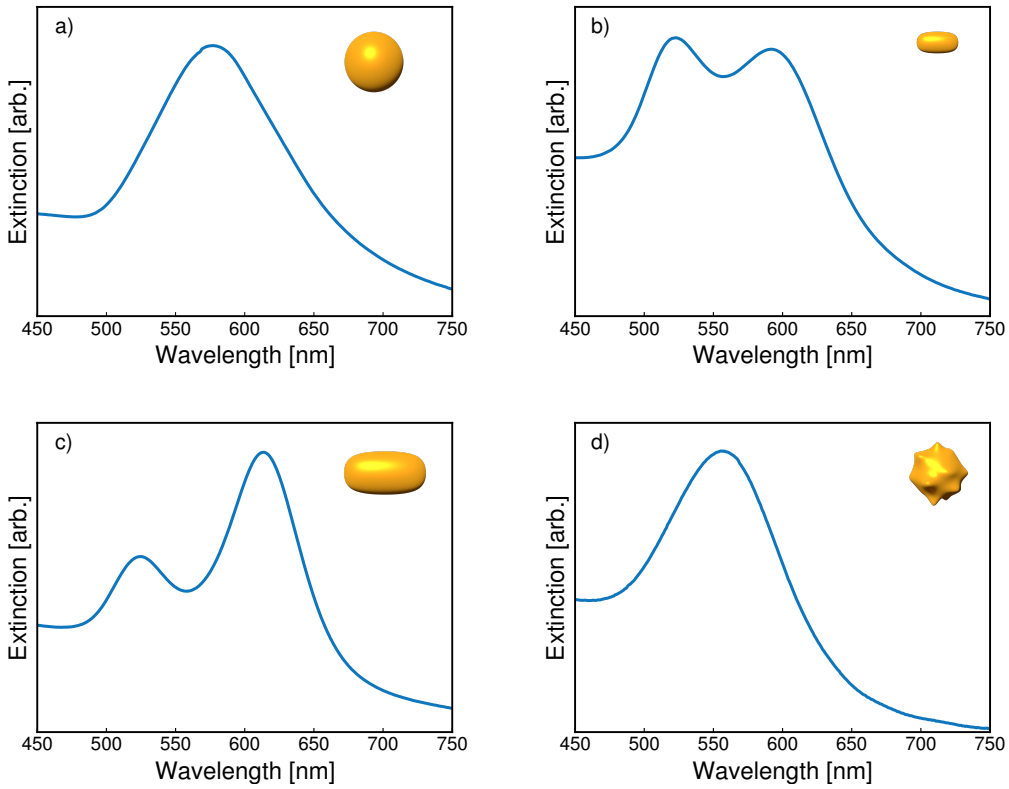

Figure 4.2: Extinction spectra of different gold nanoparticles in water. a) nanospheres with a diameter of 100 nm b) nanorods with a short axis diameter of 10 nm, c) nanorods with a short axis diameter of 40 nm, both types of rods possess an aspect ratio of approximately 2:1, d) nanoflowers with a diameter of around 70 nm.

To investigate the interaction between the excitons in excited aggregates and the plasmons of gold nanoparticles, particles with a resonance close to the dye resonance were chosen. The plasmon resonance of small gold nanospheres is actually around 520 nm. Larger particles, however, show retardation effects, scattering losses and higher dipole moments as discussed previously. Therefore, the resonance of spheres with a diameter of 100 nm was suitable for coupling experiments. Their extinction spectrum in water is presented in Figure 4.2a. The extinction maximum is located around 580 nm. The linewidth is much broader than that theoretically predicted in the previous chapter. Besides the scattering losses, that were already discussed, the broadening is caused by size dispersion, i.e. variations of the particle size within one sample. Since the resonance position for particles beyond the dipole approximation is size dependent, this polydispersity translates to various slightly shifted spectra. Their sum is, what is actually recorded in the measurement and consequently seems wider than single particle spectra. This effect is called *inhomogeneous broadening*. It can be avoided in single particle measurements but not in ensemble measurements. The particles eventually used for the articles were purchased from *Sigma-Aldrich*.

The spectral match between excitons and plasmons in gold spheres was induced by the large size of 100 nm. Smaller spheres have a blue-shifted resonance in comparison to TDBC. To also investigate the coupling with smaller nanoparticles, gold nanorods were utilised. As discussed in the previous

chapter, nanorods possess two resonances. One for electric fields that are polarised along the short particle axis (transverse resonance) and one for electric fields that are polarised along the long particles axis (longitudinal resonance). The longitudinal resonance strongly depends on the aspect ratio, that is the relation between long and short axis. Its position can therefore be easily tuned, also for small particles. For the coupling to TDBC, particles with a longitudinal resonance around 600 nm were used. Particles with various sizes were purchased from *Nanopartz* with an aspect ratio of approximately 2:1. As example, the spectra of nanorods in water with short axis diameters of 10 nm and 40 nm are presented in Figure 4.2b and c, respectively. The two resonances can nicely be distinguished with a transverse peak position around 525 nm and the longitudinal resonance around 590 nm (10 nm-rods) and 610 nm (40 nm-rods), respectively. Here, the linewidth is even more dominated by inhomogeneous broadening since here not only size differences cause different resonance positions but also changes in shape resulting in a variation of the aspect ratio. In comparison to theoretical predictions, the peak of the transverse resonance is, especially for the smaller rods, quite high. The additional peak height can be attributed to residual spheres which are present within the sample.

Another nanoparticle shape that was used to fabricate core–shell particles was that of gold nanostars. When small enough, their plasmon resonance is dominated by the dipole mode. The extinction in water is presented in Figure 4.2c with one resonance around 555 nm. The nanoflowers were produced by my colleagues Radwan Sarhan and Qianling Cui [135] after a method developed by Xie et al. [136]. The particle size was around 70 nm. The linewidth is determined by inhomogeneities not only in size but also in the distribution of the spikes.

Coating gold nanoparticles with TDBC: The electric field enhancement in metal nanoparticles is strongest directly at the surface. To investigate the coupling between plasmons and excitations on an emitter, it is therefore reasonable to bring the emitters as close to the surface as possible. This is achieved by homogenously coating the particles with the dye to a core–shell geomtery. A simple method for coating gold nanopartilces with a layer of TDBC was introduced by Lekeufack et al. [137]. This procedure was taken as basis for the particle coating presented in this work. The starting point of the technique were gold particles coated with a stabilisation layer of citrate ions. These were simply mixed with an aqueous solution of TDBC and the dye would gradually replace the citrate ions.

The TDBC solution was prepared by suspending the TDBC powder in water with a small amount of NaOH as buffer. The latter, with a concentration of 10^{-5} M, was added to keep the pH above 7. The TDBC concentration was varied and will be discussed later. The solution was stirred for 5–10 minutes and afterwards placed in an ultrasonic bath for 15 minutes. This procedure ensured the separation of clusters with molecule orientations that did not support the exciton delocalisation that might exist in powder. After preparation, the solution needed to be kept cold and in the dark to prevent bleaching.

The concentration of particles in colloidal solution was chosen to cause an optical density of OD=1. The particles were mixed with the TDBC solution in a ratio of 1:1. After mixing, the solution was placed in an ultrasonic bath for 15 minutes and subsequently left undisturbed in the dark to give the TDBC time to homogeneously adsorb onto the gold surface. The adsorption time could vary as discussed below without a big effect on the result. After adsorption the core–shell particles were separated from the solution with residual TDBC by centrifugation.

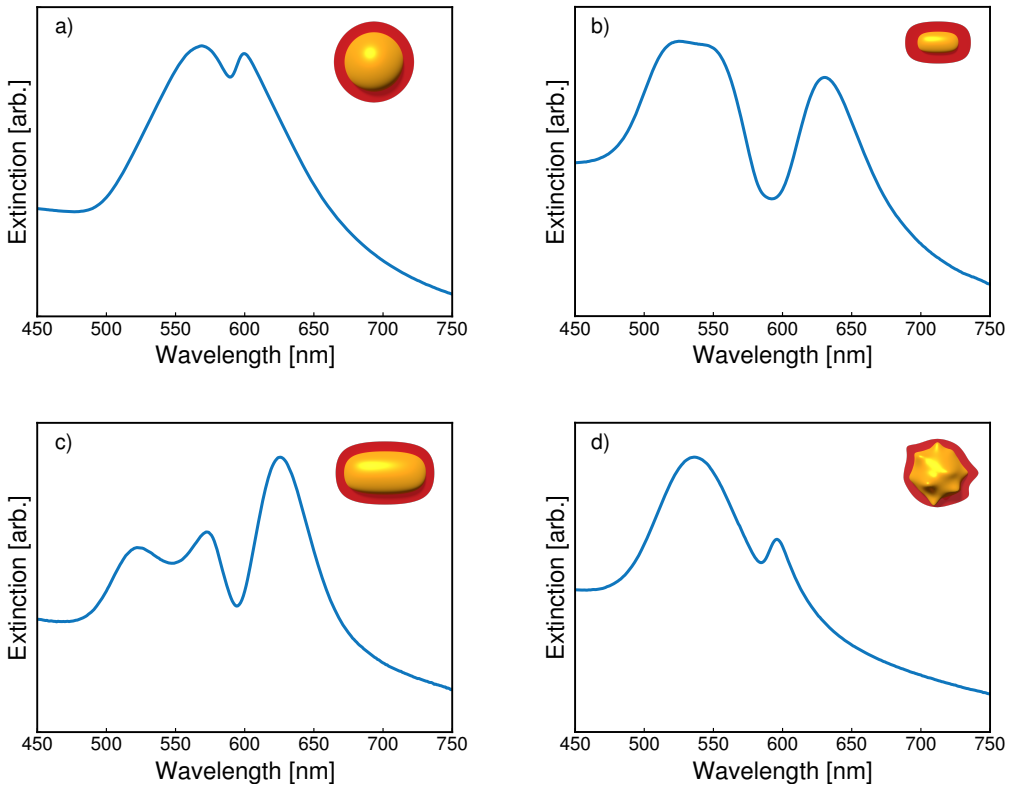

Figure 4.3: Extinction spectra of the same gold nanoparticles as in Figure 4.2, now with a coating of TDBC. The plasmon resonances now show a splitting with a dip at the original exciton position.

A successful coating was confirmed by the extinction spectrum after the process. In Figure 4.3, the spectra in water are presented for the particle types presented in Figure 4.2. In all cases, a dip can now be seen in the broad plasmon peak indicating a plasmon–exciton coupling. In case of high coupling strengths, this dip can rather be identified as two new peaks emerging from the coupling similar to the example spectra given in Figure 3.27. The real nature of the spectrum modifications can only be identified by further experiments like anticrossing measurements. This was done for Article I where the spectra of core–shell nanospheres were compared to those of smaller core–shell nanorods.

The width of the dip is strongly connected to the particle size since the field enhancement increases with decreasing particle volumes. This is the main reason for the different widths of the dips / peak splittings. A closer look at the connection between particle size and coupling strength was taken for Article II for core–shell nanorods of different sizes.

The nanoflowers were eventually not used for the articles. The main reason was, that they represent a more complicated system that can no more be described by Mie theory. Articles III and IV are based on Mie descriptions of the particles making a use of nanoflowers impractical. Another reason was that the particles could not so easily be deposited on substrates. This hindered deeper investigations like anticrossing tests that were conducted for Articles I and II. Their spectra are shown here to give another example of particles exhibiting plasmon–exciton coupling besides the spheres and rods that were used for the articles.

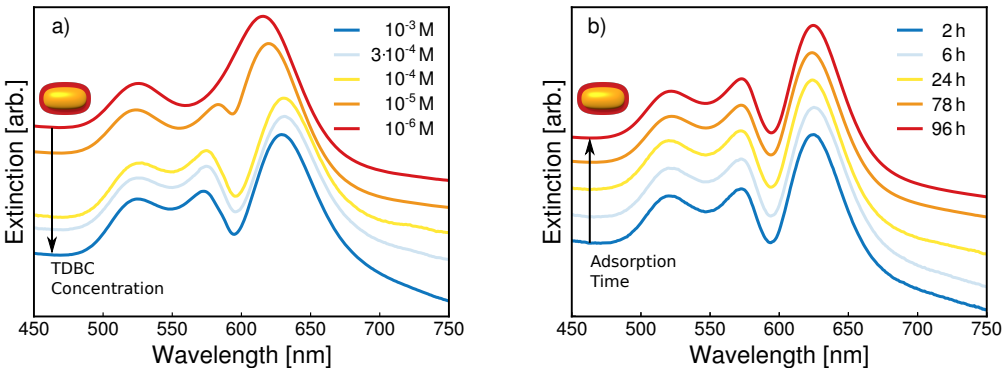

Figure 4.4: a) Dependence of the peak splitting on the dye concentration during the coating process. For low concentrations, no splitting is visible, above a concentration of $c = 10^{-4}$ M, the splitting saturates and does not widen further for higher concentrations. This indicates a complete coating for concentrations above $c = 10^{-4}$ M. b) Dependence of the peak splitting on the adsorption time of the coating process. In all cases, the splitting is identical indicating a complete coating already after 2 h. In both panels, the spectra are shifted by different offsets for clarity.

TDBC concentration dependence: The TDBC concentration in the dye solution has an impact on the coating quality. To optimise the process, different concentrations were tested. The result is presented in Figure 4.4a which depicts the extinction spectra of TDBC-coated gold nanorods with a nominal short axis diameter of 40 nm in water. Low concentrations do not exhibit an effect at all. For a concentration of $c = 10^{-5}$ M, a peak modification is visible, but the splitting is not at its maximum point. For concentrations above $c = 10^{-4}$ M the peak splitting saturates and does not widen any longer. For the articles, the eventual concentration was chosen to be around $c = 10^{-3}$ M or slightly below to ensure a sufficient dye concentration.

Adsorption time dependence: The adsorption time in the original procedure presented by Lekeufack et al. suggested an adsorption time of 24 hours. Figure 4.4b presents the spectra for different times between mixing of the TDBC solution with the gold particles and the centrifugation. Apparently, the adsorption is completed already after much shorter times and already after two hours, the splitting reaches its maximum value. On the other hand, the splitting does not degrade with longer adsorption times. Thus, to be sure, the coating is completed and for organisation reasons, the adsorption times used for the articles varied between 2 and 5 days.

Influence of centrifugation speed: To separate the particles from residual TDBC after coating, the solution was centrifuged after the dye adsorption. The centrifugation speed needed to be chosen with care. For too slow rotaion speeds, not all particles would sediment at the bottom whereas too high centrifugation speeds can cause clustering of the particles [138]. For each particle size, the slowest possible speed was chosen at which all particles would separate from the solution. The centrifugation time was chosen to be 30 minutes, enabling slower speeds than shorter times. The centrifuge in use was an *Eppendorf Mini spin* with a centrifugation radius of 6 cm. For larger particles like nanorods with a short axis diameter of 40 nm a centrifugation speed of 2500 rpm was sufficient, for those with 10 nm short axis diameter 8000 rpm were necessary.

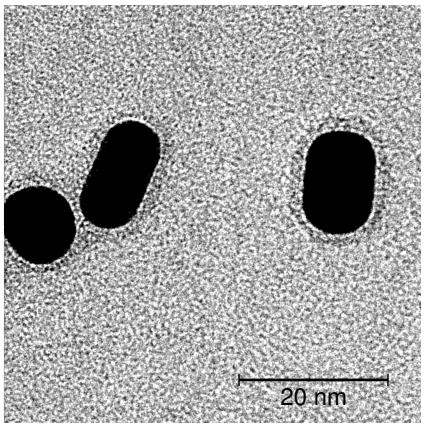

Figure 4.5: TEM images of TDBC coated gold nanorods with a nominal transverse diameter of 10 nm. A homogeneous coating is clearly visible with a thickness of approximately 3 nm. The image was recorded by Zdravko Kochovski at Humboldt University of Berlin.

The particles were centrifuged twice while being redispersed in water between the two centrifugation steps. After the second centrifugation, the sample was again filled up with water. The amount of water was chosen depending on the desired particle concentration. This amount varied between 20 % and 100 % of the original amount of solution.

A TEM image of a few core–shell nanorods with a nominal transverse diameter of 10 nm is shown in Figure 4.5. The homogeneous TDBC coating can nicely be seen around the particles with a thickness of approximately 3 nm. The image also illustrates the polydispersity in the sample causing the inhomogeneous broadening of the spectrum. It is typical that also a sphere can be seen which explains the comparably high peak in the region around 520 nm, which is not only caused by transverse resonances of the rods but also by nanospheres already present in the solution as bought from the manufacturer.

In comparison to many other J-aggregate forming dyes, TDBC is rather easy to handle when it comes to coating of gold nanoparticles. The process is quite simple, robust and reproducible. It is therefore often used in the research of plasmon–exciton coupling [62, 103]. For other dyes, the coating process can be much more difficult. As an example, the following part presents the more complex procedure of coating another J-aggregate forming dye onto gold nanorods.

Coating gold nanorods with S 2284: TDBC J-aggregates are resonant around 600 nm. In the visible, however, interband transitions cause huge losses in plasmonic excitations on gold nanoparticles. With wavelengths around 800 nm, these interband transitions are no longer excited. This increases the lifetime and reduces the losses of plasmons in this spectral range. Additionally, the majority of commercial fs-lasers works in spectral regions around 800 nm. Both these facts raise interest in the plasmon–exciton coupling in the infrared range.

Together with the undergraduate student Steffen Mittmann, I therefore tried to develop a method to fabricate core–shell particles with gold nanorods as core material and a dye that forms J-aggregates in the infrared. A coupled core–shell system with resonances around 800 nm had been presented in literature [139]. In this case, an emitter with several exciton resonances was used that all coupled to the

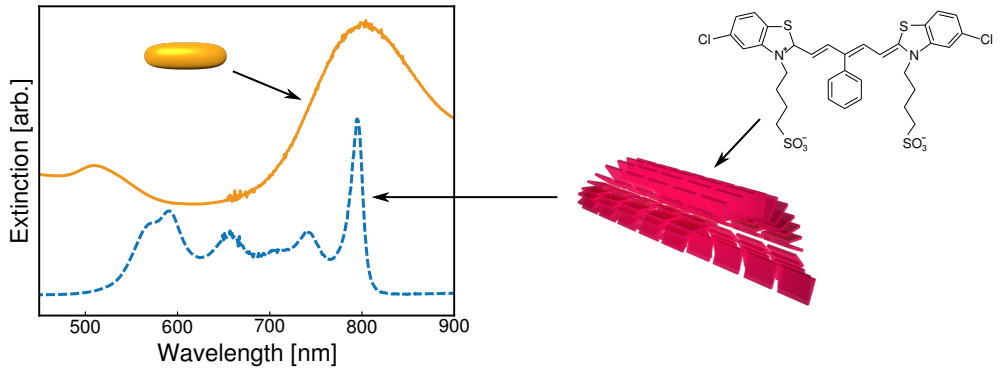

Figure 4.6: Gold nanorods and J-aggregates with resonances in the infrared. The right side depicts the chemical structure of S 2284 and the tubular structure of its J-aggregate. The respective extinction spectrum is presented in the left panel by the dashed blue line exhibiting a sharp J-aggregate peak around 800 nm. The panel also shows the extinction of gold nanorods with a nominal transverse resonance at 800 nm as orange line. The spectra are shifted by an offset for clarity.

plasmon but none of them very strongly. After our experiments, another architecture with an infrared dye dissolved in a solution around nandiscs was introduced [140].

We tried to fabricate a core–shell system with a structure already established for TDBC as shell material. The phenol-substituted thiacarbocyanine Cy5 dye (*5-chloro-2-[5-[5-chloro-3-(4-sulfobutyl)-3H-benzothiazol-2-ylidene]-3-phenyl-penta-1,3-dienyl]-3-(4-sulfobutyl)-benzothiazol-3-ium hydroxide, inner salt, triethylammonium salt*) was purchased from *FEW chmicals*. Here, the dye shall be referred to as *S 2284*. Under addition of NaCl, the dye forms tubular J-aggregates with a resonance around 796 nm [141]. The spectrum in aqueous solution with a NaCl concentration of 0.5 M is shown in Figure 4.6. The rods were chosen to 10 nm wide and to possess a longitudinal resonance around 800 nm. Figure 4.6 also presents the rods' extinction in solution.

The simple mixing of dye and rods did however not result in a successful coating. To account for the negative charge of the dye, gold nanorods that were coated with the positively charged ligand PAH (which will be introduced later) were purchased from *Nanopartz*. This way, the dye should be attracted to the gold by Coulomb forces. Yet, simply mixing the solutions did still not show different features in the spectrum than the simple sum of the two components. The spectrum is shown as dashed orange line in Figure 4.7. There was still an energy barrier that needed to be overcome. This was eventually achieved by heating the mixture to 65 °C for ten minutes. As seen in the blue line in Figure 4.7, there is now a dip in the plasmon resonance at the position of the J-aggregate resonance.

The same feature could be obtained for shorter rods with a resonance position at 780 nm. They, too, were functionalised with PAH and the spectral modification was achieved by heating to 65 °C. In this case, the peak is split in two equally intense parts and the detuning between plasmon and exciton resonance seems to be close to zero.

The results have not beed published, yet, due to complications in confirming that the dip indeed is caused by the same plasmon-exciton interaction as is the case for TDBC–gold particles. This is due to the fact that we have not yet achieved to deposit the particles on substrate without forming clusters.

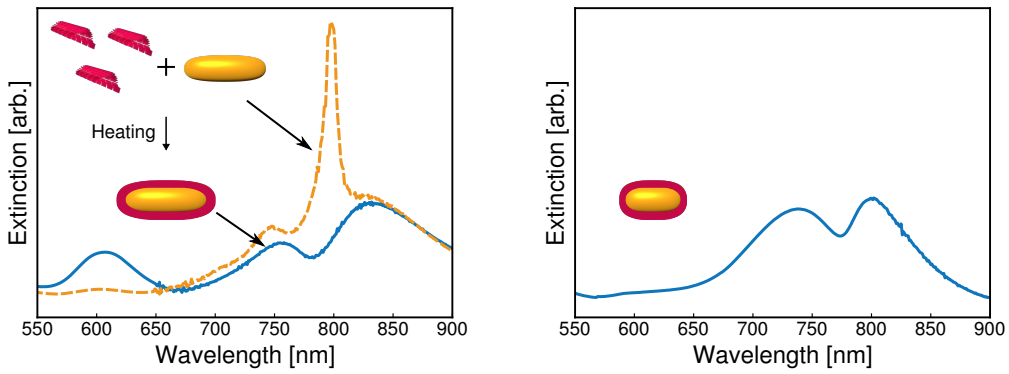

Figure 4.7: Illustration of coupling between gold nanorods and S 2284. Left panel: Coating of nanorods with a transverse resonance of 800 nm. The dashed orange line represents the extinction after mixing of colloidal nanorod solution and dye solution. The uncoupled resonances of both systems are visible. After heating the mixture at 65 °C, the typical spectrum of coupled core–shell particles emerges (blue line). The right panel shows the coupled spectrum between S 2284 and gold nanorods with a transverse resonance of 780 nm.

Besides representing a part of my unpublished work, the results are shown here here to first demonstrate an alternative to TDBC as emitter material and second, to underline that indeed, the process of coating TDBC around gold nanoparticles is comparably simple. The main reason for this simplicity is probably the structure of J-aggregtes of TDBC. While for example S 2284 forms tubular aggegates [141] as indicated in Figure 4.6, TDBC J-aggregates are found in the brick structure [74] presented in Figure 3.12.

The previous part established the process of coating gold nanoparticles with the cyanine dye TDBC. Such core–shell systems were utilised in Articles I – IV. For Articles III and IV, TDBC coated gold nanorods were directly used in solution, for Articles I and II, the particles were deposited on substrates and subsequently covered with polyelectrolytes. Both processes shall be discussed in the next sections.

4.1.2 Layer-by-Layer Deposition of Polyelectrolytes

A powerful method to produce charged substrates and to create layers of polymers with nm-thickness is the layer-by-layer deposition of polyelectrolytes. Polyelectrolytes are polymers constituted by monomers that possess an electrolyte group which dissolves in contact with water. In cationic polyelectrolytes, the positively charged part is bound to the monomers, whereas the anion can dissolve. In anionic polyelectrolytes, the cationic part can move freely while the negatively charged part is bound to the molecules.

A monolayer can be formed when a polyelectrolyte is brought in contact with a surface of opposite charge. The mechanism behind this effect is the maximisation of entropy [142]. Initially, all polyelectrolytes are dissolved in NaCl solution. The NaCl ions serve as counterions located in the vicinity of the polymers. Let now a cationic polyelectrolyte, surrounded by Cl^- ions, get close to an anionic polyelectrolyte, surrounded by Na^+ ions: the entropy is maximised if the numerous Na and Cl ions dissolve in water

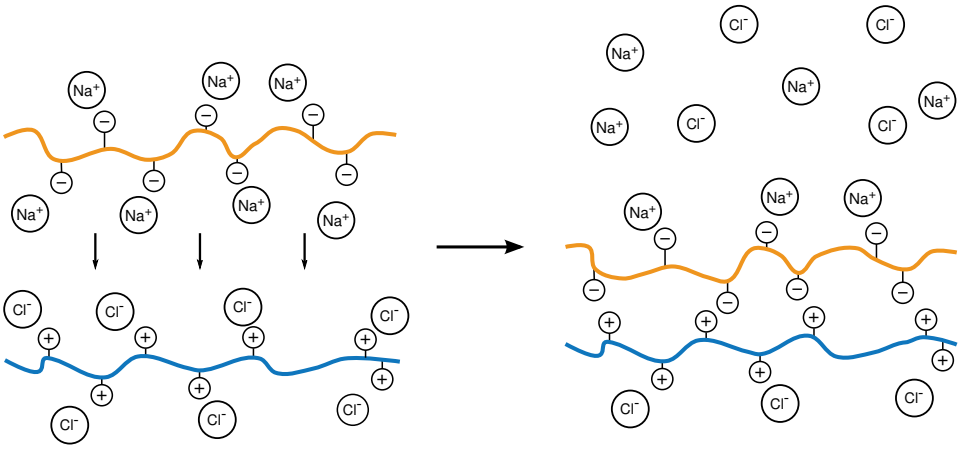

Figure 4.8: Mechanism of layer formation of polyelectrolytes. When two oppositely charged polyelectrolytes approach each other, entropy strongly increases when the counter ions dissolve in water. The polymers are then directly attracted by Coulomb forces and form a double layer.

becoming able to move freely while the two polyelectrolytes directly stick together. The process is schematically shown in Figure 4.8. After washing away the liberated counterions, a firmly connected double layer remains. For the polyelectrolytes used for this work, such a double layer is around 2.5 nm thick [47].

This process was utilised to create stable multilayer polymer films with defined charge and thickness in the nanometer range. The layer formation can be obtained by immersing a substrate into a solution of the respective polyelectrolyte and subsequently immersing the substrate in water. As a next step a polyelectrolyte layer with an alternating charge can be formed on top by repeating the two previous steps [142]. For this work however, the faster and less material consuming method of spin-coating assisted layer-by-layer deposition was applied. The process is schematically illustrated by Figure 4.9: The substrate is fixated on a rotatable table that rotates with a speed of 3000 rpm. A few drops of polyelectrolyte solution (5 – 10 drops) are deposited onto the substrate under rotation. The centrifugal force evenly spreads the solution on the whole substrate. After 5 – 10 seconds, the residual solution is

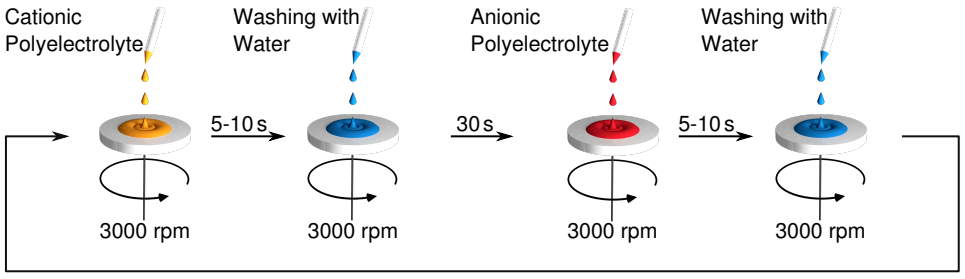

Figure 4.9: Scheme of layer-by-layer deposition. A few drops of a polyelectrolyte are deposited onto the fast rotating sample. The residuals are washed away with water after a few seconds. After approximately 30 s, the process can be repeated with a polyelectrolyte of opposite charge. For the polyelectrolytes used for this work, one cycle lead to the formation of a double layer with thickness of 2.5 nm.

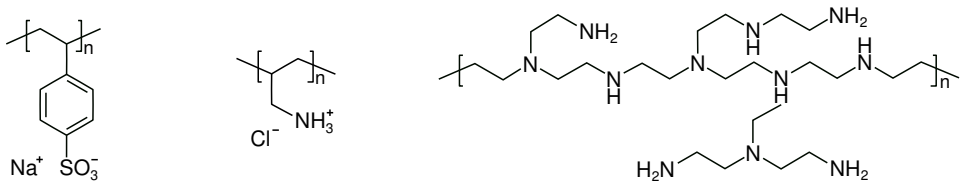

Figure 4.10: Chemical structures of the polyelectrolytes in use. The structures of PSS, PAH and PEI are depicted from left to right.

washed away with water (again 5 – 10 drops). After a short waiting time of around 30 seconds, the water has vanished and as result, a monolayer of the applied polyelectrolyte has formed. This process can be repeated as often as desired with alternatingly charged polyelectrolytes.

Three different types of polyelectrolytes were employed: The cationic *poly-allylamine hydrochloride* (PAH) and *poly-ethyleneimine* (PEI) together with the anionic *poly-sodium 4-styrenesulfonate* (PSS). The chemical structures are given in Figure 4.10. All three polymers were purchased from *Sigma-Aldrich*. PSS is a linear anionic polymer with a molecular weight of 206 g/mol. Before use, the powder as purchased from the manufacturer needed to be dialysed in order to remove chains consisting of only a few monomers. PAH is a linear cationic polymer. It was also purchased as powder with a molecular weight of 94 g/mol. PEI is a branched cationic polyelectrolyte. It was delivered as 50 wt% solution with a molecular weight of 163 g/mol. All three polymers were dissolved NaCl solution with a polymer concentration to 1 wt%. The NaCl concentration was $c = 0.7\,\mathrm{M}$ for PAH and PSS and $c = 1\,\mathrm{M}$ in case of PEI.

Layer-by-layer deposition was used for Articles I and II to functionalise the substrates before the deposition of nanoparticles. Uncoated gold particles possess a negative surface charge and they could be well deposited on substrates with a cationic polyelectrolyte as topmost layer, while TDBC coated particles could be immobilised on negatively charged surfaces. Subsequently, the technique was used to cover the particles with films of defined thickness to gradually change their dielectric environment. Like this, the plasmon resonance could be tuned and the anticrossing discussed in the previous chapter could be revealed. The details of this sample fabrication are discussed in the next section.

4.1.3 Deposition of Nanoparticles on a Substrate

The following part discusses the preparation of samples that were used for Articles I and II. Core–shell particles were deposited on glass substrates and subsequently covered with polyelectrolytes utilising layer-by-layer deposition. After the recording of spectra, the dye was photobleached in order to determine the original plasmon resonance position, i.e. the resonance position of the particles without TDBC shell under the polyelectrolyte cover.

Deposition of uncoated nanoparticles on a substrate: Gold nanospheres with a citrate layer as stabiliser possess a slightly negative surface charge. This can be used to imobilise the particles on a

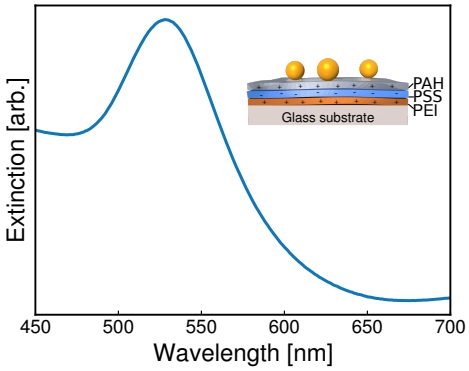

Figure 4.11: Extinction spectrum of bare gold nanospheres on a substrate. The particles with a diameter of 100 nm were deposited on a functionalised substrate with PAH as topmost layer.

substrate by funcionalising the substrate with layer-by-layer deposition. As a starting layer, a layer of PEI is coated on a glass slide that was cleaned with ethanol and water before use. A double layer of PSS/PAH is deposited on top of the PEI with PAH as topmost layer. This way, the substrate has a positive surface charge on top and particles with negative surface charge can stick to it. Around 300 µl of the particle solution is then deposited on the subtrate. After roughly 90 minutes adsorption time, the solution is washed away with water. Simply letting the solution dry in is not possible because in this case, the particle form clusters and only few stay isolated. But particles that lie too close to each other can interact. This interaction can cause a shift in resonance, similar to the effect discussed for J-aggregates in the previous chapter. Therefore, cluster formation should be avoided and the distance between neighbouring particles should be larger than the particle size since this is the interaction range of the plasmons [47]. The adsorption time was chosen to achieve maximum particle density on the substrate without the formation of clusters. A spectrum of gold nanospheres with a diameter of 100 nm is presented in Figure 4.11. The plasmon resonance can nicely be seen. The deviation of the resonance position compared to the extinction in water presented above can be attributed to the change in the environment and its permittivity.

Deposition of core–shell nanoparticles on a substrate: One might expect that the deposition of core–shell particles would work the same way as the deposition of bare gold particles. In first attempts however, the extinction spectra did not resemble the spectra in solution. Often, hardly any features were obeserved in the visible range. Sometimes, the samples exhibited spectra like that presented in Figure 4.12. Besides the very weak feature that can be assigned to core–shell spheres, an equally strong peak that could be assigned to uncoupled TDBC J-aggregates is visible. Additionally a wide peak in the infrared is visible. One explanation was that the particles clustered, leading to new plasmon resonances without overlap with the exciton peak. An SEM image of the sample on the right side of Figure 4.12 supports this idea. Only very few particles are lying on their own while most of the others are sticking together as clusters. Also, Lekeufack et al. who introduced the method of TDBC coating of nanoparticles report formation of clusters in their systems [137].

By measuring the particles' zeta potential via their electrophoretic mobility – this is in principle particle mobility in solution under a constant applied electric fields –, the surface charge of the particles can

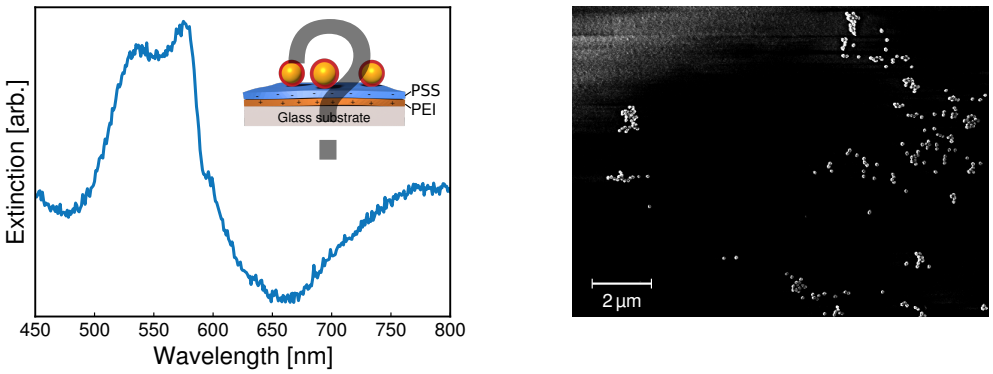

Figure 4.12: Extinction spectrum (left) and SEM image (right) of a functionalised glass substrate on which TDBC coated gold nanospheres were deposited. The spectrum contains a peak at the resonance of uncoupled J-aggregates as well as a peak in the infrared indicating the formation of clusters. The SEM image confirms this hypothesis showing a very uneven and clustered distribution of particles on the substrate.

be determined. As previously mentioned, citrate capped gold nanoparticles possess a negative surface charge as confirmed by the mobility measurements. On the other hand, the measurements indicated that TDBC coated nanoparticles possess a positive surface charge. This difference suggests that cluster formation might have occurred already during the TDBC coating process between not yet completely coated particles.

A possible way to avoid the formation of clusters during the coating process, has been presented by Aslan and Pérez-Luna [143]. They suggest to introduce the non-ionic surfactant *Tween-20* in an intermediate step. This surfactant encloses the particles and lowers their surface charge. The interaction between Tween-20 and gold is weaker than that of TDBC since Tween-20 is only weakly physisorbed on the gold surface. It can be gradually replaced by TDBC. Regions that are not yet coated with TDBC would still be covered with Tween-20 lowering the attraction between not completely coated particles

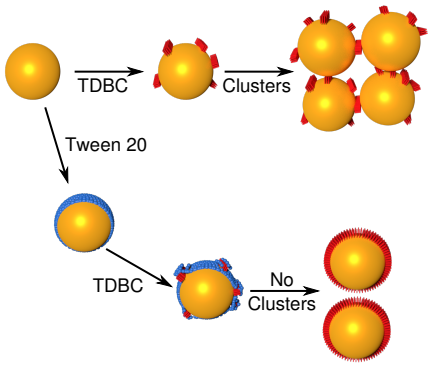

Figure 4.13: Scheme of the functionality of an intermediate Tween-20 coating. If the particles are directly coated with TDBC, the diverging surface charge of partly coated particles causes the formation of clusters. An intermediate coating with Tween-20 screens the charges and therefore hinders cluster formation. Illustration modified from Reference 143.

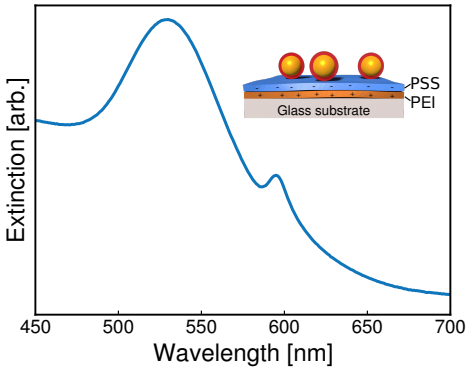

Figure 4.14: Extinction spectrum of TDBC–gold core–shell nanospheres on a glass substrate. The smooth spectrum indicates a successful and homogeneous deposition of particles on the substrate with PSS as topmost layer.

and thus preventing cluster formation. The process is schematically depicted in Figure 4.13.

After using Tween-20 in an intermediate step and leaving the coating process otherwise unchanged as described above, the TDBC coated particles could be immobilised just as the uncoated particles. Only the topmost layer of the functionalised substrate needed to be PSS due to the positive surface charge of the core–shell particles. Also, the particles needed to be given more time to adsorb on the substrate. For spheres, the solution was left on the substrate for 4 hours before being washed away, for rods, the adsorption time was 12 hours.

As an example for a successful deposition of TDBC coated gold nanoparticles, Figure 4.14 presents the extinction spectrum of nanospheres with a diameter of 100 nm on a substrate. The sample shows a nice and well defined extinction and the two peaks can well be seen. Again, the difference to the spectrum in solution shown above is caused by different media and consequently different plasmon resonance positions. Possibly, there was no significant formation of clusters during the coating process. The spectra in solution presented previously and in Articles III and IV do not show any resonances in the infrared, a strong sign for clusters, but seem to mainly represent single particles. But before using Tween-20, no TDBC–gold particles could not be deposited on any substrate, whereas after using Tween-20, this problem did not occur. This is why all core–shell particles that were to be deposited on substrates were pretreated with Tween-20.

Covering particles with polyelectrolytes: To reveal the anticrossing in the coupled systems, the immobilised particles were covered with polyelectrolytes. This way, the environment of the particles was changed and consequently, the plasmon resonance shifted. Each polyelectrolyte layer would replace air in the particles' vicinity and slightly shift the plasmon resonance. As an exemplification, Figure 4.15 depicts the extinction spectra of gold nanospheres with 100 nm diameter under covers with various thicknesses. All spectra stem from the same sample whose extinction was measured in between the chosen covering steps. The red-shift can be recognised well for increasing cover thickness. The situation is very similar to the example of nanoparticles with a silica shell depicted in Figure 3.10. Each additional cover causes a smaller red-shift than the previous ones. In the picture of the oscillating electron cloud, this fact can easily be understood phenomenologically: A compensating dipole that is located at larger

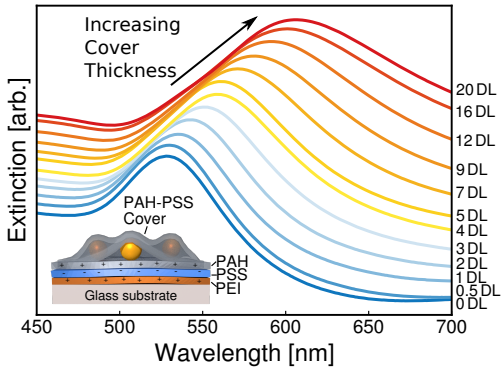

Figure 4.15: Extinction spectra of bare gold nanospheres gradually covered with polyelectrolytes. Spheres with a diameter of 100 nm were deposited onto a glass substrate and gradually covered with polyelectrolytes. In between covering steps, the extinction spectra were recorded. The number of double layers covering the particles at the time of measurement is indicated on the right with the abbreviation DL. The spectra are shifted by an offset for clarity. A clear red-shift of the plasmon resonances is visible for increasing cover thicknesses. This red-shift can be explained by the increasing permittivity of the medium surrounding the particles.

distance from the particle has a lower impact on the restoring force and consequently contributes less to the red-shift. With this technique, the plasmon resonance position can nicely be tuned and controlled.

For TDBC–gold core–shell particles, the process was expected to work as well. This is in principle true, however, the dye showed signs of bleaching during the coating process. This is exemplified in Figure 4.16a which depicts the spectra of TDBC coated gold nanorods with a short axis diameter of 25 nm under covers of increasing thickness. Again, the spectra where all taken for one single sample. The resonances show a red-shift that can be explained by a red-shift of the plasmon resonance. The

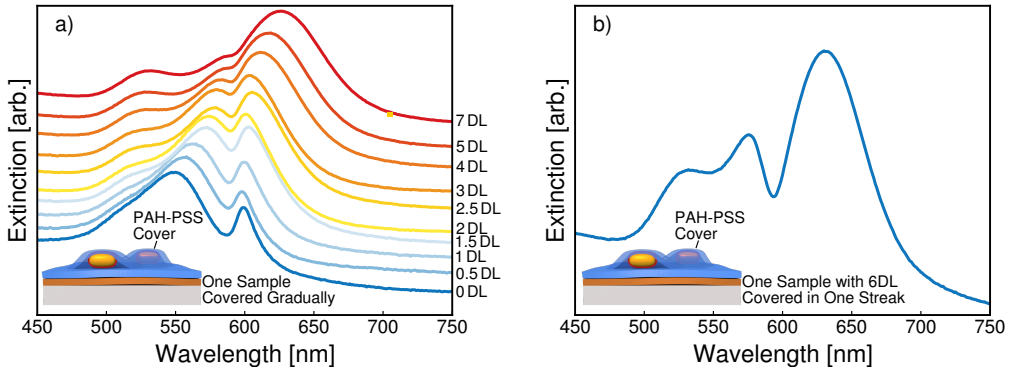

Figure 4.16: a) Extinction spectra of TDBC coated gold nanorods gradually covered with polyelectrolytes. The procedure and presentation is the same as for the bare nanospheres shown in Figure 4.15. For increasing cover thicknesses, the dip becomes smaller indicating a bleaching of the dye. b) Extinction spectrum of TDBC coated gold nanospheres directly coated with 6 double layers of polyelectrolytes without intermediate recording of spectra. In this case, a clear peak splitting is still visible.

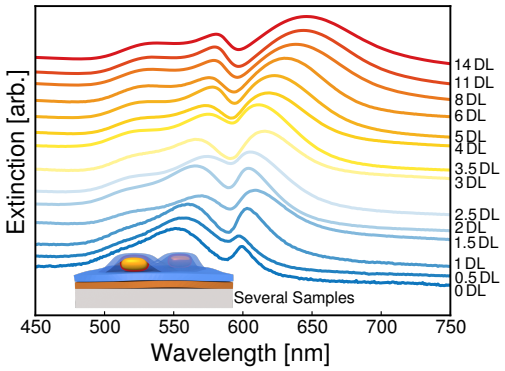

Figure 4.17: Extinction spectra of TDBC coated gold nanorods with polyelectrolyte covers of varying thickness. For each spectrum, a new sample was produced and continuously covered with a cover thickness indicated on the right side (DL again stands for *double layer*). The spectra are shifted by an offset for clarity. A red shift of both coupled peaks is visible while the peaks do not meet. This indicates an anticrossing of the resonances.

transverse peak is only visible as a shoulder for thin covers. It is not as sensitive to the environment as the longitudinal peak, as discussed in the precious chapter. Thus, for increasing cover thicknesses, the longitudinal resonance shifts stronger and the transverse resonance becomes more and more visible.

The dip in the longitudinal resonance stays in the same position as the exciton resonance is not affected by the polyelectrolyte cover. However, it becomes increasingly smaller for increasing cover thicknesses. This might be an intrinsic feature of core-shell particles covered with thicker polyelectrolyte covers. On the other hand, continuously coating 6 double layers without intermediate breaks for extinction measurements resulted in a spectrum with a wide peak splitting. This indicates that the TDBC bleaches during the covering process when spectra are recorded in between the deposition of two layers. Fabricating a sample without recording spectra intermediately, but taking equally long breaks would cause the same bleach, excluding the extinction measurement from possible sources for the bleaching. This was again tested by measuring the extinction several times over a day on the same sample. The spectra did not change. It was potentially the alternating exposure to water and air, that caused the bleaching. As a consequence, a new sample was fabricated for each cover thickness. This way no sample and consequently no spectrum for any cover thickness was affected by dye bleaching. The result is presented in Figure 4.17, again for gold nanorods with a short axis diameter of 25 nm. The spectra look very similar to those in Figure 4.16a, but now the dip does not lose its depth for increasing cover thicknesses. This means that now, there are two coupled resonances that show a red-shift separated by a dip that does not change its position.

Photobleaching TDBC in core–shell particles: From the previous spectra, the resonance positions of the coupled systems can be retrieved. For a complete anticrossing, also the detuning between the resonances of the uncoupled original systems needs to be identified. Pure TDBC did not show any shifts under polyelectrolyte covers. Its resonance can be assumed to be identical for all samples. Thus, the knowledge of the original plasmon resonance would include the knowledge of the detuning, at least up to an offset, since the precise exciton resonance might change on the gold surface. Despite the larger amount of work, the necessity of preparing a new sample for each cover thickness came

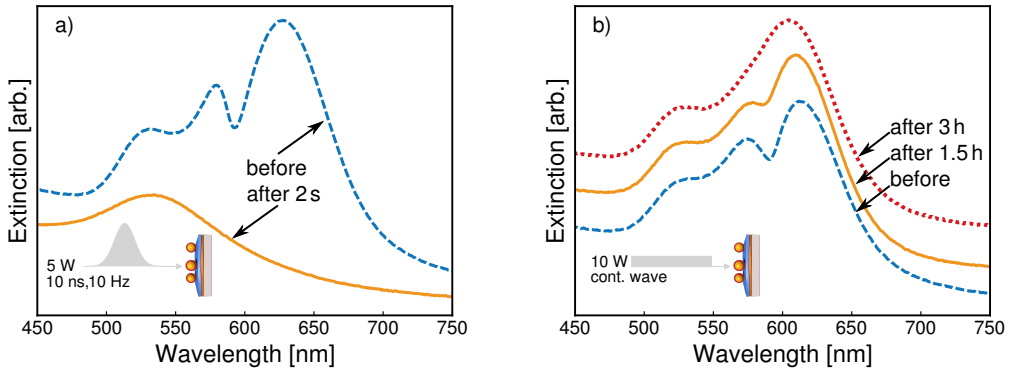

Figure 4.18: Photobleaching of the TDBC in core–shell particles. a) Attempt to bleach the dye with a pulsed laser with a power of 5 W at a repetition rate of 10 Hz with a pulse duration of approximately 10 ns. The gold particles with a former extinction spectrum indicated by the dashed blue line seem to melt already after 2 seconds as shown by the solid orange line. The spectrum looks now like that of gold nanospheres and shows no more signs of transverse rod resonances. b) Photobleaching with a 10 W cw laser. The dashed blue line represents the extinction before illumination. After 1.5 h, the dip is already smaller as seen in the solid orange line. The spectrum after three hours illumination is represented by the dotted red line and shows that the peak splitting has almost completely disappeared indicating a successful photobleaching of the dye. The constance in the transverse plasmon resonance shows that the gold is still unchanged. The spectra are shifted by an offset for clarity.

now as an advantage. In each sample, the TDBC could be photobleached under controlled conditions. Subsequently, for each coupled spectrum, a respective pure plasmon spectrum could be recorded and the spectra could directly be related to each other.

A suitable method to bleach the TDBC was yet to be found. An obvious way would be to expose the samples alternatingly to water and air since this process already proved to bleach the dye. But this only works for thin polyelectrolyte covers. Thicker covers stabilise the core–shell particles chemically. By photobleaching this obstacle could be overcome without changing the medium itself. I tested different methods to photobleach the particles under controlled conditions. Gold nanoparticles tend to melt very easily [144] therefore, a light source was desired with enough intensity to bleach the dye but with low enough intensity to not destroy the particle cores. An example of a light source that both bleached the dye and melted the gold, is a laser that generated ns-laser pulses with a repetition rate of only 10 Hz at a total power of 5 W. Consequently, the energy of 0.5 J per pulse was huge in this case. Directing the beam width a width of approximately 1 cm onto a sample only a few seconds already caused a change in the spectrum of core–shell rods that is presented in Figure 4.18. Apparently, all resonances are reduced to one single resonance that looks like that of gold nanoparticles. The cause of this change is that the rods melted and formed liquid droplets on the substrate that subsequently froze [145, 146]. The asymmetry of the rods was lost and only one resonance approximately at the sphere position was left. I also tried to utilise other light sources like Xe lamps, a Hg lamp, various lasers and also the sun. Non of them was able to reliably and reproducibly bleach the TDBC and at the same time leave the gold particles unchanged.

In the end, a cw-laser with a wavelength of 532 nm and a power of 10 W did the job. Its beam was

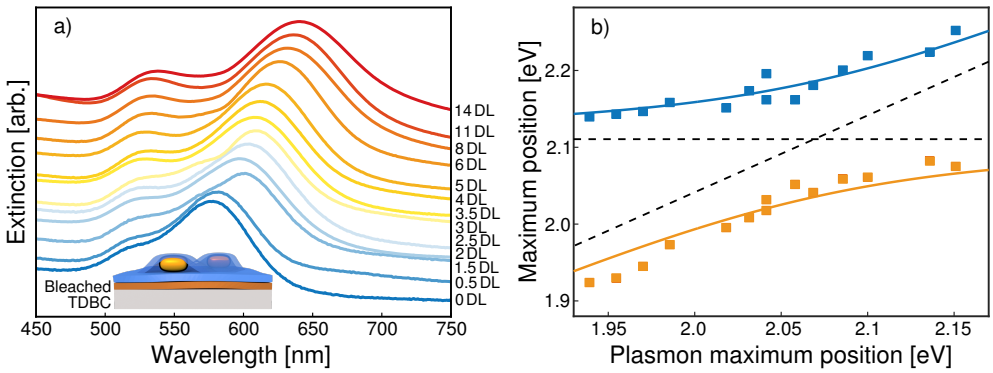

Figure 4.19: a) Extinction spectrum of the photobleached samples previously presented in Figure 4.17. The peak splitting has now vanished and pure plasmon resonances appear. The longitudinal plasmon resonance exhibits the expected red-shift for thicker covers. b) Anticrossing of the TDBC–gold core–shell nanorods. The maximum positions of the coupled peaks are plotted against the maximum positions of longitudinal resonances of the bleached particles. The anticrossing is underlined by a fit of Equation 3.128 as blue (upper polariton) and orange (lower polariton) line.

widened to a waist width of 1 cm. The advantage of such a wide beam is not only that the intensity is reduced to a value below the particles' damage threshold, but also that one sample could be completely illuminated and thus be bleached at once. Yet, this took rather long as shown in Figure 4.18. It depicts the evolution of the spectrum of core–shell nanorods under illumination. The dip becomes gradually smaller until it has completely vanished after 3 hours. In some cases, the bleaching time was a bit longer. Therefore, the samples were illuminated for 8 hours to make sure, no residual exciton resonances were found. Tests with pure gold rods showed that the particles themselves were not affected by the laser making this method the method of choice to reveal the original plasmon resonance of the samples.

After bleaching, the spectra of the samples that were presented in Figure 4.17 were recorded again. Their extinction is shown on the left side of Figure 4.19. Now, only the plasmon resonance is visible. The resonance position could then be read off. Assuming the the exciton position does not shift, these resonance positions describe the detuning between plasmon and exciton except for a constant offset. Thus, the maximum positions of the coupled resonances plotted against the maximum positions of the bleached spectra directly yields the anticrossing of the coupling. It is depicted in the right plot of Figure 4.19. Discussions and interpretations of the anticrossings are presented in Articles I and II.

The anticrossing of plasmon–exciton nanoparticles can be achieved not only by changing the dielectric environment. The most common method to shift the plasmon resonance that is presented in literature, is changing size or shape of the nanoparticles [118, 140, 147]. However, this seems to be a problematic approach when trying to determine the coupling strength of the system because the coupling strength is directly connected to the particle size as discussed in Article II. Therefore, changing the particle size within one system might lead to erroneous conclusions.

This previous section gave an introduction of the samples used in the first four articles of this work. For

Articles I and II, gold nanospheres and -rods were coated with TDBC, deposited on substrates, covered with polyelectrolytes and eventually, the dye was photobleached. This way, the anticrossing could be retrieved and the coupling regime could be assessed. For Articles III and IV, gold nanorods were coated with TDBC and directly investigated in solution. The next section will introduce respective measurement tools used in all articles.

4.2 Measurements

The plasmon resonances in gold nanoparticles fall into the visible range. Optical spectroscopy is therefore an obvious method to investigate the properties of both coupled and uncoupled systems. For this work, various variants of spectroscopic measurements were employed: Transmission, scattering, absorption and Raman spectroscopy were conducted as well as pump–probe spectroscopy. Additionally X-ray diffraction measurements, both with and without temporal resolution were conducted.

Transmission, scattering and absorption measurements can be regarded as linear spectroscopic tools and will be discussed in the first part of this section. In all three cases, a system's answer to a weak incoherent light source is recorded. The difference in information that can be gained about plasmon–exciton core–shell systems with these methods is discussed in Article I. Absorption spectroscopy was also the measurement tool employed for Article II whereas the results in Article III are based on transmission spectroscopy.

Article IV discusses the particles' behaviour in the short time after a pulsed optical excitation. This can be investigated by time resolved pump–probe spectroscopy, a widespread method to assess processes on timescales down to a few fs or even below. For this method, two laser pulses are guided onto the sample with a defined temporal distance, the first pulse excites (pumps) the sample whereas the second one probes the samples' transmission (or reflection) after excitation. The basics of this time resolved spectroscopy technique are introduced in the second part of the section.

The two subsequent parts discuss X-ray diffraction as a method to assess a crystal's lattice structure, first in a static regime and afterwards with temporal resolution applying the pump–probe technique. Time resolved X-ray measurements were conducted for Article V, again to assess the temporal response of gold nanotriangles after excitation. Article VI makes use of the strong connection between lattice structure and temperature and employs X-ray diffraction as local thermometer.

With this local thermometer, the temperature of the nanotriangles used as plasmonic catalyser was directly measured. The yield of the catalysis was then controlled by surface enhanced Raman spectroscopy (SERS). This technique will be presented in the end of this section.

4.2.1 Linear Spectroscopy

When a light beam hits a plasmonic nanoparticle, it can be modified in three different ways illustrated in Figure 4.20: The light can simply pass the particle, it can be elastically scattered in an arbitrary direction

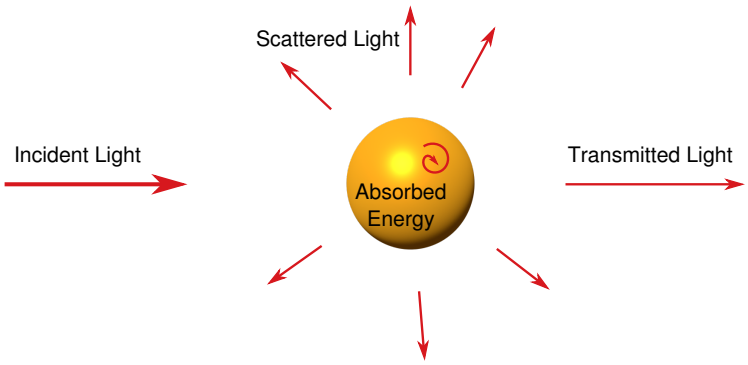

Figure 4.20: Possible ways of influencing an incident light beam for a nanoparticle. Light can be transmitted, scattered or absorbed.

or it can be absorbed. The efficiency of each process is determined by the respective cross section introduced in Section 3.2.

To assess the different cross sections, different methods of spectroscopy need to be employed. The most common and least complex method is transmission spectroscopy. Here, for each wavelength, the ratio between transmitted light is directly measured. The transmitted light is the part of the incoming light that was neither scattered nor absorbed. Transmission spectroscopy is therefore strongly connected to the extinction cross section. The latter can directly be measured except for a proportionality factor. The basic concept is presented in Figure 4.21.

Two different situations occurred: Measurements in solution and measurements of films with single particle thickness. In solution, the amount of transmitted light follows the Beer-Lambert-Law. The fraction of light I_T/I_0 that passes the sample exponentially decays with the distance d it travels through the solution, the particle density n and the extinction cross section σ_{ext}.

$$I_T = I_0 e^{-nd\sigma_{ext}} . \tag{4.1}$$

I_0 and I_T are directly measured in transmission spectroscopy and thus, the extinction cross section can be determined to a proportionality factor nd via

$$\sigma_{ext} = \frac{1}{nd} \ln\left(\frac{I_0}{I_T}\right) . \tag{4.2}$$

The extinction spectrum E is defined as $E = \ln(I_0/I_T)$ and is sometimes referred to as *absorbance* of the sample.

For particles on a substrate, the amount of light that can pass the sample is determined by the area that is not covered with particles. The area that is covered with particles, or, to be more correct, the area in which light would be scattered or absorbed is given by the areal particle density n_A multiplied with the

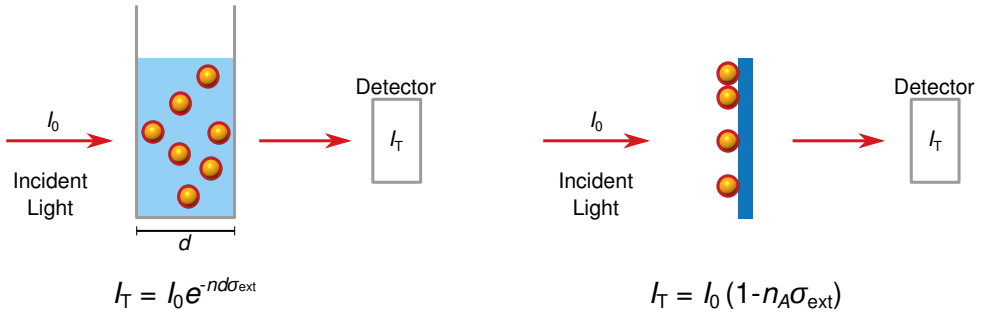

Figure 4.21: Scheme of transmission spectroscopy of nanoparticles in solution or on substrate. In both cases an incident beam with known intensity I_0 is guided through the samples and recorded by a detector. The transmitted light intensity is determined by Equations 4.1 and 4.3, respectively. The extinction cross section can then directly be retrieved.

extinction cross section. This means that for the transmitted light,

$$I_\mathrm{T} = I_0 \left(1 - n_\mathrm{A} \sigma_\mathrm{ext}\right) . \tag{4.3}$$

This expression can also be derived as the first term of the Taylor series of Equation 4.1 with small d. The extinction cross section for a particle on a substrate can be retrieved to the proportionality factor n_A as

$$\sigma_\mathrm{ext} = \frac{1}{n_\mathrm{A}} \left(1 - \frac{I_\mathrm{T}}{I_0}\right) . \tag{4.4}$$

Here, the extinction spectrum is given by $(1 - I_\mathrm{T}/I_0)$ and is again directly proportional to the extinction cross section. For the articles, the transmission measurements were conducted with a *Cary 5e* spectrometer and a *Cary 5000* spectrometer.

To measure the absorption and scattering cross sections, an integrating sphere needs to be used. This is a hollow sphere with a strongly scattering white inside surface, with an entrance hole for the incoming light and, if desired, an exit hole for the outgoing light. The sphere enables a measurement of all light that is scattered by the sample while simultaneously being able to record the transmitted or specularly reflected light.

For both scattering and absorption spectroscopy, two measurements must be conducted. In a scattering measurement, first the forward scattered light is recorded. For this, the sample is fixated in front of the entrance hole. The light that passes the sample is either absorbed, transmitted or scattered. The part of the light that is scattered in forward direction is reflected by the sphere's wall arbitrarily often with nearly 100 % reflection efficiency until it reaches the detector as signal I_FS. Light that is transmitted through the sample or absorbed does not reach the detector. Neither does backscattered light. To record the latter, the sample is planely fixated at the exit hole in a second measurement. This time, only light that is backscattered by the sample reaches the detector as signal I_BS. The two measurements are illustrated on the left side of Figure 4.22. The sum of the two intensities in relation to the incoming spectrum gives

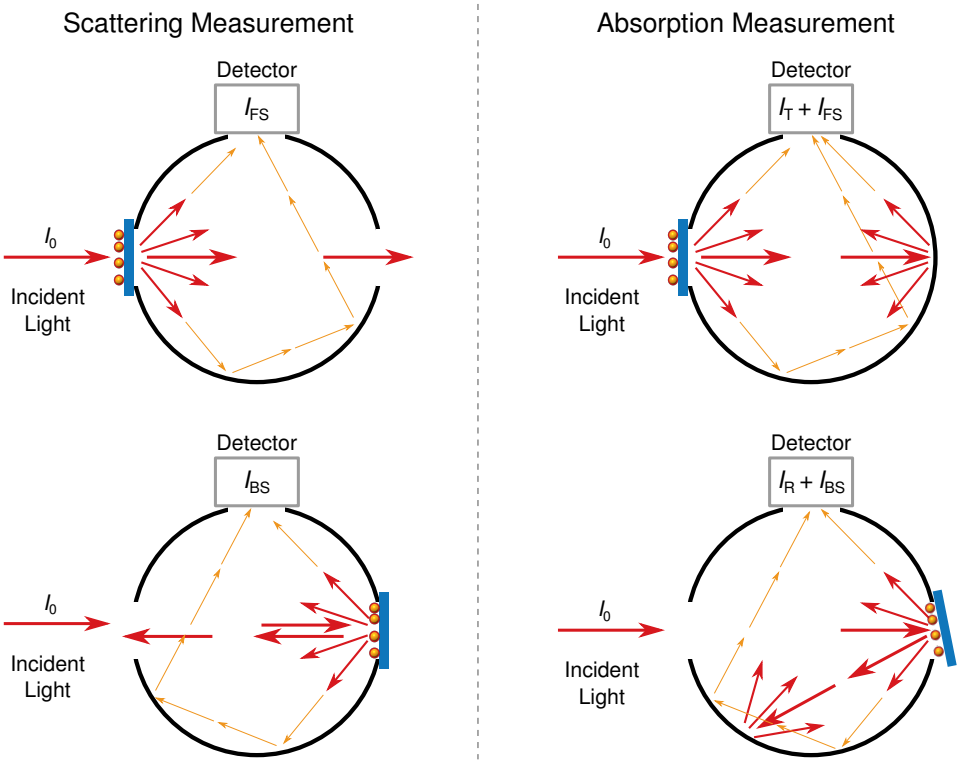

Figure 4.22: Scheme of scattering (left) and absorption (right) spectroscopy of nanoparticles on substrate. In both cases, a measurement consists of two steps. The integrating sphere is assumed to detect all light that reaches its walls. This way, the sphere is able to detect all forward scattered light (upper left) and all backwards scattered light (lower left) that can be summed to the scattering spectrum. In an absorption measurement, the forward scattered spectrum is recorded together with the transmission through the sample (upper right). In the second step, the sphere detects all light that is scattered backwards by the sample and its specular reflection (lower right). The absorption can be determined with Equation 4.6.

then the total scattering spectrum S of the sample, that is

$$S = \frac{I_{FS} + I_{BS}}{I_0} . \tag{4.5}$$

Like in the case of extinction, this spectrum is directly proportional to the scattering cross section and to the areal particle density n_A.

The absorption of a sample is not directly measured but accessed by recording all other light paths. This is again done in two steps. The first part is similar to the forward scattering measurement. This time however, the exit hole is closed. By that, also the transmitted light is detected as I_T. In the second step, not only the backscattered light is recorded, but also the specularly reflected light I_R. This way, all light that is not absorbed by the sample reaches the detector in one of the two measurements. The absorption spectrum A, again proportional to the absorption cross section, is then retrieved by subtracting all

measured relative signals from the incoming spectrum that is

$$A = 1 - \frac{I_T + I_{FS} + I_R + I_{BS}}{I_0} . \tag{4.6}$$

Obviously, correct absorption and scattering measurements demand a rather high experimental effort in comparison to transmission or extinction spectroscopy. The extinction however is only made up of scattering and absorption and cannot differentiate between those two. Complete information about the optical properties of a sample is therefore only gained if absorption and scattering are recorded independently. This is discussed in Article I. Article II presents pure absorption spectra of core–shell rods on substrates with polyelectrolyte covers. For Article III, particle spectra were recorded in solution. Thus, for simplicity, the extinction was measured which was then taken into account in the discussion.

4.2.2 Time Resolved Spectroscopy

For Article IV, a different kind of spectroscopy was applied. The article discusses the reaction of the core–shell nanoparticles to optical heating. To record the spectrum of the particles shortly after an external excitation, I reconstructed an optical pump–probe set-up for time resolved spectroscopy measurements.

The method works as follows: A laser pulse excites the sample and short time later, a second pulse, mostly a white light pulse, records the spectrum of the excited sample. The temporal distance between the first (pump) and second (probe) pulse can be precisely adjusted by tuning the length of the optical path of the pump pulse before hitting the sample. This way, time resolved spectra can be recorded with a temporal resolution only restricted by the pulse length.

In detail, the set-up works as depicted in Figure 4.23: A titanium-sapphire (Ti:Sa) laser generates laser pulses with a duration of approximately 150 fs at a central wavelength of 795 nm with a repetition rate of 5 kHz. Of the laser's output, 20 % are used in the set-up. A beam splitter separates a small fraction of the pulse energy to be used as probe pulse while allowing most of the light to pass as pump light. The pump wavelength was chosen to be the second harmonic of the laser source around 400 nm. The light was frequency doubled by second harmonic generation in a β-Barium borate crystal (BBO). Before the second harmonic generation, the beam passes a half-wave plate combined with a polariser. The combination of the two allows precise control over the power and polarisaiton of the pump beam. After the second harmonic generation, the beam is guided via a delay stage. The path length on the stage can be adjusted by moving the backreflecting mirrors. After the delay stage, the light passes a chopper, that alternatingliy lets the pump light pass or blocks it with a frequency of 125 Hz. Then, the pump light is directed onto the sample. The probe pulse is focussed on a saphhire crystal to generate a supercontinuum [148] that means pulses consisting of wavelengths ranging from 450 nm to 700 nm. These white light pulses are then also focussed onto the sample with a focal spot that is smaller than the pumped area to make sure that the complete probed area has also been pumped. Behind the sample, the probe light is guided to an *AvaSpec* multichannel spectrometer from *Avantes* .

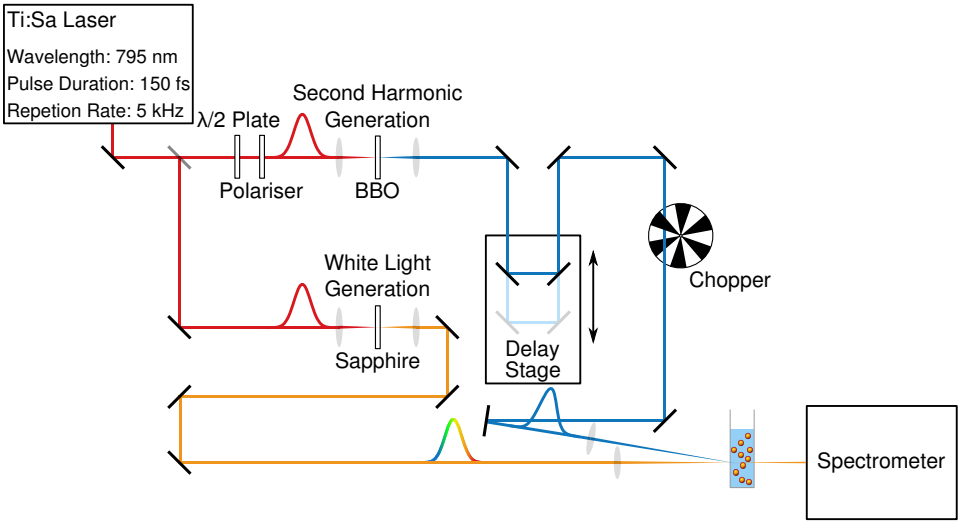

Figure 4.23: Sketch of the set-up for pump–probe spectroscopy. A Ti:Sa laser generates pulses with a duration of 150 fs at a wavelength of 795 nm and a repetition rate of 5 kHz. The light is split up into a pump and a probe path. The pump beam is frequency doubled in a BBO, guided over the delay stage and through a chopper and focussed onto the sample. The pump power that reaches the sample can be adjusted by the combination of a $\lambda/2$ plate and a polariser. The probe beam is guided over an equal distance as the pump beam before it is focussed onto the sample. In its path, it is focussed onto a sapphire plate to generate supercontinuum pulses. The transmission of the pump pulse through the sample is eventually recorded by a spectrometer.

The chopper enables alternating measurements of pumped and unpumped situations. The relative signal between adjacent pumped and unpumped measurements can reduce noise for example from fluctuations in the laser energy. The resulting relative transmission change

$$\Delta T = \frac{T_{\text{pumped}} - T_{\text{unpumped}}}{T_{\text{unpumped}}} \tag{4.7}$$

is recorded simultaneously for the whole spectrum of the white light probe beam. The time delay between pump and probe is then varied in the range of interest. The resulting data can be plotted as heatmap as is done here exemplarily in the left panel of Figure 4.24. It shows the relative transmission of TDBC–gold core–shell nanorods with a short axis diameter of 25 nm in solution.

Due to dispersion in optical components like lenses and polarisers, the white light pulse is strongly chirped, that means different parts of the spectrum are temporally shifted relative to each other. Therfore, different parts of the spectrum arive at different times. For further analysis, the data needs to be modified in a sense that at all frequencies, the point of no delay between pump and probe is located at the same time. This chirp correction is often conducted by characterising the probe pulse with a polarisation-gate *freqency resolved optical gating* (FROG) [149] measurement from which time zero can be determined for each wavelength. With these values, the data can be corrected for further analysis as plotted in the right panel of Figure 4.24. The interpretation of the data is discussed in Article IV.

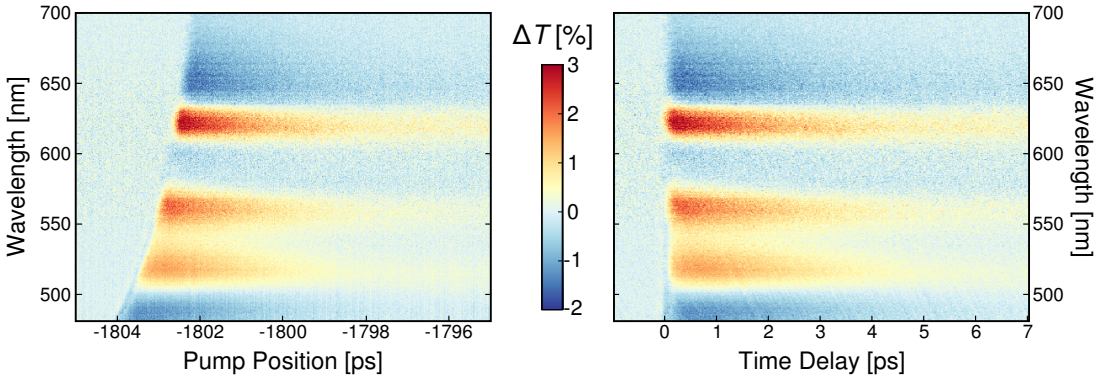

Figure 4.24: Raw data (left) and FROG corrected data (right) of a typical pump–probe measurement of TDBC coated gold nanorods. The chirp causes a temporal distortion within the probe pulse. This shifts the moment of concurrent incidence with the pump pulse for different wavelengths. The chirp can be measured by a frequency resolved optical gating (FROG) measurement and the pump–probe data can be corrected and a mutual time zero can be found for all wavelengths.

4.2.3 X-Ray Diffraction

As seen in the discussion about the photobleaching of the dye in core–shell particles, the heating and melting behaviour of gold nanoparticles differs from that of bulk gold. A thorough understanding of heated particles is indispensable for many applications using gold nanoparticles. A way to directly access the temperature of nanoparticles is X-ray diffraction. It is based on Bragg's condition for constructive interference of electromagnetic waves reflected at crystal planes. The condition is schematically once more illustrated in Figure 4.25.

Constructive interference occurs when the angle θ between incoming wave and a crystal plane fulfils the condition

$$2d \sin\theta = m\lambda \,. \tag{4.8}$$

Here, λ is the wavelength of the incoming radiation, m a natural number and d the distance between two lattice planes. This distance is temperature dependent according to the material's thermal expansion

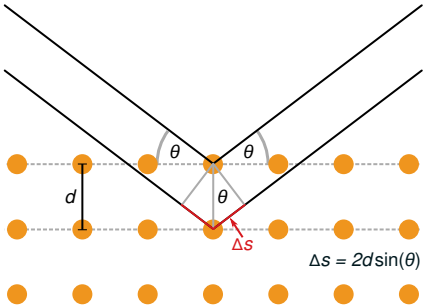

Figure 4.25: Illustration of the Bragg condition. Waves whose optical path difference Δs – determined by the lattice constant d and the scattering angle θ – is a multiple of the wavelength interfere constructively.

coefficient enabling the use of X-ray diffraction as a material selective thermometer. With this technique it is for example possible to directly determine the (lattice) temperature of gold nanoparticles under optical excitation. For Article VI, the effect was utilised to monitor the temperature of gold nanotriangles under continuous cw excitation with a high intensity infrared beam.

4.2.4 Time Resolved X-Ray Diffraction

In case the X-ray radiation is available in pulsed form, X-ray diffraction can be combined with the methods of pump–probe spectroscopy to directly observe the crystal lattice in nanoparticles after optical excitation. Our group, the UDKM, operates a laser-driven plasma X-ray source that generates femtosecond X-ray pulses at copper K_α energy [150, 151]. The X-ray pulses are generated in a thin copper band by focussed 7 mJ laser pulses emitted by a *Coherent Legend Elite* system. Using a 10 % fraction of the system's laser energy as optical pump beam, a set-up can be built that works in a similar way as the optical pump–probe set-up depicted in Figure 4.23. In this case, the probe pulses are hard X-rays instead of the white light pulses. The set-up was used to directly investigate the behaviour of gold nanotriangles after optical excitation for Article V. The detection and data analysis is different to that of optical spectroscopy. However, it was conducted by colleagues and shall therefore not be discussed here.

4.2.5 SERS

Surface enhanced Raman spectroscopy (SERS) is the most developed application for localised plasmons. It was used for Article VI to investigate the photocatalytic properties of gold nanotriangles under optical heating. For preliminary measurements, I designed and constructed a homebuilt Raman microscope. The measurements helped to assess the optimal parameters like laser power that were eventually used in the actual experiment at the KMC3-XPP end station of the Berlin synchrotron radiation facility BESSY II which determined the lattice temperature of gold nanoparticles under laser excitation as explained in Section 4.2.3. The basic principles of SERS shall briefly be summarised here.

Raman scattering is a well studied effect that was first discovered by V.C. Raman in 1928 [152]. It describes inelastic scattering of incident light by transitions between different vibrational levels of a molecule via a virtual state. The resulting state can be of higher (Stokes scattering) or lower (Antistokes scattering) vibrational energy than the original state. The principle is depicted in Figure 4.26.

Each molecule possesses vibrational normal modes with a specific energy and has a specific Raman spectrum defined by all (Raman active) vibrational resonances. This spectrum can thus be regarded as unique fingerprint of a molecule. Therefore, Raman spectroscopy represents a highly precise detection method for chemical compounds.

In free molecules, Raman scattering is rather weak is especially in comparison to ellastic Rayleigh scattering. However, in direct vicinity of metal nanostructures, the high electric fields provided by localised plasmons can strongly enhance Raman signals making the technique a highly sensitive tool

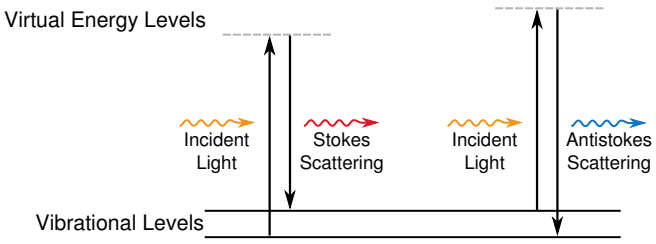

Figure 4.26: Illustration of Raman scattering. Incident light can excite a molecule to a virtual electronic energy level. This virtual state relaxes again to the initial electronic level but to a different vibrational state. If the final state is at higher energy, the Raman scattered light is red-shifted to the incident light (Stokes scattering on the left), if the final state is at lower energy, the Raman scattered light is blue-shifted (Antistokes scattering on the right).

for chemical analysis. The strong enhancement is rooted in the fact that both incoming and outgoing light are enhanced by the plasmonic structure. The field E_{loc} that excites the molecule at a surface is the g times enhanced incident field E_0. This excitation induces a dipole moment $\mu = \alpha_{\mathrm{R}} g E_0$ in the molecule with the Raman polarisability α_{R} [153]. The field that is scattered by the dipole is again enhanced by a factor g' (which can be slightly different to g due to the difference in frequency). Thus, the scattered field $E_{\mathrm{SERS}} = \alpha_{\mathrm{R}} g g' E_0$ is enhanced by gg' in comparison to a non-surface enhanced Raman scattered field. The Raman intensity is therefore enhanced by $|gg'|^2$ [153]. For small Raman shifts, one can assume the enhancement factors to be equal [154]. This leads to a total enhancement of the Raman intensity of g^4 [153]. Combined with the enhancement factors of localised plasmon resonances, extremely large signals can be obtained and even single molecules can be detected [155, 156].

In the home-built Raman set-up, a small band cw-laser with a wavelength of 633 nm is coupled into the objective via a longpass and a shortpass filter. The longpass filter only reflects light with wavelengths below 640 nm allowing a separation between the exciting laser and the Raman signal. The shortpass filter transmits wavelengths below 550 nm and allows an optical control over the sample without affecting the Raman signal. The light that is scattered by the sample, including the Raman signal, is collected by the objective and guided via the shortpass filter back to the longpass filter. The (Stokes) Raman signal is red-shifted from the original laser wavelength and is therefore transmitted by the filter. Residual laser light is filtered out by an additional notch filter before the signal is guided via an optical fibre to the spectrometer consisting of an *Acton 300i* spectrograph and an *Andor iDus* CCD camera. For optical control over the sample and the investigated region, the light of a halogen lamp illuminates the sample after passing the shortpass filter. This light is collected by the objetive and is transmitted by the shortpass filter on its way back from the sample. Via a beam splitter and a tube lens, the light is focussed on a CMOS camera creating an image of the region of interest. A sketch of the set-up is depicted in Figure 4.27.

The set-up was used to monitor the plasmon assisted dimerisation of 4–nitrothiophenol (4–NTP) into 4,4'–dimercaptoazobenzene (DMAB). 4–NTP was positioned on a monolayer of gold nanotriangles. Especially in hot-spots the molecules reacted to DMAB under laser irradiation. The DMAB possess a different Raman spectrum that can be used to monitor if the reaction took place. The right panel of Figure 4.27 shows an example SERS spectrum with marked peaks that are only observed in the spectrum

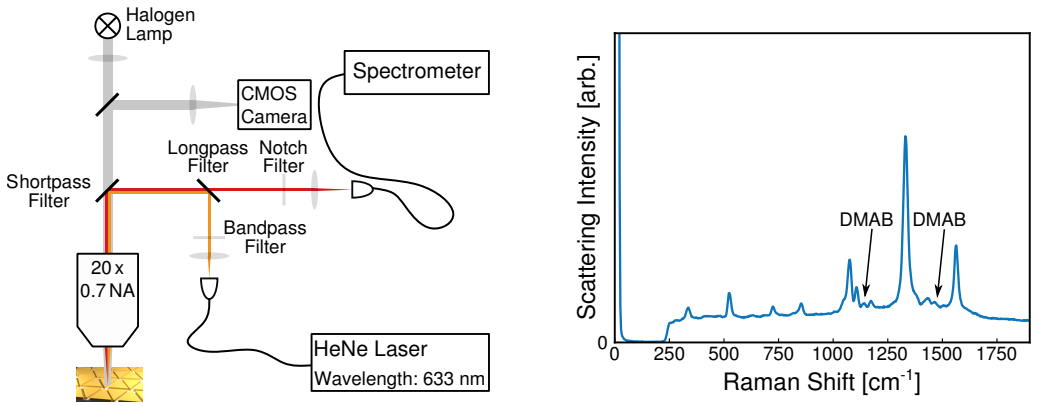

Figure 4.27: Left: Sketch of the homebuilt Raman microscope. Light of a HeNe laser is guided via a longpass filter and a shortpass filter into an objective (20× magnification, NA = 0.75) and focussed onto the sample. The backscattered light is collected by the objective, reflected by the shortpass filter and transmitted by the longpass filter. A notch filter discriminates residual laser light. A spectrometer then record the (Stokes scattered) Raman spectrum. Additionally, a halogen lamp and a CMOS camera allow the use as convenient microscope and enable optical control over the investigated region. The white light to image the sample in the camera is coupled in and out of the optical path through the shortpass filter which transmits wavelengths below 550 nm. Right: Typical SERS spectrum of 4-NTP of which parts have reacted to DMAB. The marked peaks occur only in the DMAB spectrum and indicate therefore a successful reaction.

of DMAB. These peaks indicate that dimerisation occurred under the given conditions.

This short section about SERS closes the chapter about the experimental methods that were utilised for the articles that are presented in the next chapter. A detailed description of the TDBC–gold core–shell particles that were used in Articles I – IV was followed by the introduction of the method of layer-by-layer deposition. This technique was used to immobilise the particles on a substrate and cover them with polyelectrolyte covers a precisely adjustable thickness. Eventually, the dye was photobleached to access the original plasmon resonances.

In the second part of the chapter, the experimental tools were described in detail. Extinction, scattering and absorption spectroscopy – the main tools used in Articles I–III – were discussed as well as pump-probe spectroscopy – the method used for Article IV. Articles V and VI relied on X-ray diffraction with and without temporal resolution, respectively. Both methods were described followed by a brief introduction of surface enhanced Raman spectroscopy used for Article VI.

At this point all necessary background should be given to understand the articles that constitute this thesis. These articles are now presented in the following chapter representing the scientific main results of my time as doctoral researcher.

5 | Articles

The following chapter presents the articles I worked on in the past years. They can be separated in two topics: Articles I – IV investigate the coupling between gold nanoparticles and organic dyes in a core–shell geometry, Articles IV – VI discuss the reaction of gold nanoparticles to optical heating. The following introduction into this chapter shall present the mutual connection between the articles and additionally give insight into the scientific context in which the articles were created.

Article I was the first article of the UDKM published in the field of plasmon–exciton coupling. It discusses the two example systems of gold nanospheres and gold nanorods both coated with a layer of the J-aggregate forming organic dye TDBC. The main focus lies on the demonstration of strong coupling. The most common method to assess the coupling strength is via the anticrossing of the system's energy levels. In core–shell nanoparticles, this anticrossing is revealed by tuning the plasmon resonance. This can be done for example by changing the aspect ratio in nanorods [118], by changing the shell thickness of nanoshells [147] or the size of nanodiscs [133]. This article introduces a new way of resonance tuning in coupled plasmon–exciton system: The precise changing of the environment via layer-by-layer deposition of polyelectrolytes. Details of the techinque were given in Section 4.1.2. This technique had been used previously for bare particles [47], but not yet in context of plasmon–exciton coupling. Interestingly, while Article I was under review, a very similar way of revealing the anticrossing was published using alumina instead of polyelectrolytes [131]. One great advantage of such external tuning is that the particles themselves are not altered. As we saw in Section 3.5, the coupling strength changes with the mode volume which again is strongly dependent on the particle volume [109]. Thus, changing the size of a nanoparticle also changes the the coupling strength. This makes approaches of tuning the plasmon resonance for example via the aspect ratio susceptible to errors.

Another topic of Article I is the correct identification of strong coupling. Strong coupling between plasmonic nanoparticles and excitonic emitters has been reported previously by several researchers [49, 50, 117–119, 130, 133, 137, 139, 140, 147, 157–163]. However, in most cases, the strong coupling regime was only identified via the particles' extinction. Article I demonstrates experimentally, that this method might lead to erroneous results. The extinction spectrum is composed of both scattering and absorption. These two might have diverging features which are undiscernible under bare recording of the extinction. Article I investigates two kinds of gold nanoparticles, in one case nanospheres, in the other nanorods, both coated with TDBC. Both show similar features in their extinction and a similar anticrossing. This similarity is annulled in the absorption spectra. In contrast to the rods, the spheres do not exhibit an anticrossing. Such an effect had previously not been investigated experimentally. Only a theoretical study predicted the splitting in the absorption to occur at weaker couplings than that in absorption [93].

A third aspect of Article I is a coupled oscillator model that directly explains the emergence of a

peak splitting in the scattering at weaker coupling strength than in the absoprption. Classical coupled oscillators have often been used to model coupled plasmon–exciton systems [61, 112, 120, 164]. Article I is however the first to use this modelling to assign the respective contributions of the two subsystems to absorption and scattering.

The technique of tuning the particle environment to determine the coupling strength which was introduced in Article I forms the basis of Article II. The latter discusses the relationship between particle size and coupling strength in core–shell nanorods with a gold core and a TDBC shell. Theoretical studies have predicted a strong dependence of the coupling strength on the particle size [93], but this connection had not been investigated experimentally. Article II closes this gap. It makes use of the fact that the technique of layer-by-layer depsition of polyelectrolytes leaves the particles unchanged. In contrast, techniques like the changing of the aspcet ratio to reveal an anticrossing cannot assess the size dependence of the coupling strength as the particle size is changed within one set of experiments. Article II shows that the coupling becomes stronger for decreasing particle sizes. It also gives a qualitative explanation using Equation 3.132. This equation determines the coupling strength via the transition dipole moment of the emitters and the plasmonic mode volume. This mode volume had been shown to be comparable to the physical particle volume [109, 165] for gold particles with a diameter below 50 nm. Using this insight and literature values for the transition dipole moment of TDBC, Article II is able to explain the coupling strengths of four different nanorod sizes and predict that of any other nanoparticle.

One goal of light–matter coupling is the strong coupling between plasmonic cavities and single emitters [62]. A few studies had previously reported the achivement of this mile stone [54, 116, 132, 166]. The reported systems demanded a comparably high effort. Article II argues that single emitter strong coupling is even possible with simple gold nanoparticles. It predicts the possibility of strong coupling between a single TDBC J-aggregate and a gold nanorod with short and long axis diameters of 6 nm and 12 nm, respectively.

Article III directly used the results of Article II. But it first discusses a very general phenomenon of light–matter coupling: the saturation of an absorber due to the vacuum fluctuations in an electromagnetic cavity. This effect had previously not been included in discussions about plasmon–exciton coupling [26]. Article III demonstrates that it yet does play a role. Vacuum induced saturation had been known to the community of cavity quantum electrodynamics before. There, strong light–matter coupling was generated under tremendous effort in optical cavities [167] and vacuum induced saturation occurred rather as a side effect. Article III shows, that in plasmonic cavities, vacuum induced saturation can occur even under ambient conditions in simple core–shell geometries. It gives a criterion that connects the emergence of saturation with the absorber linewidth and the coupling strength. It also shows that for plasmonic cavities, vacuum induced saturation can occur independently of strong coupling.

The article gives an expression for the susceptibility that includes the effect. With this, it recreates the spectra of the TDBC coated nanorods that were used for Article II. The coupling strength that was extracted from the anticrossing is included in Article III to account for the saturation. The agreement between the model and the experimental data is remarkable. Previously reported theoretical studies based on Mie scattering or finite element modelling predicted an additional peak in the extinction that was attributed to a mode whose energy is completely stored in the shell [93, 168]. This shell mode had however not been observed experimentally. With the model in Article III, this redundant peak disappears

naturally and theory and experiments can be reconciled.

Article IV connects the topic of plasmon–exciton coupling, which is discussed in the first three articles, to optical heating of metal nanoparticles, which is analysed in the last three articles. The article discusses the optical response of the plasmon–exciton core–shell nanorods to excitation by a short laser pulse. The article presents qualitative simulations of the extinction of gold nanorods with a TDBC shell after excitation with a femtosecond laser pulse. Previous publications have discussed similar scenarios [169–172], but the measured spectra were only explained phenomenologically via oscillator models [171] or approximations of the peaks as Lorentz resonances [170]. Article III has introduced a correct way to simulate static spectra. Article IV now makes use of theses new insights and combines them with the model of Renzo Rosei which was introduced in Section 3.4.1. The model allows temperature dependent simulations of gold's permittivity and consequently enables the identification of the heat contribution to the change in the spectra after excitation. Several studies have explained the spectral changes of gold nanoparticles that are not strongly coupled to their environment with the change of the electron and phonon temperature in the first picoseconds after excitation plugged into the Rosei model [39, 96, 100, 173]. Article IV is the first one to transfer the well-established methods to coupled plasmon–exciton systems.

Articles V and VI are two additional articles that I co-authored that also examine the reaction of plasmonic nanoparticles to optical heating. Both discuss gold nanotriangles that are excited by either laser pulses (Article V) or continuous wave laser light (Article VI). The acoustic response of nanoparticles to femtosecond laser pulses has been investigated in previous publications also beyond the first picoseconds after excitation [102, 174]. Article V is however the first to probe this response with ultrashort X-ray pulses. Due to the fast temperature increase after excitation by a femtosecond laser pulse that rapidly raises electron and phonon pressure, the particle volume starts to oscillate with a period of a few picoseconds. This *breathing mode* induces a change in the electron density and consequently in the Drude contribution to the permittivity. This change can therefore be studied with optical spectroscopy. However, this is actually only an indirect way to look at the particle expansion. X-ray diffraction allows a direct investigation of the ion lattice and Article V demonstrates its applicability to plasmonic nanoparticles.

Article VI discusses the response of the gold nanotriangles to continuous laser irradiation with a special focus on their melting behaviour. Catalytic activity of plasmonic nanoparticles is often investigated in microscopes with small laser foci to excite the structures [175]. On the other hand, industrial applications require large scale excitations for high material yield. Article VI studies the effect of a larger illumination area. It shows that even at lower intensities, larger excitation spots can cause particle melting. It argues, that the induced heat can be transported in three dimensions if the laser spot is very small. For large spots however, heat can only flow into the sample. Thus, higher temperatures can accumulate inside nanoparticles in larger illumination areas leading to particle melting even at lower intensities. This effect is of great importance when designing large scale plasmon assisted catalysis set-ups.

After this overview, the articles are presented in the following. In the end, Chapter 6 will give a short summary of this work and an outlook to future implications.

Article I

Signatures of Strong Coupling on Nanoparticles: Revealing Absorption Anticrossing by Tuning the Dielectric Environment

Felix Stete, Wouter Koopman, and Matias Bargheer

ACS Photonics 4, 7 (2017)

ACS Photonics

Article

pubs.acs.org/journal/apchd5

Signatures of Strong Coupling on Nanoparticles: Revealing Absorption Anticrossing by Tuning the Dielectric Environment

Felix Stete,[†,‡] Wouter Koopman,[*,†] and Matias Bargheer[†,§]

[†]Institut für Physik & Astronomie, Universität Potsdam, Karl-Liebknecht-Straße 24-25, 14476 Potsdam, Germany

[‡]School of Analytical Sciences Adlershof (SALSA), Humboldt-Universität zu Berlin, Unter den Linden 6, 10999 Berlin, Germany

[§]Helmholtz Zentrum Berlin, Albert-Einstein-Straße 15, 12489 Berlin, Germany

Supporting Information

ABSTRACT: In the strong coupling regime, exciton and plasmon excitations are hybridized into combined system excitations. The correct identification of the coupling regime in these systems is currently debated, from both experimental and theoretical perspectives. In this article we show that the extinction spectra may show a large peak splitting, although the energy loss encoded in the absorption spectra clearly rules out the strong coupling regime. We investigate the coupling of *J*-aggregate excitons to the localized surface plasmon polaritons on gold nanospheres and nanorods by fine-tuning the plasmon resonance via layer-by-layer deposition of polyelectrolytes. While both structures show a characteristic anticrossing in extinction and scattering experiments, the careful assessment of the systems' light absorption reveals that strong coupling of the plasmon to the exciton is not present in the nanosphere system. In a phenomenological model of two classical coupled oscillators, a Fano-like regime causes only the resonance of the light-driven oscillator to split up, while the other one still dissipates energy at its original frequency. Only in the strong-coupling limit do both oscillators split up the frequencies at which they dissipate energy, qualitatively explaining our experimental finding.

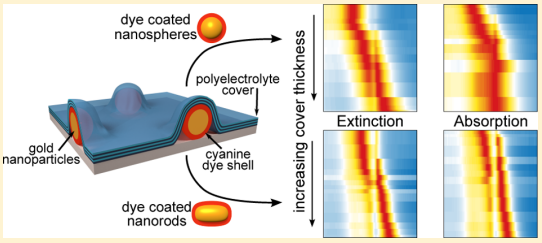

KEYWORDS: *hybrid nanoparticles, exciton plasmon coupling, layer-by-layer deposition, strong coupling, absorption measurements*

The electromagnetic coupling of molecular excitations to plasmonic nanoparticles offers a promising method to manipulate the light−matter interaction at the nanoscale. This approach is frequently used to enhance the optical cross-section of molecules, e.g., in surface-enhanced Raman scattering (SERS),[1] enhancement of fluorescence[2] and infrared absorption,[3,4] plasmon-enhanced light harvesting in dye-sensitized solar cells,[5] or plasmon-enhanced dye lasers.[6]

The coupling strength between molecular excitations and plasmons is given by the rate of energy exchange between the two components. In the so-called vacuum limit for a small number of excitations this is[7,8] $\Omega = E_{vac} \times \mu/\hbar$. Here μ describes the transition dipole moment of the emitter and E_{vac} the vacuum field at the emitter position, which is proportional to the inverse square root of the mode volume V,[9,10] $E_{vac} \propto V^{-1/2}$. Due to their ability to concentrate light into subwavelength mode volumes, nanoparticles are able to support high coupling strengths. A particularly interesting coupling regime occurs if Ω surpasses all damping rates in the system. In this so-called strong-coupling regime hybrid light−matter states emerge. If damping is neglected, the hybrid resonances result from the plasmon resonance ω_p and the exciton resonance ω_{ex} as[11,12]

$$\omega_{\pm} = \frac{1}{2}(\omega_p + \omega_{ex}) \pm \sqrt{\frac{1}{4}(\omega_p - \omega_{ex})^2 + g^2} \quad (1)$$

where g is the coupling parameter. Hence, the presence of the new hybrid states can be detected by observing characteristic linear optical spectra showing two new resonances with a separation of $\Delta = (\omega_+ - \omega_-)$, the vacuum splitting. In general, this spectral splitting scales with $(n + 1)^{0.5}$, where n is the number of photons involved. In the case of weak probe light $n \approx 0$, and the splitting indeed characterizes the vacuum coupling.

Realizing strong light−matter coupling on the nanoscale promises both interesting possibilities for the fundamental study of light−matter interaction and a great potential for applications. Suggestions include thresholdless lasing,[8] all-optical switching,[13] the manipulation of chemical reactions,[14] the adjustment of work functions,[15] and in particular applications in the context of nanoscale quantum optics[8] such as quantum information processing.[16]

The most frequently used approach for achieving strong light−matter coupling on nanoparticles is the fabrication of hybrid core−shell particles with a noble-metal core and a molecular shell. Several hybrid nanoparticles that allegedly show strong coupling have been presented in recent

Received: February 6, 2017
Published: June 22, 2017

DOI: 10.1021/acsphotonics.7b00113
ACS Photonics 2017, 4, 1669−1676

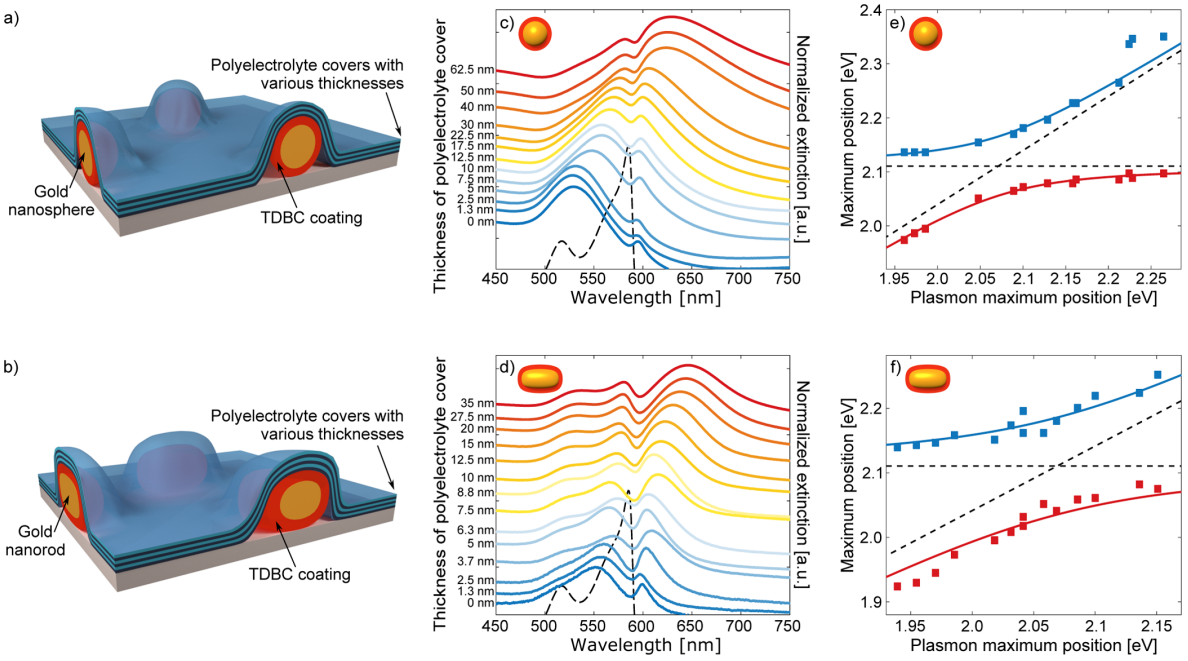

Figure 1. Sketches of the samples of polyelectrolyte-covered core−shell particles with a TDBC shell and a gold nanosphere (a) or nanorod (b) core. The extinction spectra for different cover thicknesses are presented in (c) for the spheres and in (d) for the rods together with the extinction of unaffected TDBC *J*-aggregates (black dashed line). A clear dip at the resonance position of the *J*-aggregates as well as a red-shift for thicker covers is visible. Maximum positions are plotted against the maximum positions of photobleached samples to reveal an anticrossing for both spheres (e) and rods (f). The red and blue lines are fits according to eq 1 with a small shift along the horizontal axis (see text).

literature.[17−21] In several cases these claims have however been challenged,[22,23] as an unambiguous determination of the coupling regime for hybrid nanoparticles is difficult. A clear proof for the presence of strong coupling is obtained if Ω is bigger than the spectral line width of both the plasmon and the molecular resonance. For nanoparticles, however, the spectral line widths are frequently masked by inhomogeneous broadening, mostly caused by particle-size dispersion and local variations in the chemical environment. Due to this broadening, solely using the line width criterium to determine the coupling regime for ensembles of hybrid nanoparticles can lead to erroneous conclusions.

Because of the difficulties in determining the correct line widths from the ensemble spectrum, the presence of strong coupling is often claimed on the basis of observing a "dip" in the extinction[17,18,24,25] or scattering spectrum,[19] which is interpreted as the emergence of hybrid states. This incautious use of extinction or scattering spectra for discussing the coupling regime of hybrid particles can however easily lead to erroneous conclusions.[22,23] In particular, real strong coupling can be confused with Fano-like interference effects, which appear in the weak-coupling regime.[23,26] This brings up the question of how to prove the presence of strong coupling for an ensemble of hybrid nanoparticles. Extensive numerical simulations by Antosiewicz et al. showed that real absorption measurements of the hybrid particles can be used to distinguish between Fano interferences in the scattering sprectum and the real strong-coupling regime.[23] However, to date, no real absorption measurements on hybrid nanoparticles have been presented.

As further evidence for the presence of strong coupling, data showing a modulation of the extinction spectrum are often supplemented by presenting an anticrossing in the functional dependence of the observed resonance frequencies on the uncoupled plasmon frequency ω_p.[17,20,21,25,27] For hybrid nanoparticles these anticrossing relations are usually obtained by changing the particle size.[17,25] This is a highly problematic approach, as it is well known that the coupling strength changes with the particle size.[23]

This article presents an experimental approach to assess the coupling regime of hybrid nanoparticles without knowledge of the homogeneous line widths. It describes an experimental procedure: (a) to measure the real absorption spectrum of particle ensembles and (b) to determine the anticrossing relation without nanoparticle size variation, but via shifting the plasmon resonance by layer-by-layer deposition of polyelectrolytes.[28] The different coupling regimes are exemplified by two core−shell nanoparticle systems, gold nanorods and nanospeheres, which are both coated with an excitonic molecular shell. Both particle types have been claimed to support strong coupling[19,25] on grounds of an observed dip in the extinction spectrum and a related anticrossing. However, while for rods the presence of strong coupling has been supported by fluorescence measurements,[25,29] theory shows that gold nanospheres cannot reach the strong coupling regime for fundamental reasons.[26] The absorption measurements discussed in this article support this classification. Using a classical coupled pendulum model with an appropriate coupling to the periodic excitation, we discuss which information can be obtained from scattering and absorption measurements and

DOI: 10.1021/acsphotonics.7b00113
ACS Photonics 2017, 4, 1669−1676

illustrate the underlying mechanism leading to the observed differences in absorption, extinction, and scattering spectra.

PLASMON TUNING

The samples used in the experiments were based on 100 nm gold nanospheres and 25 nm × 57 nm gold nanorods, coated with a shell of 5,5′,6,6′-tetrachloro-1,1′-diethyl-3,3′-di(4-sulfobutyl)benzimidazolocarbocyanine (TDBC) dyes. TDBC is the most widely used dye in plasmon−exciton coupling experiments due to its ability to organize in a *J*-aggregate fashion on gold surfaces.[18,30] The formation of these aggregates is beneficial for reaching the strong-coupling regime, as *J*-aggregate excitons possess transition dipole moments far higher than the combined dipole moments of the constituting molecules.[31]

Equation 1 states that the resonance wavelengths of the coupled system strongly depend on the exciton−plasmon detuning $\delta = \omega_p - \omega_{ex}$. The essential parameter for discussing the coupling regime is the resonance splitting $\Omega = 2g$, which describes the peak splitting at $\delta = 0$. As assuring the spectral coincidence of exciton and plasmon resonance is difficult, the coupling regime is frequently discussed by plotting the resonances of the coupled system $\omega_\pm$ as a function of ω_p. This procedure is similar to the measurement of the dispersion relation for coupled propagating plasmons and excitons, where the observation of an avoided crossing (anticrossing) of the plasmon and exciton dispersion relations is generally accepted as proof for strong coupling.[8,32] Conversely, observing an anticrossing of $\omega_\pm$ as a function of ω_p can be interpreted as a sign for strong coupling in nanoparticle systems.[17,20,21,25,27]

The conventional way for tuning ω_p is changing the particle size[25] or, in the case of nanoshells, the shell thickness.[17] Using this approach to discuss the coupling strength has, however, several drawbacks. On one hand, particles of only a few different particle sizes are usually available, and hence the curves obtained this way consist of only a few points.[25] More importantly, different particle sizes are predicted to support different maximum coupling strengths.[23] Therefore, we consider the approach to change the particle size for discussing the coupling regime to be questionable.

In contrast, our experimental approach consists of shifting the plasmon resonance by adjusting the permittivity ϵ_{med} of the particles' environment. The plasmon resonance is determined by the (dipole) polarizability α of the particle in this environment:[28,33]

$$\alpha \propto \frac{\epsilon_{mat} - \epsilon_{med}}{\epsilon_{mat} + f\epsilon_{med}} \quad (2)$$

Here ϵ_{mat} denotes the permittivity of the nanoparticle, while the geometrical factor f takes into account the shape of the particle. The plasmon resonance occurs at the wavelength for which the denominator becomes minimal. To change ϵ_{med}, we embedded the particles in a polyelectrolyte−air matrix (see Figure 1a and b). The particles were deposited on a polymer-covered glass substrate and subsequently covered using layer-by-layer deposition of polyelectrolytes. Due to the low thickness of about 1.25 nm for each layer, the effective ϵ_{med} experienced by the particle is the average of the permittivity of the polymer cover and of the adjacent air. The stepwise addition of thin polymer layers then leads to an increase of the effective ϵ_{med}, which in turn shifts the plasmon resonance.[28,34] We fabricated a separate sample for each cover thickness. This method allows a very fine-tuning of the exciton−plasmon overlap, much more precise and facile than the tuning by particle size variation.

EXTINCTION ANTICROSSING

For nanoparticle systems the coupled resonances have been investigated in the past by linear extinction or scattering measurements.[11,17−22,24,25,27,30,35] In order to contrast these measurements to an approach based on the real particle absorption, we initially determined the extinction spectra of our samples as a function of ω_p. Extinction E is a measure for the fraction of a light beam not transmitted through a sample. It can be measured as $E = 1 - T$, where the transmission coefficient $T = I_t/I_i$ is the ratio of transmitted versus incident intensity. The extinction spectra recorded for both particle types exhibit a dip at the spectral position of the *J*-aggregate absorption (Figure 1c and d). The rod spectra show an additional shoulder on the blue spectral side originating from the transverse localized surface plasmon resonance. However, as it does not have a significant spectral overlap with the exciton absorption, it is only weakly coupled to the exciton and of no interest for the following discussion. Upon covering the hybrid particles with polymer layers, the spectral weight of the coupled extinction spectra shifts to longer wavelengths. This is a consequence of the changing ω_p, which leads to shifts of $\omega_\pm$ according to eq 1. For each cover thickness, the plasmon resonance $\omega_{p,b}$ was measured after photobleaching the TDBC in the same samples that were used to obtain the coupled spectra. Compared to measuring ω_p on separate reference samples, the advantage of this procedure is that inhomogeneities in the sample structure are reflected in the measurements of both $\omega_\pm$ and $\omega_{p,b}$ likewise. The maximum cover thickness was chosen such that the plasmon resonance clearly shifted across the exciton resonance.

Figure 1e and f present the energies $\hbar\omega_\pm$ describing the maximum positions of the extinction peaks versus the resonance energy $\hbar\omega_{p,b}$ of the plasmon. This yields a characteristic anticrossing curve typical of two strongly coupled oscillators. The coupling frequency $\Omega = 2g$ corresponds to the minimum distance between the branches. The horizontal dashed line indicates the exciton energy $\hbar\omega_{ex}$, which is independent of the cover layer thickness and represents an asymptotic solution of eq 1 for $\omega_p - \omega_{ex} \gg \Omega$. The tilted dashed line describes the asymptote corresponding to ω_p, which is slightly shifted with respect to $\omega_{p,b}$. This is because the chemical changes associated with TDBC photobleaching alter the background refractive index of the layer. The resulting change of the dye-shell permittivity in turn shifts the plasmon resonance.[36] Taking into account this shift by assuming $\omega_p \approx \omega_{p,b} - 40$ meV, eq 1 for the undamped coupled oscillator yields an excellent fit to the data in Figure 1e,f, and a splitting of 150 meV for rods and of 102 meV for spheres can be extracted. A straightforward method to deduce the coupling regime would be to compare the splitting to the line widths of the uncoupled spectra. However, as no information concerning the inhomogeneous broadening is available, the true uncoupled line widths cannot be measured. One might therefore be tempted to ignore the line width argument for hybrid nanoparticle ensembles and to conclude from the pure presence of an anticrossing relation the presence of strong coupling.[17,20,21,27] But, a spectral splitting and a corresponding anticrossing relation can also be observed in the weakly coupled regime as a result of Fano interference.[37,38] In many cases, the difference between the presence of a Fano antiresonance and of true strong coupling

DOI: 10.1021/acsphotonics.7b00113
ACS Photonics 2017, 4, 1669−1676

can be very well observed in the absorption spectrum of the particles. The latter considers only the dissipation of energy in the particle, while the extinction spectra also contain information about the light scattered by the particles.[39] These combined spectra are difficult to interpret if the scattering and absorption fractions differ considerably from each other, which can be the case for nanoparticles.[23,33,39] In the following, we therefore discuss the coupling regime on the basis of the disentangled absorption and scattering spectra of the particles.

■ ABSORPTION AND SCATTERING

Absorption and scattering spectra of nanoparticles can be obtained using a spectrometer with an integrating sphere, which captures the total light scattered by the particles.[36] Two measurements are necessary for each spectrum, as illustrated in Figure 2. To obtain the absorption spectrum, the sum of the

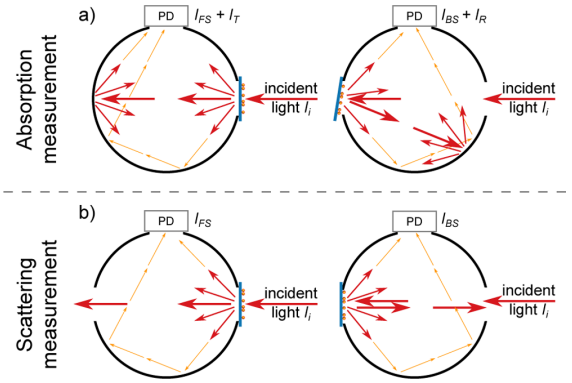

Figure 2. Configurations for measuring the absorption (a) and scattering (b) of a sample using a spectrometer with an integrating sphere.

forward scattered and directly transmitted light intensity $I_{FS} + I_T$ is captured in a first measurement and the backscattered and reflected light $I_{BS} + I_R$ in a second. The absorption is then $A = 1 - (I_{FS} + I_T + I_{BS} + I_R)/I_i$, where I_i denotes the intensity of the incoming light. Similarly, the scattering spectrum S is determined by measuring the forward and backward scattered light fraction without the transmitted beam and without specular reflection: $S = (I_{FS} + I_{BS})/I_i$. We measured absorption and scattering spectra for the same set of samples for which the extinction spectra were obtained.

In Figure 3, we show the absorption $A(\hbar\omega_{pm})$ and scattering $S(\hbar\omega_{pm})$ spectra of TDBC-coated gold nanospheres and -rods with increasing polymer cover thicknesses in a 3D color plot, where the horizontal axis labels the increasing polymer cover thickness via the plasmon resonance position $\omega_{p,b}$. Note that especially for large particles the absorption and scattering maxima are shifted due to retardation effects.[33,39] Only in the 3D plots of the rods' scattering spectra we have subtracted contributions from clustered particles at near-infrared energies. These contributions appeared for both coupled and bleached samples and could be quantified by fitting the bleached samples' spectra.

The scattering spectra for both particle types are comparable to the extinction spectra (spheres Figure 3a, rods Figure 3e). They show a spectral dip at the exciton resonance wavelength, while the spectral weights shift to lower energies for thicker

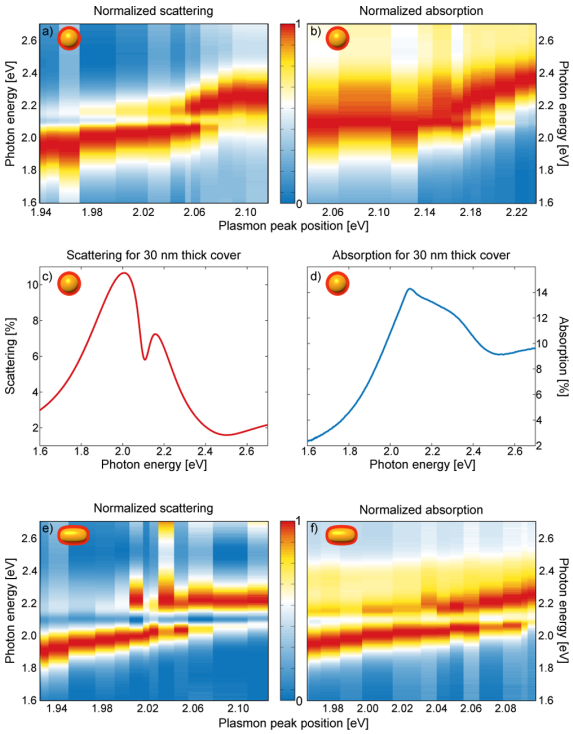

Figure 3. Scattering and absorption spectra of TDBC-coated gold nanospheres (top row) and gold nanorods (bottom row) covered with polyelectrolyte layers of various thickness. For the spheres only the scattering (a) shows an anticrossing, whereas in absorption (b) the two branches do cross, indicating that the system is not strongly coupled. The situation is exemplified for the sample with 30 nm cover thickness for scattering (c) and absorption (d). For the rods both scattering (e) and absorption (f) show an anticrossing, indicating that this system indeed is strongly coupled.

polymer covers, caused by a shift of the plasmon resonance. The rods exhibit somewhat smaller line widths and a deeper modulation than the spheres, which is reflected in the wider splitting of 173 meV for the rods compared to 140 meV for the spheres. While the scattering spectra of both particles are qualitatively similar, the absorption spectra differ markedly. For the rods, also the absorption spectrum shows a behavior similar to the extinction, a dip, and a corresponding anticrossing with a splitting of 155 meV, as expected for a strongly coupled system. In contrast, the absorption spectrum for the spheres does not show a perceptible dip, but rather resembles a superposition of the separated exciton and plasmon absorption spectra, a behavior expected in the limit of weak coupling. To clarify this behavior, Figure 3c and d present the scattering and absorption spectra for the spheres with a 30 nm thick polyelectrolyte cover.

The differences between absorption and scattering spectra can be understood by considering the different contributions of core and shell to scattering and absorption spectra. Scattering is in principle a collective property of the entire hybrid particle. However, as the scattering cross-section of the plasmonic core vastly exceeds that of the molecular shell, the contribution of the latter can be neglected in the total scattering[23,40] (see also the Supporting Information). The absorption spectrum, on the other hand, presents the total energy dissipation in all parts of the particle. The situation in this case is different from

DOI: 10.1021/acsphotonics.7b00113
ACS Photonics 2017, 4, 1669−1676

scattering, because even if the direct interaction of the shell with the incoming light is neglected, a large amount of light energy is scattered from the plasmonic core to the weakly absorbing excitonic shell by near-field coupling. This antenna effect of plasmonic particles is well known and is, for example, the mechanism underlying SERS.[1] Thus, a considerable fraction of the incoming light is transferred to and dissipated by the molecular shell. In other words, the experimental scattering spectrum illustrates the behavior of only the plasmonic response, while the absorption spectrum includes the behavior of both plasmonic dissipation and dissipation in the TDBC shell.[23,41]

COUPLED OSCILLATOR MODEL

The observed experimental spectra can be qualitatively explained by means of a coupled oscillator model, in which two classical oscillators are coupled by a linear coupling constant.[42] Of course the real system is more complex, as for a full description the particle geometry and corresponding field symmetry have to be taken into account. Numerical simulations considering the full electromagnetic solution were performed, e.g., by Antosiewicz et al.[23] The oscillator model, on the other hand, allows a deeper conceptual insight than numerical simulations, as it provides direct access to the coupling strength parameter. At the same time, it retains the ability to qualitatively reproduce the behavior of the coupled system,[30,41−44] as long as only dipole coupling is involved and no quantum mechanical effects have to be taken into account.

The coupled spring pendulum (Figure 4a) presents the conceptually simplest mechanical equivalent to a system of coupled dipoles.[37,38] Two pendula, X and Y, with resonance frequencies ω_i, masses m_i, and dampings γ_i, represent the core and shell resonances. The coupling is quantified by G, representing a third spring between both oscillators. For simplicity, we discuss the case for which the oscillators are in resonance ($\omega_X = \omega_Y = \omega_0$) and have the same masses ($m_X = m_Y = m$). The higher damping of the plasmon compared to the excitons is taken into account by a 5 times higher damping γ_X for X than the damping γ_Y for Y. The system is driven by an external force F with a frequency ω. As discussed earlier, we assume that only the oscillator X appreciably couples to the light field. Therefore, only X is excited by F. Mathematically, the coupled oscillators are described by their equations of motion:

$$\ddot{x} + \gamma_X\dot{x} + {\omega_0}^2 x + Gy = \frac{F}{m}e^{-i\omega t}$$
$$\ddot{y} + \gamma_Y\dot{y} + {\omega_0}^2 y + Gx = 0 \quad (3)$$

Here x is the deflection of X and y the deflection of Y. The Fourier−Ansatz $x(t) = A_X\, e^{-i\omega t}$ and $y(t) = A_Y\, e^{-i\omega t}$ and inversion of the resulting system of equations give the corresponding complex amplitudes for both oscillators:

$$A_X = \frac{{\omega_0}^2 - \omega^2 - i\gamma_Y\omega}{({\omega_0}^2 - \omega^2 - i\gamma_X\omega)({\omega_0}^2 - \omega^2 - i\gamma_Y\omega) - G^2}\frac{F}{m} \quad (4)$$

and

$$A_y = \frac{G}{({\omega_0}^2 - \omega^2 - i\gamma_X\omega)({\omega_0}^2 - \omega^2 - i\gamma_Y\omega) - G^2}\frac{F}{m} \quad (5)$$

Absorption and scattering can then be calculated from the complex oscillator amplitudes. The absorption P_{loss} for oscillator X is given by the loss due to friction:[45]

$$\overline{P_{loss}} = \overline{-m\gamma_X\dot{x}^2} = -\frac{m\gamma_X}{2}(\omega|A_x|)^2 \quad (6)$$

The power, P_{scatt}, scattered by X, assuming the oscillators are of dipolar character, is proportional to[33]

$$P_{scatt} \propto \omega^4|A_X|^2 \quad (7)$$

Analogous formulas hold for oscillator Y. As both quantities are proportional to the absolute square of the oscillator amplitudes, we will discuss only the latter in the remaining argument.

Figure 4b and c illustrate the absolute square of the oscillator amplitudes for X and Y for different coupling strengths. As eqs 4 and 5 have the same denominators, one might expect similar resonance behavior for both oscillators and in particular a transistion from one to two resonances at the same coupling strength. However, Figure 4b and c show that this is clearly not the case. On the contrary, the driven oscillator X shows a minimum at ω_0 as soon as the coupling is turned on, while the resonance for oscillator Y splits in two only for coupling higher than approximately $(\gamma_X + \gamma_Y)/2$, indicated by a dashed white line. The latter is a criterium frequently applied in the literature to determine the strong coupling regime.[46−49] Indeed, the graphs in Figure 4 show that the transition to the strong coupling regimes does not follow a sharp threshold behavior at this criterium. Rather the change between the coupling regimes occurs smoothly with increasing coupling strength.

The reason for the different behavior of both oscillators is founded in the numerator of the driven oscillator X, which has a dependence on ω that causes a minimum at $\omega = \omega_0$, as soon as

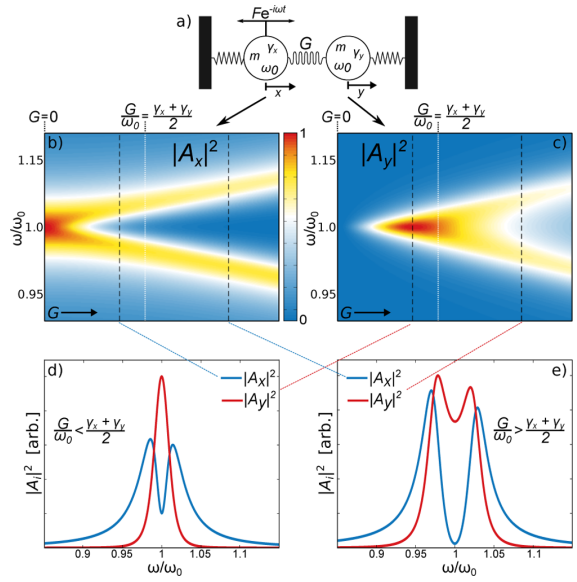

Figure 4. Sketch of two coupled oscillators (a) and the respective normalized absolute squares of the oscillator amplitudes A_X (b) and A_Y (c) for increasing coupling strengths. The white dashed line marks the limit of strong coupling. Cross-sections along the black dotted lines are shown in the lower panels to exemplify the situation for weak (d) and strong (e) coupling.

DOI: 10.1021/acsphotonics.7b00113
ACS Photonics 2017, 4, 1669−1676

$G > 0$. While the presence of this minimum erroneously could be interpreted as the occurrence of new resonances, it rather presents an antiresonance caused by a Fano-like interference. The second oscillator, on the other hand, has a constant numerator, implying that no antiresonance is present. Thus, a splitting of this oscillator corresponds indeed to the presence of strong coupling. The different behavior of the two oscillators is once more illustrated in Figure 4d and e. Above the strong coupling condition both oscillators' amplitude spectra show two resonances, while below it Y has only one resonance.

The origin of the spectral splitting can be understood more intuitively by considering the excitation transfer in the time domain.[38,50] Let us consider the situation where X is excited at its resonance frequency ω_0: Due to the oscillator coupling, the motion of X acts as an excitation force on Y. As the oscillators have the same (individual) resonance frequencies, a phase shift of $\pi/2$ occurs between the oscillation of X and Y. The coupling however works in both directions; hence the oscillator X experiences also a feedback from Y. Since for Y the coupling is stronger than all other decay channels, represented by γ_Y, the main part of the energy is transferred back to the first oscillator X. The respective periodic force exerted by oscillator Y on oscillator X again has a phase jump of $\pi/2$. Thus, the total phase difference between the oscillation on X induced by the external force and the feedback from oscillator Y is exactly π. In other words, two out-of-phase oscillatory forces, which have opposite directions, act on oscillator X. This reduces the total oscillation amplitude of X to values below those of the uncoupled oscillator, and possibly even to a complete suppression of the oscillation at this frequency. As a result, a dip occurs in the amplitude spectrum of X. This effect is commonly known as Fano interference and occurs in the weak-coupling regime already. The only prerequisite is that only one oscillator is driven.

For the strong-coupling regime to occur, a second feedback, this time from X to Y, has to be possible. This means that the transfer from X to Y has to be faster than any other decay channel. In this case, the two force components exerted from X to Y have a phase shift of π and cancel each other out, such that no energy is transferred to Y at all. Thus, in the strong-coupling regime at least one oscillation period relative to both oscillators has to be completed before the dissipation essentially destroys the feedback.

The simplified coupled oscillator model discussed above is not suitable to quantitatively reproduce the experimental spectra we obtained for hybrid nanoparticles. However, Antosiewicz et al. obtained analogous results from numerical simulations on hybrid exciton−plasmon nanospheres. Their simulations showed that a double resonance in the absorption spectra of core and shell is a necessary condition for strong coupling, which is consistent with the necessity for a splitting of both oscillators to obtain strong coupling in the coupled oscillator model. This similarity of the numerical results to those discussed for the coupled oscillator model clearly shows that the latter can be used to qualitatively understand the observed experimental spectra.[23]

When comparing the oscillator amplitude functions to the experimental spectra, one should keep in mind that the scattering spectrum contains contributions only from the plasmon, while the absorption has contribution from both. In other words, the scattering spectrum corresponds to the amplitude spectrum of the driven oscillator X. It therefore shows an antiresonance as soon as a coupling between exciton and plasmon exists. Consequently, both particle types show a double-peaked scattering spectrum. The absorption, on the other hand, corresponds to a combination of both oscillators' amplitudes. In the case of the spheres, by comparing the form of the absorption spectrum to the oscillator amplitudes, it becomes rather clear that the excitonic contribution has only a single resonance, and thus the particles are in the weak-coupling regime.

The previous insights also explain the differences in the splitting values deduced from extinction, scattering, and absorption for each particle type. Since the splitting in the core contribution is always wider than that in the shell, the splitting of the scattering is expected to be wider than that of the absorption. Clearly this is the case for the spheres where the absorption does not show a splitting at all. But also in case of the rods the splitting of the scattering resonance is wider than the splitting of the corresponding absorption (173 meV compared to 155 meV). However, here both splitting values are comparably large. The extinction as a sum of absorption and scattering is expected to have a splitting value between those of scattering and absorption. This is indeed the case for the spheres where both scattering and absorption contribute equally strong to the extinction. For the rods, in contrast, the extinction is dominated by the absorption. Thus, also the splitting value is on the order of that of the absorption. In fact it is even slightly smaller but within a range of potential measurement inaccuracies. It should be clear from this discussion that the extinction spectra are not always the best choice for discussing the coupling regime or strength.

CONCLUSIONS

In conclusion, we presented an experimental assessment of the coupling regimes for exciton−plasmon hybrid nanoparticles and discussed the common experimental pitfalls in terms of both the correct use of experimental spectra and the correct method of obtaining an anticrossing relation. We discussed the significance of the different experimental spectra by comparison to a coupled harmonic oscillator model. We exemplified that absorption spectra can reveal the difference between the presence of a Fano antiresonance and the presence of two resonances in a case where extinction spectra suggest wrong conclusions. Thus, in ambiguous situations, in which the splitting of the extinction is similar to or smaller than the line width of the unmodulated plasmon peak, only an absorption spectroscopy that accounts for the scattering appropriately can conclusively rule out Fano effects. We reported an approach for identifying the coupling strength by fine-tuning the resonances of hybrid exciton−plasmon particles via layer-by-layer deposition of polyelectrolytes. We selected two similar nanoparticle systems, TDBC-coated hybrid nanospheres and -rods, which both exhibit extinction spectra with a pronounced dip and an anticrossing behavior. Careful distinction of transmission, reflection, and scattering allows for measuring the pure absorption, which revealed that indeed in the sphere-like particles' plasmon resonance was only weakly coupled to the excitons. To understand the physical mechanism for this behavior we discussed the analog of a classical coupled oscillator model, where only one oscillator is directly excited by the driving light field.The model clarifies that the coupling induces a feedback between the two oscillators. This leads to a dip in the absorption spectrum, only if the excitation can oscillate at least two times forth and back between the driven and the dark oscillator, before the phase information is lost by

DOI: 10.1021/acsphotonics.7b00113
ACS Photonics 2017, 4, 1669−1676

ACS Photonics Article

dissipation. In contrast, the scattering spectrum of hybrid particles is dominated by the plasmon contribution, and the negative feedback already shows up for a weak coupling that transfers the energy to the dark oscillator and back once. We expect that these results will facilitate the further development of strongly coupled plasmon−exciton hybrid nanoparticles by assisting the community to assess respective coupling regimes.

METHODS

TDBC was purchased from FEW Chemicals, the gold nanospheres (diameter 100 nm, ligand citrate), polyallylamine hydrochloride, poly(sodium 4-styrenesulfonate), poly(ethylenimine), and Tween-20 were purchased from Sigma-Aldrich, and gold nanorods (res. 25-600, ligand citrate) came from Nanopartz.

Coating of Nanoparticles with TDBC. The fabrication process of TDBC-coated nanoparticles mainly followed the approach by Lekeufack et al.;[18] however to prevent the formation of clusters, an intermediate coating with a nonionic surfactant was established.[51] The TDBC was dissolved in aqueous NaOH solution ($c_{NaOH} = 10^{-5}$ mol/L) to obtain a concentration of ca. $c_{dye} \approx 1$ mmol/L. The mixture was stirred for 5 min and placed in an ultrasonic bath for 15 min.

The gold nanoparticles had a negative surface charge. To prevent clustering with positively surface charged TDBC-coated particles, 1 mL of particle solution was mixed with 20 μL of the nonionic surfactant Tween-20 and left to rest for 2 h. This mixture was then added to the TDBC solution. The ratio between particle solution and TDBC solution was 1:1. After an ultrasonic bath with a duration of 7 min the mixture was stored for 48 h.

After the resting time the solutions were centrifuged twice at 3000 rpm for 30 min (rods) or 4000 rpm for 20 min (spheres). After the second centrifugation and removal of the excess, particles were redissolved in water: rods in 0.7 times the excess volume and spheres in 0.25 times the excess volume.

Deposition of Particles on Substrate. For functionalization of substrates and the creation of polyelectrolyte layers polyethylenimine (PEI, cationic), poly(sodium 4-styrenesulfonate) (PSS, anionic), and polyallylamine hydrochloride (PAH, cationic) were used. The polymers were dissolved in a NaCl solution with a polymer concentration of 1 wt % (PEI) or 0.1 wt % (PSS, PAH) and a salt concentration of 0.7 mol/L. Glass substrates were cleaned in an ultrasonic methanol bath for 15 min and subsequently washed in an ultrasonic water bath for 15 min. They were then funcionalized by spin coating one layer of PEI, followed by a layer of PSS. To create a homogeneous monolayer, 5−7 drops of a polymer solution were deposited on the substrate spinning at a rotation speed of 3000 rpm and after a few seconds washed way with 5−7 drops of water. Subsequently 350 μL of TDBC-nanoparticles were deposited on the substrate. After an adsorption time of 4 h for spheres and 12 h for rods, excess particles were rinsed away with water and the desired amount of alternating layers of PSS and PAH (starting with PSS) was spin coated on top.

Photobleaching of TDBC. TDBC was photobleached with a continuous-wave laser working at 532 nm at 10 W. The laser beam was widened to an area of approximately 1 cm^2 to photobleach one whole sample simultaneously and not melt the gold particles. The bleaching time was 8 h.

Measurements. Absorption and scattering spectra were recorded in a Cary 5000 spectrometer; extinction measurements were executed in a Cary 5e spectrometer.

ASSOCIATED CONTENT

Supporting Information

The Supporting Information is available free of charge on the ACS Publications website at DOI: 10.1021/acsphotonics.7b00113.

Mie simulations of cross-sections of uncoupled particles and TDBC shells (PDF)

AUTHOR INFORMATION

Corresponding Author

*E-mail: koopman@uni-potsdam.de. Phone: +49 (0)331 977 5723. Fax: +49 (0)331 977 5493.

ORCID

Wouter Koopman: 0000-0001-5402-345X

Matias Bargheer: 0000-0002-0952-6602

Notes

The authors declare no competing financial interest.

ACKNOWLEDGMENTS

F.S. acknowledges financial support by the DFG via the graduate school SALSA.

REFERENCES

(1) Stiles, P. L.; Dieringer, J. A.; Shah, N. C.; van Duyne, R. P. Surface-enhanced Raman spectroscopy. *Annu. Rev. Anal. Chem.* **2008**, *1*, 601−626.

(2) Kinkhabwala, A.; Yu, Z.; Fan, S.; Avlasevich, Y.; Müllen, K.; Moerner, W. E. Large single-molecule fluorescence enhancements produced by a bowtie nanoantenna. *Nat. Photonics* **2009**, *3*, 654−657.

(3) Neubrech, F.; Pucci, A.; Cornelius, T. W.; Karim, S.; Garcia-Etxarri, A.; Aizpurua, J. Resonant plasmonic and vibrational coupling in a tailored nanoantenna for infrared detection. *Phys. Rev. Lett.* **2008**, *101*, 157403.

(4) Adato, R.; Yanik, A. A.; Amsden, J. J.; Kaplan, D. L.; Omenetto, F. G.; Hong, M. K.; Erramilli, S.; Altug, H. Ultra-sensitive vibrational spectroscopy of protein monolayers with plasmonic nanoantenna arrays. *Proc. Natl. Acad. Sci. U. S. A.* **2009**, *106*, 19227−19232.

(5) Qi, J.; Dang, X.; Hammond, P. T.; Belcher, A. M. Highly efficient plasmon-enhanced dye-sensitized solar cells through metal@oxide core-shell nanostructure. *ACS Nano* **2011**, *5*, 7108−7116.

(6) Noginov, M. A.; Zhu, G.; Belgrave, A. M.; Bakker, R.; Shalaev, V. M.; Narimanov, E. E.; Stout, S.; Herz, E.; Suteewong, T.; Wiesner, U. Demonstration of a spaser-based nanolaser. *Nature* **2009**, *460*, 1110−1112.

(7) Vasa, P.; Wang, W.; Pomraenke, R.; Lammers, M.; Maiuri, M.; Manzoni, C.; Cerullo, G.; Lienau, C. Real-time observation of ultrafast Rabi oscillations between excitons and plasmons in metal nanostructures with J-aggregates. *Nat. Photonics* **2013**, *7*, 128−132.

(8) Törmä, P.; Barnes, W. L. Strong coupling between surface plasmon polaritons and emitters: a review. *Rep. Prog. Phys.* **2015**, *78*, 13901.

(9) Reithmaier, J. P.; Sek, G.; Loffler, A.; Hofmann, C.; Kuhn, S.; Reitzenstein, S.; Keldysh, L. V.; Kulakovskii, V. D.; Reinecke, T. L.; Forchel, A. Strong coupling in a single quantum dot-semiconductor microcavity system. *Nature* **2004**, *432*, 197−200.

(10) Yoshie, T.; Scherer, A.; Hendrickson, J.; Khitrova, G.; Gibbs, H. M.; Rupper, G.; Ell, C.; Shchekin, O. B.; Deppe, D. G. Vacuum Rabi splitting with a single quantum dot in a photonic crystal nanocavity. *Nature* **2004**, *432*, 200−203.

(11) Zengin, G.; Wersäll, M.; Nilsson, S.; Antosiewicz, T. J.; Käll, M.; Shegai, T. Realizing Strong Light-Matter Interactions between Single-Nanoparticle Plasmons and Molecular Excitons at Ambient Conditions. *Phys. Rev. Lett.* **2015**, *114*, 157401.

DOI: 10.1021/acsphotonics.7b00113
ACS Photonics 2017, 4, 1669−1676

(12) Rudin, S.; Reinecke, T. L. Oscillator model for vacuum Rabi splitting in microcavities. *Phys. Rev. B: Condens. Matter Mater. Phys.* **1999**, *59*, 10227−10233.
(13) Vasa, P.; Pomraenke, R.; Cirmi, G.; de Re, E.; Wang, W.; Schwieger, S.; Leipold, D.; Runge, E.; Cerullo, G.; Lienau, C. Ultrafast Manipulation of Strong Coupling in Metal−Molecular Aggregate Hybrid Nanostructures. *ACS Nano* **2010**, *4*, 7559−7565.
(14) Hutchison, J. A.; Schwartz, T.; Genet, C.; Devaux, E.; Ebbesen, T. W. Modifying Chemical Landscapes by Coupling to Vacuum Fields. *Angew. Chem., Int. Ed.* **2012**, *51*, 1592−1596.
(15) Hutchison, J. A.; Liscio, A.; Schwartz, T.; Canaguier-Durand, A.; Genet, C.; Palermo, V.; Samorì, P.; Ebbesen, T. W. Tuning the Work-Function Via Strong Coupling. *Adv. Mater.* **2013**, *25*, 2481−2485.
(16) Imamoğlu, A.; Awschalom, D. D.; Burkard, G.; DiVincenzo, D. P.; Loss, D.; Sherwin, M.; Small, A. Quantum Information Processing Using Quantum Dot Spins and Cavity QED. *Phys. Rev. Lett.* **1999**, *83*, 4204−4207.
(17) Fofang, N. T.; Park, T.-H.; Neumann, O.; Mirin, N. A.; Nordlander, P.; Halas, N. J. Plexcitonic Nanoparticles: Plasmon−Exciton Coupling in Nanoshell−J-Aggregate Complexes. *Nano Lett.* **2008**, *8*, 3481−3487.
(18) Djoumessi Lekeufack, D.; Brioude, A.; Coleman, A. W.; Miele, P.; Bellessa, J.; de Zeng, L.; Stadelmann, P. Core-shell gold J-aggregate nanoparticles for highly efficient strong coupling applications. *Appl. Phys. Lett.* **2010**, *96*, 253107.
(19) Uwada, T.; Toyota, R.; Masuhara, H.; Asahi, T. Single Particle Spectroscopic Investigation on the Interaction between Exciton Transition of Cyanine Dye J-Aggregates and Localized Surface Plasmon Polarization of Gold Nanoparticles. *J. Phys. Chem. C* **2007**, *111*, 1549−1552.
(20) Balci, S.; Kocabas, C.; Küçüköz, B.; Karatay, A.; Akhüseyin, E.; Gul Yaglioglu, H.; Elmali, A. Probing ultrafast energy transfer between excitons and plasmons in the ultrastrong coupling regime. *Appl. Phys. Lett.* **2014**, *105*, 51105.
(21) Ni, W.; Yang, Z.; Chen, H.; Li, L.; Wang, J. Coupling between molecular and plasmonic resonances in freestanding dye-gold nanorod hybrid nanostructures. *J. Am. Chem. Soc.* **2008**, *130*, 6692−6693.
(22) Zengin, G.; Gschneidtner, T.; Verre, R.; Shao, L.; Antosiewicz, T. J.; Moth-Poulsen, K.; Käll, M.; Shegai, T. Evaluating Conditions for Strong Coupling between Nanoparticle Plasmons and Organic Dyes Using Scattering and Absorption Spectroscopy. *J. Phys. Chem. C* **2016**, *120*, 20588−20596.
(23) Antosiewicz, T. J.; Apell, S. P.; Shegai, T. Plasmon-Exciton Interactions in a Core-Shell Geometry: From Enhanced Absorption to Strong Coupling. *ACS Photonics* **2014**, *1*, 454−463.
(24) Fofang, N. T.; Grady, N. K.; Fan, Z.; Govorov, A. O.; Halas, N. J. Plexciton Dynamics: Exciton−Plasmon Coupling in a J-Aggregate−Au Nanoshell Complex Provides a Mechanism for Nonlinearity. *Nano Lett.* **2011**, *11*, 1556−1560.
(25) Melnikau, D.; Esteban, R.; Savateeva, D.; Sánchez-Iglesias, A.; Grzelczak, M.; Schmidt, M. K.; Liz-Marzán, L. M.; Aizpurua, J.; Rakovich, Y. P. Rabi Splitting in Photoluminescence Spectra of Hybrid Systems of Gold Nanorods and J-Aggregates. *J. Phys. Chem. Lett.* **2016**, *7*, 354−362.
(26) Faucheaux, J. A.; Fu, J.; Jain, P. K. Unified Theoretical Framework for Realizing Diverse Regimes of Strong Coupling between Plasmons and Electronic Transitions. *J. Phys. Chem. C* **2014**, *118*, 2710−2717.
(27) Cade, N. I.; Ritman-Meer, T.; Richards, D. Strong coupling of localized plasmons and molecular excitons in nanostructured silver films. *Phys. Rev. B: Condens. Matter Mater. Phys.* **2009**, *79*, 241404.
(28) Mitzscherling, S.; Cui, Q.; Koopman, W.; Bargheer, M. Dielectric function of two-phase colloid-polymer nanocomposite. *Phys. Chem. Chem. Phys.* **2015**, *17*, 29465−29474.
(29) Wersäll, M.; Cuadra, J.; Antosiewicz, T. J.; Balci, S.; Shegai, T. Observation of Mode Splitting in Photoluminescence of Individual Plasmonic Nanoparticles Strongly Coupled to Molecular Excitons. *Nano Lett.* **2017**, *17*, 551−558.
(30) Zengin, G.; Johansson, G.; Johansson, P.; Antosiewicz, T. J.; Käll, M.; Shegai, T. Approaching the strong coupling limit in single plasmonic nanorods interacting with J-aggregates. *Sci. Rep.* **2013**, *3*, 3074.
(31) Kobayashi, T. *J-aggregates*; World Scientific, 2012; Vol. *2*.
(32) Novotny, L. Strong coupling, energy splitting, and level crossings: A classical perspective. *Am. J. Phys.* **2010**, *78*, 1199.
(33) Bohren, C. F.; Huffman, D. R. *Absorption and Scattering of Light by Small Particles*; Wiley-VCH Verlag GmbH: Weinheim, Germany, 1998.
(34) Kiel, M.; Klötzer, M.; Mitzscherling, S.; Bargheer, M. Measuring the range of plasmonic interaction. *Langmuir* **2012**, *28*, 4800−4804.
(35) DeLacy, B. G.; Qiu, W.; Soljačić, M.; Hsu, C. W.; Miller, O. D.; Johnson, S. G.; Joannopoulos, J. D. Layer-by-layer self-assembly of plexcitonic nanoparticles. *Opt. Express* **2013**, *21*, 19103−19112.
(36) Darby, B. L.; Auguié, B.; Meyer, M.; Pantoja, A. E.; Le Ru, E. C. Modified optical absorption of molecules on metallic nanoparticles at sub-monolayer coverage. *Nat. Photonics* **2016**, *10*, 40−45.
(37) Joe, Y. S.; Satanin, A. M.; Kim, C. S. Classical analogy of Fano resonances. *Phys. Scr.* **2006**, *74*, 259.
(38) Miroshnichenko, A. E.; Flach, S.; Kivshar, Y. S. Fano resonances in nanoscale structures. *Rev. Mod. Phys.* **2010**, *82*, 2257.
(39) Quinten, M. *Optical Properties of Nanoparticle Systems*; Wiley-VCH Verlag GmbH & Co. KGaA: Weinheim, Germany, 2011; Vol. *121*.
(40) Jain, P. K.; Lee, K. S.; El-Sayed, I. H.; El-Sayed, M. a. Calculated absorption and scattering properties of gold nanoparticles of different size, shape, and composition: applications in biological imaging and biomedicine. *J. Phys. Chem. B* **2006**, *110*, 7238−7248.
(41) Lovera, A.; Gallinet, B.; Nordlander, P.; Martin, O. J. Mechanisms of Fano Resonances in Coupled Plasmonic Systems. *ACS Nano* **2013**, *7*, 4527−4536.
(42) Wu, X.; Gray, S. K.; Pelton, M. Quantum-dot-induced transparency in a nanoscale plasmonic resonator. *Opt. Express* **2010**, *18*, 23633−23645.
(43) Liu, N.; Langguth, L.; Weiss, T.; Kästel, J.; Fleischhauer, M.; Pfau, T.; Giessen, H. Plasmonic analogue of electromagnetically induced transparency at the Drude damping limit. *Nat. Mater.* **2009**, *8*, 758−762.
(44) Gallinet, B.; Martin, O. J. Ab initio theory of Fano resonances in plasmonic nanostructures and metamaterials. *Phys. Rev. B: Condens. Matter Mater. Phys.* **2011**, *83*, 235427.
(45) Kats, M. A.; Yu, N.; Genevet, P.; Gaburro, Z.; Capasso, F. Effect of radiation damping on the spectral response of plasmonic components. *Opt. Express* **2011**, *19*, 21748−21753.
(46) Khitrova, G.; Gibbs, H.; Kira, M.; Koch, S. W.; Scherer, A. Vacuum Rabi splitting in semiconductors. *Nat. Phys.* **2006**, *2*, 81−90.
(47) Wang, W.; Vasa, P.; Pomraenke, R.; Vogelgesang, R.; De Sio, A.; Sommer, E.; Maiuri, M.; Manzoni, C.; Cerullo, G.; Lienau, C. Interplay between Strong Coupling and Radiative Damping of Excitons and Surface Plasmon Polaritons in Hybrid Nanostructures. *ACS Nano* **2014**, *8*, 1056−1064.
(48) Rempe, G.; Thompson, R.; Kimble, H. Cavity quantum electrodynamics with strong coupling in the optical domain. *Phys. Scr.* **1994**, *1994*, 67.
(49) Savona, V.; Andreani, L.; Schwendimann, P.; Quattropani, A. Quantum well excitons in semiconductor microcavities: Unified treatment of weak and strong coupling regimes. *Solid State Commun.* **1995**, *93*, 733−739.
(50) Yang, Z.-J. Coherent Energy Transfers between Orthogonal Radiant and Weakly Radiant Plasmonic Nanorod Resonators. *J. Phys. Chem. C* **2015**, *119*, 26079−26085.
(51) Aslan, K.; Pérez-Luna, V. H. Surface Modification of Colloidal Gold by Chemisorption of Alkanethiols in the Presence of a Nonionic Surfactant. *Langmuir* **2002**, *18*, 6059−6065.

DOI: 10.1021/acsphotonics.7b00113
ACS Photonics 2017, 4, 1669−1676

Supporting information for "Signatures of strong coupling on nanoparticles: Revealing absorption anticrossing by tuning the dielectric environment"

F. Stete,[†,‡] W. Koopman,[*,†] and M. Bargheer[†,¶]

†*Institut für Physik & Astronomie, Universität Potsdam, Karl-Liebknecht-Str. 24-25, 14476 Potsdam, Germany*

‡*Humboldt-Universität zu Berlin, School of Analytical Sciences Adlershof (SALSA), Unter den Linden 6, 10999 Berlin, Germany*

¶*Helmholtz Zentrum Berlin, Albert-Einstein-Str. 15, 12489 Berlin, Germany*

E-mail: koopman@uni-potsdam.de

Phone: +49 (0)331 977 5723. Fax: +49 (0)331 977 5493

Cross sections of uncoupled components

The aim of this supporting information is to underline the fact that the direct interaction of the dye shell with the light field can be neglected in the coupled oscillator model. For this we approximate the scattering and absorption cross sections of a pure gold particle and a dye shell. For particle dimensions far below the light's wavelength the polarisability α a spherical gold particle can be described by[1]

$$\alpha_{core} = 4\pi r^3 \frac{\epsilon_{Au} - \epsilon_{med}}{\epsilon_{Au} + 2\epsilon_{med}} \tag{1}$$

where r describes the particle radius, ϵ_{Au} the dielectric function of gold and ϵ_{med} the dielectric function of the surrounding medium.

The polarisability of a dye shell can be approximated as[1]

$$\alpha_{shell} = 4\pi r_{out}^3 \frac{(\epsilon_{dye} - \epsilon_{med})(\epsilon_{med} + 2\epsilon_{dye}) + f(\epsilon_{med} - \epsilon_{dye})(\epsilon_{med} + 2\epsilon_{dye})}{(\epsilon_{dye} + 2\epsilon_{med})(\epsilon_{med} + 2\epsilon_{dye}) + f(2\epsilon_{dye} - 2\epsilon_{med})(\epsilon_{med} - \epsilon_{dye})} \tag{2}$$

Here f is given by $f = r_{in}^3/r_{out}^3$ where r_{in} and r_{out} describe the inner and outer radius of the shell. ϵ_{dye} represents the dielectric function of the shell while ϵ_{med} describes that of the medium inside and outside of the shell. For this study we assumed a shell thickness of 2 nm

The dielectric function for gold is taken from literature[2], the dielectric function of the shell can be approximated by[3]

$$\epsilon_{dye} = \epsilon_\infty + f_0 \frac{\omega_0^2}{\omega_0^2 - \omega^2 - i\gamma_0\omega} \tag{3}$$

We assumed a relative oscillator strength of $f_0 = 0.05$, a resonance width of $\hbar\gamma_0 = 50\,\text{meV}$, and a high-frequency background constant of $\epsilon_\infty = 1.69$, which are reasonable values for realistic dye shells[3].

The cross-sections are then given by

$$\sigma_{scatt} = \frac{k^4}{6\pi}|\alpha|^2 \tag{4}$$

$$\sigma_{abs} = k\text{Im}(\alpha) \tag{5}$$

For a gold particle with a diameter of 100 nm we found a maximum scattering cross section of $2.12 \cdot 10^{-14}\,\text{m}^2$ and a maximum absorption cross section of $4.42 \cdot 10^{-14}\,\text{m}^2$. A shell with its resonance at 589 nm only has a maximum absorption of $6.56 \cdot 10^{-16}\,\text{m}^2$ and a far

only the plasmon oscillator seems as reasonable as neglecting the shell contribution to the total scattering.

References

(1) Bohren, C. F.; Huffman, D. R. *Absorption and Scattering of Light by Small Particles*; Wiley-VCH Verlag GmbH: Weinheim, Germany, 1998.

(2) Johnson, P. B.; Christy, R. W. Optical Constants of the Noble Metals. *Phys. Rev. B* **1972**, *6*, 4370–4379.

(3) Antosiewicz, T. J.; Apell, S. P.; Shegai, T. Plasmon–Exciton Interactions in a Core–Shell Geometry: From Enhanced Absorption to Strong Coupling. *ACS Photonics* **2014**, *1*, 454–463.

Article II

Size-Dependent Coupling of Hybrid Core–Shell Nanorods: Toward Single-Emitter Strong-Coupling

Felix Stete, Phillip Schoßau, Wouter Koopman, and Matias Bargheer

The Journal of Physical Chemistry C 122, 31 (2018)

THE JOURNAL OF PHYSICAL CHEMISTRY C

Article

Cite This: J. Phys. Chem. C 2018, 122, 17976−17982

pubs.acs.org/JPCC

Size-Dependent Coupling of Hybrid Core− Shell Nanorods: Toward Single-Emitter Strong-Coupling

Felix Stete,[†,‡] Phillip Schoßau,[†] Matias Bargheer,[†,§] and Wouter Koopman*[,†]

[†]Institut für Physik und Astronomie, Universität Potsdam, Karl-Liebknecht-Str. 24-25, 14476 Potsdam, Germany

[‡]School of Analytical Sciences Adlershof (SALSA), Humboldt-Universität zu Berlin, Unter den Linden 6, 10999 Berlin, Germany

[§]Helmholtz Zentrum Berlin, Albert-Einstein-Str. 15, 12489 Berlin, Germany

ABSTRACT: Owing to their ability of concentrating electromagnetic fields to subwavelength mode volumes, plasmonic nanoparticles foster extremely high light−matter coupling strengths reaching far into the strong-coupling regime of light−matter interaction. In this article, we present an experimental investigation on the dependence of coupling strength on the geometrical size of the nanoparticle. The coupling strength for differently sized hybrid plasmon−core exciton−shell nanorods was extracted from the typical resonance anticrossing of these systems, obtained by controlled modification of the environment permittivity using layer-by-layer deposition of polyelectrolytes. The observed size dependence of the coupling strength can be explained by a simple model approximating the electromagnetic mode volume by the geometrical volume of the particle. On the basis of this model, the coupling strength for particles of arbitrary size can be predicted, including the particle size necessary to support single-emitter strong coupling.

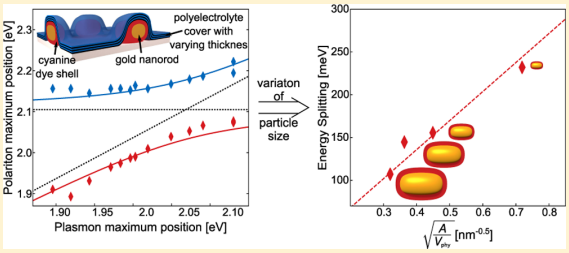

INTRODUCTION

The optical properties of an emitter are not intrinsic to the material, but depend rather strongly on its electromagnetic environment. In particular, the presence of a cavity changes the ability of absorbing or emitting light by modi fication of the local electromagnetic mode density. Depending on whether the cavity increases or decreases the emitter-resonant mode density, the emitter possesses a higher or lower probability of absorbing or emitting photons.

Modification of optical properties of an emitter in the presence of a cavity has been utilized for various applications. Examples include the Purcell enhancement of absorption and emission,[1] suppression of spontaneous emission,[2] enhancement of nonlinear optical properties,[3] surface-enhanced Raman spectroscopy,[4] or plasmon-enhanced nanolasing.[5] All of these effects have in common that they occur in the regime of weak light−matter coupling. The excitations are lost from the emitter−cavity system faster than the characteristic interaction time between the emitter and the cavity.

An even more interesting regime occurs if the coupling between the cavity and the emitter is high enough that the characteristic interaction time exceeds all other decay channels. In this strong-coupling regime, photon and matter excitations hybridize to form a new type of quasi-particle. These so-called polaritons are revealed by two new, energetically shifted, optical resonances. They possess both light- and matterlike characteristics, which make them interesting candidates for a whole range of applications. Proposals include the control of intermolecular energy transfer,[6,7] biological quantum optical systems,[8] and the coherent control of chemical reactions[9,10] to name a few. The most advanced applications envision the use of strongly coupled systems in quantum communication and quantum information processing.[11,12] Here, the controllable strong coupling of a single emitter to a cavity would, for example, allow one to map the quantum state of the localized emitter qubit to a traveling photon qubit.[12] For this type of applications, it is paramount to achieve strong coupling of a single emitter to a cavity.

The coupling strength between N emitters equally coupled to an electromagnetic cavity is quantifi ed by the coupling parameter, g, via[13,14]

$$g = \frac{1}{\hbar}\sqrt{N}\mu E_{\mathrm{vac}} \tag{1}$$

Here, μ denotes the transition-dipole moment of one emitter, whereas E_{vac} represents the vacuum electric field present in the cavity. The latter can be expressed as[15,16]

$$E_{\mathrm{vac}} = \sqrt{\frac{\hbar\omega}{2\epsilon\epsilon_0 V}} \tag{2}$$

Hence, the coupling strength is proportional to the inverse square root of the mode volume of the cavity, V.

Received: May 3, 2018
Revised: July 12, 2018
Published: July 13, 2018

DOI: 10.1021/acs.jpcc.8b04204
J. Phys. Chem. C 2018, 122, 17976−17982

In macroscopic cavities, the mode volume is rather large, resulting in low light−matter coupling strengths. To observe strong light−matter coupling in these systems, decoherence caused by cavity losses and thermal excitations must be prevented. Cavities with extremely high quality factors and the use of cryogenic temperatures of some milli-kelvins are required in this approach.[17−19] Owing to these tremendous experimental efforts, these systems cannot easily be scaled up for practical purposes. Hence, although many fundamental quantum optical experiments in the single-emitter limit have been realized with such systems,[20] they are unsuitable from an applied technological perspective.

Higher coupling strengths, and thus less strict requirements on the prevention of decoherence, can be achieved by reducing the mode volume. A reduction to the micrometer scale was realized by employing semiconductor Bragg-mirror cavities.[16,21] The possible size reduction, and therefore the achievable coupling strength, of these photonic cavities is ultimately limited by diffraction. Hence, although the very high demands on the cavity quality could be somewhat reduced this way, most semiconductor microcavities still require cryogenic temperatures to reach the strong-coupling regime.[13]

The use of plasmonic instead of photonic cavities can overcome this limitation. As plasmons effectively are a form of matter-bound electromagnetic fields, their size is not limited by the optical diffraction limit, but rather by the geometrical size of the plasmonic structure. As a result, they can concentrate optical fields to regions much smaller than the vacuum wavelength. This way, extremely high coupling strengths can be realized. Moreover, although plasmon cavities are very lossy, the strong-coupling regime can be reached—even at ambient temperatures.

In recent years, plasmon-based strong-coupling has been demonstrated for various systems.[8,22−27] Among the most promising are those based on core−shell nanoparticles, consisting of a plasmonic core and an excitonic shell.[28,29] On the one hand, these systems can easily be mass fabricated by simple wet-chemical methods.[30,31] On the other hand, their extremely small sizes, down to some nanometers, potentially allow for very high coupling strengths.

Considering these advantages of strong coupling in plasmon−exciton systems over traditional macro- and microscopic cavities, it is of no surprise that the realization of strong coupling of a single emitter to a plasmonic cavity has been a long-standing goal in the plasmonics community.[14] Recently, first claims of single-emitter strong coupling with plasmonic nanoparticles have been reported.[32,33] Both approaches to reach single-emitter strong coupling rely on the use of nanostructures with sharp edges to locally enhance the mode density. For those structures, the correct calculation of the mode volume is difficult, and both claims have been challenged on the basis of a wrong method for calculating the effective mode volume.[28] Realizing single-emitter strong coupling with geometrically much simpler gold nanorods (GNRs) would enormously simplify the interpretation of the experimental data.

For single GNRs, the mode volume can be reduced straightforward by reducing their geometrical size. Theoretical[34,35] and experimental[29,36] investigations have demonstrated the possibility of achieving strong coupling with GNRs and organic molecules. Here, we report an experimental investigation on the size dependence of the coupling strength in hybrid GNRs. We demonstrate a simple relationship between geometrical size and coupling strength experimentally and show that remarkably high coupling strengths far in the strong-coupling regime can be realized for ultrasmall particles. To our knowledge, such studies have only been conducted theoretically.[37] The lack of prior measurements on the size dependence of the coupling strength is closely related to the experimental difficulty in correctly determining the coupling strength for core−shell particles. The coupling strength can, in principle, be extracted from the energetic difference between the newly formed polaritons if the employed plasmons and excitons are resonant. However, this condition is very difficult to realize in practice. The common workaround is to tune the plasmon resonance relative to the exciton resonance and subsequently deduce the coupling strength from the resulting anticrossing relation.[38] However, the plasmon tuning is mostly realized by tuning the particle dimensions.[24,39] This way, the actual size dependence cannot be investigated; on the contrary, the size dependence even has to be neglected to deduce a constant value for the coupling.

We recently introduced a technique to reveal the anticrossing relation in core−shell systems without changing the size or shape of the particles.[36] In this technique, the plasmon resonance is tuned over the exciton resonance by controlled modification of the permittivity of the particles' environment[36] via layer-by-layer deposition of polyelectrolytes. The coupling strength is then extracted from the position of the polariton bands relative to the plasmon detuning.

In this study, we utilized this technique to compare the coupling strengths of four differently sized hybrid nanorods. The observed size dependence can be quantitatively modeled by taking into account the plasmon mode volume and the number of contributing molecules. A comparison of the coupling strength to the line width showed that the smallest particles are indeed strongly coupled. On the basis of the found relation between coupling strength and particle size, we predict that single-exciton strong coupling can be reached for nanorods with a transversal diameter around 6 nm, a realistic value for the size of GNRs.

METHODS

Hybrid core−shell nanoparticles were realized on the basis of gold nanorods (GNRs), as several reports claim strong-coupling and polariton formation for systems involving GNRs.[24,40] For investigating the size dependence, we used rods with four different transversal diameters of 10, 25, 40, and 50 nm (Nanopartz). The longitudinal length was chosen such that the aspect ratios and therefore the plasmon resonances of all rods were approximately 2 for all rods. It was specified as 19, 57, 67, and 100 nm, respectively. The rods were coated with an approximately 2 nm-thick excitonic shell consisting of a monolayer of 5,5′,6,6′-tetrachloro-1,1′-diethyl-3,3′-di(4-sulfobutyl)benzimidazolocarbocyanine (TDBC, FEW Chemicals). TDBC is a cyanine dye that is known to form J-aggregates with particularly high transition-dipole moments μ, which is favorable to reach high coupling strengths. In the rest of the article, we will refer to the different rods by the short-axis diameter of their gold core.

In the limit of low losses, the newly formed resonances of the coupled system are related to the resonances of the uncoupled exciton, ω_{ex}, and plasmon, ω_p, according to[14,41]

$$\omega_{\pm} = \frac{1}{2}(\omega_p + \omega_{ex}) \pm \sqrt{\frac{1}{4}(\omega_p - \omega_{ex})^2 + g^2} \quad (3)$$

DOI: 10.1021/acs.jpcc.8b04204
J. Phys. Chem. C 2018, 122, 17976−17982

The Journal of Physical Chemistry C Article

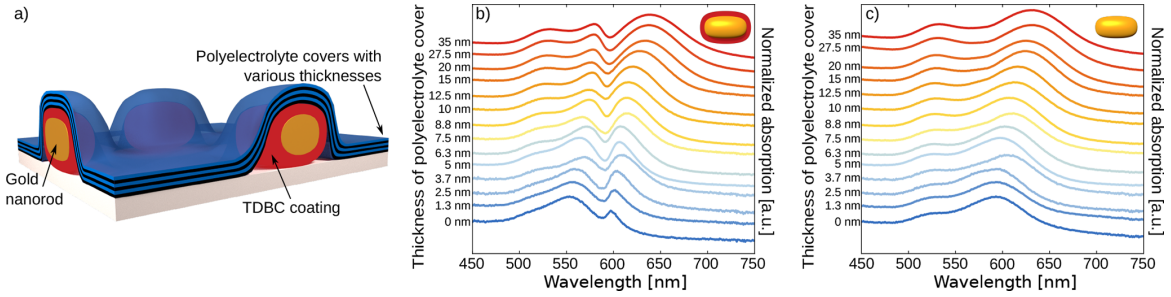

Figure 1. (a) Sketch of a typical sample. TDBC-coated gold nanoparticles are covered by polyelectrolyte layers of varying thicknesses. (b) Absorption spectra of particles with a short-axis diameter of 25 nm for various cover thicknesses. A clear splitting and a red-shift for increasing co ver thicknesses are visible. (c) Absorption spectra of the same samples after photobleaching. The splitting disappears and the resonances of the uncoupled plasmons become visible.

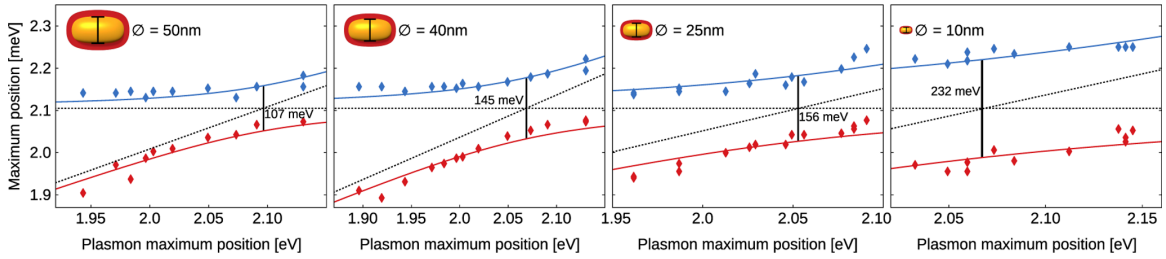

Figure 2. Absorption anticrossings for core−shell particles with short-axis diameters of 50, 40, 25, and 10 nm (from left to right). The splitting increases for decreasing particle sizes.

These polariton resonances display a characteristic anticrossing relation with a minimum separation of $\Delta = (\omega_+ - \omega_-)$ when the frequencies of the uncoupled system are resonant. The energy splitting yields in this case: $\hbar\Delta|_{\omega_p=\omega_{ex}} = 2\hbar g$. The coupling could therefore theoretically be extracted from the spectrum of a perfectly resonance-matched plasmon−exciton system. However, the exact match of ω_{ex} and ω_p is experimentally difficult to establish and verify. We tune the resonance of the uncoupled plasmon across that of the exciton by layer-by-layer deposition of polyelectrolytes.[36,42] The coupling strength is then extracted by fitting eq 3 to the measured anticrossing relation.

It should be noted that eq 3 does not take into account the damping of plasmon γ_p and exciton γ_{ex}. Including the dampings in eq 3 leads to the expression $\hbar\Delta|_{\omega_p=\omega_{ex}} = \hbar\sqrt{4g^2 - (\gamma_p - \gamma_{ex})^2}$ for the energy splitting. In principle, the additional term caused by damping lowers the spectral splitting for a given coupling strength. Thus, coupling strengths extracted by neglecting the damping present a lower limit for the actual g. We did not consider the damping term as the experimentally observed plasmon line widths are subject to inhomogeneous broadening, which leads to an overestimation of the damping frequencies and hence an overestimation of the actual g. However, one should keep in mind that the actual coupling strength is likely larger than the g discussed in the following.

We realized the tuning of the plasmon resonance by successively increasing the permittivity of the environment of the particles, ϵ_{med}, which shifts the plasmon resonance to lower energies.[42] To modify the permittivity, the particles were covered with double layers of the polyelectrolytes poly-sodium 4-styrenesulfonate and poly-allylamine hydrochloride (see Figure 1a). The plasmon resonance can then be obtained from the nanoparticle polarizability, α,

$$\alpha \propto \frac{\epsilon_{mat} - \epsilon_{med}}{\epsilon_{mat} + f\epsilon_{med}} \tag{4}$$

Here, ϵ_{mat} describes the permittivity of the particle material and f is a form factor accounting for the particle shape. The plasmon resonance occurs at wavelength λ for which the denominator becomes minimal ($\epsilon_{mat}(\lambda) = f\epsilon_{med}(\lambda)$). For each particle size, we fabricated a series of samples with various cover thicknesses. The thickness of a single cover layer is about 1.25 nm. Each additional cover layer replaces air in the direct environment, leading to an increase of ϵ_{med} that causes a red-shift of the plasmon resonance.

We determined the spectral splitting from the pure absorption spectrum. In general, the extinction spectra of nanoparticles, recorded by simple transmission measurements, contain contributions from scattering and absorption processes. The relative weight of these contributions changes with particle size. Thus, to guarantee comparability between the coupling strengths obtained from differently sized particles, the spectral splitting must be determined from either the disentangled scattering or absorption spectra and not from the extinction. Both spectra can be measured separately using a spectrometer equipped with an integrating sphere.[36] The scattering efficiency of the smallest nanoparticles in our study (10 nm core-diameter) was too low to measure the spectral splitting. Hence, we determined the coupling strength for all particle sizes from the pure absorption spectra.

As an example, we present the absorption spectra of the rods with a transversal diameter of 25 nm for different cover thicknesses in Figure 1b. A clear dip can be seen at the position of the exciton accompanied by two new resonances resulting

DOI: 10.1021/acs.jpcc.8b04204
J. Phys. Chem. C 2018, 122, 17976−17982

from a coupling between the exciton and the longitudinal plasmon mode. For thicker covers, a red-shift of the plasmon resonances occurs, as expected from eq 4. An additional peak around 520 nm marks the transversal plasmon resonance. Owing to a strong detuning between the latter and the exciton resonance, the coupling is very weak and can be neglected. We obtained the resonance frequency of the uncoupled GNRs by measuring the absorption of the same samples after photobleaching the TDBC shell by a continuous-wave laser (Figure 1c).

We determined the resonance energy from the maximum spectral positions. Before extracting the maximum position, a Savitzky–Golay filter (4th order)[43] was used to smooth the data. The resonance anticrossing (Figure 2), typical of two coupled systems,[38] results from plotting the coupled resonance positions against the uncoupled plasmon resonance positions. The measured positions of the uncoupled plasmons are slightly red-shifted with regard to the real plasmon resonances, caused by chemical changes in the photobleached TDBC shell.[36] Taking this shift into account, the coupling strength was obtained by fitting eq 3 to the data shown in Figure 2.

RESULTS

The coupled versus uncoupled resonance positions for all four particle sizes are depicted in Figure 2. The resonances, $\hbar\omega_{\pm}$, of the coupled particles are plotted against the resonances, $\hbar\omega_{p,b}$, of the bleached samples with the same cover thickness. The uncoupled exciton resonance, $\hbar\omega_{ex}$, is independent of the cover thickness. It is represented by a horizontal dashed black line in all plots. The uncoupled plasmon resonances are indicated by the diagonal dashed black lines. As expected, all particles show an anticrossing of the upper (blue) and lower (red) polariton branches. Solid lines indicate a fitting of the measured values according to eq 3.

The coupling is given by the energy splitting between the two branches, that is, $\hbar\Delta|_{\omega_p=\omega_{ex}} = 2\hbar g$. The results are presented in Table 1. The biggest particles exhibit the smallest energy splitting of 107 meV. For decreasing particle sizes, the coupling becomes stronger (145 meV for the 40 nm particles and 156 meV for the 25 nm particles) and culminates in the largest energy splitting of 232 meV for the smallest particles with a transversal diameter of 10 nm.

Table 1. Energy Splitting for the Differently Sized Rods[a]

short-axis diameter (nm)	long axis diameter (nm)	energy splitting (meV)
10	19	232 ± 8
25	57	156 ± 8
40	67	145 ± 7
50	100	107 ± 9

[a]The size variation in all dimensions is specified as 10% by the manufacturer.

DISCUSSION

The results can be explained quantitatively by a rather simple model. Changing the particles' size affects essentially two factors: the mode volume, V, and the number of emitters contributing to the coupling, N. We assume N to be proportional to the particle surface, A. This assumption is rooted in the observation that the dye forms a monolayer coating irrespective of the particle size.[30] Realistically, we expect only the emitters in the hotspots to contribute to the coupling.[44] However, as long as the fraction of emitters in the hotspots remains constant, the proportionality between N and A remains valid. An accurate description of the mode volume in nanoparticles is difficult. The mode volume is strictly defined only for closed, lossless cavities. Nanoparticles, on the contrary, are intrinsically open systems with a high degree of radiative and absorption losses in the form of scattered and absorbed light. The correct description of the mode density and volume under these circumstances is therefore a topic of ongoing research.[45,46] Fortunately, for small spherical particles with a diameter below 50 nm, the mode of a nanoparticle is dominated by the energy deposited inside the metal and hence the mode volume approximately equals its physical volume, V_{phy}.[44,47] We assume that this is also the case for small nanorods with similar dimensions and therefore $V = V_{phy}$. With these two assumptions, eqs 1 and 2 can be used to predict the size dependence of the coupling strength

$$g \propto \sqrt{\frac{A}{V_{phy}}} \tag{5}$$

Figure 3 presents a plot of the energy splittings against the square root of the surface-to-volume ratio, A/V, where we, as for the rest of this report, assumed an ellipsoidal shape for the particles. The dashed line represents the proportionality according to eq 5. Indeed, the measured values for the coupling strength agree surprisingly well with the theoretical prediction, despite the rough assumptions on the mode volume and the number of emitters. In particular, the good agreement for the largest particles is remarkable, as the approximation of the mode volume by the physical volume is assumed to break down at large sizes.[47]

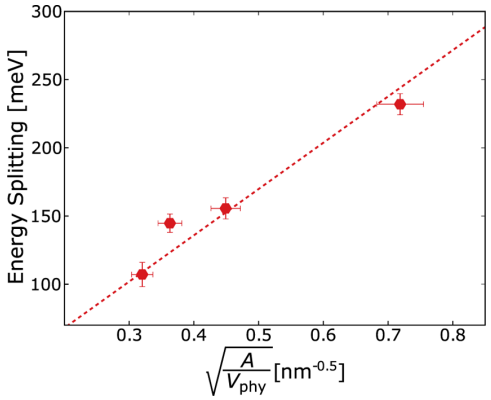

Figure 3. Coupling strength plotted against the square root of the surface-to-volume ratio (diamonds). The dashed line represents the proportionality predicted in eq 5. The close agreement to the data suggests that the equation indeed describes the correct relation between coupling strength and particle shape.

In the strong-coupling regime, energy transfer between the coupling partners is more probable than dissipation via other decay channels. This is equivalent to the requirement that the coupling strength exceeds all other decay channels.[14] The standard procedure for evaluating the coupling regime is to compare g to the full width at half maximum line widths γ_p and γ_{ex} of the uncoupled components. This approach is only strictly

DOI: 10.1021/acs.jpcc.8b04204
J. Phys. Chem. C 2018, 122, 17976−17982

valid if the observed line widths are the homogeneous line widths of plasmon and exciton. In the presence of inhomogeneous broadening, the strong-coupling regime might already be reached if g does not fulfill the criterion for strong coupling.

As a criterion for evaluating the coupling regime of the hybrid nanorods, we used $2g/\gamma = 4g/(\gamma_p + \gamma_{ex}) > 1$.[13,28] We determined γ_p for the plasmon cavities from the spectra of the bleached samples,[42,48] whereas γ_{ex} = 47 meV was determined from the J-aggregate line width in water.

The only particles that fulfill the criterion using the inhomogeneous line width and that are therefore unquestionably in the strong-coupling regime are those with a transversal diameter of 10 nm. With a plasmon line width of γ_p = 320 meV and a coupling-to-line width ratio of $2g/\gamma$ = 1.12, these particles are indeed far in the strong-coupling regime.

The 25 nm particles show an inhomogeneous plasmon line width of γ_p = 309 meV. With a resulting $2g/\gamma$ = 0.88, the particles fail to fulfill the criterion for strong coupling. However, nanoparticles tend to show a large dispersion around their nominal size, and therefore the plasmon line width is strongly inhomogeneously broadened. Hence, we can assume that also these particles are at least very close to the strong-coupling regime.

The lesson that can be learned from these measurements is that the coupling strength can be increased by simply increasing the surface-to-volume ratio of the particles. In principle, two strategies can be employed: on the one hand, the shape of nanoparticles can be altered such that the surface increases with minimal increase of volume, for example, as for nanostars or nanoflowers.[49] However, the mode volume in this case is even more complex and cannot necessarily be approximated simply by the particle volume. Moreover, increasing the surface area to increase the coupling strength at the same time increases the number of emitters. Although this might not be an issue in some cases, it is not a useful strategy for reaching single-emitter strong coupling, necessary for quantum information applications.

On the other hand, the surface-to-volume ratio can be increased by simply shrinking the particles further. This approach has the advantage that whereas the coupling strength increases, also less emitters are involved. A similar strategy of shrinking the mode volume was employed in recent claims of single-emitter strong coupling.[32,33] The basic idea in this case was to reduce the effective mode volume by strongly concentrating the electric field to sharp features of the nanostructures. This approach to reach single-emitter strong coupling has been challenged on the basis that the energy dissipated within the metal has not been considered correctly.[28] Indeed, following the work of Koenderink,[47] it can be argued that the mode volume of plasmonic nanoparticles is generally dominated by energy stored within the particle.

Our experimental data suggest that the approximation of the mode volume for small nanorods by its physical volume is correct. Determining the mode volume is therefore straightforward in this case. Using eqs 1 and 2, we can deduce the approximate amount of emitters contributing to the coupling. With a transition-dipole moment of μ = 20.5 D[23] for TDBC-J-aggregates, we determine a value of N = 6.65 for the smallest particles. With a similar calculation, we can also asses the mode volume of hybrid TDBC−GNRs necessary to support single-exciton strong coupling. If we assume a plasmon line width of γ_{pl} = 320 meV, as for the smallest of our particles, the strong-coupling criterion would require a mode (and thus physical) volume of 242 nm^3. For rods with an aspect ratio of 2:1, this translates to a transversal diameter of 6 nm.

Although this is not much smaller than the particles available in this study, several points have to be considered for the practical implementation of such a system. First, particles with less than 10 nm transversal diameter are difficult to fabricate as the common "seed-based" synthesis cannot be used for such small particles;[50] however, the plasmon damping in such particles might differ strongly from the damping in particles fabricated with traditional methods.[51] Second, at very small particle sizes, surface damping of the plasmon resonance has an increasing influence. This might prevent the system from reaching the strong-coupling limit. For spherical particles, an increase of the plasmon width is observed starting at a particle diameter of approximately 10 nm.[52] As the necessary particle length for the envisioned GNR in the longitudinal direction is about 12 nm (assuming a ratio of 2:1), surface damping might still be low enough. Finally, third, the estimation above assumes that the emitter is located at the point of the highest electric-field strength, in the case of GNRs that is at the tips of the rod. The deterministic positioning of TDBC aggregates at the tips might prove difficult. Hence, one should rely on finding suitable single particles by microscopic techniques.

Clearly, in our calculation, we employed the inhomogeneously broadened plasmon line width. The calculated particle size thus presents only a lower limit necessary to achieve single-emitter strong coupling. Thus, despite the difficulties discussed earlier, we are confident that an unambiguous realization of single-exciton strong coupling is in principle possible using the simple gold nanorods provided small enough particles are available.

CONCLUSIONS

In this article, we have experimentally investigated the dependence of the exciton−plasmon coupling strength on the geometrical size of the particle and demonstrated a simple relationship between both. We investigated dye-coated gold nanorods of four different sizes. Their coupling strengths were determined from the typical resonance anticrossing relation of coupled emitter−cavity systems. We tuned the nanoparticle-cavity resonance across the exciton resonance employing a recently introduced method based on modifying the environment permittivity via layer-by-layer deposition of polyelectrolytes. Using this method, no tuning of the particle size or shape is necessary to obtain the anticrossing relation. The maximum observed coupling strength was 235 meV, which is well above the value necessary to reach the strong-coupling regime.

The data can be explained quantitatively assuming that the mode volume is proportional to the physical volume of the particle, whereas the number of excitons involved scales with the particle surface. With these assumptions, the measured coupling strength is proportional to the square root of the surface-to-volume ratio of particles. This clear proportionality between the coupling strength and the surface-to-volume ratio of the particles shows that the coupling strength necessary to reach single-molecule strong-coupling can be achieved by reducing the particle size to GNRs with a transversal diameter of 6 nm. Thus, the facile realization of single-exciton strong-coupling using simple gold nanorods is within reach.

DOI: 10.1021/acs.jpcc.8b04204
J. Phys. Chem. C 2018, 122, 17976−17982

AUTHOR INFORMATION

Corresponding Author

*E-mail: koopman@uni-potsdam.de. Phone: +49 (0)331 977 5723. Fax: +49 (0)331 977 5493.

ORCID

Matias Bargheer: 0000-0002-0952-6602

Wouter Koopman: 0000-0001-5402-345X

Notes

The authors declare no competing financial interest.

ACKNOWLEDGMENTS

F.S. acknowledges financial support by the DFG via the graduate school SALSA.

REFERENCES

(1) Purcell, E. M. Spontaneous Emission Probabilities at Radio Frequencies. *Phys. Rev.* **1946**, *69*, 681.

(2) Yablonovitch, E. Inhibited Spontaneous Emission in Solid-State Physics and Electronics. *Phys. Rev. Lett.* **1987**, *58*, 2059−2062.

(3) Atkin, J. M.; Berweger, S.; Jones, A. C.; Raschke, M. B. Nano-Optical Imaging and Spectroscopy of Order, Phases, and Domains in Complex Solids. *Adv. Phys.* **2012**, *61*, 745−842.

(4) Stiles, P. L.; Dieringer, J. A.; Shah, N. C.; van Duyne, R. P. Surface-Enhanced Raman Spectroscopy. *Annu. Rev. Anal. Chem.* **2008**, *1*, 601−626.

(5) Noginov, M. A.; Zhu, G.; Belgrave, A. M.; Bakker, R.; Shalaev, V. M.; Narimanov, E. E.; Stout, S.; Herz, E.; Suteewong, T.; Wiesner, U. Demonstration of a Spaser-Based Nanolaser. *Nature* **2009**, *460*, 1110−1112.

(6) Rodarte, A. L.; Tao, A. R. Plasmon-Exciton Coupling between Metallic Nanoparticles and Dye Monomers. *J. Phys. Chem. C* **2017**, *121*, 3496−3502.

(7) Wang, L.; May, V. Control of Intermolecular Electronic Excitation Energy Transfer: Application of Metal Nanoparticle Plasmons. *J. Phys. Chem. C* **2017**, *121*, 13428−13433.

(8) Lishchuk, A.; Kodali, G.; Mancini, J. A.; Broadbent, M.; Darroch, B.; Mass, O. A.; Nabok, A.; Dutton, P. L.; Hunter, C. N.; Tö rmä, P.; et al. Synthetic Biological Quantum Optical System. *Nanoscale* **2018**, 13064.

(9) Hutchison, J. A.; Schwartz, T.; Genet, C.; Devaux, E.; Ebbesen, T. W. Modifying Chemical Landscapes by Coupling to Vacuum Fields. *Angew. Chem., Int. Ed.* **2012**, *51*, 1592−1596.

(10) Hutchison, J. A.; Liscio, A.; Schwartz, T.; Canaguier-Durand, A.; Genet, C.; Palermo, V.; Samorì, P.; Ebbesen, T. W. Tuning the Work-Function Via Strong Coupling. *Adv. Mater.* **2013**, *25*, 2481−2485.

(11) Imamoğlu, A.; Awschalom, D. D.; Burkard, G.; DiVincenzo, D. P.; Loss, D.; Sherwin, M.; Small, A. Quantum Information Processing Using Quantum Dot Spins and Cavity QED. *Phys. Rev. Lett.* **1999**, *83*, 4204−4207.

(12) Monroe, C. Quantum Information Processing with Atoms and Photons. *Nature* **2002**, 238−246.

(13) Khitrova, G.; Gibbs, H.; Kira, M.; Koch, S.; Scherer, A. Vacuum Rabi Splitting in Semiconductors. *Nat. Phys.* **2006**, *2*, 81−90.

(14) Törmä, P.; Barnes, W. L. Strong Coupling between Surface Plasmon Polaritons and Emitters: a Review. *Rep. Prog. Phys.* **2015**, *78*, No. 013901.

(15) Yoshie, T.; Scherer, A.; Hendrickson, J.; Khitrova, G.; Gibbs, H. M.; Rupper, G.; Ell, C.; Shchekin, O. B.; Deppe, D. G. Vacuum Rabi Splitting with a Single Quantum Dot in a Photonic Crystal Nanocavity. *Nature* **2004**, *432*, 200−203.

(16) Reithmaier, J. P.; Sek, G.; Loffler, A.; Hofmann, C.; Kuhn, S.; Reitzenstein, S.; Keldysh, L. V.; Kulakovskii, V. D.; Reinecke, T. L.; Forchel, A. Strong Coupling in a Single Quantum Dot-Semiconductor Microcavity System. *Nature* **2004**, *432*, 197−200.

(17) Kaluzny, Y.; Goy, P.; Gross, M.; Raimond, J. M.; Haroche, S. Observation of Self-Induced Rabi Oscillations in Two-Level Atoms Excited Inside a Resonant Cavity: The Ringing Regime of Superradiance. *Phys. Rev. Lett.* **1983**, *51*, 1175−1178.

(18) Raimond, J. M.; Brune, M.; Haroche, S. Manipulating Quantum Entanglement with Atoms and Photons in a Cavity. *Rev. Mod. Phys.* **2001**, *73*, 565−582.

(19) Hood, C. J.; Chapman, M. S.; Lynn, T. W.; Kimble, H. J. Real-Time Cavity QED with Single Atoms. *Phys. Rev. Lett.* **1998**, *80*, 4157−4160.

(20) Mabuchi, H.; Doherty, A. C. Cavity Quantum Electrodynamics: Coherence in Context. *Science* **2002**, *298*, 1372−1377.

(21) Weisbuch, C.; Nishioka, M.; Ishikawa, A.; Arakawa, Y. Observation of the Coupled Exciton-Photon Mode Splitting in a Semiconductor Quantum Microcavity. *Phys. Rev. Lett.* **1992**, *69*, 3314−3317.

(22) Vasa, P.; Wang, W.; Pomraenke, R.; Lammers, M.; Maiuri, M.; Manzoni, C.; Cerullo, G.; Lienau, C. Real-time Observation of Ultrafast Rabi Oscillations between Excitons and Plasmons in Metal Nanostructures with J-Aggregates. *Nat. Photonics* **2013**, *7*, 128−132.

(23) Zengin, G.; Wersäll, M.; Nilsson, S.; Antosiewicz, T. J.; Käll, M.; Shegai, T. Realizing Strong Light-Matter Interactions between Single-Nanoparticle Plasmons and Molecular Excitons at Ambient Conditions. *Phys. Rev. Lett.* **2015**, *114*, No. 157401.

(24) Melnikau, D.; Esteban, R.; Savateeva, D.; Sánchez-Iglesias, A.; Grzelczak, M.; Schmidt, M. K.; Liz-Marzán, L. M.; Aizpurua, J.; Rakovich, Y. P. Rabi Splitting in Photoluminescence Spectra of Hybrid Systems of Gold Nanorods and J-Aggregates. *J. Phys. Chem. Lett.* **2016**, *7*, 354−362.

(25) Chikkaraddy, R.; de Nijs, B.; Benz, F.; Barrow, S. J.; Scherman, O. A.; Rosta, E.; Demetriadou, A.; Fox, P.; Hess, O.; Baumberg, J. J. Single-Molecule Strong Coupling at Room Temperature in Plasmonic Nanocavities. *Nature* **2016**, *535*, 127−130.

(26) Wen, J.; Wang, H.; Wang, W.; Deng, Z.; Zhuang, C.; Zhang, Y.; Liu, F.; She, J.; Chen, J.; Chen, H.; et al. Room-Temperature Strong Light-Matter Interaction with Active Control in Single Plasmonic Nanorod Coupled with Two-Dimensional Atomic Crystals. *Nano Lett.* **2017**, *17*, 4689−4697.

(27) Zengin, G.; Gschneidtner, T.; Verre, R.; Shao, L.; Antosiewicz, T. J.; Moth-Poulsen, K.; Käll, M.; Shegai, T. Evaluating Conditions for Strong Coupling between Nanoparticle Plasmons and Organic Dyes Using Scattering and Absorption Spectroscopy. *J. Phys. Chem. C* **2016**, *120*, 20588−20596.

(28) Baranov, D. G.; Wersäll, M.; Cuadra, J.; Antosiewicz, T. J.; Shegai, T. Novel Nanostructures and Materials for Strong Light-Matter Interactions. *ACS Photonics* **2018**, *5*, 24−42.

(29) Simon, T.; Melnikau, D.; Sánchez-Iglesias, A.; Grzelczak, M.; Liz-Marzán, L. M.; Rakovich, Y.; Feldmann, J.; Urban, A. S. Exploring the Optical Nonlinearities of Plasmon-Exciton Hybrid Resonances in Coupled Colloidal Nanostructures. *J. Phys. Chem. C* **2016**, *120*, 12226−12233.

(30) Djoumessi Lekeufack, D.; Brioude, A.; Coleman, A. W.; Miele, P.; Bellessa, J.; de Zeng, L.; Stadelmann, P. Core-Shell Gold J-Aggregate Nanoparticles for Highly Efficient Strong Coupling Applications. *Appl. Phys. Lett.* **2010**, *96*, No. 253107.

(31) Ghosh Chaudhuri, R.; Paria, S. Core/Shell Nanoparticles: Classes, Properties, Synthesis Mechanisms, Characterization, and Applications. *Chem. Rev.* **2012**, *112*, 2373−2433.

(32) Liu, R.; Zhou, Z.-K.; Yu, Y.-C.; Zhang, T.; Wang, H.; Liu, G.; Wei, Y.; Chen, H.; Wang, X.-H. Strong Light-Matter Interactions in Single Open Plasmonic Nanocavities at the Quantum Optics Limit. *Phys. Rev. Lett.* **2017**, *118*, No. 237401.

(33) Santhosh, K.; Bitton, O.; Chuntonov, L.; Haran, G. Vacuum Rabi Splitting in a Plasmonic Cavity at the Single Quantum Emitter Limit. *Nat. Commun.* **2016**, *7*, No. 11823.

(34) Faucheaux, J. A.; Fu, J.; Jain, P. K. Unified Theoretical Framework for Realizing Diverse Regimes of Strong Coupling between Plasmons and Electronic Transitions. *J. Phys. Chem. C* **2014**, *118*, 2710−2717.

DOI: 10.1021/acs.jpcc.8b04204
J. Phys. Chem. C 2018, 122, 17976−17982

(35) Gómez, D. E.; Giessen, H.; Davis, T. J. Semiclassical Plexcitonics: Simple Approach for Designing Plexcitonic Nanostructures. *J. Phys. Chem. C* **2014**, *118*, 23963−23969.
(36) Stete, F.; Koopman, W.; Bargheer, M. Signatures of Strong Coupling on Nanoparticles: Revealing Absorption Anticrossing by Tuning the Dielectric Environment. *ACS Photonics* **2017**, *4*, 1669−1676.
(37) Antosiewicz, T. J.; Apell, S. P.; Shegai, T. Plasmon-Exciton Interactions in a Core-Shell Geometry: From Enhanced Absorption to Strong Coupling. *ACS Photonics* **2014**, *1*, 454−463.
(38) Novotny, L. Strong Coupling, Energy Splitting, and Level Crossings: A Classical Perspective. *Am. J. Phys.* **2010**, *78*, 1199.
(39) Fofang, N. T.; Park, T.-H.; Neumann, O.; Mirin, N. A.; Nordlander, P.; Halas, N. J. Plexcitonic Nanoparticles: Plasmon-Exciton Coupling in Nanoshell-J-Aggregate Complexes. *Nano Lett.* **2008**, *8*, 3481−3487.
(40) Wurtz, G. A.; Evans, P. R.; Hendren, W.; Atkinson, R.; Dickson, W.; Pollard, R. J.; Zayats, A. V.; Harrison, W.; Bower, C. Molecular Plasmonics with Tunable Exciton-Plasmon Coupling Strength in J-Aggregate Hybridized Au Nanorod Assemblies. *Nano Lett.* **2007**, *7*, 1297−1303.
(41) Rudin, S.; Reinecke, T. L. Oscillator Model for Vacuum Rabi Splitting in Microcavities. *Phys. Rev. B* **1999**, *59*, 10227−10233.
(42) Mitzscherling, S.; Cui, Q.; Koopman, W.; Bargheer, M. Dielectric Function of Two-Phase Colloid-Polymer Nanocomposite. *Phys. Chem. Chem. Phys.* **2015**, *17*, 29465−29474.
(43) Savitzky, A.; Golay, M. J. E. Smoothing and Differentiation of Data by Simplified Least Squares Procedures. *Anal. Chem.* **1964**, *36*, 1627−1639.
(44) Yang, Z.-J.; Antosiewicz, T. J.; Shegai, T. Role of Material Loss and Mode Volume of Plasmonic Nanocavities for Strong Plasmon-Exciton Interactions. *Opt. Express* **2016**, *24*, 20373−20381.
(45) Sauvan, C.; Hugonin, J. P.; Maksymov, I. S.; Lalanne, P. Theory of the Spontaneous Optical Emission of Nanosize Photonic and Plasmon Resonators. *Phys. Rev. Lett.* **2013**, *110*, No. 237401.
(46) Kristensen, P. T.; Hughes, S. Modes and Mode Volumes of Leaky Optical Cavities and Plasmonic Nanoresonators. *ACS Photonics* **2014**, *1*, 2−10.
(47) Koenderink, A. F. On the Use of Purcell Factors for Plasmon Antennas. *Opt. Lett.* **2010**, *35*, 4208−4210.
(48) Kiel, M.; Klotzer, M.; Mitzscherling, S.; Bargheer, M. Measuring the Range of Plasmonic Interaction. *Langmuir* **2012**, *28*, 4800−4804.
(49) Melnikau, D.; Savateeva, D.; Susha, A.; Rogach, A. L.; Rakovich, Y. P. Strong Plasmon-Exciton Coupling in a Hybrid System of Gold Nanostars and J-Aggregates. *Nanoscale Res. Lett.* **2013**, *8*, 134.
(50) An, L.; Wang, Y.; Tian, Q.; Yang, S. Small Gold Nanorods: Recent Advances in Synthesis, Biological Imaging, and Cancer Therapy. *Materials* **2017**, *10*, 1372.
(51) Ali, M. R. K.; Snyder, B.; El-Sayed, M. A. Synthesis and Optical Properties of Small Au Nanorods Using a Seedless Growth Technique. *Langmuir* **2012**, *28*, 9807−9815.
(52) Quinten, M. *Optical Properties of Nanoparticle Systems*; Wiley-VCH Verlag GmbH & Co. KGaA: Weinheim, Germany, 2011.

DOI: 10.1021/acs.jpcc.8b04204
J. Phys. Chem. C 2018, 122, 17976−17982

Article III

Vacuum Induced Saturation in Plasmonic Nanoparticles

Felix Stete, Wouter Koopman, Günter Kewes, Carsten Henkel, Oliver Benson, and Matias Bargheer

submitted, (2020)

Vacuum-Induced Saturation in Plasmonic Nanoparticles

Felix Stete,[1,2] Wouter Koopman,[1] Günter Kewes,[3] Carsten Henkel,[1] Oliver Benson,[3] and Matias Bargheer[1,4]
[1)] *Institut für Physik & Astronomie, Universität Potsdam, Karl-Liebknecht-Str. 24-25, 14476 Potsdam, Germany*
[2)] *School of Analytical Sciences Adlershof (SALSA), Humboldt-Universität zu Berlin, Unter den Linden 6, 10999 Berlin, Germany*
[3)] *Institut für Physik, Humboldt-Universität zu Berlin, Newtonstraße 15, 12489 Berlin, Germany*
[4)] *Helmholtz Zentrum Berlin, Albert-Einstein-Str. 15, 12489 Berlin, Germany*

Vacuum fluctuations are a fundamental feature of quantized fields. It is usually assumed that observations connected to vacuum fluctuations require a system well isolated from other influences. In this work we demonstrate that effects of the quantum vacuum can already occur in simple colloidal nano-assemblies prepared by wet chemistry. We claim that the electromagnetic field fluctuations at the zero-point level saturate the absorption of dye molecules self-assembled at the surface of plasmonic nano-resonators. For this effect to occur, reaching the strong coupling regime between the plasmonic and excitonic excitations is not required. This intriguing effect of vacuum-induced saturation (VISA) is discussed within a simple quantum optics picture and demonstrated by comparing the optical spectra of gold–dye core–shell nanorods to electromagnetic simulations.

In recent years, advances in the fabrication of plasmonic nanostructures have pushed the limits of photonics to the sub-diffraction scale. Plasmonic structures are characterized by intense near fields that effectively localize electromagnetic (EM) radiation to nanoscale volumes. This concentrated optical energy is at the heart of groundbreaking applications like surface enhanced Raman scattering for single molecule spectroscopy,[1] nano-lasing[2,3] or plasmon-driven chemistry.[4–6] Even more, plasmons are a route to the facile realization of quantum cavity systems,[7] which are in demand for future quantum technologies.[8] In contrast to more traditional quantum cavities that utilize high quality-factors at cryogenic temperatures, plasmonic cavities allow the observation of quantum electrodynamic (QED) effects at ambient conditions and in the bad cavity limit.[7] Conversely, QED effects must be considered in the majority of plasmon-molecule experiments.

One of the most intriguing results of QED is the presence of an EM vacuum state with a fluctuating intensity. These vacuum fluctuations cause non-classical behaviours such as the Lamb shift,[9] the Purcell effect,[10] or vacuum Rabi splitting,[11] all of which have also been studied on plasmonic nanoparticles.[12–14] In this article, we discuss a further way in which empty plasmon-mode fluctuations affect adsorbates: the vacuum-induced saturation (VISA) of the adsorbate resonance. In traditional QED experiments this effect is discussed in terms of a critical photon number below unity,[15] but to our knowledge it has not yet been studied in the plasmonic context. Here, we demonstrate that VISA plays a role even in simple colloidal metal–dye core–shell nanoparticles at room temperature.

The saturation of a two-level absorber is schematically shown in Fig. 1. Strong EM fields diminish the absorber polarizability and consequently lower the probability of a transition between ground and excited state. Conventionally, high intensity laser fields with a large number of photons are necessary to achieve a notable saturation. Plasmonic nanoparticles, on the other hand, can concentrate EM fields to ultrasmall volumes to achieve similar intensities with only a few photons, down to the limit where on average less than one photon is necessary to cause absorber saturation. In this limit, the saturation is a result of vacuum fluctuations. Note that this does not mean that energy is actually shifted from the vacuum to the absorber but that the vacuum lowers the absorption probability for a photon probing the system.

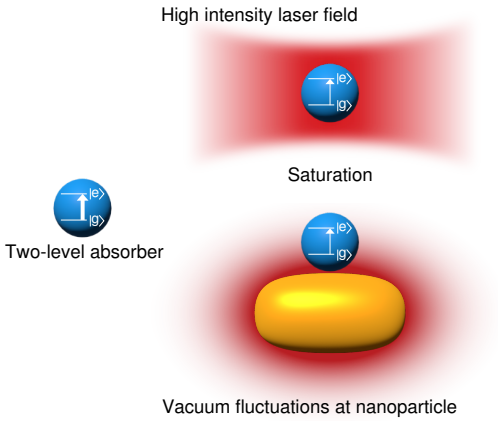

FIG. 1. Sketch of the phenomenon. A two-level absorber is saturated by high intensities. These can be reached by a high intensity laser or by the vacuum field fluctuations in ultrasmall cavities.

We motivate the occurrence of VISA with well-known quantum mechanical arguments and present a modified expression for the susceptibility of quantum absorbers. On the example of Au–TDBC core–shell nanorods we demonstrate that for high plasmon–exciton coupling strengths, inclusion of saturation effects is necessary for a correct simulation of the optical nanoparticle spectra. Indeed, the inclusion of VISA removes the discrepancy

between experiments[16,17] and previously published simulations based on non-saturating models.[18,19] The latter predict a mode which is purely localized in the shell, that is not observed experimentally. Inclusion of saturation into the model removes this rogue resonance and allows the simulation of extinction spectra with a remarkable accuracy. The saturation approach is shown to hold well for changing particle size and, as expected, its influence becomes weaker for increasing mode volumes. These results show that VISA cannot only change a system's features quantitatively but can also alter them qualitatively. It is therefore not only a fascinating aspect from a fundamental physics point of view but of interest for all plasmonic nanoparticle systems with high coupling strength.

VACUUM SATURATION

In most cases, the optical properties of atoms or molecules can be approximated by those of a quantum mechanical two-level system. Contrary to classical oscillators, the absorption of a two-level system can be saturated. This nonlinear effect becomes relevant when the intensity of the EM mode I exceeds the saturation intensity I_{sat} of the absorber defined as[20]

$$I_{\mathrm{sat}} = \frac{1}{4} c\epsilon_0 \frac{\hbar^2 \gamma^2}{\mu^2} \,. \tag{1}$$

It relates to the bare absorber's linewidth γ and transition dipole moment μ: for $I = I_{\mathrm{sat}}$, its resonant polarizability is halved compared to the weak-field limit[21] and it approaches zero for $I \gg I_{\mathrm{sat}}$.

In the classical field description, saturation disappears for a vanishing electric field. In a full quantum picture, however, the absorber is always exposed to field fluctuations, even in the vacuum state. This suggests that we relate the vacuum fluctuations to the saturation intensity so that for $I_{\mathrm{vac}} > I_{\mathrm{sat}}$, the absorber shows saturation even in the absence of photons.

The vacuum state $|0\rangle$ of a cavity is defined by the absence of fundamental EM cavity excitations (photons). The expectation value of the electric field vanishes in this state, as $\langle E \rangle = \langle 0| E |0\rangle = 0$. However, the intensity has the non-vanishing average[21]

$$I_{\mathrm{vac}} = \frac{1}{2} c\epsilon_0 \langle 0| E^2 |0\rangle = \frac{\hbar \omega_{\mathrm{EM}} c}{4 V_{\mathrm{EM}}} \,. \tag{2}$$

Here, V_{EM} represents the cavity's EM mode volume and ω_{EM} is the mode frequency. The intensity of the vacuum fluctuations is thus largely determined by the geometrical confinement of the EM mode, as quantified by V_{EM}. Thus, plasmonic cavities featuring sub-diffraction limit mode volumes possess very high vacuum intensity fluctuations.

It is a fundamental finding of QED that the non-vanishing vacuum intensity allows an empty EM mode to interact with an absorber, even in the absence of photons. This interaction is expressed in a non-vanishing coupling energy of

$$\hbar \Omega_0 = \mu \sqrt{\frac{2 I_{\mathrm{vac}}}{c\epsilon_0}} \,. \tag{3}$$

between the states $|0, e\rangle$ and $|1, g\rangle$ involving the excited and ground states of the absorber (within the singly-excited manifold of the Jaynes-Cummings ladder.[21]) Here, Ω_0 denotes the vacuum Rabi frequency and μ the absorber's dipole moment. Comparing the expressions for the coupling strength and the saturation intensity, we find the criterion for VISA to be

$$\Omega_0 > \frac{\gamma}{\sqrt{2}} \,. \tag{4}$$

That is, the absorber's polarizability at resonance is reduced to 1/2 by vacuum fluctuations when the vacuum Rabi frequency Ω_0 reaches 70% of the system's linewidth γ. In other words, VISA becomes relevant when the vacuum Rabi frequency makes the system flop between the states $|1, g\rangle$ and $|0, e\rangle$ with a period comparable to the excited state lifetime.

VISA has the same roots as vacuum Rabi splitting, also referred to as the regime of strong coupling. However, these two effects are not identical. While strong coupling implies the emergence of new light–matter hybrid modes, saturation only relates to the properties of the absorber. This is reflected in the formal criteria for the effects: for strong coupling, Ω_0 needs to exceed the mean of absorber linewidth γ and cavity linewidth κ,[22,23] while VISA does not depend on cavity losses according to equation (4). In systems coupled to plasmons, cavity losses often dominate the total energy decay and $\kappa > \gamma$. So even in such bad-cavity set-ups, the vacuum fluctuations can diminish the probability to absorb an external photon although the systems do not exhibit full mode hybridisation. We can therefore identify VISA as an intermediate coupling regime that is reached before strong coupling is established.

SUSCEPTIBILITY OF SATURATED ABSORBERS

Investigating the implications of VISA in principle requires a full QED treatment of the plasmon–absorber system, which includes both vacuum fluctuations and the two-level nature of the absorber. However, due to the strong radiative and dissipative losses, modeling a plasmonic system in a full quantum approach is challenging.[24] Hence, plasmonic systems are mostly described by classical electromagnetic fields.[18] Absorbers can be included in such a model through their susceptibility χ. In the following, we will discuss how to modify the expression for χ in order to consider the two-level nature of the absorber and include VISA.

Commonly, an absorber is approximated as a Lorentz oscillator with resonance frequency ω_0. For an ensemble of oscillators, a macroscopic material model can be

derived, represented by a susceptibility χ_{class} as[25]

$$\chi_{\text{class}}(\omega) = \frac{f\omega_0^2}{\omega_0^2 - \omega^2 + i\gamma\omega} \approx \frac{f\omega_0}{2} \frac{\omega_0 - \omega + i\frac{\gamma}{2}}{(\omega_0 - \omega)^2 + \frac{\gamma^2}{4}} \quad (5)$$

where the dimensionless oscillator strength f is proportional to the absorber density. The approximation is valid for $\omega \gg \gamma$, close to resonance.

Within this linear response model, no saturation can occur. Non-linearities are included in the more precise semi-classical approach that treats the absorbers as two-level systems in an oscillating classical electric field $E = E_0 \cos \omega t$. In this case, the susceptibility can be derived from the optical Bloch equations and reads[21,25]

$$\chi(\omega) = \frac{f\omega_0}{2} \frac{\omega_0 - \omega + i\frac{\gamma}{2}}{(\omega_0 - \omega)^2 + \frac{\gamma^2}{4} + \frac{\Omega^2}{2}} \,. \quad (6)$$

where $\Omega = \mu E_0/\hbar$ is the Rabi frequency. It is instructive to write χ in terms of a saturation parameter s:

$$\chi(\omega) = \frac{\chi_{\text{class}}(\omega)}{1 + s(\omega)} \quad (7)$$

with

$$s(\omega) = \frac{\frac{\Omega^2}{2}}{(\omega_0 - \omega)^2 + \frac{\gamma^2}{4}} = \frac{I}{I_{\text{sat}}} \frac{\frac{\gamma^2}{4}}{(\omega_0 - \omega)^2 + \frac{\gamma^2}{4}} \,. \quad (8)$$

When s is small, χ is not different from the classical solution. As soon as s becomes non-negligible (around $I = I_{\text{sat}}$), χ is diminished according to equation 7 and for extremely high intensities pushed towards zero.

Traditionally, the high field intensities that are required for saturation are generated by a large number of photons, for example in intense laser beams.[26] Hence, the saturation parameter is often thought to be negligible in the low excitation regime.[25] However, in plasmonic cavities I_{vac} can be in the region of I_{sat}. We therefore argue that these fluctuations need to be taken into account in the low excitation regime. We do so by replacing Ω with the non-vanishing vacuum coupling Ω_0 in equation (6). For small mode volumes and the concomitant high vacuum intensities, the absorber susceptibility is thus altered even without additional excitation.

In general, the effect of VISA is difficult to detect experimentally since it mainly causes the susceptibility to broaden. As the oscillator strength f and the linewidth γ are often adjustable to fit a model to experimental data, saturation effects can easily be overseen. We do however speculate that VISA may have hindered the realization of experiments in which researchers aimed at coupling extremely narrow-linewidth emitters to plasmonic nanoparticle resonators:[27] the narrower the excitonic linewidth γ, the quicker it will saturate due to a reduction of the saturation intensity.

Here, we discuss another manifestation of VISA, which shows a clear qualitative effect: the suppression of a shell-mode caused by excitonic absorbers coupled to plasmonic nanoparticles in a core–shell geometry.

SATURATION IN HYBRID NANORODS

Plasmonic nanoparticles form ultrasmall cavities for EM modes which are usually modeled by classical EM approaches. In the highly symmetric case of (layered) spherical nanoparticles, Mie theory and simplifications like the quasi static approximation[28] as well as and the elliptical generalization by Gans provide an analytical solution. For more irregular particle shapes different numerical approaches such as finite difference time domain (FDTD) and finite element method (FEM) are employed.[29,30]

Here, we show the influence of VISA on the modeled spectra of plasmon–exciton core–shell nanoparticles. We first use Mie–Gans theory to simulate the extinction spectrum of a nanorod consisting of a gold core and a few-nm thin shell of the J-aggregate forming dye TDBC and compare this model to measured extinction data. To verify that the results are not an artefact of the highly symmetrical geometry used in Maxwell-Garnet theory, we later model the extinction spectra with an FEM solver for Maxwell's equations (JCMsuite).

Mie–Gans theory provides an expression for the polarizability α_k of a core–shell nanospheroid along the long ($k = a$) or short ($k = b$) axis. From this polarizability, the calculation of the extinction cross section is straightforward by accounting for the finite particle size within the modified wavelength approximation,[31] adding scattering and absorption cross sections and averaging over the orientation of the spheroids.[28,32] With the permittivities of the core (ϵ_1), the shell (ϵ_2) and the surrounding medium (ϵ_3), the polarizability reads as[28,32]

$$\alpha_k = V \frac{(\epsilon_2 - \epsilon_3)\epsilon_{\text{u}} + g\epsilon_2(\epsilon_1 - \epsilon_2)}{(\epsilon_3 + L_k^{(2)}(\epsilon_2 - \epsilon_3))\epsilon_{\text{u}} + gL_k^{(2)}\epsilon_2(\epsilon_1 - \epsilon_2)} \,. \quad (9)$$

Here, $\epsilon_{\text{u}} = \epsilon_2 + (\epsilon_1 - \epsilon_3)(L_k^{(1)} - gL_k^{(2)})$ with the depolarization factors $L_k^{(1,2)}$ for the inner (1) and outer (2) spheroid and g as the inner spheroid's volume fraction of the total volume V.

Fig. 2a presents the simulated extinction spectrum for a bare gold nanorod (dash-dotted blue line) as calculated by Mie–Gans theory in comparison to an experimentally measured spectrum of an aqueous colloidal nanorod solution (orange line). The data were collected in the low excitation limit, that means the average time between two consecutive photons reaching a particle exceeded by far the average lifetime of the plasmon and a lowering of probe light intensity had no influence on the spectrum. The two resonances correspond to the transverse (520 nm - short axis) and the longitudinal mode (600 nm - long axis) of the rod. The short axis diameter of the particles was determined by transmission electron microscopy (TEM) to be 18 nm, the long axis is left adjustable to fit the plasmon resonance. A 1 nm citrate capping layer is included in the simulation as shell.[33] The simulation reproduces the measurement data very well when using literature values for the dielectric function of gold.[34] The discrepancy in the magnitude of the transverse resonance

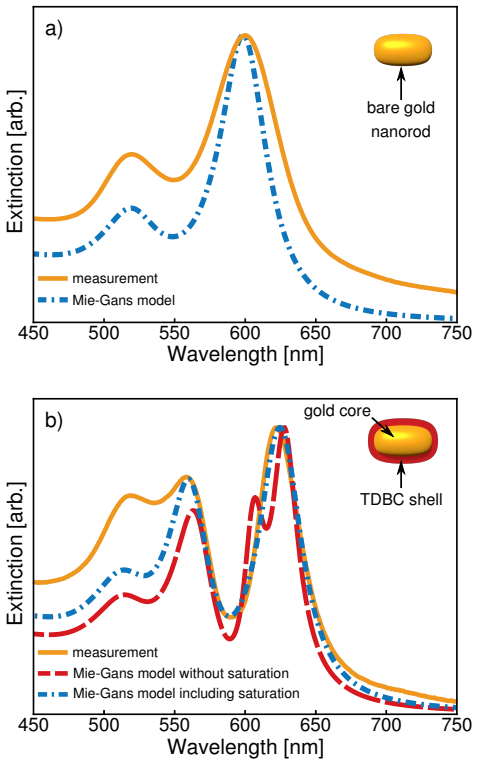

FIG. 2. a) Extinction spectrum of gold nanorods as measured (solid orange line) and simulated with Mie–Gans theory (dash-dotted blue line). b) Extinction spectrum of gold nanorods coated with TDBC as measured (solid orange line), simulated with a classical shell susceptibility (dashed red line) and a shell susceptibility including VISA (dash-dotted blue line).

is a known issue in EM nanorod simulations.[29,35] We mainly attribute the differences between theory and experiment in the height of the transverse peak to agglomerations of rods in solutions and secondary particles like spheres in the ensemble spectrum.

The extinction spectrum changes considerably when the particles are coated with TDBC (orange line in Fig. 2b). The coupling between core and shell causes a splitting in the longitudinal plasmon resonance.[7] In a simulation that does not take VISA into account, the shell permittivity in equation (9) is $\epsilon_2 = \epsilon_\infty + \chi_{\text{class}}$ with ϵ_∞ as correction for off-resonant absorber transitions of higher energy. We assume the parameters to be $\epsilon_\infty = 1.7$,[18] $\hbar\gamma = 47\,\text{meV}$,[36] and a shell thickness of $3\,\text{nm}$[37], an absorber resonance $\hbar\omega_0 = 2.0\,\text{eV}$ ($612\,\text{nm}$) and an oscillator strength of $f = 0.08$. All of these parameters were chosen to be in agreement with literature values for TDBC and such that the observed mode splitting could be reproduced. Indeed, the simulation reproduces the splitting of longitudinal mode (dashed red line in Fig. 2b). However, the simulation shows a striking difference compared to the measurement: an additional third peak emerges close to the uncoupled absorber resonance frequency. Altering the parameters cannot remove this peak while keeping the experimentally observed mode separation. This phenomenon has been described theoretically and has been attributed to a mode whose field intensity is geometrically concentrated on the absorber shell.[18,19] However, to our knowledge, it was never observed experimentally for plasmon–absorber core–shell particles.

The presented model can be reconciled with the experimental data when including VISA. For high coupling strengths between an ensemble of emitters and a cavity, the emitters act like one giant J-aggregate.[38] The spectral shift of the two-exciton state and the occurrence of ground state bleaching[39] allow the approximation of the shell as two-level system. We therefore replace the susceptibility with $\chi(\omega)$ of equation (6) and insert the vacuum Rabi frequency Ω_0. An *ab initio* determination of Ω_0 via V_{EM} and μ is in principle possible within the framework of quasi normal modes.[24,40] However, for an exact calculation, all parameters for the emitter in the respective chemical environment need to be known precisely, a requirement that is usually not met. Therefore, we use measured values for Ω_0. To determine Ω_0, we deposited the particles on substrates and subsequently covered the samples with thin layers of polyelectrolytes.[41] The anticrossing resulting from a change of plasmon resonance directly yielded Ω_0 for the particles investigated here.[36]

The resulting simulation of the extinction spectra including VISA reproduces the experimental spectrum almost perfectly (dash-dotted blue line in Fig. 2b) except for the previously mentioned issue with the magnitude of the transverse resonance. We used the same set of parameters as for the unsaturated oscillator, except for a slightly higher oscillator strength of $f = 0.11$[37] and a vacuum Rabi frequency of $\hbar\Omega_0 = 85\,\text{meV}$. The striking agreement between simulation and experiment in Fig. 2b indicates that indeed, VISA must and can be taken into account in the presented way.

We further tested the saturation model by simulating the spectra of rods with four different volumes, but similar aspect ratios. Different particle sizes support different coupling energies.[36] Consequently, if the model is correct, the saturation parameter should vary from size to size while all other dye parameters should remain the same for all spectra. We simulated the spectra not only with the presented Mie–Gans model but also with a numerical FEM solver using the same saturated shell susceptibility from equation (6). For all sizes, TEM images provided the particle dimensions which were used to fit the bare particle spectra. The model for the coupled spectra used the same parameters for TDBC mentioned earlier while varying Ω_0 according to the measured mode splittings. The upper row in Fig. 3 presents measurement and simulations for particles with a transverse di-

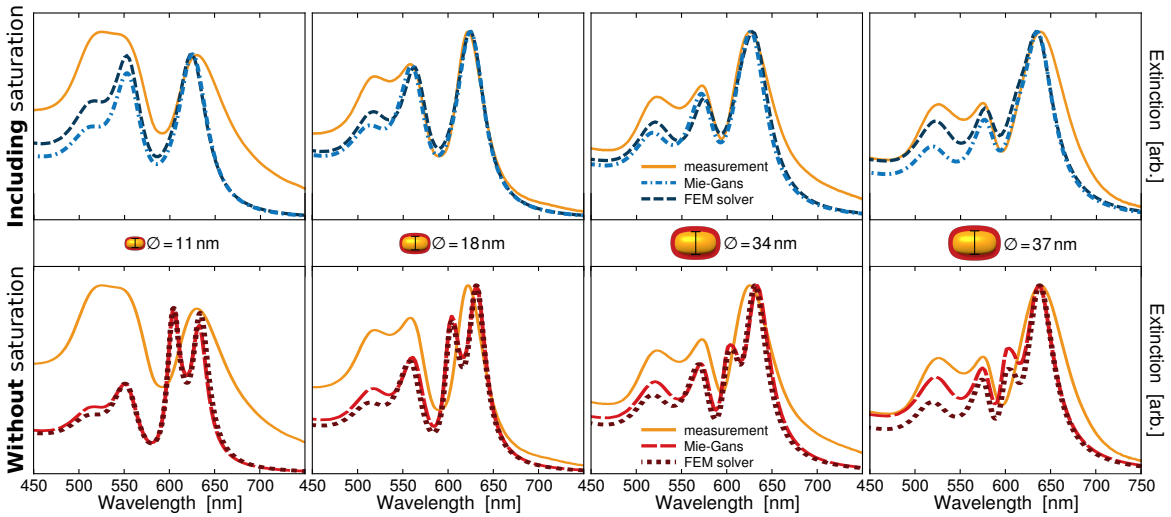

FIG. 3. The upper row shows the extinction spectra of TDBC-coated gold nanorods of different sizes as measured (orange solid lines) and simulated with to the Mie–Gans model (dash-dotted blue lines) and FEM (dashed dark blue lines). Both models include VISA. All particles have the same aspect ratio but a varying transverse diameter of 11 nm, 18 nm, 34 nm, and 37 nm (from left to right). The simulations included VISA. The lower row presents the same measured spectra for the same particles (orange lines) with Mie–Gans-simulated (dashed red lines) and FEM–simulated (dotted dark red lines) that did not include saturation.

ameter of 11 nm, 18 nm, 34 nm, and 37 nm. Experimentally, we obtained $\hbar\Omega_0$ for the four particle sizes to be 116 meV, 78 meV, 73 meV, and 54 meV (from smallest to largest particles, respectively).[36] For a perfect fit, we used values of 100 meV, 85 meV, 77 meV, and 65 meV in the simulations. The difference in these values can easily be explained by the difference of chemical environments in the two sets of experiments. The agreement between measured spectra and model is remarkable. Mie–Gans and FEM simulations are consistent, no shell resonances appear at the positions of the uncoupled resonances and the split resonance in all cases fits very well to the experimental spectra. Only for the smallest particles, there is a slight deviation between simulation and measurement. This can most likely be explained by size dependent modifications of ϵ_1.[42] To show the contrast between a model including VISA and a classical model, the lower row in Fig. 3 presents Mie–Gans and FEM simulations for the same particles using the same parameters as above only with a saturation parameter set to zero. In all cases, additional peaks emerge that do not reflect the measured spectra. We emphasize that indeed, saturation occurs even for systems that do not fulfill the strong coupling criterion since only the smallest particles exhibit full mode hybridisation whereas for all particles, the coupling strength is on the order of or higher than the exciton linewidth.

These spectra show that the description of core–shell nanoparticles needs to incorporate VISA and that using equation (6) with the vacuum Rabi frequency accounting for saturation leads to correct results. The model is coherent for all particle sizes for both analytical and numerical approaches. Note again that all spectra were recorded in a conventional transmission spectrometer in the low excitation limit. This means that a single photon in the spectrometer can already probe the saturation. This is similar to the situation of vacuum Rabi splitting, where the spectrometer photon already "sees" the mode splitting of the coupled modes.

CONCLUSION

In conclusion, we presented the vacuum-induced saturation (VISA) of absorbers in a plasmonic cavity by the example of a simple Au-dye core-shell nanorod and provided a criterion to examine the relevance of the effect. VISA is caused by the intensity fluctuations of an electromagnetic mode, which are inversely proportional to its mode volume. Plasmonic modes with sub-diffraction volumes hence possess extreme vacuum intensity fluctuations. These cause a polarization of the absorber that reduces the absorption probability and effectively saturates its resonance.

We make our predictions accessible to numerical modeling by including VISA into the susceptibility, which is the essential parameter in the context of Mie scattering. In our experimental system of core–shell nanorods with a plasmonic core and an excitonic absorber shell, classical models predict a resonant mode of the particle shell that has never been observed in experiments. This

mode is indeed suppressed when VISA is included in the model. We take the fact that the inconsistencies of experiment and theory can be removed elegantly with a single parameter, the coupling strength, as a strong evidence that VISA occurs in plasmon absorber systems and can be incorporated into the modeling as specified. The evidence is further supported by the fact that only the coupling strength has to be adjusted for simulating differently sized rods.

The presented insights suggest that QED effects can be relevant in plasmonic systems well outside the strong-coupling regime and at least a part of the rich physics of quantum non-linearties,[43] such as large single photon phase shifts, strongly non-classical photon statistics of scattered light or applications such as single photon logical gates,[44] might be accessible with less effort in simple and cost-effective systems. Moreover, the extremely short lifetimes of plasmonic excitations can be a potential benefit for ultrafast photon routing or switching in high-rate quantum information processing.

METHODS

Here we give a concise summary of the relevant experimental methods.[36,41]

Coating of Nanorods with TDBC: TDBC (from FEW Chemicals) was dissolved in NaOH ($c_{\mathrm{NaOH}} = 10^{-5}$ mol/l) to a concentration of $c_{\mathrm{TDBC}} \approx 1$ mmol/l. Gold nanorods with a citrate ligand (from Nanopartz) were added with a ratio of 1:1. After 48 h, the TDBC coated nanorods were washed by centrifugation.

Measurement of Vacuum Rabi Frequency: Glass substrates were modified by spin-coating a layer of polyelectrolyte layers poly-ethyleneimine (PEI) and a layer of poly-sodium 4-styrenesulfonate (PSS). The TDBC coated nanorods were drop-cast onto the substrates and given 12 h time for adsorption before residuals were washed away with purified water. A series of samples with different thicknesses of spin coated multilayers of PSS and poly-allylamine hydrochloride (PAH) on top of the particles was created. All mentioned chemicals were purchased form Sigma Aldrich. For each sample, an absorption spectrum was recorded. In order to separately assess the shift of the plasmon spectrum in the absence of TDBC, each sample was photobleached with a continuous-wave laser working at 532 nm with a power of 10 W. Again, a spectrum was recorded of each sample after the bleaching process to determine the spectral position of the 'bare' plasmon resonance. The (longitudinal) maximum positions of the coupled spectra were eventually plotted against the (longitudinal) maximum positions of the bleached spectra. The resulting anticrossing could be fitted[36,41] by

$$\omega_{\pm} = \frac{\omega_{\mathrm{pl}} + \omega_{\mathrm{ex}}}{2} \pm \sqrt{\frac{(\omega_{\mathrm{pl}} - \omega_{\mathrm{em}})^2}{4} + \Omega_0^2} \qquad (10)$$

with $\omega_{\pm}$ as upper and lower branch of the anticrossing and ω_{i} as resonance of plasmon ($i = \mathrm{pl}$) or exciton ($i = \mathrm{ex}$). The fit directly yields the vacuum Rabi frequency Ω_0.

Analytical Simulations: The analytical simulation was performed according to the established procedure by Mie-Gans as detailed by Bohren & Huffmann.[28] The calculations were implemented in Python code using the numpy package. The particle dimensions were obtained from SEM microscopy. The resulting simulation of the uncoupled spectra fitted the experimental spectra reasonably well without further optimization.

Numerical Simulations: We used the commercial finite element method (FEM) solver for Maxwell's equations JCMSuite and applied cylindrical coordinates. Instead of ellipsoids, we used cylinders with rounded edges to model the rods. Rod dimensions and curvatures were retrieved from TEM images. The other parameters (shell thickness, permittivities) were identical to those used in the analytical simulations as described in the text. Cross sections were calculated as the mean from three plane wave light sources, one propagating parallel and two orthogonal to the long axis of the rod, respectively. The latter two are either polarized along the short or the long axis of the rod. This average was tested to yield the same results as a significantly more time consuming average over all possible angles of incidence that must be used in principle for non-spherical particles with larger aspect ratios.

ACKNOWLEDGEMENTS

We thank Ferenc Liebig for recording the TEM images for particle size determination. Additionally, G.K. and O.B. acknowledge financial support by the Deutsche Forschungsgemeinschaft (DFG, German Research Foundation), projectnumber 182087777 - SFB 951. Also, F.S. wants to thank the DFG for financial support via the graduate school SALSA. Moreover, we would like to thank the JCMwave team for fruitful discussions.

COMPETING INTERESTS

The authors declare no competing interest.

[1] Kneipp, K.; Wang, Y.; Kneipp, H.; Perelman, L. T.; Itzkan, I.; Dasari, R. R.; Feld, M. S. Single Molecule Setection Using Surface-Enhanced Raman Scattering (SERS). *Phys. Rev. Lett.* **1997**, *78*, 1667.

[2] Oulton, R. F.; Sorger, V. J.; Zentgraf, T.; Ma, R.-M.; Gladden, C.; Dai, L.; Bartal, G.; Zhang, X. Plasmon lasers at deep subwavelength scale. *Nature* **2009**, *461*, 629.

[3] Ma, R.-M.; Oulton, R. F.; Sorger, V. J.; Bartal, G.; Zhang, X. Room-temperature sub-diffraction-limited plasmon laser by total internal reflection. *Nat. Mater.* **2011**, *10*, 110.

[4] Mukherjee, S.; Libisch, F.; Large, N.; Neumann, O.; Brown, L. V.; Cheng, J.; Lassiter, J. B.; Carter, E. A.; Nordlander, P.; Halas, N. J. Hot Electrons Do the Impossible: Plasmon-Induced Dissociation of H_2 on Au. *Nano Lett.* **2013**, *13*, 240–247.

[5] Hartland, G. V.; Besteiro, L. V.; Johns, P.; Govorov, A. O. What's so Hot about Electrons in Metal Nanoparticles? *ACS Energy Lett.* **2017**, *2*, 1641–1653.

[6]Sarhan, R. M.; Koopman, W.; Schuetz, R.; Schmid, T.; Liebig, F.; Koetz, J.; Bargheer, M. The importance of plasmonic heating for the plasmon-driven photodimerization of 4-nitrothiophenol. *Sci. Rep.* **2019**, *9*, 3060.
[7]Baranov, D. G.; Wersäll, M.; Cuadra, J.; Antosiewicz, T. J.; Shegai, T. Novel Nanostructures and Materials for Strong Light–Matter Interactions. *ACS Photonics* **2018**, *5*, 24–42.
[8]O'Brien, J. L.; Furusawa, A.; Vučković, J. Photonic quantum technologies. *Nat. Photonics* **2009**, *3*, 687.
[9]Lamb, W. E.; Retherford, R. C. Fine Structure of the Hydrogen Atom by a Microwave Method. *Phys. Rev.* **1947**, *72*, 241–243.
[10]Purcell, E. M. Spontaneous Emission Probabilities at Radio Frequencies. *Phys. Rev.* **1946**, *69*, 681.
[11]Thompson, R. J.; Rempe, G.; Kimble, H. J. Observation of Normal-Mode Splitting for an Atom in an Optical Cavity. *Phys. Rev. Lett.* **1992**, *68*, 1132–1135.
[12]Sun, Q.; Al-Amri, M.; Kamli, A.; Zubairy, M. S. Lamb shift due to surface plasmon polariton modes. *Phys. Rev. A* **2008**, *77*, 062501.
[13]Anger, P.; Bharadwaj, P.; Novotny, L. Enhancement and Quenching of Single-Molecule Fluorescence. *Phys. Rev. Lett.* **2006**, *96*, 113002.
[14]Groß, H.; Hamm, J. M.; Tufarelli, T.; Hess, O.; Hecht, B. Near-field strong coupling of single quantum dots. *Sci. Adv.* **2018**, *4*, eaar4906.
[15]Kimble, H. J. Strong Interactions of Single Atoms and Photons in Cavity QED. *Phys. Scr.* **1998**, *T76*, 127.
[16]Djoumessi Lekeufack, D.; Brioude, A.; Coleman, A. W.; Miele, P.; Bellessa, J.; de Zeng, L.; Stadelmann, P. Core–Shell Gold J-Aggregate Nanoparticles for Highly Efficient Strong Coupling Applications. *Appl. Phys. Lett.* **2010**, *96*, 253107.
[17]Melnikau, D.; Esteban, R.; Savateeva, D.; Sánchez-Iglesias, A.; Grzelczak, M.; Schmidt, M. K.; Liz-Marzán, L. M.; Aizpurua, J.; Rakovich, Y. P. Rabi Splitting in Photoluminescence Spectra of Hybrid Systems of Gold Nanorods and J-Aggregates. *J. Phys. Chem. Lett.* **2016**, *7*, 354–362.
[18]Antosiewicz, T. J.; Apell, S. P.; Shegai, T. Plasmon–Exciton Interactions in a Core–Shell Geometry: From Enhanced Absorption to Strong Coupling. *ACS Photonics* **2014**, *1*, 454–463.
[19]Sukharev, M.; Nitzan, A. Numerical Studies of the Interaction of an Atomic Sample with the Electromagnetic Field in Two Dimensions. *Phys. Rev. A* **2011**, *84*, 043802.
[20]Novotny, L.; Hecht, B. *Principles of Nano-Optics*; Cambridge University Press, Cambridge, 2006.
[21]Grynberg, G.; Aspect, A.; Fabre, C. *Introduction to Quantum Optics: From the Semi-Classical Approach to Quantized Light*; Cambridge university press, 2010.
[22]Rempe, G.; Thompson, R.; Kimble, H. Cavity Quantum Electrodynamics with Strong Coupling in the Optical Domain. *Phys. Scr.* **1994**, *1994*, 67.
[23]Khitrova, G.; Gibbs, H.; Kira, M.; Koch, S.; Scherer, A. Vacuum Rabi splitting in semiconductors. *Nat. Phys.* **2006**, *2*, 81–90.
[24]Lalanne, P.; Yan, W.; Vynck, K.; Sauvan, C.; Hugonin, J.-P. Light Interaction with Photonic and Plasmonic Resonances. *Laser Phot. Rev.* **2018**, *12*, 1700113.
[25]Törmä, P.; Barnes, W. L. Strong coupling between surface plasmon polaritons and emitters: a review. *Rep. Prog. Phys.* **2015**, *78*, 13901.
[26]Shen, Y.-R. The principles of nonlinear optics. *Wiley-Interscience, New York* **1984**,
[27]Chen, X.-W.; Sandoghdar, V.; Agio, M. Coherent Interaction of Light with a Metallic Structure Coupled to a Single Quantum Emitter: From Superabsorption to Cloaking. *Phys. Rev. Lett.* **2013**, *110*, 153605.
[28]Bohren, C. F.; Huffman, D. R. *Absorption and Scattering of Light by Small Particles*; John Wiley & Sons, 2008.
[29]Myroshnychenko, V.; Carbó-Argibay, E.; Pastoriza-Santos, I.; Pérez-Juste, J.; Liz-Marzán, L. M.; García de Abajo, F. J. Modeling the Optical Response of Highly Faceted Metal Nanoparticles with a Fully 3D Boundary Element Method. *Adv. Mater.* **2008**, *20*, 4288–4293.
[30]Biagioni, P.; Huang, J.-S.; Hecht, B. Nanoantennas for visible and infrared radiation. *Rep. Prog. Phys.* **2012**, *75*, 024402.
[31]Kelly, K. L.; Coronado, E.; Zhao, L. L.; Schatz, G. C. The Optical Properties of Metal Nanoparticles: The Influence of Size, Shape, and Dielectric Environment. *J. Phys. Chem. B* **2003**, *107*, 668–677.
[32]Zengin, G.; Johansson, G.; Johansson, P.; Antosiewicz, T. J.; Käll, M.; Shegai, T. Approaching the strong coupling limit in single plasmonic nanorods interacting with J-aggregates. *Sci. Rep.* **2013**, *3*, 3074.
[33]Park, J.-W.; Shumaker-Parry, J. S. Structural Study of Citrate Layers on Gold Nanoparticles: Role of Intermolecular Interactions in Stabilizing Nanoparticles. *J. Am. Chem. Soc.* **2014**, *136*, 1907–1921.
[34]Olmon, R. L.; Slovick, B.; Johnson, T. W.; Shelton, D.; Oh, S.-H.; Boreman, G. D.; Raschke, M. B. Optical dielectric function of gold. *Phys. Rev. B* **2012**, *86*, 235147.
[35]Chen, H.; Shao, L.; Li, Q.; Wang, J. Gold Nanorods and Their Plasmonic Properties. *Chem. Soc. Rev.* **2013**, *42*, 2679–2724.
[36]Stete, F.; Schoßau, P.; Bargheer, M.; Koopman, W. Size-Dependent Coupling of Hybrid Core–Shell Nanorods: Toward Single-Emitter Strong-Coupling. *J. Phys. Chem. C* **2018**, *122*, 17976–17982.
[37]Zengin, G.; Wersäll, M.; Nilsson, S.; Antosiewicz, T. J.; Käll, M.; Shegai, T. Realizing Strong Light-Matter Interactions between Single-Nanoparticle Plasmons and Molecular Excitons at Ambient Conditions. *Phys. Rev. Lett.* **2015**, *114*, 157401.
[38]Haroche, S.; Raimond, J.-M. *Exploring the Quantum: Atoms, Cavities, and Photons*; Oxford university press, 2006.
[39]Fofang, N. T.; Grady, N. K.; Fan, Z.; Govorov, A. O.; Halas, N. J. Plexciton Dynamics: Exciton–Plasmon Coupling in a J-Aggregate–Au Nanoshell Complex Provides a Mechanism for Nonlinearity. *Nano Lett.* **2011**, *11*, 1556–1560.
[40]Kewes, G.; Binkowski, F.; Burger, S.; Zschiedrich, L.; Benson, O. Heuristic Modeling of Strong Coupling in Plasmonic Resonators. *ACS Photonics* **2018**, *5*, 4089–4097.
[41]Stete, F.; Koopman, W.; Bargheer, M. Signatures of Strong Coupling on Nanoparticles: Revealing Absorption Anticrossing by Tuning the Dielectric Environment. *ACS Photonics* **2017**, *4*, 1669–1676.
[42]Stoller, P.; Jacobsen, V.; Sandoghdar, V. Measurement of the complex dielectric constant of a single gold nanoparticle. *Opt. Lett.* **2006**, *31*, 2474–2476.
[43]Wang, D.; Kelkar, H.; Martin-Cano, D.; Rattenbacher, D.; Shkarin, A.; Utikal, T.; Götzinger, S.; Sandoghdar, V. Turning a molecule into a coherent two-level quantum system. *Nat. Phys.* **2019**, *15*, 483.
[44]Turchette, Q. A.; Hood, C. J.; Lange, W.; Mabuchi, H.; Kimble, H. J. Measurement of Conditional Phase Shifts for Quantum Logic. *Phys. Rev. Lett.* **1995**, *75*, 4710–4713.

Article IV

Optical Non-Linearities in Plasmon–Exciton Core–Shell Systems: The Role of Heat

Felix Stete, Wouter Koopman, and Matias Bargheer

submitted, (2020)

Optical Non-Linearities in Plasmon–Exciton Core–Shell Systems: The Role of Heat

Felix Stete,[1,2] Wouter Koopman,[1] and Matias Bargheer[1,3]
[1)] *Institut für Physik & Astronomie, Universität Potsdam, Karl-Liebknecht-Str. 24-25, 14476 Potsdam, Germany*
[2)] *School of Analytical Sciences Adlershof (SALSA), Humboldt-Universität zu Berlin, Unter den Linden 6, 10999 Berlin, Germany*
[3)] *Helmholtz Zentrum Berlin, Albert-Einstein-Str. 15, 12489 Berlin, Germany*

Abstract: Strong coupling between plasmons and excitons gives rise to new hybrid polariton states with various fields of potential applications. Despite a plethora of research on plasmon–exciton systems, their transient behaviour is not yet fully understood. Besides Rabi oscillations in the first femtoseconds after an optical excitation, coupled systems show interesting non-linear features on the picosecond time scale. Here, we conclusively show that the source of these features is heat that is generated inside the particles. Until now, this hypothesis was only based on phenomenological arguments. We investigate the role of heat by recording transient spectra of plasmon–exciton core–shell nanoparticles with excitation off the polariton resonance. We present analytical simulations that precisely recreate the measurements solely by assuming an initial temperature rise of the electron gas inside the particles. The simulations combine established strategies for describing uncoupled plasmonic particles with a recently published model for static spectra. The simulations are consistent for various excitation powers confirming that indeed heating of the particles is the root of the changes in the transient signals.

The small mode volume of localized surface plasmons on gold nanoparticles greatly enhances external electric fields. This enhancement enables high coupling strengths with excitonic emitters on the particle surface. In the so-called strong coupling regime, new hybrid resonances emerge, an upper and a lower polariton. These polaritons possess both plasmonic and excitonic characteristics, a feature that is of interest for applications like quantum networks,[1] parametric optical signal amplification,[2] manipulation of chemical reactions[3], thresholdless lasing[4] and many more.

Strong coupling between excitonic emitters and metal nanoparticles has been realized for various particle types. Examples are silver rods,[5] silver triangles,[6] silver shells,[7] gold rods,[8] aluminum discs[9]. When excited, the energy oscillates between purely plasmonic and purely excitonic modes at the Rabi frequency. For metal nanoparticles, this frequency is on the order of a few fs making a direct observation difficult. Additionally, the short life time of plasmons on the order of 10 fs hinders a long coherent oscillation between excitonic and plasmonic parts. The strongly damped Rabi oscillations have been observed for surface plasmon polariton systems[10] but not yet for localized plasmons on nanoparticles.

Also on longer time scales after an initial excitation, strongly coupled plasmon–exciton nanoparticles show interesting non-linear features that can be of great importance for future applications. Several studies have discussed the transient behaviour of coupled plasmon–exciton systems on a time for scale beyond the polariton life time.[11–13] The main source for changes in the transient spectra at the polariton resonances was argued to be heat in the metal cores. But the arguments were rather phenomenological than rigid.

For bare nanoparticles, ab initio simulations have successfully been introduced to explain changes of optical properties upon heating or the transient behaviour after an initial excitation.[14–16] Their main approach is to model the metal's permittivity depending on the electron and lattice temperature in the particle since for bare particles, heat is the source of changes in the transient spectra. This model has not yet been applied to the situation of plasmon–exciton particles to precisely discuss the role of heat in the metal.

We want to close this gap with this study by presenting simulations of the transient spectra of coupled plasmon–exciton nanoparticles which are exited off the polariton resonance. We combine, on the one hand, the well-established method of reproducing the transient behaviour of gold nanoparticles via Rosei's model[16,17] and, on the other hand, a recently presented expansion of the Mie–Gans model to describe the static extinction of coupled core–shell particles taking into account saturation of the absorption by the quantum fluctuations of the vacuum field.[18] The simulations essentially model how the increased electron temperature changes the occupied electronic states according to the Fermi-distribution and the lattice temperature adds a correction to the free electron damping. We calibrate the simulations by comparison to static spectra of the bare gold particles and core–shell particles. Finally, we model the electron and phonon temperatures in a two-temperature model and compare the simulated spectra to the results of pump–probe measurements of coupled plasmon–exciton core–shell nanorods. Our model system consists of a gold core and shell of the cyanine dye TDBC. The particles show strong coupling or at least verge on the strong coupling regime.[19,20] The comparison between simulations and measurements for various pump powers demonstrates good agreement supporting previous studies which had to argue phenomenologically.[11,12]

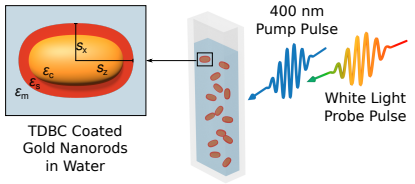

FIG. 1. Sketch of the experimental setting: TDBC coated gold nanorods were dissolved in water and excited by a 400 nm pump pulse. A white light probe pulse detected the change in transmission after excitation. A magnified particle is shown on the left with the parameters used later in the simulations.

EXPERIMENTAL METHODS

We measured the change in transmission of white light laser pulses through a solution of dye coated gold nanorods for various delay times after excitation with a fs-pump pulse at 400 nm (Figure 1).

TDBC-coated gold nanorods: The cyanine dye 5, 5', 6, 6'-tetrachloro-1-1'-diethyl-3, 3'-di (4-sulfobutyl)-benzimidazolocarbocyanine (TDBC) was obtained from *FEW chemicals* and used as received. It was dissolved in an aqueous NaOH solution ($c_{\mathrm{NaOH}} = 10^{-5}$ mol/l) with a concentration of $c_{\mathrm{TDBC}} = 1$ mmol/l, stirred for 5 min and placed in an ultrasonic bath for 15 min. Citrate stabilized gold nanorods with a nominal transverse diameter of 25 nm and a longitudinal plasmon resonance at 600 nm were purchased from *Nanopartz*. Contrary to CTAB ligands, conventionally used for stabilizing gold nanorods, citrate ligands can easily be exchanged by TDBC. Particle and dye solution were mixed in a ratio of 1:1, placed in an ultrasonic bath for 15 min and left undisturbed for 48 h. After this resting time, the unadsorbed TDBC was removed by centrifuging twice for 30 min at 3000 rpm and refilling with purified water. During the measurements, the particle solution was filled into cuvettes with a path length of 1 mm.

Static measurements: Static transmission spectra were recorded with a *Cary 5e* spectrometer.

Pump–probe measurements: Laser pulses with a pulse length of 140 fs at a central wavelength of 795 nm and a repetition rate of 5 kHz were generated in a Ti:sapphire laser system (*MaiTai/Spitfire Pro* by *Spectra-Physics*). A part of the light was frequency doubled and focussed on the particle solution as pump beam with a focal spot size of approximately 300 µm. The power was varied between 1 mW and 4.5 mW. A small part of the output of the laser system was used to generate super continuum (white light) pulses in a 1 mm thick sapphire plate. These white light pulses were used to probe the transmission through the sample with an arbitrary delay to the pump excitation. After correction for the chirp of the white light as measured by polarisation-gated frequency-resolved optical gating (PG-FROG) the white light conserves the time resolution of the pump pulse. The time delay t between pump and probe could be controlled with a delay stage. The pump beam was chopped at rate of 125 Hz to measure the relative change in transmission between the pumped ($T_0 + \Delta T$) and the unpumped (T_0) sample. The change in transmission is directly connected to the change in extinction $\Delta\sigma_{\mathrm{ext}}$ of the particles via $\Delta T(t) \approx nL\Delta\sigma_{\mathrm{ext}}(t)$ with n representing the particle density and L the sample thickness[17].

SIMULATIONS

This study discusses simulations of transient spectra of core–shell nanoparticles based on the heat-induced change of the core's permittivity ϵ_{c}. For simplicity, we assume here that the excitonic shell permittivity ϵ_{c} is not affected by the excitation.

The simulation procedure was perfomed as follows: In a first step, we simulated the static spectra at room temperature by combining the theoretical description of the gold permittivity at room temperature by Rosei[21–24] with the Mie–Gans model for core–shell nanospheroids.[18] Transient spectra were then obtained by modeling the effect of the transient temperature rise on the Rosei-permittivity. The single steps on this route are described in detail below.

Static spectra: We simulated the static spectrum of our particles based on the Mie-Gans model.[18] The extinction cross section σ_{ext} of a nanoparticle can be obtained by calculating its polarisability α. In a dipolar approximation, the polarisability $\alpha_{0,j}$ along the long ($j = z$) or the short ($j = x, y$) axis of a spheroid is given by[25,26]

$$\alpha_{0,j} = V \frac{(\epsilon_{\mathrm{s}} - \epsilon_{\mathrm{m}})\epsilon_{\mathrm{a}} + g\epsilon_{\mathrm{s}}(\epsilon_{\mathrm{c}} - \epsilon_{\mathrm{s}})}{(\epsilon_{\mathrm{m}} + L_j^{(2)}(\epsilon_{\mathrm{s}} - \epsilon_{\mathrm{m}}))\epsilon_{\mathrm{a}} + gL_j^{(2)}\epsilon_{\mathrm{s}}(\epsilon_{\mathrm{c}} - \epsilon_{\mathrm{s}})} \,. \quad (1)$$

Here, $\epsilon_{\mathrm{a}} = \epsilon_{\mathrm{s}} + (\epsilon_{\mathrm{c}} - \epsilon_{\mathrm{m}})(L_j^{(1)} - gL_j^{(2)})$ with ϵ_{c}, ϵ_{s} and ϵ_{m} representing the permittivity of the core, the shell or the surrounding medium, respectively (Figure 1). g describes the volume fraction of the core and $L_j^{(1,2)}$ the geometrical factors of the inner (1) and outer (2) spheroid.

To account for the finite particle size, we applied the *modified long wavelength approximation* (MLWA) as[27]

$$\alpha_j = \alpha_{0,j} \left(1 - i\frac{\alpha_{0,j}}{6\pi\epsilon_0}k^3 - \frac{\alpha_{0,j}}{4\pi\epsilon_0}\frac{k^2}{s_j}\right)^{-1} \quad (2)$$

where k is the wave vector in the medium and s_j the respective semiaxis. Subsequently, an expression for the particle extinction was derived as

$$\sigma_{\mathrm{ext,j}} = \frac{k^4}{6\pi\epsilon_0^2}|\alpha_j|^2 + \frac{k}{\epsilon_0}\mathrm{Im}(\alpha_j) \,. \quad (3)$$

For this study, the particles were dissolved in water and thus randomly oriented in reference to the light polarisation. This is taken into account by weighing the contribution of each main axis with a factor of 1/3.

Apparently, the extinction is directly related to the permittivities ϵ_i of the involved materials. In the following, we want to present the models for ϵ_{s} and ϵ_{c}.

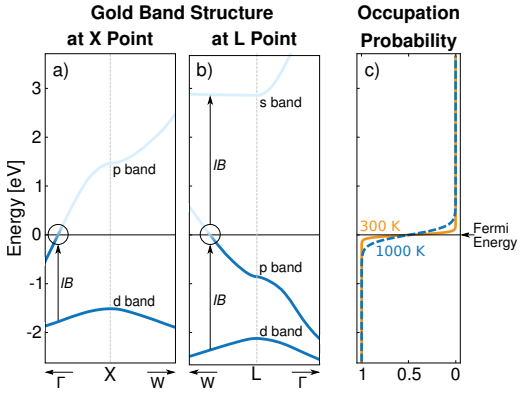

FIG. 2. Band structure of gold at the X (a) and L (b) point in the Brillouin zone and the corresponding occupation probability given by the Fermi distribution $f(E,T)$ (c). Vertical arrows indicate the interband transitions (IB) with transition energies in the visible. The Fermi distribution is plotted for $T = 300\,\mathrm{K}$ (solid orange line) and $T = 1000\,\mathrm{K}$ (dashed blue line) to illustrate the smearing of the Fermi edge.

For a correct simulation of the shell permittivity ϵ_s, the saturation of the molecular transition by the strong electric fields at the particle surface has to be taken into account. The saturated permittivity of a two-level system in a cavity is given by[18]

$$\epsilon_\mathrm{s} = \epsilon_\infty + \frac{f\omega_0}{2}\frac{\omega_0 - \omega + i\frac{\gamma}{2}}{(\omega_0-\omega)^2 + \frac{\gamma^2}{4} + \frac{\Omega_0^2}{2}}\,. \tag{4}$$

Here, f, γ and ω_0 represent the system's oscillator strength, linewidth and resonance position, respectively while Ω_0 denotes the vacuum Rabi frequency, quantifying the molecule-particle coupling.

A theoretical model for the temperature-dependence of the Au-permittivity was established by Rosei and colleagues[21–24] and has successfully been used to describe the transient behaviour of gold nanoparticles.[16,17] It includes the contribution of the conduction electrons ϵ_Dr via the Drude model as well as the contribution of interband transitions ϵ_IB via the joint density of states. Combining the different contributions allows the calculation of the imaginary part $\mathrm{Im}(\epsilon)$. The real part of the permittivity $\mathrm{Re}(\epsilon)$ is then obtained via the Kramers-Kronig integral.

The optical response of the quasi-free electrons at the Fermi edge is described by the Drude contribution to the permittivity as

$$\epsilon_\mathrm{Dr}(\omega) = 1 + \frac{\omega_\mathrm{p}^2}{\omega^2 + i\gamma_\mathrm{Dr}\omega}\,. \tag{5}$$

To correctly describe the permittivity of gold in the visible region down to 400 nm, three interband transitions need to be taken into account in addition to the Drude contribution: The transition from the d band to the p band close to the X point of the Brillouin zone (Figure 2a) and the transitions from the d band to the p band and from the p band to the s band in the vicinity of the L point of the Brillouin zone[17] (Figure 2b). The basis for the contribution of the transition from band i to band j is the energy distribution of the joint density of states $D_{i\to j}(E,\hbar\omega)$.[21] It describes the density of transitions with energy $\hbar\omega$ and initial energy E. To find the probability of a transition this term needs to weighted with the probability that the initial state is occupied while the final state is not. This occupation probability is determined by the Fermi distribution $f(E,T)$ whose edge at the Fermi energy changes with temperature (Figure 2c). The transition probability from band i to band j with energy $\hbar\omega$ is then[17]

$$\begin{aligned} J_{i\to j}(\hbar\omega) = &\int_{E_\mathrm{min}}^{E_\mathrm{max}} D_{i\to j}(E,\hbar\omega) \\ &\times [f(E,T)(1-f(E+\hbar\omega,T))]dE\,. \end{aligned} \tag{6}$$

Each interband transition is weighted with an oscillator strength $A_{i\to j}$[21] to model the imaginary part of the permittivity. Considering the contribution of the three relevant transitions, ϵ_IB then reads[17]

$$\begin{aligned} \mathrm{Im}(\epsilon_\mathrm{IB}(\omega)) = &\frac{4\pi^2 q_\mathrm{e}^2}{\epsilon_0 m_\mathrm{e}^2\omega^2}(A^\mathrm{X}_{d\to p}J^\mathrm{X}_{d\to p}(\omega) \\ &+ A^\mathrm{L}_{d\to p}J^\mathrm{L}_{d\to p}(\omega) + A^\mathrm{L}_{p\to s}J^\mathrm{L}_{p\to s}(\omega))\,. \end{aligned} \tag{7}$$

Combining Drude and interband contributions, we obtain an *ab initio* expression for the imaginary part of the permittivity of gold. The real part is then directly retrieved via Kramers-Kronig integration. The necessary parameters for the model can be retrieved from the detailed calculated band structure of gold.[17] However, for simplicity and higher precision, they are usually found by fitting the permittivity model to the experimental data. For this study, we used the values provided by Ref 28.

Temperature dependent spectra: The Rosei model allows simulating the temperature dependence of the permittivity. Heating causes a smearing of the Fermi edge (Figure 2c) and thus affects $J_{i\to j}(\hbar\omega)$ as calculated in eq 6. In other words, heating alters the occupation probability of the final or initial state and thus affects the different interband transitions. The Drude part is affected by heating via a change in the scattering rate γ_Dr. For weak and moderate excitation, the change in electron–electron scattering can be negelcted and γ_Dr is purely modified by a change in the electron–phonon scattering[29] i.e. by the phonon temperature T_ph.

To simulate the effect of transient gold heating, we need to find expressions for the time dependent electron and phonon temperatures, $T_\mathrm{e}(t)$ and $T_\mathrm{ph}(t)$, which are incorporated into the Rosei model to determine the time dependent permittivity $\epsilon_\mathrm{core}(t)$ of the gold. Subsequently, $\Delta\sigma_\mathrm{ext}(t)$ is calculated via Equations 1–3 and compared to the measured data.

In metals, the energy of an incoming laser pulse is absorbed only by the electrons. They thermalize within

a few tens of femtoseconds. Due to the fast thermalisation (in comparison to the temporal resolution of the set-up), we can assume here that directly after the excitation, all electrons are described by a Fermi distribution with temperature $T_{e,0}$. This temperature is derived from the absorbed pulse energy and the particle's absorption cross section. Since the interaction between the lattice and light can be neglected, the electrons and the lattice need to be described with two different temperatures which equilibrate via electron–phonon coupling in the first few picoseconds after excitation. Since both subsytems contribute to the permittivity (the electron temperature to the interband transitions, the phonon temperature to the Drude part), a two-temperature model is required to describe the transient behaviour of metal nanoparticles. The temperatures $T_i(t)$, where i represents the electron (e) or lattice (l) system, are connected via the system of coupled differential equations[15]

$$C_\mathrm{e}(T_\mathrm{e})\frac{\partial T_\mathrm{e}}{\partial t} = -G_\mathrm{e\text{–}ph}(T_\mathrm{e} - T_\mathrm{l})\,, \tag{8a}$$

$$C_\mathrm{l}(T_\mathrm{l})\frac{\partial T_\mathrm{l}}{\partial t} = G_\mathrm{e\text{–}ph}(T_\mathrm{e} - T_\mathrm{l})\,. \tag{8b}$$

The two-temperature model is parametrized by the electron and lattice heat capacities $C_i(T_i)$, as well as the electron-phonon coupling constant $G_\mathrm{e\text{–}ph}$. Coupling to the environment has been neglected in this expression since it occurs on longer times scales than the ones discussed here. The heat capacity of the gold lattice is $C_\mathrm{l} = 3k_\mathrm{B}n$ with k_B as Boltzmann constant and $n = 5.9 \times 10^{-28}\,\mathrm{m}^{-3}$.[16] The electron heat capacity is temperature dependent via $C_\mathrm{e} = \gamma_\mathrm{e}T_\mathrm{e}$ with a Sommerfeld constant of $\gamma_\mathrm{e} = 71.5\,\mathrm{Jm}^{-3}\mathrm{K}^{-2}$.[16] As electron phonon coupling, we use $G_\mathrm{e\text{–}ph} = 2.1 \times 10^{16}\,\mathrm{W/m}^3$.[30]

The solution of these equations yields the two temperatures and consequently allows for a calculation of the permittivity at any time after excitation. The electron temperature determines the form of the Fermi distribution while the phonon temperature affects the free electron scattering rate γ_Dr as[17]

$$\frac{\Delta\gamma_\mathrm{Dr}}{\gamma_\mathrm{Dr,0}} = \frac{\Delta T_\mathrm{ph}}{T_0}\,. \tag{9}$$

In conclusion, this model allows the simulation of the permittivity of gold and consequently of the strongly coupled plasmon–exciton system after an initial excitation. In the following section, we will present the results of both measurement and simulation and their remarkable match.

RESULTS AND DISCUSSION

The static extinction spectrum of the dye coated nanorods shows three peaks (upper, dark blue line in Figure 3). The transverse plasmon peak is located around 520 nm while around 570 nm and 630 nm, the hybrid resonances of the coupled plasmon–exciton system become visible. For comparison, the extinction spectrum of bare gold nanorods (lower, bright blue line in Figure 3) shows a longitudinal resonance around 600 nm. The splitting in the plasmon–exciton spectrum originates from the strong coupling of this longitudinal plasmon resonance to the exciton resonance of TDBC around 600 nm. The hybrid coupled excitations are known as the upper and lower polariton peak.

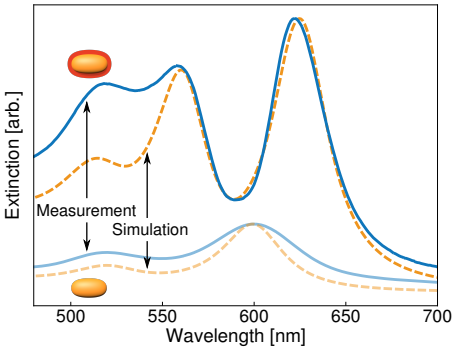

FIG. 3. Measured and simulated static extinction spectra of bare and TDBC-coated gold nanorods. The solid blue lines represent the experimental data, the dashed orange lines represent the simulations. The two lower lines describe the bare particles whereas the two upper lines describe the coupled situation.

The static simulations are represented by the dashed orange lines in Figure 3. The parameters used here are identical to those in Reference 18. However, for this study, the gold permittivity is now not directly taken from measured data[28] but simulated via the Rosei model that fully reproduces this measured permittivity. The simulations of the extinction of the bare and coupled systems agree quite well with the data. Just the intensity of the transverse resonance is not fully recovered. This is a well known problem in simulations of nanorod spectra.[31,32] In this case, nanospheres in the sample as well as particle clusters that can both be observed in SEM images seem to be the main reason for a higher peak in the measured data. In the region of interest i.e. the region of the coupled resonances, the model fits the data very well. We hence conclude that our model is suitable to further investigate the transient behavior of the coupled system.

In the following, we discuss the transient spectra of the same particles. The relative change in transmission $\Delta T/T_0$ after excitation with a 400 nm pump pulse at a pump power of 2 mW is presented in Figure 4a for various time delays. At the position of the static resonances, long lasting signal changes can be observed. The change at the transverse resonance can directly be attributed to the heating of the particles and effectively describes a broadening of the resonance.[17] The two polariton resonances possess similar features with the same lifetime. On a first glance, two possible explanations seem appro-

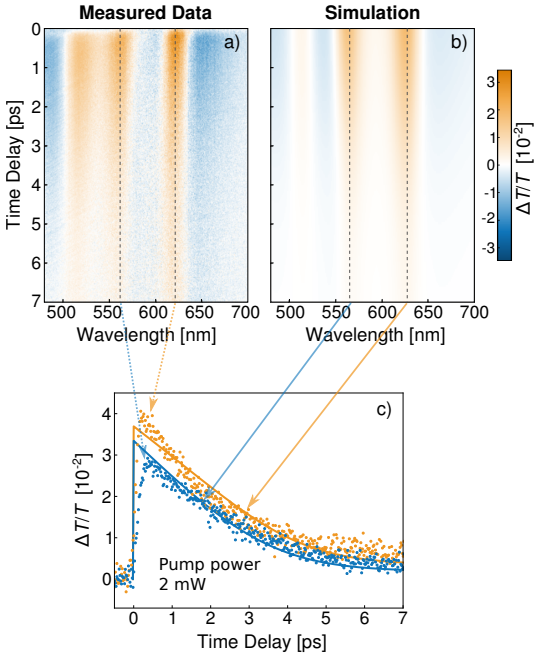

FIG. 4. Measured and simulated transient pump–probe spectra of gold–TDBC core–shell nanorods pumped with 2 mW at 400 nm. a) heatmap of the measured signal and b) heatmap of the simulated signal. c) transient signal at the position of the upper (blue) and lower (orange) polariton. The dots represent the measured signals, the solid lines the simulation.

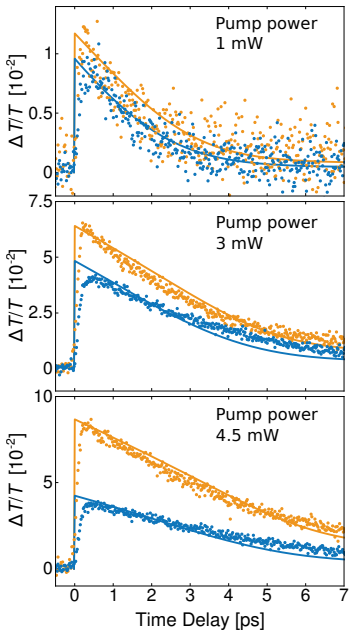

FIG. 5. Measured and simulated transient signals at the polariton resonances of gold–TDBC core–shell nanorods pumped with 1 mW, 3 mW and 4.5 mW (from top to bottom). Dots mark the experimental results while solid lines represent the simulations. The signal along the upper polariton indicated by blue marks, the signal along the lower polariton by orange ones.

priate. On the one hand, the excitation of polaritons has been suggested previously.[33] On the other hand, the signal change directly translates to a widening of the peaks. Therefore, a higher damping of the resonances caused by particle heating has been proposed to be the source of the signal change also at the polariton resonances.[11,12]

To calculate the influence of the transient heating, we inserted time dependent temperatures, obtained from the two-temperature model, into the simulation of the gold permittivity. This permittivity is then used in the Mie–Gans model. The initial conditions for solving eq 8 are given by the electron and phonon temperatures at $t = 0$. The lattice is initially at room temperature T_{room} since the light is absorbed only by the electrons. Assuming that all absorbed light energy uniformly raises the temperature of the thermalized electron gas,[17] the electron temperature at $t = 0$ is[34]

$$T_{\mathrm{e},0} = \sqrt{\frac{2\Delta Q}{V\gamma} + T_{\mathrm{room}}^2} \tag{10}$$

where V represents the particle volume. The energy ΔQ deposited inside the particle is obtained from the laser fluence and the particle's absorption cross section. For an ensemble measurement in solution, determining $T_{\mathrm{e},0}$ is however not necessarily practicable due to variations in spot size and optical attenuation by the solution which lead to an uncertainty in ΔQ[16]. In a first simulation, we therefore leave the electron temperature after excitation variable. We will however later make use of eq 10 to compare the transient spectra of various pump fluences.

Figure 4 presents both measured and simulated data for a pump power of 2 mW. For the simulation (Figure 4a), the only fitting parameter was $T_{\mathrm{e},0}$ (and a normalisation parameter). With $T_{\mathrm{e},0} = 1000$ K, the model reproduces the measurement (Figure 4b) quite well. While the simulation closely resembles the measurements at the polariton resonances, it somewhat underestimates the magnitude at the transverse plasmon resonance, due to the underestimation of the transverse peaks as discussed earlier. The agreement can be verified by taking a closer look at the behaviour at the polariton wavelengths (Figure 4c). The simulation at these resonances agrees with the measurements reasonably well.

To further strengthen the hypothesis of a purely thermal origin of the transient signal as suspected in literature,[11,12] we additionally investigated the temporal behaviour for pump powers of 1 mW, 3 mW and 4.5 mW. We can safely assume that the energy deposited inside

a particle ΔQ is proportional to the pump power. Consequently, using $T_{e,0} = 1000\,\mathrm{K}$ for 2 mW pump power, eq 10 predicts initial electron temperatures of 738 K, 1206 K and 1462 K for the pump powers of 1 mW, 3 mW and 4.5 mW, respectively. Figure 5 presents the simulations using these initial temperatures in comparison to the measured data. The characteristic crossover from an exponential to an almost linear decay[34] is nicely reproduced. Note that for the two higher pump powers, the ratio between the two signals (at upper and lower polariton position) was not ideal for the simulations. We therefore had to normalise the two signals separately to account for the higher measured change of the lower polariton. This discrepancy might be rooted in bleaching of the dye for higher pump powers which is not incorporated in our model. Yet, this consistency of the model for different pump powers clearly supports the hypothesis of heat as the main source of transient signal also for strongly coupled nanoparticles. The high fluence transients can surely be fitted better if one allows for an adjustment of the various parameters entering the model. We think, however, that this consistent fit for several fluences demonstrates that the gold heating is at the origin of the observed dynamics.

Although the signal change arises mainly at the polariton positions, it is unlikely that excited coupled states induce this change. On the one hand, the particles were pumped with 400 nm, a wavelength at which polaritons are not directly excited, on the other hand, the lifetime of such plasmon–exciton states is in the order of a few tens of femtoseconds, a timescale far below the lifetime of the signals in our measurements.

CONCLUSION

In conclusion, we presented a method for the simulation of the full transient spectra of coupled plasmon-dye core-shell nanorods excited off the polariton resonance. To this end, we combined a well-established method for the transient description of bare gold nanoparticles with a method to simulate spectra of strongly coupled metal-dye particles that includes the dye saturation by the strong plasmon fields. The remarkable agreement between measured and simulated data in the present work confirms the suggestion of earlier studies that the ps-dynamics of these hybrid nanoparticles is dominated by transient heating effects.

ACKNOWLEDGEMENTS

We thank Günter Kewes for fruitful discussions. Additionally, F.S. acknowledges financial support by the DFG via the graduate school SALSA.

[1] A. Imamoğlu, D. D. Awschalom, G. Burkard, D. P. DiVincenzo, D. Loss, M. Sherwin, and A. Small, "Quantum information processing using quantum dot spins and cavity qed," Phys. Rev. Lett. **83**, 4204–4207 (1999).

[2] M. Saba, C. Ciuti, J. Bloch, V. Thierry-Mieg, R. André, L. S. Dang, S. Kundermann, A. Mura, G. Bongiovanni, J. Staehli, *et al.*, "High-temperature ultrafast polariton parametric amplification in semiconductor microcavities," Nature **414**, 731 (2001).

[3] J. A. Hutchison, T. Schwartz, C. Genet, E. Devaux, and T. W. Ebbesen, "Modifying chemical landscapes by coupling to vacuum fields," Angew. Chem., Int. Ed. **51**, 1592–1596 (2012).

[4] P. Törmä and W. L. Barnes, "Strong coupling between surface plasmon polaritons and emitters: A review," Rep. Prog. Phys. **78**, 013901 (2014).

[5] D. Zheng, S. Zhang, Q. Deng, M. Kang, P. Nordlander, and H. Xu, "Manipulating coherent plasmon–exciton interaction in a single silver nanorod on monolayer wse2," Nano Lett. **17**, 3809–3814 (2017).

[6] G. Zengin, M. Wersäll, S. Nilsson, T. J. Antosiewicz, M. Käll, and T. Shegai, "Realizing Strong Light–Matter Interactions between Single-Nanoparticle Plasmons and Molecular Excitons at Ambient Conditions," Phys. Rev. Lett. **114**, 157401 (2015).

[7] N. Zhou, M. Yuan, Y. Gao, D. Li, and D. Yang, "Silver nanoshell plasmonically controlled emission of semiconductor quantum dots in the strong coupling regime," ACS Nano **10**, 4154–4163 (2016).

[8] D. Melnikau, R. Esteban, D. Savateeva, A. Sánchez-Iglesias, M. Grzelczak, M. K. Schmidt, L. M. Liz-Marzán, J. Aizpurua, and Y. P. Rakovich, "Rabi splitting in photoluminescence spectra of hybrid systems of gold nanorods and j-aggregates," J. Phys. Chem. Lett. **7**, 354–362 (2016).

[9] E. Eizner, O. Avayu, R. Ditcovski, and T. Ellenbogen, "Aluminum nanoantenna complexes for strong coupling between excitons and localized surface plasmons," Nano Lett. **15**, 6215–6221 (2015).

[10] P. Vasa, W. Wang, R. Pomraenke, M. Lammers, M. Maiuri, C. Manzoni, G. Cerullo, and C. Lienau, "Real-Time Observation of Ultrafast Rabi Oscillations between Excitons and Plasmons in Metal Nanostructures with J-Aggregates," Nat. Photonics **7**, 128–132 (2013).

[11] Y.-W. Hao, H.-Y. Wang, Y. Jiang, Q.-D. Chen, K. Ueno, W.-Q. Wang, H. Misawa, and H.-B. Sun, "Hybrid-state dynamics of gold nanorods/dye j-aggregates under strong coupling," Angew. Chem. Int. Ed. **123**, 7970–7974 (2011).

[12] T. Simon, D. Melnikau, A. Sánchez-Iglesias, M. Grzelczak, L. M. Liz-Marzán, Y. Rakovich, J. Feldmann, and A. S. Urban, "Exploring the optical nonlinearities of plasmon-exciton hybrid resonances in coupled colloidal nanostructures," J. Phys. Chem. C **120**, 12226–12233 (2016).

[13] E. Eizner, K. Akulov, T. Schwartz, and T. Ellenbogen, "Temporal Dynamics of Localized Exciton–Polaritons in Composite Organic–Plasmonic Metasurfaces," Nano Lett. **17**, 7675–7683 (2017).

[14] C. Voisin, N. Del Fatti, D. Christofilos, and F. Vallée, "Ultrafast electron dynamics and optical nonlinearities in metal nanoparticles," J. Phys. Chem. B **105**, 2264–2280 (2001).

[15] J. H. Hodak, I. Martini, and G. V. Hartland, "Spectroscopy and Dynamics of Nanometer-Sized Noble Metal Particles," J. Phys. Chem. B **102**, 6958–6967 (1998).

[16] S. Park, M. Pelton, M. Liu, P. Guyot-Sionnest, and N. F. Scherer, "Ultrafast resonant dynamics of surface plasmons in gold nanorods," J. Phys. Chem. C **111**, 116–123 (2007).

[17] T. Stoll, P. Maioli, A. Crut, N. Del Fatti, and F. Vallée, "Advances in femto-nano-optics: ultrafast nonlinearity of metal nanoparticles," Eur. Phys. J. B **87**, 260 (2014).

[18] F. Stete, W. Koopman, K. Günter, C. Henkel, O. Benson, and M. Bargheer, "Vacuum-Induced Emitter Saturation in Plasmonic Nanoparticles," submitted.

[19] F. Stete, W. Koopman, and M. Bargheer, "Signatures of strong coupling on nanoparticles: Revealing absorption anticrossing by tuning the dielectric environment," ACS Photonics **4**, 1669–1676 (2017).

[20] F. Stete, P. Schoßau, M. Bargheer, and W. Koopman, "Size-dependent coupling of hybrid core–shell nanorods: Toward

single-emitter strong-coupling," J. Phys. Chem. C **122**, 17976–17982 (2018).
[21]R. Rosei, "Temperature modulation of the optical transitions involving the fermi surface in ag: Theory," Phys. Rev. B **10**, 474 (1974).
[22]R. Rosei, F. Antonangeli, and U. Grassano, "D bands position and width in gold from very low temperature thermomodulation measurements," Surf. Sci. **37**, 689–699 (1973).
[23]M. Guerrisi, R. Rosei, and P. Winsemius, "Splitting of the interband absorption edge in au," Phys. Rev. B **12**, 557–563 (1975).
[24]P. Winsemius, M. Guerrisi, and R. Rosei, "Splitting of the interband absorption edge in au: Temperature dependence," Phys. Rev. B **12**, 4570–4572 (1975).
[25]C. F. Bohren and D. R. Huffman, *Absorption and Scattering of Light by Small Particles* (John Wiley & Sons, 2008).
[26]G. Zengin, G. Johansson, P. Johansson, T. J. Antosiewicz, M. Käll, and T. Shegai, "Approaching the strong coupling limit in single plasmonic nanorods interacting with j-aggregates," Sci. Rep. **3**, 3074 (2013).
[27]K. L. Kelly, E. Coronado, L. L. Zhao, and G. C. Schatz, "The optical properties of metal nanoparticles: The influence of size, shape, and dielectric environment," J. Phys. Chem. B **107**, 668–677 (2003).
[28]R. L. Olmon, B. Slovick, T. W. Johnson, D. Shelton, S.-H. Oh, G. D. Boreman, and M. B. Raschke, "Optical Dielectric Function of Gold," Phys. Rev. B **86**, 235147 (2012).
[29]B. Rethfeld, D. S. Ivanov, M. E. Garcia, and S. I. Anisimov, "Modelling ultrafast laser ablation," J. Phys. D: Appl. Phys. **50**, 193001 (2017).
[30]J. Hohlfeld, S.-S. Wellershoff, J. Güdde, U. Conrad, V. Jähnke, and E. Matthias, "Electron and lattice dynamics following optical excitation of metals," Chem. Phys. **251**, 237–258 (2000).
[31]V. Myroshnychenko, E. Carbó-Argibay, I. Pastoriza-Santos, J. Pérez-Juste, L. M. Liz-Marzán, and F. J. García de Abajo, "Modeling the Optical Response of Highly Faceted Metal Nanoparticles with a Fully 3D Boundary Element Method," Adv. Mater. **20**, 4288–4293 (2008).
[32]H. Chen, L. Shao, Q. Li, and J. Wang, "Gold Nanorods and Their Plasmonic Properties," Chem. Soc. Rev. **42**, 2679–2724 (2013).
[33]S. Balci, C. Kocabas, B. Küçüköz, A. Karatay, E. Akhüseyin, H. Gul Yaglioglu, and A. Elmali, "Probing ultrafast energy transfer between excitons and plasmons in the ultrastrong coupling regime," Appl. Phys. Lett. **105**, 051105 (2014).
[34]N. Del Fatti, A. Arbouet, and F. Vallée, "Femtosecond optical investigation of electron–lattice interactions in an ensemble and a single metal nanoparticle," Appl. Phys. B: Lasers Opt. **84**, 175–181 (2006).

Article V

Watching the Vibration and Cooling of Ultrathin Gold Nanotriangles by Ultrafast X-ray Diffraction

Alexander von Reppert, Radwan M. Sarhan, **Felix Stete**, Jan Pudell, Natalia Del Fatti, Aurelién Crut, Joachim Koetz, Ferenc Liebig, Claudia Prietzel and Matias Bargheer

The Journal of Physical Chemistry C 120, 50 (2016)

THE JOURNAL OF PHYSICAL CHEMISTRY C

Article

pubs.acs.org/JPCC

Watching the Vibration and Cooling of Ultrathin Gold Nanotriangles by Ultrafast X-ray Diffraction

A. von Reppert,[†] R. M. Sarhan,[†,∥] F. Stete,[†,∥] J. Pudell,[†] N. Del Fatti,[‡] A. Crut,[‡] J. Koetz,[§] F. Liebig,[§] C. Prietzel,[§] and M. Bargheer*[,†,⊥]

[†]Institut für Physik & Astronomie, Universität Potsdam, Karl-Liebknecht-Str. 24-25, 14476 Potsdam, Germany

[‡]FemtoNanoOptics Group, Institut Lumière Matière, Université de Lyon, CNRS-Université Lyon 1, 69622 Villeurbanne, France

[§]Institut für Chemie, Universität Potsdam, Karl-Liebknecht-Str. 24-25, 14476 Potsdam, Germany

[∥]Humboldt-Universität zu Berlin, School of Analytical Sciences Adlershof (SALSA), Albert-Einstein-Str. 5-9, 10099 Berlin, Germany

[⊥]Helmholtz Zentrum Berlin, Albert-Einstein-Str. 15, 12489 Berlin, Germany

ABSTRACT: We study the vibrations of ultrathin gold nanotriangles upon optical excitation of the electron gas by ultrafast X-ray diffraction. We quantitatively measure the strain evolution in these highly asymmetric nano-objects, providing a direct estimation of the amplitude and phase of the excited vibrational motion. The maximal strain value is well reproduced by calculations addressing pump absorption by the nanotriangles and their resulting thermal expansion. The amplitude and phase of the out-of-plane vibration mode with 3.6 ps period dominating the observed oscillations are related to two distinct excitation mechanisms. Electronic and phonon pressures impose stresses with different time dependences. The nanosecond relaxation of the expansion yields a direct temperature sensing of the nano-object. The presence of a thin organic molecular layer at the nanotriangle/substrate interfaces drastically reduces the thermal conductance to the substrate.

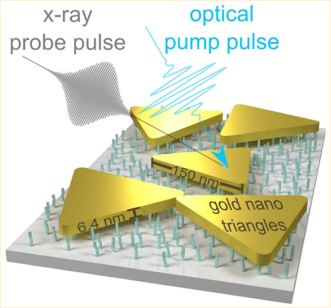

INTRODUCTION

Metallic nanoparticles have been in the focus of intensive research over decades,[1] in part because they may potentially help to realize large bandwidth optical nanoelectromechanical systems or similar small and fast devices.[2] From the perspective of physical chemistry, colloidal particles present versatile and accessible nano-objects, which can be grown as spheres, rods, cubes, pyramids, platelets, or prisms, just to name a few examples. Special shapes are useful for tailoring the plasmon-resonance and catalytic activity of the particles or to optimize them for surface-enhanced Raman scattering. Investigations of the ultrafast thermal and vibrational dynamics of such nanostructures[3−6] are often justified by applications like photothermal therapy or catalysis.[7] The strong interest in these phenomena also lies in the fundamental questions of how heat transport and vibrational response are altered on the nanoscale, when surface effects may start to play a role, making the validity of continuum descriptions questionable.[8−12] Recently the focus of ultrafast studies has shifted from spherical particles over nanorods toward truly asymmetric structures such as prisms.[4,13−15] These particles often exhibit special crystalline structures with well-defined orientation,[16] which influence not only the growth and stability but also the optical and acoustic properties.[17]

The vibrational dynamics of nano-objects have been studied by a myriad of ultrafast optical pump−probe experiments looking at absorption, reflection, or scattering of ensembles.[3,4,6] Because the polydispersity of the samples leads to a dephasing of the observed vibrations, more recently such experiments were carried out on individual nano-objects.[18,19] Although much has been learned by optical techniques and the simulations using continuum mechanics or molecular dynamics, a thorough discussion of purely optical measurements is required to obtain information about the amplitude and phase with which individual vibrational modes are excited.[4,5,20,21] Ultrafast structural tools such as ultrafast X-ray or electron diffraction are the most direct ways to study changes of the crystal lattice induced by laser excitation. Although diffraction on the femtosecond time scale started to become available 20 years ago, only very few studies of nanoparticle dynamics with dynamics faster than 100 ps have been reported.[22−24] An experiment at the free-electron laser has monitored the breathing[25] and melting[26] of a single few hundred nanometers large ellipsoidal nanocrystal. Studying asymmetric and much thinner objects has, however, remained a challenge, and, in general, ultrafast single-particle studies using X-rays can exclusively be performed at free-electron laser facilities.[10] Demonstrating the possibility to use a laser-based femtosecond X-ray source for ultrafast structural measurements on ensembles of nanoparticles is therefore a major breakthrough.

We present such ultrafast X-ray diffraction (UXRD) experiments that precisely determine the average out-of-plane

Received: November 18, 2016
Revised: November 25, 2016
Published: November 27, 2016

DOI: 10.1021/acs.jpcc.6b11651
J. Phys. Chem. C 2016, 120, 28894−28899

strain $\varepsilon(t)$ of an ensemble of <111> oriented gold nanotriangles (NTs) as a function of the time delay t after the excitation. On the basis of the sound velocity v_{111} = 3.528 nm/ps along the [111] direction,[27] the oscillation period of T = 3.6 ps corresponding to the fastest out-of-plane vibration mode yields a particle thickness $d_0 = v_{111} \cdot T/2$ = 6.4 nm, consistent with particle shape characterized by thorough TEM measurements. The amplitude of the first oscillation and the maximal expansion $\varepsilon_{max} = 3 \times 10^{-3}$ of the particle after ~20 ps are consistent with a 1D acoustic model, where the expansion mode of the film is excited by a time-dependent pressure $\sigma(t)$ imposed by hot electrons and phonons. The pump−pulse absorption is calculated by a complete 3D numerical optical model.[19,28,29] A careful analysis by electron microscopy is used to prove that the NTs shape is robust under the experimental conditions. From the measured lattice strain, ε, one can directly read the temperature change ΔT_0 via

$$\epsilon = \int_{T_0}^{T_0+\Delta T_0} \alpha_{Au}(T)\, dT \quad (1)$$

using the expansion coefficient $\alpha_{Au}(T)$ measured in thermal equilibrium. The cooling on the nanosecond time scale evidences the rather good thermal insulation given by the ~1 nm thick organic layer that was used for functionalizing the surface of the silicon substrate.

EXPERIMENTAL SECTION

Very thin gold NTs were prepared in a one-step synthesis in the presence of mixed AOT/phospholipid vesicles via a process that can be described by an Ostwald ripening growth mechanism.[31] To reduce the polydispersity of the product, the anisotropic nanoparticles were separated by using a combined polyelectrolyte/AOT micelle depletion flocculation.[31] The NTs were deposited on a silicon wafer functionalized by 3-mercaptopropyltrimethoxysilane (3-MPTMS).[32] The NTs were attached to the thiol group at a distance of ~1 nm above the Si surface. AFM investigations of >40 nanoplatelets reveal an average thickness of 8.5 ± 1.5 nm. Subtracting 1 nm of the 3-MPTMS layer, this is in full agreement with the 6.4 nm platelet thickness derived from the UXRD data. Figure 1 shows a thorough characterization of the sample by electron microscopy. The sideview (Figure 1a) of two individual NTs with 6.7 and 8.2 nm thickness illustrates the thickness of ~7.5 ± 1.5 nm. While the base length of the NTs is ~150 nm with a large size distribution (Figure 1d), the distribution of the platelet-thickness is rather sharp. The zoom into the NTs (Figure 1b)) can be Fourier-transformed to determine the periodicity of the lattice structure. Figure 1c proves the <111> orientation of the entire triangle.[30] Figure 1e confirms that the NTs are intact after UXRD experiments performed at a base temperature T_0 = 24 K with a pump wavelength of 400 nm and a fluence of F = 2.9 mJ/cm^2. Figure 1f,g shows the permanent deformation of the NTs under similar fluence conditions at room temperature. The UXRD experiments[33−35] subsequently discussed in this paper were conducted under the nondestructive conditions T_0 = 24 K and F = 2.9 mJ/cm^2. The pump pulses had a duration of ~80 fs, and the pulse length of the hard X-ray probe pulses at 8 keV derived from a laser-driven plasma source reduced the time resolution of the setup to ~200 fs.[34,35] Figure 2 illustrates the static XRD characterization of the sample in the geometry of the UXRD setup.[34] Figure 2b shows the reciprocal space map of the pristine sample, whereas the integrated X-ray diffraction intensity as a function of the Bragg angle θ in Figure 2a also reports a comparison to the diffraction from a sample after excessive irradiation with optical pump-pulses at 300 K. The reshaping of the Bragg peak indicating the permanent deformation of the gold particles at high fluence excitation at room temperature is clearly visible also in the reciprocal space map (not shown). The very weak and broad reflection from the gold (1 1 1) lattice planes (Figure 2b) renders the UXRD data acquisition extremely difficult, especially because the fluence must be reduced such that no sample damage occurs during several hours of optical pumping. Figure 2c compares the shifted Bragg peaks after 2.1 and 19 ps in the UXRD experiment with the Bragg peak at negative pump−probe delay. At low temperature and with the applied fluence the shape of these peaks is unchanged during the acquisition of the UXRD data.

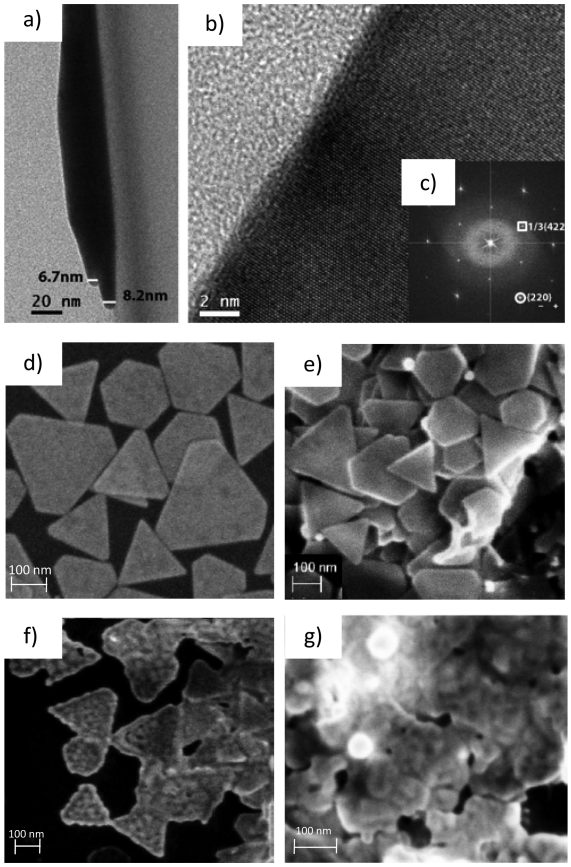

Figure 1. TEM and SEM pictures of the gold nanotriangle sample. (a) TEM sideview of gold-NTs. (b) High-resolution TEM and (c) its Fourier transform show 1/3{422} and {220} reflections characteristic of NTs with <111> orientation.[30] (d) SEM micrograph showing the polydisperse nature of the nanoplatelets. (e) SEM micrograph of the sample after the pump−probe experiment at T_0 = 24 K with F = 2.9 mJ/cm^2. (f) SEM micrograph of the sample after treatment with F = 3 mJ/cm^2 at room temperature. (g) Same for F = 5 mJ/cm^2. Triangles deform or melt together and reshape to spheres.

DOI: 10.1021/acs.jpcc.6b11651
J. Phys. Chem. C 2016, 120, 28894−28899

The Journal of Physical Chemistry C Article

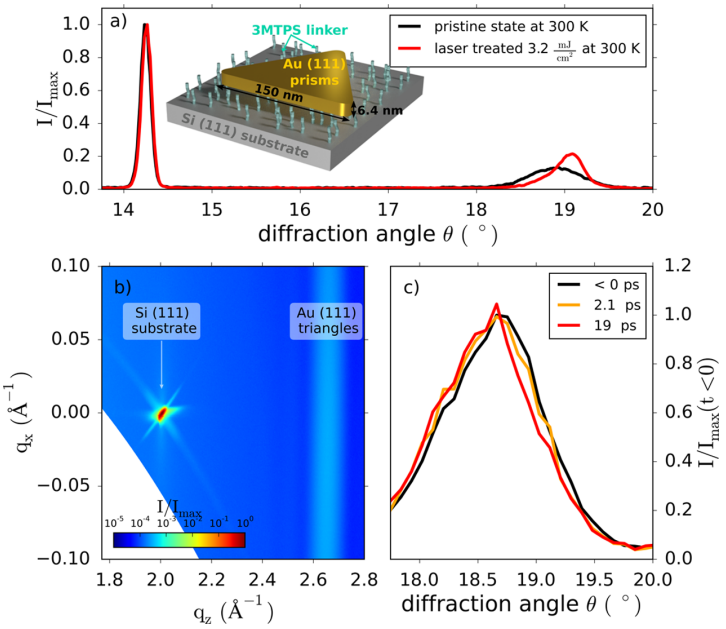

Figure 2. (a) Integrated X-ray intensity as a function of the Bragg angle θ for the pristine sample (black) and for a sample spot that was excessively irradiated at room temperature (red). Inset: Schematic of the ideal situation where all gold-NTs are attached to the surface with equally long organic spacer molecules. (b) Reciprocal space map showing the sharp Si substrate peak and the very weak and broad reflection of the gold NTs. The diffraction does not correspond to a Debye−Scherrer ring but to a single-crystal diffraction with a large mosaic spread of about ±5° originating from the nonperfect sample that also contains stacked NTs. (c) Integrated X-ray diffraction intensity for three different time delays at a fluence of 2.9 mJ/cm^2 that does not permanently modify the sample. We essentially observe a peak shift to smaller angles, indicating the ultrafast out-of-plane expansion.

RESULTS AND DISCUSSION

Figure 3 shows the lattice strain $\varepsilon(t)$ as a function of the time delay t after excitation of the gold NTs at T_0 = 24 K with 400 nm pulses. The fluence F = 2.9 mJ/cm^2 is given by the light intensity on the sample surface at the incidence angle of 40°. The femtosecond pulse excitation leads to an oscillation of the measured out-of-plane strain with a period of T = 3.6 ps, which is consistent with the fundamental breathing mode of a film with thickness 6.4 nm. The strain reaches a first maximum of $\varepsilon = 2.3 \pm 0.3 \times 10^{-3}$ after ∼2 ps. The signal oscillates and reaches a maximum of $\varepsilon_{max} = 3 \pm 0.3 \times 10^{-3}$ after ∼20 ps. The lattice slowly contracts on a nanosecond time scale as the heat flows out of the nanoparticle.

To interpret the observed maximum expansion ε_{max}, we calculated the temperature rise of a gold NT originating from the absorption of 400 nm pulses under 40° incidence. We computed the absorption cross-section using a finite-element approach accounting for the inhomogeneous nano-object environment induced by its deposition on a silicon substrate,[19,28,29] yielding σ_{abs} = 1200 nm^2 for NTs with 6.4 nm thickness and 150 nm side length. Neglecting heat transfer to the environment on short time scale, the temperature rise of a thermalized gold NT ΔT_0 = 285 K at T_0 = 24 K is calculated by numerical integration of

$$\sigma_{abs} F/(\rho_{Au} V) = \int_{T_0}^{T_0+\Delta T_0} c_{Au}(T)\, dT \quad (2)$$

where ρ_{Au} = 19.3 g/cm^3 is the density, $c_{Au}(T)$ is the strongly temperature-dependent heat capacity of gold, and V is the volume of the particle. From eq 1 we calculate an expansion of $\varepsilon^{calc} = 3 \times 10^{-3}$, in excellent agreement with the data. For room temperature, the calculation yields the same result. This can be understood by invoking the Grüneisen parameter of gold, γ, which is a temperature-independent[36,37] measure of the thermal stress $\sigma = \gamma \cdot Q$ upon deposition of an energy density Q.[37] The heat expansion coefficient $\alpha(T)$ and heat capacity $c(T)$ share the same temperature dependence, both for the electronic contribution and for the phonon contribution, which are given by their quantum nature. Therefore, the electronic and phononic Grüneisen parameters of gold $\gamma_e \sim \alpha_e(T)/c_e(T)$ and $\gamma_p \sim \alpha_p(T)/c_p(T)$ are independent of temperature.

To quantitatively describe the oscillation of the signal at short times, we have to account for the fact that the optical excitation first heats up the electron gas, yielding a corresponding electron stress σ_e driving the out-of-plane expansion of the NT. We estimate an electronic temperature rise of T_e(100 fs) = 4000 K from the electronic specific heat of $c_e(T) = \gamma_s T$, where $\gamma_s = 3.7 \times 10^{-6}$J/(gK) is the Sommerfeld-coefficient of gold.[38] The electron pressure $\sigma_e(t) = \gamma_e Q_e(t) = \gamma_e Q^e_{max} e^{-t/\tau_e}$ relaxes with the characteristic electron−phonon coupling time τ_e. With the same time constant, the phonon pressure $\sigma_p(t) = \gamma_p Q^p_{eq}(1 - e^{-t/\tau_e})$ rises until the electron and phonon temperatures have equilibrated. The electron−phonon coupling time in gold in the low perturbation limit is 1 ps at room temperature and 0.6 ps at 24 K.[39,40] However, under strong excitation conditions, the electronic heat capacity c_e rises with temperature, and equilibration times can exceed 5 ps under our conditions.[38,41,42] At t = 20 ps, we can safely assume that the electron and phonon system have reached a mutual

DOI: 10.1021/acs.jpcc.6b11651
J. Phys. Chem. C 2016, 120, 28894−28899

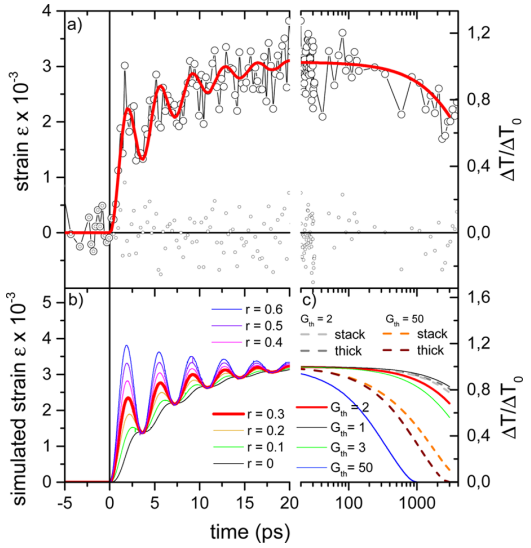

Figure 3. (a) Time-dependent strain measured by UXRD (open circles) together with the best fits from the models (red lines). The time axis is split according to the two models. The small dots represent the difference of the data and the simulation indicating only little contributions from additional vibrational modes. The relative error 3×10^{-4} of the strain measurement is estimated from the variation of data for $t < 0$ and around the maximum. (b) Model simulation according to eq 4 with a single oscillator driven by the phononic and electronic stresses according to eq 3. $r = \gamma_e/\gamma_p$ is ratio of the electronic and phononic Grüneisen parameters. (c) Results from the 3D heat-transport simulations. The thin lines are obtained for a single Au triangle separated from Si by a layer with a thermal interface conductance G_{th} in MW/(m^2 K). The fat red line indicates the best fit that is reproduced in panel a. The dashed lines are cross-checks for heat transport out of three stacked NTs (see the text).

thermal equilibrium so that a single temperature suffices to describe both systems.

The UXRD data provide a unique access to the phase and amplitude of the oscillations, which are both sensitive to the exact form of the total driving stress, which is given by the following functional form[42−44]

$$\sigma(t) = \sigma_e(t) + \sigma_p(t) = \sigma_\infty H(t)\left(1 + \left(\frac{\gamma_e}{\gamma_p} - 1\right)e^{-t/\tau_e}\right) \quad (3)$$

where $H(t)$ denotes the Heaviside function. The maximum stress $\sigma_\infty = C_{eff}\varepsilon(20\text{ ps})$ can be deduced from the measured strain and the effective elastic modulus C_{eff} along the [111] direction. To model the early time vibrations (Figure 3a), we consider the homogeneous increase of the particle thickness $d(t)$ as the only relevant vibrational mode with frequency ω_0 and damping rate η. It is excited by the time-dependent stress $\sigma(t)$ stated in eq 3. The explicit differential equation used to describe the time-dependent out-of-plane strain $\varepsilon(t) = \frac{d(t) - d_0}{d_0}$ of the particles is then

$$\frac{d^2\varepsilon}{dt^2} + 2\eta\frac{d\varepsilon}{dt} + \omega_0^2\varepsilon = P\sigma(t) \quad (4)$$

The constant prefactor P on the right-hand side is due to dimensional reasons as it relates the driving stress $\sigma(t)$ to an acceleration of the strain. The equation of motion can be solved using the Green's function of the damped harmonic oscillator $G(t, t') = H(t - t')\frac{i}{\omega_- - \omega_+}(e^{i\omega_+(t-t')} - e^{i\omega_-(t-t')})$, where $\omega_\pm = i\eta \pm \sqrt{\omega_0^2 - \eta^2}$. The time-dependent strain can then simply be found via integration

$$\varepsilon(t) = P\int_{-\infty}^{t'} G(t, t')\sigma(t')\,dt' \propto \int_{-\infty}^{t'} G(t, t')\sigma(t')\,dt' \quad (5)$$

The magnitude of the prefactor P is dictated by the strain that is attained after the oscillations are damped out. We vary $P{\cdot}\sigma_\infty$ to match the signal at t = 20 ps and adjust the ratio r of the Grüneisen parameters to $r = \gamma_e/\gamma_p = 0.3$ and the damping constant η = 0.15 ps^{-1} to match the amplitude of the first oscillations. The time constant τ_e = 6.5 ps is found to be close to those previously measured in similar strong perturbation conditions.[38] Figure 3a shows the measured data (open circles) together with the fit according to this model (red line) up to 20 ps. The black dots in Figure 3 represent the difference $\varepsilon_{exp}(t) - \varepsilon_{sim}(t)$ of the data and the simulation. They give an estimate of how much vibrational modes with lower frequency contribute to the out-of-plane expansion of the NTs. Because of the lateral size distribution, we expect that contributions by low-frequency modes rapidly dephase and thus are below the noise level. The left panel of Figure 3b shows simulations with a ratio $r = \gamma_e/\gamma_p$ varied from 0 to 0.6. The best fit is obtained for r = 0.3, a value that is smaller than the theoretical ratio expected for bulk gold r = 0.5[42] but consistent with other experiments performed on acoustic vibrations of small noble-metal nanoparticles.[43] We note that for $0 < r < 1$ the phase of the oscillation is delayed more and more as r approaches zero. For $r > 1$ the oscillations would start somewhat earlier. Therefore, both the amplitude and the phase of the observed UXRD signal allow us to assess the temporal form of the driving stress $\sigma(t)$.

For larger time delays (right panel), we plot the data on a logarithmic time axis and the red line represents the results of a 3D finite-element model of NT cooling, accounting for both 3D heat diffusion and thermal resistance at the triangle/substrate interface. We simulated a 6.4 nm thick gold triangle with initial temperature $T_i = T_0 + \Delta T$, which is attached to a Si substrate with a fixed temperature of T_0 = 24 K at the backside. Initial heating of the absorbing substrate was neglected as it weakly affects the cooling dynamics of the triangle due to the high thermal conductivity of silicon. We take the temperature-dependent bulk values[45−47] of the heat capacity $c_{Au/Si}$ and thermal conductivity $\kappa_{Au/Si}$ for Si and Au and account for the 1 nm thick organic layer by imposing a thermal interface conductance of G_{th} = 2 MW/(m^2 K) between Au and Si. This numerical value yields the best fit to the data in the model where a single gold particle is separated from the Si surface by an organic layer. For an epitaxial Au film on Si, one would expect an interface conductance of 50 to 150 MW/(m^2 K), which would lead to a much faster cooling.[48] For convenience, heat diffusion simulations with varying interface conductance are shown in Figure 3c for t > 20 ps as thin solid lines. The best fit G_{th} = 2 MW/(m^2 K) is shown as a thick line. To estimate the systematic error originating from the model, we also simulated the heat flow out of a "stack" of three gold NTs, which, in addition to the finite Au/Si thermal interface conductance G_{th}, have the same interface conductance between each gold

DOI: 10.1021/acs.jpcc.6b11651
J. Phys. Chem. C 2016, 120, 28894−28899

particle. As a further crosscheck, we have plotted results for "thick" NTs with a triple thickness and with only one interface with G_{th} from the gold to Si. All three models require the heat flow out of the particles to be strongly reduced by the 1 nm organic layer in comparison with a direct contact of Au on Si to achieve a good fit. The interface conductance is considerably lower than the values above 50 MW/(m^2 K) derived for Au–water interfaces with various surface functionalizations[49] and for the interface conductance of Au to Quartz across a self-assembled monolayer.[50,51] The attempt to rationalize the reduced heat flow by a low thermal conductivity of the 1 nm thick 3-MPTMS layer would require a value of 2×10^{-3}W/mK typical of dilute gases. We can therefore conclude that the slow cooling dynamics observed experimentally mostly originates from a low thermal conductance at the Au–Si interface.

CONCLUSIONS

Ultrafast X-ray diffraction measurements on an ensemble of 6.4 nm thick gold NTs directly and quantitatively measure the out-of plane expansion dynamics after optical excitation at 400 nm. The primary oscillatory motion can be explained by a single damped out-of-plane breathing mode with a period of T = 3.6 ps. The phase and amplitude of the UXRD signal are sensitive measures of the functional form $\sigma(t)$ of the time-dependent stress from hot electrons and phonons. The cooling time of several nanoseconds is dictated by the 1 nm thin organic layer that connects the gold-NTs to the silicon substrate. We can rationalize the observations by numerical models. In comparison with the situation expected for a thin gold layer on Si, our experiments demonstrate a slight modification of the relative ratio of the electronic and phononic Grüneisen parameters and a surprisingly strong reduction of heat conduction by a thin organic functional layer. Future UXRD studies on monodisperse asymmetric Au nanoparticles might also be able to quantify the contributions of other vibrational modes and can finally lead to a microscopic understanding of their reshaping under laser excitation. We believe that this pioneering experiment studying the dynamics of nanoparticles with a laser-based femtosecond X-ray source may trigger a broad range of novel experiments, for example, studying the nanoparticle temperature in photocatalytic experiments or during the magnetic heating of nanoparticles for catalysis. We emphasize that the heat-transport characteristics can be obtained by our method via synchrotron-based time-resolved X-ray diffraction, which is accessible for users from any field of natural sciences.

AUTHOR INFORMATION

Corresponding Author

*E-mail: bargheer@uni-potsdam.de. Tel: +49 (0)331 977 4272. Fax: +49 (0)331 977 5493.

ORCID

M. Bargheer: 0000-0002-0952-6602

Notes

The authors declare no competing financial interest.

ACKNOWLEDGMENTS

R.M.S. and F.S. acknowledge financial support by the DFG via the graduate school SALSA, J.P. is supported by the DFG via BA 2281/8-1, and F.L. is supported via KO 1387/14-1.

REFERENCES

(1) Tchebotareva, A.; Ruijgrok, P.; Zijlstra, P.; Orrit, M. Probing the Acoustic Vibrations of Single Metal Nanoparticles by Ultrashort Laser Pulses. *Laser Photonics Reviews* **2010**, *4*, 581–597.

(2) Chen, K.; Razinskas, G.; Feichtner, T.; Grossmann, S.; Christiansen, S.; Hecht, B. Electromechanically Tunable Suspended Optical Nanoantenna. *Nano Lett.* **2016**, *16*, 2680–2685.

(3) Crut, A.; Maioli, P.; Del Fatti, N.; Vallée, F. Time-Domain Investigation of the Acoustic Vibrations of Metal Nanoparticles: Size and Encapsulation Effects. *Ultrasonics* **2015**, *56*, 98–108.

(4) Crut, A.; Maioli, P.; Del Fatti, N.; Vallée, F. Acoustic Vibrations of Metal Nano-Objects: Time-Domain Investigations. *Phys. Rep.* **2015**, *549*, 1–43.

(5) Huang, W.; Qian, W.; El-Sayed, M. A. Coherent Vibrational Oscillation in Gold Prismatic Monolayer Periodic Nanoparticle Arrays. *Nano Lett.* **2004**, *4*, 1741–1747.

(6) Hartland, G. V. Coherent Excitation of Vibrational Modes in Metallic Nanoparticles. *Annu. Rev. Phys. Chem.* **2006**, *57*, 403–430.

(7) Blum, O.; Shaked, N. Prediction of Photothermal Phase Signatures from Arbitrary Plasmonic Nanoparticles and Experimental Verification. *Light: Sci. Appl.* **2015**, *4*, e322.

(8) Cahill, D. G.; Ford, W. K.; Goodson, K. E.; Mahan, G. D.; Majumdar, A.; Maris, H. J.; Merlin, R.; Phillpot, S. R. Nanoscale Thermal Transport. *J. Appl. Phys.* **2003**, *93*, 793–818.

(9) Cahill, D. G.; Braun, P. V.; Chen, G.; Clarke, D. R.; Fan, S.; Goodson, K. E.; Keblinski, P.; King, W. P.; Mahan, G. D.; Majumdar, A.; et al. Nanoscale Thermal Transport. II. 2003–2012. *Appl. Phys. Rev.* **2014**, *1*, 011305.

(10) Hartland, G. V.; Shang Lo, S. Spectroscopy Beyond the Single-Particle Limit. *Science* **2013**, *341*, 36–37.

(11) Sauceda, H. E.; Mongin, D.; Maioli, P.; Crut, A.; Pellarin, M.; Del Fatti, N.; Vallée, F.; Garzón, I. L. Vibrational Properties of Metal Nanoparticles: Atomistic Simulation and Comparison with Time-Resolved Investigation. *J. Phys. Chem. C* **2012**, *116*, 25147–25156.

(12) Juvé, V.; Crut, A.; Maioli, P.; Pellarin, M.; Broyer, M.; Del Fatti, N.; Vallée, F. Probing Elasticity at the Nanoscale: Terahertz Acoustic Vibration of Small Metal Nanoparticles. *Nano Lett.* **2010**, *10*, 1853–1858.

(13) Major, T. A.; Lo, S. S.; Yu, K.; Hartland, G. V. Time-Resolved Studies of the Acoustic Vibrational Modes of Metal and Semiconductor Nano-objects. *J. Phys. Chem. Lett.* **2014**, *5*, 866–874.

(14) Mahmoud, M. A.; O'Neil, D.; El-Sayed, M. A. Shape- and Symmetry-Dependent Mechanical Properties of Metallic Gold and Silver on the Nanoscale. *Nano Lett.* **2014**, *14*, 743–748.

(15) Fedou, J.; Viarbitskaya, S.; Marty, R.; Sharma, J.; Paillard, V.; Dujardin, E.; Arbouet, A. From Patterned Optical Near-Fields to High Symmetry Acoustic Vibrations in Gold Crystalline Platelets. *Phys. Chem. Chem. Phys.* **2013**, *15*, 4205–4213.

(16) Köth, A.; Appelhans, D.; Prietzel, C.; Koetz, J. Asymmetric Gold Nanoparticles Synthesized in the Presence of Maltose-Modified Poly(ethyleneimine). *Colloids Surf., A* **2012**, *414*, 50–56.

(17) Goubet, N.; Yan, C.; Polli, D.; Portalès, H.; Arfaoui, I.; Cerullo, G.; Pileni, M.-P. Modulating Physical Properties of Isolated and Self-Assembled Nanocrystals through Change in Nanocrystallinity. *Nano Lett.* **2013**, *13*, 504–508.

(18) Zijlstra, P.; Orrit, M. Single Metal Nanoparticles: Optical Detection, Spectroscopy and Applications. *Rep. Prog. Phys.* **2011**, *74*, 106401.

(19) Crut, A.; Maioli, P.; Del Fatti, N.; Vallée, F. Optical Absorption and Scattering Spectroscopies of Single Nano-Objects. *Chem. Soc. Rev.* **2014**, *43*, 3921–3956.

(20) Del Fatti, N.; Voisin, C.; Chevy, F.; Vallée, F.; Flytzanis, C. Coherent Acoustic Mode Oscillation and Damping in Silver Nanoparticles. *J. Chem. Phys.* **1999**, *110*, 11484–11487.

(21) Bonacina, L.; Callegari, A.; Bonati, C.; van Mourik, F.; Chergui, M. Time-Resolved Photodynamics of Triangular-Shaped Silver Nanoplates. *Nano Lett.* **2006**, *6*, 7–10.

DOI: 10.1021/acs.jpcc.6b11651
J. Phys. Chem. C 2016, 120, 28894–28899

(22) Ruan, C.-Y.; Murooka, Y.; Raman, R. K.; Murdick, R. A. Dynamics of Size-Selected Gold Nanoparticles Studied by Ultrafast Electron Nanocrystallography. *Nano Lett.* **2007**, *7*, 1290−1296.
(23) Plech, A.; Kürbitz, S.; Berg, K.-J.; Graener, H.; Berg, G.; Grésillon, S.; Kaempfe, M.; Feldmann, J.; Wulff, M.; von Plessen, G. Time-Resolved X-Ray Diffraction on Laser-Excited Metal Nanoparticles. *Europhys. Lett.* **2003**, *61*, 762−768.
(24) Plech, A.; Kotaidis, V.; Grésillon, S.; Dahmen, C.; von Plessen, G. Laser-Induced Heating and Melting of Gold Nanoparticles Studied by Time-Resolved X-Ray Scattering. *Phys. Rev. B: Condens. Matter Mater. Phys.* **2004**, *70*, 195423.
(25) Clark, J. N.; Beitra, L.; Xiong, G.; Higginbotham, A.; Fritz, D. M.; Lemke, H. T.; Zhu, D.; Chollet, M.; Williams, G. J.; Messerschmidt, M.; et al. Ultrafast Three-Dimensional Imaging of Lattice Dynamics in Individual Gold Nanocrystals. *Science* **2013**, *341*, 56−59.
(26) Clark, J. N.; Beitra, L.; Xiong, G.; Fritz, D. M.; Lemke, H. T.; Zhu, D.; Chollet, M.; Williams, G. J.; Messerschmidt, M. M.; Abbey, B.; et al. Imaging Transient Melting of a Nanocrystal using an X-Ray Laser. *Proc. Natl. Acad. Sci. U. S. A.* **2015**, *112*, 7444−7448.
(27) Neighbours, J. R.; Alers, G. A. Elastic Constants of Silver and Gold. *Phys. Rev.* **1958**, *111*, 707−712.
(28) Davletshin, Y. R.; Lombardi, A.; Cardinal, M. F.; Juvé, V.; Crut, A.; Maioli, P.; Liz-Marzán, L. M.; Vallée, F.; Del Fatti, N.; Kumaradas, J. C. A Quantitative Study of the Environmental Effects on the Optical Response of Gold Nanorods. *ACS Nano* **2012**, *6*, 8183−8193.
(29) Pertreux, E.; Lombardi, A.; Florea, I.; Spuch-Calvar, M.; Gómez-Graña, S.; Ihiawakrim, D.; Hirlimann, C.; Ersen, O.; Majimel, J.; Tréguer-Delapierre, M.; et al. Surface Plasmon Resonance of an Individual Nano-Object on an Absorbing Substrate: Quantitative Effects of Distance and 3D Orientation. *Adv. Opt. Mater.* **2016**, *4*, 567−577.
(30) Germain, V.; Li, J.; Ingert, D.; Wang, Z. L.; Pileni, M. P. Stacking Faults in Formation of Silver Nanodisks. *J. Phys. Chem. B* **2003**, *107*, 8717−8720.
(31) Liebig, F.; Thünemann, A.; Koetz, J. Ostwald Ripening Growth Mechanism of Gold Nanotriangles in Vesicular Template Phases. *Langmuir* **2016**, *32*, 10928−10935.
(32) Xie, W.; Walkenfort, B.; Schlücker, S. Label-Free SERS Monitoring of Chemical Reactions Catalyzed by Small Gold Nanoparticles Using 3D Plasmonic Superstructures. *J. Am. Chem. Soc.* **2013**, *135*, 1657−1660.
(33) Schick, D.; Shayduk, R.; Bojahr, A.; Herzog, M.; von Korff Schmising, C.; Gaal, P.; Bargheer, M. Ultrafast Reciprocal-Space Mapping with a Convergent Beam. *J. Appl. Crystallogr.* **2013**, *46*, 1372−1377.
(34) Schick, D.; Bojahr, A.; Herzog, M.; von Korff Schmising, C.; Shayduk, R.; Leitenberger, W.; Gaal, P.; Bargheer, M. Normalization Schemes for Ultrafast X-Ray Diffraction Using a Table-Top Laser-Driven Plasma Source. *Rev. Sci. Instrum.* **2012**, *83*, 025104.
(35) Schick, D.; Bojahr, A.; Herzog, M.; Gaal, P.; Vrejoiu, I.; Bargheer, M. Following Strain-Induced Mosaicity Changes of Ferroelectric Thin Films by Ultrafast Reciprocal Space Mapping. *Phys. Rev. Lett.* **2013**, *110*, 095502.
(36) Nix, F. C.; MacNair, D. The Thermal Expansion of Pure Metals: Copper, Gold, Aluminum, Nickel, and Iron. *Phys. Rev.* **1941**, *60*, 597−605.
(37) McLean, K. O.; Swenson, C. A.; Case, C. R. Thermal Expansion of Copper, Silver, and Gold Below 30 K. *J. Low Temp. Phys.* **1972**, *7*, 77−98.
(38) Del Fatti, N.; Arbouet, A.; Vallée, F. Femtosecond Optical Investigation of Electron-Lattice Interactions in an Ensemble and a Single Metal Nanoparticle. *Appl. Phys. B: Lasers Opt.* **2006**, *84*, 175−181.
(39) Groeneveld, R. H. M.; Sprik, R.; Lagendijk, A. Femtosecond Spectroscopy of Electron-Electron and Electron-Phonon Energy Relaxation in Ag and Au. *Phys. Rev. B: Condens. Matter Mater. Phys.* **1995**, *51*, 11433−11445.
(40) Arbouet, A.; Voisin, C.; Christofilos, D.; Langot, P.; Del Fatti, N.; Vallée, F.; Lermé, J.; Celep, G.; Cottancin, E.; Gaudry, M.; et al. Electron-Phonon Scattering in Metal Clusters. *Phys. Rev. Lett.* **2003**, *90*, 177401.
(41) Kiel, M.; Möhwald, H.; Bargheer, M. Broadband Measurements of the Transient Optical Complex Dielectric Function of a Nanoparticle/Polymer Composite upon Ultrafast Excitation. *Phys. Rev. B: Condens. Matter Mater. Phys.* **2011**, *84*, 165121.
(42) Nicoul, M.; Shymanovich, U.; Tarasevitch, A.; von der Linde, D.; Sokolowski-Tinten, K. Picosecond Acoustic Response of a Laser-Heated Gold-Film Studied with Time-Resolved X-Ray Diffraction. *Appl. Phys. Lett.* **2011**, *98*, 191902.
(43) Voisin, C.; Del Fatti, N.; Christofilos, D.; Vallée, F. Time-Resolved Investigation of the Vibrational Dynamics of Metal Nanoparticles. *Appl. Surf. Sci.* **2000**, *164*, 131−139.
(44) Wright, O. B. Ultrafast Nonequilibrium Stress Generation in Gold and Silver. *Phys. Rev. B: Condens. Matter Mater. Phys.* **1994**, *49*, 9985−9988.
(45) Ho, C. Y.; Powell, R. W.; Liley, P. E. Thermal Conductivity of the Elements. *J. Phys. Chem. Ref. Data* **1972**, *1*, 279−421.
(46) Flubacher, P.; Leadbetter, A.; Morrison, J. The Heat Capacity of Pure Silicon and Germanium and Properties of their Vibrational Frequency Spectra. *Philos. Mag.* **1959**, *4*, 273−294.
(47) Geballe, T. H.; Giauque, W. F. The Heat Capacity and Entropy of Gold from 15 to 300K. *J. Am. Chem. Soc.* **1952**, *74*, 2368−2369.
(48) Duda, J. C.; Yang, C.-Y. P.; Foley, B. M.; Cheaito, R.; Medlin, D. L.; Jones, R. E.; Hopkins, P. E. Influence of Interfacial Properties on Thermal Transport at Gold:Silicon Contacts. *Appl. Phys. Lett.* **2013**, *102*, 081902.
(49) Ge, Z.; Cahill, D. G.; Braun, P. V. Thermal Conductance of Hydrophilic and Hydrophobic Interfaces. *Phys. Rev. Lett.* **2006**, *96*, 186101.
(50) Losego, M.; Grady, M.; Sottos, N.; Cahill, D.; Braun, P. Effects of Chemical Bonding on Heat Transport Across Interfaces. *Nat. Mater.* **2012**, *11*, 502−506.
(51) O'Brien, P.; Shenogin, S.; Liu, J.; Chow, P.; Laurencin, D.; Mutin, P.; Yamaguchi, M.; Keblinski, P.; Ramanath, G. Bonding-Induced Thermal Conductance Enhancement at Inorganic Heterointerfaces Using Nanomolecular Monolayers. *Nat. Mater.* **2012**, *12*, 118−122.

DOI: 10.1021/acs.jpcc.6b11651
J. Phys. Chem. C 2016, 120, 28894−28899

Article VI

Scaling-Up Nano-Plasmon Catalysis: The Role of Heat Dissipation

Radwan M. Sarhan, Wouter Koopman, Jan Pudell, **Felix Stete**, Matthias Rössle, Marc Herzog, Clemens Schmitt, Ferenc Liebig, Joachim Koetz, and Matias Bargheer

The Journal of Physical Chemistry C 123, 14 (2019)

THE JOURNAL OF PHYSICAL CHEMISTRY C

Article

Cite This: J. Phys. Chem. C 2019, 123, 9352−9357

pubs.acs.org/JPCC

Scaling Up Nanoplasmon Catalysis: The Role of Heat Dissipation

Radwan M. Sarhan,[†,§] Wouter Koopman,*[,†] Jan Pudell,[†] Felix Stete,[†,§] Matthias Rössle,[∥] Marc Herzog,[†] Clemens N. Z. Schmitt,[⊥] Ferenc Liebig,[‡] Joachim Koetz,[‡] and Matias Bargheer*[†,∥]

[†]Institute of Physics and Astronomy and [‡]Institute of Chemistry, University of Potsdam, 14476 Potsdam, Germany

[§]School of Analytical Sciences Adlershof (SALSA), Humboldt-Universita¨t zu Berlin, Albert-Einstein-Str. 5-9, 10099 Berlin, Germany

[∥]Helmholtz Zentrum Berlin, Albert-Einstein-Straße 15, 12489 Berlin, Germany

[⊥]Max Planck Institute of Colloids and Interfaces, 14476 Potsdam, Germany

Supporting Information

ABSTRACT: Nanoscale heating by optical excitation of plasmonic nanoparticles offers a new perspective of controlling chemical reactions, where heat is not spatially uniform as in conventional macroscopic heating but strong temperature gradients exist around microscopic hot spots. In nanoplasmonics, metal particles act as a nanosource of light, heat, and energetic electrons driven by resonant excitation of their localized surface plasmon resonance. As an example of the coupling reaction of 4-nitrothiophenol into 4,4′-dimercaptoazobenzene, we show that besides the nanoscopic heat distribution at hot spots, the microscopic distribution of heat dictated by the spot size of the light focus also plays a crucial role in the design of plasmonic nanoreactors. Small sizes of laser spots enable high intensities to drive plasmon-assisted catalysis. This facilitates the observation of such reactions by surface-enhanced Raman scattering, but it challenges attempts to scale nanoplasmonic chemistry up to large areas, where the excess heat must be dissipated by one-dimensional heat transport.

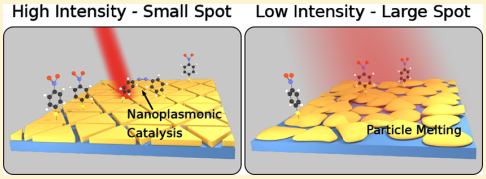

INTRODUCTION

Thermoplasmonics is a recently developed field of research, which started in 2002 for medical purposes.[1] Metal nanoparticles (NPs) have been used as a nanosource of heat for several applications such as photothermal cancer therapy,[2−5] bioimaging,[6] and nanosurgery.[7] Likewise, chemistry can benefit from nanoplasmonics, since many chemical reactions are heavily influenced by heat.[8−11]

Plasmonic metal nanostructures can be tuned to efficiently interact with light, converting the photons' energy into energetic charge carriers and heat. This allows noble metal nanoparticles to act as nanoreactors.[12] Chemical transformations of molecules attached to the particles' surfaces are fostered by the enhanced electromagnetic field at the particle surface along with generated energetic charge carriers and heat. As a result, plasmonic NPs present a unique playground for steering chemical transformation by light at the nanoscale.[13]

The first indications of nanoplasmonic chemistry were discovered in investigations using a micro-Raman apparatus to study surface enhanced Raman scattering (SERS) activity on nanoparticle templates.[14−16] In several microscope-based SERS experiments, the photons used for the Raman spectroscopy happen to also drive a catalytic reaction.[17−19] Recently, several important reaction types have been reported to be driven or catalyzed by plasmonic NPs such as the decomposition of organic molecules,[20,21] dissociation of hydrogen,[22,23] and oxidation−reduction reactions.[24,25]

In the current understanding, these chemical transformations are initialized by photogenerated energetic electrons. In addition, several studies have shown that the heat deposited in the particles by optical excitation enhances the reactions.[26−29] Heating by optical excitation of NPs is different from the conventional macroscopic heating because the heated volume is confined to certain hot spots or to the nanoparticle size. This may be exploited for controlling reactions at the nanometer scale and at specific locations. Around hot spots the cooling is generally three-dimensional (3D) and hence for low NP concentrations the heat can be quickly dissipated. Studying this nanoparticle heating is however rather difficult, as nanoscale thermometers are required.

In this article, we provide experimental evidence that removal of excess heat from the nanoscopic reaction site is a crucial factor for successful plasmonic chemistry, more importantly, for scaling up the plasmonic catalysis. In particular, the cooling geometry and the heat conductivity of the structure limits the maximum area of the plasmon-driven reaction, given by the spot size of the optical excitation. On the one hand, the light intensity (power per unit area) must have a minimum value to trigger plasmon-assisted catalytic reaction, but at the same time, the maximum power (not intensity) is limited by NP melting and/or destruction of the reactant or product molecules by excessive laser-driven static heating.

Received: December 31, 2018
Revised: March 7, 2019
Published: March 11, 2019

DOI: 10.1021/acs.jpcc.8b12574
J. Phys. Chem. C 2019, 123, 9352−9357

We investigated the static heating imposed on gold nanotriangles (NTs) by optical excitation by monitoring the shift of the nanoparticles' Bragg reflection via synchrotron-based X-ray diffraction (XRD). Subsequently, we verified, by SERS microscopy at very low light intensity, whether the plasmon-assisted reaction took place. Our measurements show that for small laser excitation spot sizes, the product formation could proceed, whereas for large spot sizes for the same light intensities, the SERS spectrum completely vanished. We reason that for microscopic excitation spot sizes, the deposited heat can be dissipated into a half sphere of the substrate in all three dimensions. In contrast, for very large excitation areas, the heat transport into the substrate is only in one dimension and therefore less effective. Therefore, the heat is trapped in the substrate for a much longer time, which enables melting of the plasmonic particles (the reaction platform). XRD measurements of the nanotriangles' lattice constant confirm that small laser excitation spot sizes lead to a lower temperature increase compared to the large spots for the same incident intensity. The faster rate of the 3D heat dissipation in a small excitation spot allows the excitation of the system with high light intensities necessary for the formation of the reaction product. In contrast, slower one-dimensional (1D) heat dissipation perpendicular to the substrate plane occurs for large spots sizes. The less efficient heat removal leads to higher temperatures and melting of the nanotriangles, as confirmed by scanning electron microscopy (SEM).

This phenomenon does not only explain the great success of observing plasmon-driven chemical reaction in SERS microscopes but also simultaneous absence of experiments evidencing plasmon-driven reactions over large surface areas. It also hints at the main advantage of nanoplasmonics for controlling chemical reactions, since unprecedented large heat dissipation rates can be found in a narrow spatial region of the hot spots.

MATERIALS AND EXPERIMENTAL METHODS

We used the plasmon-driven dimerization of 4-nitrothiophenol (4-NTP) into 4,4′-dimercaptoazobenzene (DMAB) as a model reaction.[30−32] This reaction is known to occur only in the presence of a plasmonic platform such as gold, silver, and copper nanoparticles.[33,34] The reaction is reasoned to occur as a result of the hot electrons generated upon the plasmon excitation,[35−37] whereas the influence of the plasmon-generated heat is a point of debate.[29,38] Here, we used a homogeneous large-scale monolayer of approximately 7 nm thick gold nanotriangles (NTs) deposited on substrates as the plasmonic platform.[39] The gold NTs were prepared using a one-step method in a mixed dioctyl sodium sulfo-succinate (AOT)/phospholipon vesicle phase in the presence of poly(*N*,*N*′-diallyl-*N*,*N*′-dimethylammonium-*alt*-3,5-bis-carboxyphenylmaleamic carboxylate (PalPhBisCarb) as a structure-directing agent and separated from spherical gold nanoparticles by depletion flocculation in the presence of AOT micelles.[40] The monolayer was formed at the liquid/air interface using a mixture of ethanol and toluene,[39] and it was then deposited on glass and silicon substrates after controlled evaporation of the solvents (compare Figure 1a). The extinction spectrum of the monolayer displayed a broad plasmon band located in the range of 500−2000 nm (inset in Figure 1), where it is in a good resonance with the excitation wavelengths. 4-NTP molecules were self-assembled on the gold NTs monolayer.

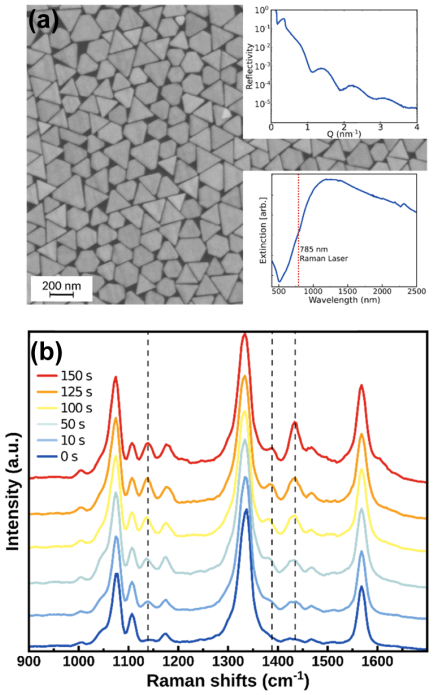

Figure 1. (a) SEM images of the gold NTs monolayer. The upper inset shows the X-ray reflectometry (XRR) data confirming a large-scale monolayer of approximately 7 nm thickness. The lower inset shows the optical extinction of a NT monolayer. (b) Time-dependent SERS spectra of 4-NTP assembled on the monolayer. Dashed lines indicate the three main product vibrational bands of DMAB.

The reaction was studied by SERS microscopy. Pronounced differences in the Raman spectra of the reactant (NTP) and product (DMAB) allowed us to assess the formation of DMAB. The heat expansion of the nanotriangles induced by continuous laser irradiation was measured by static X-ray diffraction at the KMC3-XPP end station of the Berlin synchrotron radiation facility BESSY II. A flat monolayer ordering of the nanotriangle SERS platform guaranteed that the lattice constant perpendicular to the triangles was oriented out of the substrate plane for all particles, which allows for low-intensity X-ray diffraction measurements in the symmetric Bragg configuration in any conventional XRD device.[39,41] The out-of-plane lattice expansion of the gold nanotriangles was calibrated by a careful measurement of the particles' lattice temperature. We conducted all experiments on different irradiated spots with varying sizes using different focusing conditions.

RESULTS AND DISCUSSION

We start our explanation by showing spectra of the 4-NTP molecules chemisorbed on our gold nanotriangle template in a typical SERS microscope with a 5 μm spot size (full width at half maximum, FWHM) using a continuous wave laser of 785 nm wavelength with a power of 30 mW. Figure 1a shows the transmission electron microscopy images of the well-ordered template and the X-ray reflectometry (XRR) results (inset) confirming that the platform indeed consists of a large area monolayer of gold nanotriangles with a thickness of 7 ± 2 nm on silicon. In this experiment, the laser light is simultaneously

DOI: 10.1021/acs.jpcc.8b12574
J. Phys. Chem. C 2019, 123, 9352−9357

The Journal of Physical Chemistry C Article

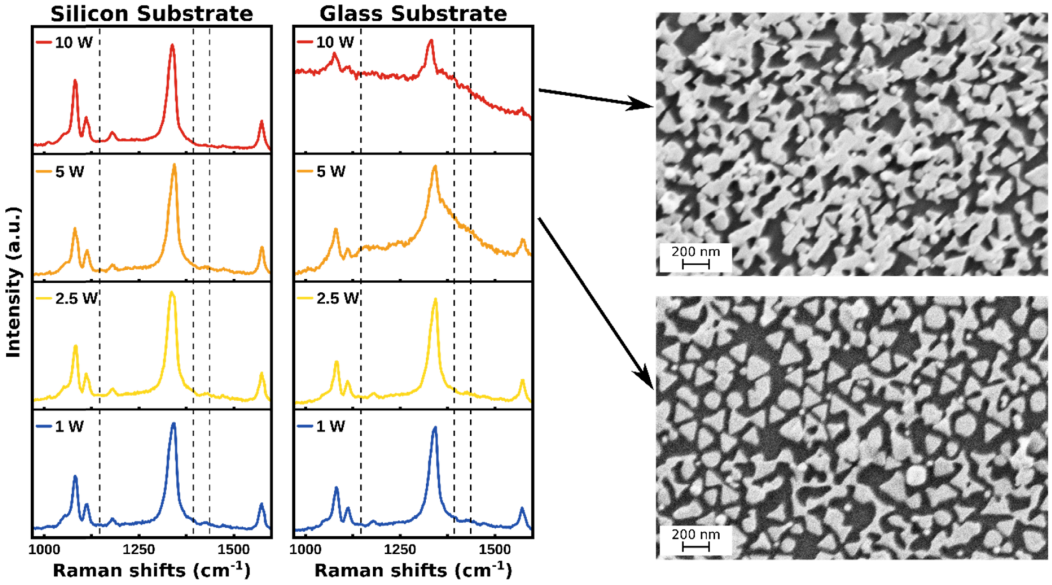

Figure 2. Low-intensity SERS spectra of 4-NTP assembled on gold NTs deposited on silicon and glass substrate probed after the sample was irradiated with different laser powers with 5 mm spot size for 5 min. Dashed lines show the frequencies, where the DMAB product would be expected. SEM images show the melting of the gold NTs on glass substrate for 5 W (lower image) and for 10 W (upper image).

responsible for SERS detection and for triggering the plasmon-assisted reaction. The time-dependent SERS spectra in Figure 1b confirm the transformation of 4-NTP to DMAB. The 4-NTP spectrum at 0 s displays main vibrational modes at 1082, 1332, and 1575 cm^{-1}, assigned to the C−H bending, NO_2 symmetric stretching, and C═C stretching modes of the 4-NTP,[42,43] respectively. After few seconds, new Raman peaks appear at 1134, 1387, and 1434 cm^{-1}, which are assigned to the C−N symmetric stretching and the N═N stretching vibrational modes of the DMAB confirming the coexistence of both molecules.[44,45] The light intensity in these experiments attains a very high value of 10 kW/cm^2. In the rest of the paper, we use far less intensity for SERS sensing to avoid driving the chemical reaction with the SERS laser.

In a first naïve attempt to drive the same reaction across an area that was larger than typically investigated in a microscope, we used a high-power diode laser module operating at 920 nm with a power up to 25 W. We increased the irradiated area by a factor of 10^6 to 5 mm spot diameter (FWHM), varying the irradiation power from 1 to 10 W, i.e., a 30- to 300-fold increase of the laser power. After irradiation for 5 min, the irradiated spots were investigated using the Raman microscope with very low laser power and short integration time (0.5 mW and 1 s). The SERS spectra of such spots are displayed in Figure 2 for the NTs deposited on silicon and glass substrates. The reaction clearly did not occur (no bands at the dashed lines, which indicate where product bands are expected). No signature of DMAB molecules was observed because we in fact decreased the intensity $I = P/A$ by a factor of 3000 to 30 000 compared to the microscopic irradiation. The Raman spectrum of the sample on glass changes at 5 W, acquiring a large background contribution, and the Raman peaks become hardly visible for 10 W irradiation. Melting of the NTs was found to be the reason as confirmed by SEM images (Figure 2), despite the very low laser intensity. Similar damage and no DMAB was observed for the silicon substrate after irradiating the sample with 15 W. The melting at higher laser power is related to the thermal conductivity of the glass, which is 2 orders of magnitude smaller than that for the silicon substrate. Therefore, the heating of the gold induced by light is dissipated more quickly by the substrate to avoid melting of the NPs.

The fact that the particles already melt at the intensity of 400 mW/cm^2 under the large spot really makes it surprising that in a microscope focus the intensity can be easily increased by 3 orders of magnitude above this intensity without any signs of melting. It illustrates at the same time the great opportunities of nanoscale heating.

To check the role of the focusing conditions, the laser driving the reaction was focused through different plano-convex lenses onto the sample irradiating spots of different sizes. The laser power was tuned to obtain approximately the same final laser intensity.

Figure 3 shows the Raman spectra taken from spots irradiated with an intensity of about 50 kW/cm^2. The SERS spectra recorded on the spots with 70 and 115 μm diameter generated by 30 and 50 mm focusing lenses show the characteristic DMAB Raman peaks, which indicate the plasmon-driven coupling reaction. The intensity of the DMAB peak decreases relative to the 4-NTP peak with increasing spot size. For the 175 μm spots (75 mm lens), the peaks are hardly discernible and for the 230 μm spots (100 mm lens), the Raman spectrum only consists of a noisy electronic background from the hot and molten NPs, which is confirmed by SEM images similar to the ones shown in Figure 2. The hot spots of the plasmonic platform, which provide the largest SERS enhancement and the largest reaction yield, melts first and therefore the excessive heating deteriorates the reaction rate.

The heat dissipation, excluding light absorption, was numerically calculated solving the 3D heat equation by means of a numerical finite elements (FEM) solver (COMSOL

DOI: 10.1021/acs.jpcc.8b12574
J. Phys. Chem. C 2019, 123, 9352−9357

The Journal of Physical Chemistry C Article

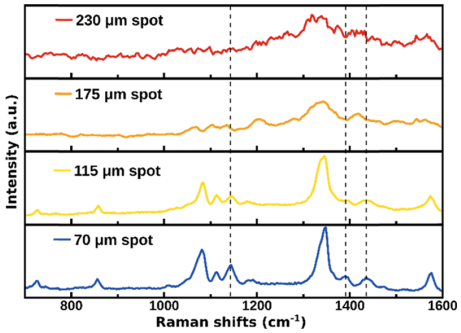

Figure 3. SERS spectra of 4-NTP assembled on gold NTs and probed with different laser spot sizes of 70, 115, 175, and 230 μm diameter. The intensity of the exciting laser beam in all four measurements is identical.

Multiphysics) using the temperature-dependent heat capacity and heat conductivity for gold,[46,47] silicon,[46−48] and glass.[49,50] In our model, the laser heating was simulated using a homogeneous heating of an area of the size of the laser spot (von Neumann boundary condition), whereas the lower substrate interface was kept at a constant temperature of T = 288.15 K. Indeed, the irradiated spot size strongly influences the rate of heat dissipation. Small spots demonstrate a three-dimensional temperature gradient (Figure 4a), indicative of a three-dimensional heat flow. On the other hand, in the center portions of the larger spots with the same excitation intensity, the heat mainly dissipates along the temperature gradient perpendicular to the substrate (Figure 4b), resulting in less efficient one-dimensional heat transport for a large fraction of the spot. Therefore, small spots cool faster and can absorb and dissipate much larger intensities without NP melting. Such high level of absorbed and dissipated energy enables the formation of DMAB molecules. Attempts to flow the same amount of energy per unit area through a large spot inevitably leads to melting of the NPs.

Irradiating the NP continuously with different laser intensities on different spot sizes (100, 250, and 500 μm), we measured their temperatures by XRD via lattice heat expansion. The analysis is based on the detection of the shifts in the (222) Bragg reflection of the gold NTs in Θ−2Θ scans. This shift was then transformed to the temperature change of the NTs based on Bragg's law and the linear thermal expansion

$$\cot\theta\Delta\theta = \frac{\Delta c}{c} = -\alpha\Delta T$$

Here, $\Delta\theta$ is the shift of the Bragg peak, $\Delta c/c$ is the relative change of the out-of-plane lattice constant, and $\alpha = 1.49 \times 10^{-5}\ 1/K$ is the thermal expansion coefficient of the gold nanotriangles previously measured by X-ray diffraction using conventional heating, which is slightly increased compared to bulk gold.[51] To perform the Bragg-angle-based temperature measurement during laser irradiation, the sample was glued with silver paste onto a Peltier cooled sample holder with an active feedback loop stabilized to 288.15 K.

Figure 4c shows the temperature of the gold NTs measured for different spot sizes on a 0.5 mm thick Si substrate, which increases linearly with the laser intensity. For a large spot of 500 μm, a laser intensity of approximately 10 kW/cm^2 is sufficient to increase the particle temperature to 96 K. For a small spot of 100 μm, a 10 times larger intensity leads to less heating of only 70 K. For glass substrates, the heating is even more dominant, and Figure 4c compares the 500 μm spot on Si to a glass substrate. The silicon substrate has considerably higher thermal conductivity. For high laser intensities, a Bragg peak sharpening is observed that is related to an increase of the gold NTs thickness due a particle coalescence (for more information, see the Supporting Information).

FEM simulations of the temperature increases using the model described earlier confirm that the temperature changes can be fully explained by the different spot sizes (solid lines in Figure 4c,d). The simulated temperature increases indeed match the measured temperature increases very well. It should be noted that a phenomenological absorption factor was used to adapt the simulation to the measurements. It reduced the total power entering the simulation to take into account both the optical absorption coefficient of the sample and the possible heat resistances at the gold−substrate interface. The same absorption factor was used for each substrate material.

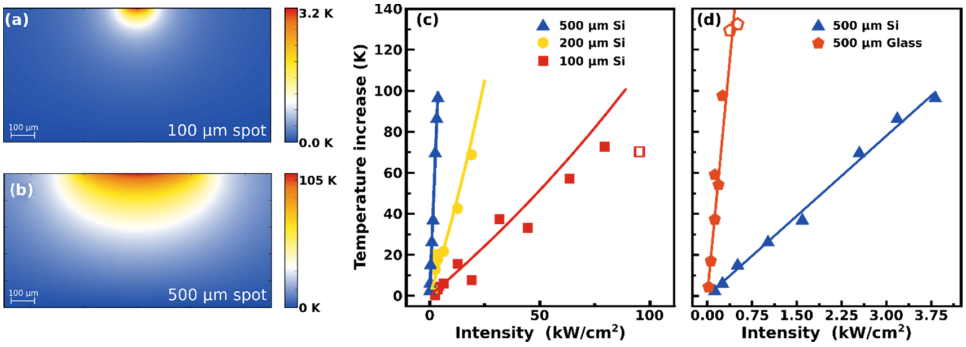

Figure 4. (a, b) FEM simulation of the temperature gradient in the substrate for an excitation intensity of 100 kW/cm^2 with two different spot sizes. The temperature change of the gold NTs as determined from the Bragg-reflection shift (c) as a function of the laser intensity due to irradiation with different laser spot sizes on silicon and (d) on different substrates for the same spot size of 500 μm. The solid lines represent the result of a FEM simulation of the temperature increase. The unfilled symbols in (c) and (d) represent intensities at which a Bragg peak sharpening was observed. The model does not consider the light absorption.

DOI: 10.1021/acs.jpcc.8b12574
J. Phys. Chem. C 2019, 123, 9352−9357

The Journal of Physical Chemistry C Article

CONCLUSIONS

In conclusion, we have shown that driving a plasmonic chemical reaction on a SERS template structure with a fixed light intensity is only possible up to a certain maximum area of the laser focus because the heat transport turns from 3D to 1D and the excessive heating destroys the sample structure. The silicon substrate turns out to be more suited for plasmonic chemistry than conventional glass substrates, since its high thermal conductivity improves the dissipation of heat and therefore a higher light intensity can be used with more photons triggering the reaction and without melting the plasmonic template structure. This is true, although additional photons are absorbed in the substrate. With laser wavelength above the silicon band gap and by appropriate thermal engineering, the substrate heating could be further reduced.

These microscopic findings underline the importance of heat transport at the nanoscale for a profound understanding of nanoplasmonic chemistry. Although time-resolved measurements of the gold NT's lattice temperature rise with subpicosecond time resolution has been recently reported, there is so far no report on driving plasmon-assisted chemistry with femtosecond laser pulses.

ASSOCIATED CONTENT

Supporting Information

The Supporting Information is available free of charge on the ACS Publications website at DOI: 10.1021/acs.jpcc.8b12574.

Damage caused by irradiation; X-ray reflectivity of gold nanotriangles; X-ray diffraction (XRD); determination of the linear expansion coefficient; temperature-dependent lattice constant (PDF)

AUTHOR INFORMATION

Corresponding Author

*E-mail: koopman@uni-potsdam.de.

ORCID

Wouter Koopman: 0000-0001-5402-345X

Joachim Koetz: 0000-0001-9113-1337

Matias Bargheer: 0000-0002-0952-6602

Notes

The authors declare no competing financial interest.

ACKNOWLEDGMENTS

R.M.S. and F.S. gratefully acknowledge the financial support by the DFG via the School of Analytical Science Adlershof (SALSA).

REFERENCES

(1) Boyer, D.; Tamarat, P.; Maali, A.; Lounis, B.; Orrit, M. Photothermal imaging of nanometer-sized metal particles among scatterers. *Science* **2002**, *297*, 1160−1163.

(2) Cognet, L.; Berciaud, S.; Lasne, D.; Lounis, B. Photothermal methods for single nonluminescent nano-objects. *Anal. Chem.* **2008**, *80*, 2288−2294.

(3) Huang, X.; Jain, P. K.; El-Sayed, I. H.; El-Sayed, M. A. Plasmonic photothermal therapy (PPTT) using old nanoparticles. *Lasers Med. Sci.* **2008**, *23*, 217−228.

(4) Hirsch, L. R.; Stafford, R. J.; Bankson, J. A.; Sershen, S. R.; Rivera, B.; Price, R. E.; Hazle, J. D.; Halas, N. J.; West, J. L. Nanoshell-mediated near-infrared thermal therapy of tumors under magnetic resonance guidance. *Proc. Natl. Acad. Sci. U.S.A.* **2003**, *100*, 13549−13554.

(5) Govorov, A. O.; Richardson, H. H. Generating heat with metal nanoparticles. *Nano Today* **2007**, *2*, 30−38.

(6) Timko, B. P.; Dvir, T.; Kohane, D. S. Remotely triggerable drug delivery systems. *Adv. Mater.* **2010**, *22*, 4925−4943.

(7) Pelton, M.; Aizpurua, J.; Bryant, G. Metal-nanoparticle plasmonics. *Laser Photonics Rev.* **2008**, *2*, 136−159.

(8) Baffou, G.; Quidant, R. Thermo-plasmonics: using metallic nanostructures as nano-sources of heat. *Laser Photonics Rev.* **2013**, *7*, 171−187.

(9) Zhang, Y.; Nelson, T.; Tretiak, S.; Guo, H.; Schatz, G. C. Plasmonic hot-carrier-mediated tunable photochemical reactions. *ACS Nano* **2018**, *12*, 8415−8422.

(10) Hattori, Y.; Abdellah, M.; Rocha, I.; Pavliuk, M. V.; Fernandes, D. L. A.; Sá, J. Light-induced ultrafast proton-coupled electron transfer responsible for H2 evolution on silver plasmonics. *Mater. Today* **2018**, *21*, 590−593.

(11) Cao, L.; Barsic, D. N.; Guichard, A. R.; Brongersma, M. L. Plasmon-assisted local temperature control to pattern individual semiconductor nanowires and carbon nanotubes. *Nano Lett.* **2007**, *7*, 3523−3527.

(12) Long, R.; Li, Y.; Song, L.; Xiong, Y. Coupling solar energy into reactions: Materials design for surface plasmon-mediated catalysis. *Small* **2015**, *11*, 3873−3889.

(13) Link, S.; Masiello, D. J. Introduction: Plasmonics in chemistry. *Chem. Rev.* **2018**, *118*, 2863−2864.

(14) Cui, L.; Wang, P.; Fang, Y.; Li, Y.; Sun, M. A plasmon-driven selective surface catalytic reaction revealed by surface-enhanced Raman scattering in an electrochemical environment. *Sci. Rep.* **2015**, *5*, No. 11920.

(15) Fang, Y.; Li, Y.; Xu, H.; Sun, M. Ascertaining p,p′-dimercaptoazobenzene produced from p-aminothiophenol by selective catalytic coupling reaction on silver nanoparticles. *Langmuir* **2010**, *26*, 7737−7746.

(16) Huang, Y.-F.; Zhu, H.-P.; Liu, G.-K.; Wu, D.-Y.; Ren, B.; Tian, Z.-Q. When the signal is not from the original molecule to be detected: chemical transformation of para-aminothiophenol on Ag during the SERS measurement. *J. Am. Chem. Soc.* **2010**, *132*, 9244−9246.

(17) van Schrojenstein Lantman, E. M.; Deckert-Gaudig, T.; Mank, A. J. G.; Deckert, V.; Weckhuysen, B. M. Catalytic processes monitored at the nanoscale with tip-enhanced Raman spectroscopy. *Nat. Nanotechnol.* **2012**, *7*, 583−586.

(18) Sun, M.; Xu, H. A novel application of plasmonics: plasmon-driven surface-catalyzed reactions. *Small* **2012**, *8*, 2777−2786.

(19) Chen, X.-J.; Cabello, G.; Wu, D.-Y.; Tian, Z.-Q. Surface-enhanced Raman spectroscopy toward application in plasmonic photocatalysis on metal nanostructures. *J. Photochem. Photobiol., C* **2014**, *21*, 54−80.

(20) Chen, H. L.; Li, C.-J.; Peng, C.-J.; Leu, H.-J.; Hung, W.-H. Plasmon-induced hot electrons on mesoporous carbon for decomposition of organic pollutants under outdoor sunlight irradiation. *ACS Appl. Mater. Interfaces* **2017**, *9*, 327−334.

(21) Kowalska, E.; Yoshiiri, K.; Wei, Z.; Zheng, S.; Kastl, E.; Remita, H.; Ohtani, B.; Rau, S. Hybrid photocatalysts composed of titania modified with plasmonic nanoparticles and ruthenium complexes for decomposition of organic compounds. *Appl. Catal., B* **2015**, *178*, 133−143.

(22) Mukherjee, S.; Libisch, F.; Large, N.; Neumann, O.; Brown, L. V.; Cheng, J.; Lassiter, J. B.; Carter, E. A.; Nordlander, P.; Halas, N. J. Hot electrons do the impossible: Plasmon-induced dissociation of H2 on Au. *Nano Lett.* **2013**, *13*, 240−247.

(23) Zhou, L.; Zhang, C.; McClain, M. J.; Manjavacas, A.; Krauter, C. M.; Tian, S.; Berg, F.; Everitt, H. O.; Carter, E. A.; Nordlander, P.; et al. Aluminum nanocrystals as a plasmonic photocatalyst for hydrogen dissociation. *Nano Lett.* **2016**, *16*, 1478−1484.

(24) Yasuda, S.; Yoshii, T.; Chiashi, S.; Maruyama, S.; Murakoshi, K. Plasmon-induced selective oxidation reaction at single-walled carbon nanotubes. *ACS Appl. Mater. Interfaces* **2017**, *9*, 38992−38998.

DOI: 10.1021/acs.jpcc.8b12574
J. Phys. Chem. C 2019, 123, 9352−9357

(25) de Nijs, B.; Benz, F.; Barrow, S. J.; Sigle, D. O.; Chikkaraddy, R.; Palma, A.; Carnegie, C.; Kamp, M.; Sundararaman, R.; Narang, P.; et al. Plasmonic tunnel junctions for single-molecule redox chemistry. *Nat. Commun.* **2017**, *8*, No. 994.
(26) Adleman, J. R.; Boyd, D. A.; Goodwin, D. G.; Psaltis, D. Heterogenous catalysis mediated by plasmon heating. *Nano Lett.* **2009**, *9*, 4417−4423.
(27) Xu, P.; Kang, L.; Mack, N. H.; Schanze, K. S.; Han, X.; Wang, H.-L. Mechanistic understanding of surface plasmon assisted catalysis on a single particle: cyclic redox of 4-aminothiophenol. *Sci. Rep.* **2013**, *3*, No. 2997.
(28) Bora, T.; Zoepfl, D.; Dutta, J. Importance of plasmonic heating on visible light driven photocatalysis of gold nanoparticle decorated Zinc oxide nanorods. *Sci. Rep.* **2016**, *6*, No. 26913.
(29) Golubev, A. A.; Khlebtsov, B. N.; Rodriguez, R. D.; Chen, Y.; Zahn, D. R. T. Plasmonic heating plays a dominant role in the plasmon-induced photocatalytic reduction of 4-nitrobenzenethiol. *J. Phys. Chem. C* **2018**, *122*, 5657−5663.
(30) Kang, L.; Han, X.; Chu, J.; Xiong, J.; He, X.; Wang, H.-L.; Xu, P. In situ surface-enhanced Raman spectroscopy study of plasmon-driven catalytic reactions of 4-nitrothiophenol under a controlled atmosphere. *ChemCatChem* **2015**, *7*, 1004−1010.
(31) Xie, W.; Walkenfort, B.; Schlu ̈cker, S. Label-free SERS monitoring of chemical reactions catalyzed by small gold nanoparticles using 3D plasmonic superstructures. *J. Am. Chem. Soc.* **2013**, *135*, 1657−1660.
(32) Yan, X.; Wang, L.; Tan, X.; Tian, B.; Zhang, J. Surface-enhanced Raman spectroscopy assisted by radical capturer for tracking of plasmon-driven redox reaction. *Sci. Rep.* **2016**, *6*, No. 30193.
(33) Dong, B.; Fang, Y.; Chen, X.; Xu, H.; Sun, M. Substrate-, wavelength-, and time-dependent plasmon-assisted surface catalysis reaction of 4-nitrobenzenethiol dimerizing to p,p′-dimercaptoazobenzene on Au, Ag, and Cu films. *Langmuir* **2011**, *27*, 10677−10682.
(34) Cho, F.-H.; Kuo, S.-C.; Lai, Y.-H. Surface-plasmon-induced azo coupling reaction between nitro compounds on dendritic silver monitored by surface-enhanced Raman spectroscopy. *RSC Adv.* **2017**, *7*, 10259−10265.
(35) Ding, Q.; Chen, M.; Fang, Y.; Zhang, Z.; Sun, M. Plasmon-driven diazo coupling reactions of p -nitroaniline via −NH 2 or −NO 2 in atmosphere environment. *J. Phys. Chem. C* **2017**, *121*, 5225−5231.
(36) Zhang, Z.; Chen, L.; Sun, M.; Ruan, P.; Zheng, H.; Xu, H. Insights into the nature of plasmon-driven catalytic reactions revealed by HV-TERS. *Nanoscale* **2013**, *5*, 3249−3252.
(37) Zhang, Z.; Kinzel, D.; Deckert, V. Photo-Induced or plasmon-induced reaction: Investigation of the light-induced azo-coupling of amino groups. *J. Phys. Chem. C* **2016**, *120*, 20978−20983.
(38) Kim, K.; Choi, J.-Y.; Shin, K. S. Surface-enhanced Raman scattering of 4-nitrobenzenethiol and 4-aminobenzenethiol on silver in icy environments at liquid nitrogen temperature. *J. Phys. Chem. C* **2014**, *118*, 11397−11403.
(39) Liebig, F.; Sarhan, R. M.; Sander, M.; Koopman, W.; Schuetz, R.; Bargheer, M.; Koetz, J. Deposition of gold nanotriangles in large scale close-packed monolayers for X-ray-based temperature calibration and SERS monitoring of plasmon-driven catalytic reactions. *ACS Appl. Mater. Interfaces* **2017**, *9*, 20247−20253.
(40) Liebig, F.; Sarhan, R. M.; Prietzel, C.; Reinecke, A.; Koetz, J. "Green" gold nanotriangles: synthesis, purification by polyelectrolyte/micelle depletion flocculation and performance in surface-enhanced Raman scattering. *RSC Adv.* **2016**, *6*, 33561−33568.
(41) von Reppert, A.; Sarhan, R. M.; Stete, F.; Pudell, J.; Del Fatti, N.; Crut, A.; Koetz, J.; Liebig, F.; Prietzel, C.; Bargheer, M. Watching the vibration and cooling of ultrathin gold nanotriangles by ultrafast X-ray diffraction. *J. Phys. Chem. C* **2016**, *120*, 28894−28899.
(42) Ling, Y.; Xie, W. C.; Liu, G. K.; Yan, R. W.; Wu, D. Y.; Tang, J. The discovery of the hydrogen bond from p-nitrothiophenol by Raman spectroscopy: guideline for the thioalcohol molecule recognition tool. *Sci. Rep.* **2016**, *6*, No. 31981.
(43) Kuo, S.-C.; Tasi, J.-J.; Li, J.-S.; Hou, Z.-H.; Li, C.-H.; Jeng, U.-S.; Lai, Y.-H. Enhancement of surface enhanced Raman scattering activity of Au nanoparticles through the mesostructured metallic nanoparticle arrays. *APL Mater.* **2014**, *2*, No. 113310.
(44) Shin, D. Two different behaviors in 4-ABT and 4,4′-DMAB surface enhanced Raman spectroscopy. *J. Raman Spectrosc.* **2017**, *48*, 343−347.
(45) Kim, K.; Shin, D.; Kim, K. L.; Shin, K. S. Surface-enhanced Raman scattering of 4,4′-dimercaptoazobenzene trapped in Au nanogaps. *Phys. Chem. Chem. Phys.* **2012**, *14*, 4095−4100.
(46) Ho, C. Y.; Powell, R. W.; Liley, P. E. Thermal conductivity of the elements. *J. Phys. Chem. Ref. Data* **1972**, *1*, 279−421.
(47) Pankratz, L. B.; Mrazek, R. V. *Thermodynamic Properties of Elements and Oxides*; U.S. Department of the Interior, Bureau of Mines, 1982.
(48) Desai, P. D. Thermodynamic properties of iron and silicon. *J. Phys. Chem. Ref. Data* **1986**, *15*, 967−983.
(49) Kingery, W. D. Heat-conductivity processes in glass. *J. Am. Ceram. Soc.* **1961**, *44*, 302−304.
(50) Lucks, C. F.; Deem, H. W.; Wood, W. D. *Thermal Properties of Six Glasses and Two Graphites*; Battelle Memorial Institute: Columbus, OH, 1960; Vol. *39*.
(51) Nix, F. C.; MacNair, D. The thermal expansion of pure metals: copper, gold, aluminum, nickel, and iron. *Phys. Rev.* **1941**, *60*, 597−605.

DOI: 10.1021/acs.jpcc.8b12574
J. Phys. Chem. C 2019, 123, 9352−9357

Scaling-Up Nano-Plasmon Catalysis: The Role of Heat Dissipation

Radwan M. Sarhan,[1,2] Wouter Koopman,[1] Jan Pudell,[1] Felix Stete,[1,2] Matthias Rössle,[3] Marc Herzog,[1] Clemens N. Z. Schmitt,[4] Ferenc Liebig,[5] Joachim Koetz,[5] and Matias Bargheer[1,3]

[1] *Institute of Physics and Astronomy, University of Potsdam, 14476 Potsdam, Germany*
[2] *School of Analytical Sciences Adlershof (SALSA), Humboldt-Universität zu Berlin, Albert-Einstein-Str. 5-9, 10099 Berlin, Germany*
[3] *Helmholtz-Zentrum Berlin, Albert-Einstein-Str. 15, 12489 Berlin, Germany*
[4] *Max Planck Institute of Colloids and Interfaces, 14476 Potsdam, Germany*
[5] *Institute of Chemistry, University of Potsdam, 14476 Potsdam, Germany*

DAMAGE CAUSED BY IRRADIATION

We confirmed by SEM (Figure S1) that the degradation of the Raman spectra presented in Figure 3 of the manuscript were caused by damages to the nanoparticle substrate. As the high total power of the excitation laser beam could not dissipate quickly enough, a partial melting of the particles occurred.

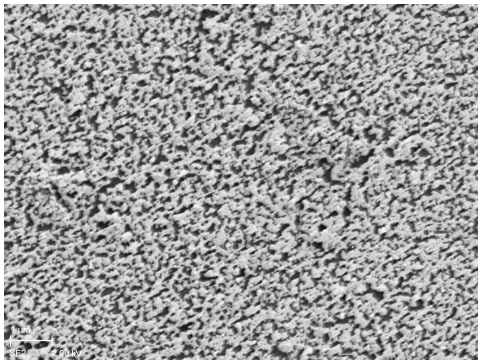

FIG. S1. **SEM 175 µm spot:** 8 µm × 5.5 µm SEM image of from the center of the irradiated spot with a diameter of 175 µm. The damage due to the melting of the nanotriangles is clearly visible.

X-RAY REFLECTIVITY OF GOLD NANO TRIANGLES

X-ray reflectivity (XRR) is a technique that allows the surface-sensitive characterization of thin layers by interference of specular reflections of the bottom and top interfaces of the layer that give rise to characteristic minima and maxima as function of the energy transfer, $Q = 4/\lambda \sin\vartheta$, with ϑ being the incidence angle of the X-rays with wavelength λ onto the sample. We measured a monolayer of gold nano triangles (NTs) on a Silicon substrate at the XPP-KMC-3 endstation at the synchrotron BESSY II. The incidence angle of the X-rays on the sample was scanned between 0 and 3° incidence angle, which corresponds to $Q = 0$ to $4\,\mathrm{nm}^{-1}$ in reciprocal space. The corresponding dataset shown in the inset of Fig. 1a) contains a dominant oscillation frequency that corresponds to a wavelength of $\lambda = 0.9\,\mathrm{nm}^{-1}$ determined by a Fourier-transformation. This wavelength corresponds to a layer-thickness of $7 \pm 2\,\mathrm{nm}$. The absence of higher frequencies in the signal proofs that our sample contains a negligible part of stacked gold-nano-triangles over the X-ray spot size of approximately $0.5 \times 10\,\mathrm{mm}^2$.

X-RAY DIFFRACTION (XRD)

We measured at the XPP-KMC-3 endstation at the synchrotron source BESSY II the 222 Bragg reflection of the [111] oriented gold NTs at the X-ray energy of 8 keV. We selected the 2nd order Bragg reflection to minimize the X-ray footprint. The sample was mounted on Peltier-cooled sample mount, which results in a stable substrate

temperature of 15°C that was attached with silver paint to the Peltier cooler. In Figure S2a) and b) we show the Bragg peaks of the gold NTs on Si and glass substrates for different Laser intensities, respectively. For every measured laser intensity, a new spot on the sample was selected and measured before illumination (black thick curves) and during illumination. For every measurement we waited 60 s for thermal equilibration between gold NTs.

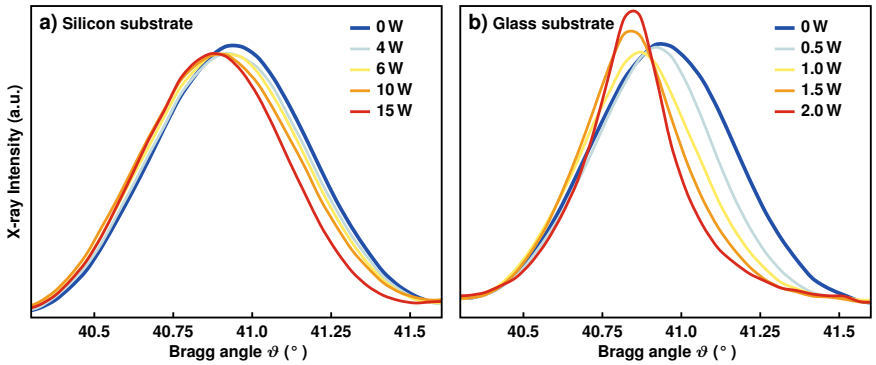

FIG. S2. **XRD results:** Bragg peak shift of gold NTs on a) a silicon substrate and b) glass substrate for different intensities. The Bragg peak shift to smaller angles due to heating of the gold NTs. On the glass substrate a sharpened peak is observed for high intensities.

We note a peak sharpening at high intensities. For very thin layer we can neglect typical Bragg broadening effects and the width of the Bragg peak is approximately given by the thickness. In our case the peak width is slightly smaller as theoretical values for 7 nm layers, which indicates a small amount of stacked gold NTs (5-10%). After illumination of the sample with glass substrate with high intensities we observe a sharpened Bragg peak that is related to thicker nano particles. This indicates a particle coalescence of the gold NTs.

DETERMINATION OF THE LINEAR EXPANSION COEFFICIENT

The temperature-dependent shift of the Bragg peak allows us to calculate the linear expansion coefficient for gold NTs along the [111] direction. It is measured with a closed-cycle cryostat setup available at the XPP-KMC-3 endstation at the synchrotron source BESSY II that allows the variation of the sample temperature from 20 to 350 K. From the Bragg Peak position the out-of-plane lattice constant in [111] direction is extracted and shown in Figure S3. A linear fit yields the linear expansion coefficient of $\alpha = 1.49 \cdot 10^{-5}\,1/\mathrm{K}$.

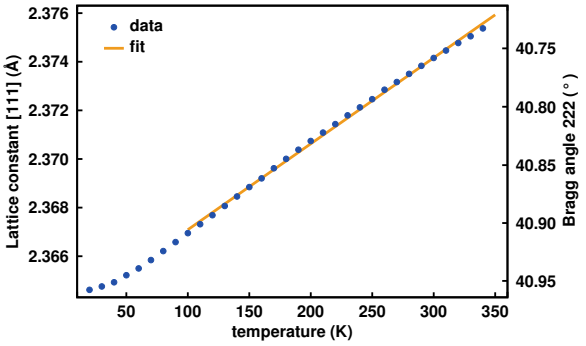

FIG. S3. **The Temperature-dependent lattice constant** is measured from 20 to 350 K and fitted to extract the linear expansion coefficient α.

6 | Conclusion and Outlook

In this dissertation, I presented my contributions to the fields of plasmon–exciton coupling and optical excitation of gold nanoparticles from my time in the group of ultrafast dynamics of condensed matter (UDKM) at the University of Potsdam.

The main findings and achievements can be summarised as follows:

- The vacuum fluctuations in plasmonic nanocavitites can become so strong that they can saturate two-level systems.
- Saturation is directly connected to the coupling strength between plasmonic cavities and excitonic two-level systems and becomes relevant when the coupling strength is on the order of the exciton linewidth. In that case, the susceptibility of the two-level systems cannot be described via a Lorentz oscillator. The work presents a modified expression that includes saturation.
- For small nanoparticles in a core–shell geometry with a plasmonic core and an excitonic shell, the coupling strength is proportional to the square root of the surface to volume ratio. Thus, it increases for decreasing particle sizes inducing for example stronger saturation effects.
- Sufficiently small nanoparticles can support strong coupling to single quantum emitters.
- A new way to tune the the plasmon resonance in coupled core–shell systems via layer-by-layer deposition of polyelectrolytes enables precise control over the particles' dielectric environment and a direct revelation of the anticrossing.
- A model to precisely simulate transient spectra of gold–dye core–shell nanoparticles confirms that the source of changes in the spectra after a pulsed optical excitation is heat that is generated within the gold cores.
- Care must be taken when changing the size of an illumination spot to excite gold nanoparticles. An increase of spot size can cause particle melting despite a contemporaneous decrease of excitation intensity. This fact is rooted in the transition from three dimensional to one dimensional heat diffusion for growing spot sizes.

Along with these highlighted findings, the thesis showed that recording extinction spectra of plasmon–exciton systems to assess the coupling regime is potentially not sufficient. Separate measurements of absorption and scattering spectra allow higher reliability since the two can exhibit different features. A simple model of classical coupled oscillators was introduced to explain these differences. Moreover, the thesis documents the direct observation of the breathing modes of gold nanoparticles after optical excitation with time resolved X-ray diffraction measurements.

These findings were presented in six scientific articles which constitute the work's scientific core. In order to make the work better accessible for researchers which are new to this field or future students in the UDKM, the articles were accompanied by a comprehensive introduction into their theoretical and methodological fundamentals. The work provided a thorough description of localised plasmons, excitons in J-aggregates and the coupling between the two. Localised plasmons and their features were discussed for metal nanospheres, nanoellipsopds and core–shell systems that are small compared to the wavelength. For larger particles, the modified long wavelength approximation was discussed. Localised plasmons were identified as collective oscillations of the free electrons in metal nanoparticles with resonances in the visible range. These resonances are accompanied by strong electric field enhancements and are localised to the direct vicinity of the particles. The resonances can be tuned via the environment, the particle material or its shape. The work introduced J-aggregates and their properties generated by the delocalisation of the electric excitations. The emission and absorption of J-aggregates are red-shifted, very sharp and exhibit hardly any Stokes shift. Their enhanced transition dipole moment makes J-aggregates excellent candidates for strong plasmon–exciton coupling systems. The nature of this kind of light–matter coupling was explained including features like energy level splitting and Rabi oscillations. For accurate simulations of the spectra of plasmon–exciton core–shell systems, precise models of the permittivity were presented.

The theoretical introduction was followed by a presentation of the experimental methods that were employed for the articles. This method part presented technical details of nanoparticle coating with TDBC together with techniques of particle deposition on substrates. Layer-by-layer deposition of polyelectrolytes also allows the tuning of the plasmon resonance and hence enables the revelation of the anticrossing of coupled core–shell particles. The samples were eventually investigated by linear spectroscopy methods, pump-probe spectroscopy, X-ray diffraction and surface enhanced Raman spectroscopy. These techniques were introduced in the last part of the methods section.

Future prospects: The core–shell nanoparticles bear great potential for future experiments. The simplicity in the fabrication process, the tunability of the plasmon resonance thanks to layer-by-layer deposition, the control of the particles on substrate and the tunability of the coupling strength via the particle size, all these features make the gold–TDBC core–shell particles a great model system for fundamental research of light–matter coupling on the nanoscale.

With its main focus on ultrafast dynamics of condensed matter, the UDKM's natural next steps are deeper invesigations of the transient behaviour of the particles, also at time scales below 100 fs. For this work, I investigated the effects of optical heating in strongly coupled core–shell nanoparticles. The coupling gives rise to Rabi oscillations on a time scale around 10 fs and it would be an interesting challenge to resolve these and investigate for example their dependence on the particle size. As a first step, we recently constructed a nonlinear optical parametric amplifier (NOPA) [176] generating broadband laser pulses with durations around 10 fs. In near future, we hope to be able to conduct pump–probe experiments that allow the observation of Rabi oscllations. Furthermore, the core–shell particles with resonances in the infrared presented in Chapter 4 might come handy for such experiments at the octave spanning ultrafast laser *FEMTOSOURCE rainbow* that generates infrared laser pulses with pulse lengths of 7 fs. Also there, pump–probe experiments bear the potential of intriguing results.

The discovery of vacuum induced saturation (VISA) gives rise to further questions and investigations. Article III argued that the shell mode that was predicted in previous publications [93, 168] does not occur (at our conditions) since it has not been observed experimentally. But the mode might as well not be optically active or hidden beneath the polariton modes. We would like to exclude these options by electron energy loss spectroscopy (EELS) which enables highly localised spectral investigations of the core–shell particles. First tests have been conducted and EELS will hopefully be able to support our hypotheses. VISA also implies non-linearities in two photon experiments even in the absence of strong coupling. Such non-linearities could for example be investigated in single particle pump–probe experiments combining ultrafast laser pulses with microscopy techniques.

Also the field of optical heating in plasmonic nanostructures is filled with open questions. A very interesting one is that of the role of heat in plasmon assisted catalysis. There is an ongoing debate if chemical reactions on gold nanoparticles are heat induced or driven by plasmon generated hot electrons and holes [177–179]. Plasmonic nanostructures could be equipped with appropriate marker molecules via etching, DNA origami or colloidal techniques. Surface enhanced Stokes and Antistokes Raman spectroscopy would then allow selective temperature measurements [180] of the marker molecules to assess the role of heat in plasmon assisted catalysis.

These are a few of many ideas how research on plasmon–exciton coupling and optical heating in gold nanoparticles can be pursued. In general, gold nanoparticles have proven to be versatile building blocks in forthcoming technologies in various fields of applications. Currently, gold nanoparticles are mostly investigated for fundamental research to which also this work is intended to contribute its share. Yet, in the near future, more and more application based studies will pave the way to a potentially golden future.

Bibliography

[1] I. Freestone, N. Meeks, M. Sax and C. Higgitt: "The Lycurgus Cup — A Roman Nanotechnology", *Gold Bull.* 40, 270 (2007)

[2] M. Kerker: "The Optics of Colloidal Silver: Something Old and Something New", *J. Colloid Interface Sci.* 105, 297 (1985)

[3] M. Ware: "Chrysotype: Photography in nanoparticle gold", *Gold Bull.* 39, 124 (2006)

[4] M. Faraday: "The Bakerian Lecture: Experimental Relations of Gold (and Other Metals) to Light", *Philos. Trans. R. Soc. London* 147, 145 (1857)

[5] G. Mie: "Beiträge zur Optik trüber Medien, speziell kolloidaler Metallösungen", *Ann. Phys.* 330, 377 (1908)

[6] R. Gans: "Über die Form ultramikroskopischer Goldteilchen", *Ann. Phys.* 342, 881 (1912)

[7] G. Baffou and R. Quidant: "Thermo-Plasmonics: Using Metallic Nanostructures as Nano-Sources of Heat", *Laser Photonics Rev.* 7, 171 (2013)

[8] K. Sztandera, M. Gorzkiewicz and B. Klajnert-Maculewicz: "Gold Nanoparticles in Cancer Treatment", *Mol. Pharmaceutics* 16, 1 (2019)

[9] E. Boulais, R. Lachaine, A. Hatef and M. Meunier: "Plasmonics for Pulsed-Laser Cell Nanosurgery: Fundamentals and Applications", *J. Photochem. Photobiol., C* 17, 26 (2013)

[10] A. W. Powell, A. Stavrinadis, I. de Miguel, G. Konstantatos and R. Quidant: "White and Brightly Colored 3D Printing Based on Resonant Photothermal Sensitizers", *Nano Lett.* 18, 6660 (2018)

[11] K. Saha, S. S. Agasti, C. Kim, X. Li and V. M. Rotello: "Gold Nanoparticles in Chemical and Biological Sensing", *Chem. Rev.* 112, 2739 (2012)

[12] A. B. Taylor and P. Zijlstra: "Single-Molecule Plasmon Sensing: Current Status and Future Prospects", *ACS Sens.* 2, 1103 (2017)

[13] A. Kristensen, J. K. Yang, S. I. Bozhevolnyi, S. Link, P. Nordlander, N. J. Halas and N. A. Mortensen: "Plasmonic Colour Generation", *Nat. Rev. Mater.* 2, 1 (2016)

[14] G. Baffou and R. Quidant: "Nanoplasmonics for Chemistry", *Chem. Soc. Rev.* 43, 3898 (2014)

[15] L. Mascaretti, A. Dutta, Š. Kment, V. M. Shalaev, A. Boltasseva, R. Zbořil and A. Naldoni: "Plasmon-Enhanced Photoelectrochemical Water Splitting for Efficient Renewable Energy Storage", *Adv. Mater.* 1805513 (2019)

[16] G. Kumari, X. Zhang, D. Devasia, J. Heo and P. K. Jain: "Watching Visible Light-Driven CO_2 Reduction on a Plasmonic Nanoparticle Catalyst", *ACS Nano* 12, 8330 (2018)

[17] K. Catchpole and A. Polman: "Plasmonic Solar Cells", *Opt. Express* 16, 21793 (2008)

[18] D. Wang, W. Wang, M. P. Knudson, G. C. Schatz and T. W. Odom: "Structural Engineering in Plasmon Nanolasers", *Chem. Rev.* 118, 2865 (2018)

[19] F. Neubrech, C. Huck, K. Weber, A. Pucci and H. Giessen: "Surface-Enhanced Infrared Spectroscopy Using Resonant Nanoantennas", *Chem. Rev.* 117, 5110 (2017)

[20] P. Anger, P. Bharadwaj and L. Novotny: "Enhancement and Quenching of Single-Molecule Fluorescence", *Phys. Rev. Lett.* 96, 113002 (2006)

[21] P. L. Stiles, J. A. Dieringer, N. C. Shah and R. P. van Duyne: "Surface-Enhanced Raman Spectroscopy", *Annu. Rev. Anal. Chem.* 1, 601 (2008)

[22] X.-M. Qian and S. M. Nie: "Single-Molecule and Single-Nanoparticle SERS: From Fundamental Mechanisms to Biomedical Applications", *Chem. Soc. Rev.* 37, 912 (2008)

[23] H. J. Kimble: "The Quantum Internet", *Nature* 453, 1023 (2008)

[24] D. Sanvitto and S. Kéna-Cohen: "The Road Towards Polaritonic Devices", *Nat. Mater.* 15, 1061 (2016)

[25] M. Hertzog, M. Wang, J. Mony and K. Börjesson: "Strong Light–Matter Interactions: a New Direction within Chemistry", *Chem. Soc. Rev.* 48, 937 (2019)

[26] P. Törmä and W. L. Barnes: "Strong Coupling between Surface Plasmon Polaritons and Emitters: A Review", *Rep. Prog. Phys.* 78, 013901 (2014)

[27] P. Zijlstra, J. W. Chon and M. Gu: "Five-Dimensional Optical Recording Mediated by Surface Plasmons in Gold Nanorods", *Nature* 459, 410 (2009)

[28] X. Yang, S. E. Skrabalak, Z.-Y. Li, Y. Xia and L. V. Wang: "Photoacoustic Tomography of a Rat Cerebral Cortex in Vivo with Au Nanocages as an Optical Contrast Agent", *Nano Lett.* 7, 3798 (2007)

[29] R. Gordon: "Nanostructured Metals for Light-Based Technologies", *Nanotechnology* 30, 212001 (2019)

[30] H. Yu, Y. Peng, Y. Yang and Z.-Y. Li: "Plasmon-Enhanced Light–Matter Interactions and Applications", *npj Comput. Mater.* 5, 45 (2019)

[31] K. Tanabe: "Field Enhancement around Metal Nanoparticles and Nanoshells: A Systematic Investigation", *J. Phys. Chem. C* 112, 15721 (2008)

[32] S. A. Maier: *Plasmonics: Fundamentals and Applications* (Springer, New York, 2007)

[33] J. D. Jackson: *Classical electrodynamics* 3rd edition

[34] S. A. Maier and H. A. Atwater: "Plasmonics: Localization and Guiding of Electromagnetic Energy in Metal/Dielectric Structures", *J. Appl. Phys.* 98, 011101 (2005)

[35] R. M. Cole, J. J. Baumberg, F. J. Garcia de Abajo, S. Mahajan, M. Abdelsalam and P. N. Bartlett: "Understanding Plasmons in Nanoscale Voids", *Nano Lett.* 7, 2094 (2007)

[36] L. Novotny and B. Hecht: *Principles of Nano-Optics* (Cambridge University Press, Cambridge, 2006)

[37] K. M. McPeak, S. V. Jayanti, S. J. P. Kress, S. Meyer, S. Iotti, A. Rossinelli and D. J. Norris: "Plasmonic Films Can Easily Be Better: Rules and Recipes", *ACS Photonics* 2, 326 (2015)

[38] G. V. Hartland: "Optical Studies of Dynamics in Noble Metal Nanostructures", *Chem. Rev.* 111, 3858 (2011)

[39] S. Link and M. A. El-Sayed: "Shape and Size Dependence of Radiative, Non-Radiative and Photothermal Properties of Gold Nanocrystals", *Int. Rev. Phys. Chem.* 19, 409 (2000)

[40] C. F. Bohren and D. R. Huffman: *Absorption and Scattering of Light by Small Particles* (Wiley-VCH, Weinheim, 1998)

[41] L. M. Liz-Marzán, M. Giersig and P. Mulvaney: "Synthesis of Nanosized Gold–Silica Core–Shell particles", *Langmuir* 12, 4329 (1996)

[42] W.-C. Wu and J. B. Tracy: "Large-Scale Silica Overcoating of Gold Nanorods with Tunable Shell Thicknesses", *Chem. Mater.* 27, 2888 (2015)

[43] S. Oldenburg, R. Averitt, S. Westcott and N. Halas: "Nanoengineering of Optical Resonances", *Chem. Phys. Lett.* 288, 243 (1998)

[44] H. Wang, D. W. Brandl, F. Le, P. Nordlander and N. J. Halas: "Nanorice: A Hybrid Plasmonic Nanostructure", *Nano Lett.* 6, 827 (2006)

[45] R. Ghosh Chaudhuri and S. Paria: "Core/shell Nanoparticles: Classes, Properties, Synthesis Mechanisms, Characterization, and Applications", *Chem. Rev.* 112, 2373 (2011)

[46] N. Toshima and Y. Wang: "Preparation and Catalysis of Novel Colloidal Dispersions of Copper/Noble Metal Bimetallic Clusters", *Langmuir* 10, 4574 (1994)

[47] M. Kiel, M. Klötzer, S. Mitzscherling and M. Bargheer: "Measuring the Range of Plasmonic Interaction", *Langmuir* 28, 4800 (2012)

[48] S. Mitzscherling, Q. Cui, W. Koopman and M. Bargheer: "Dielectric Function of Two-Phase Colloid–Polymer Nanocomposite", *Phys. Chem. Chem. Phys.* 17, 29465 (2015)

[49] X. Chen, Y.-H. Chen, J. Qin, D. Zhao, B. Ding, R. J. Blaikie and M. Qiu: "Mode Modification of Plasmonic Gap Resonances Induced by Strong Coupling with Molecular Excitons", *Nano Lett.* 17, 3246 (2017)

[50] D. Melnikau, D. Savateeva, A. Susha, A. L. Rogach and Y. P. Rakovich: "Strong Plasmon–Exciton Coupling in a Hybrid System of Gold Nanostars and J-Aggregates", *Nanoscale Res. Lett.* 8, 134 (2013)

[51] L. Zhang et al.: "Large-Scale Growth of Sharp Gold Nano-Cones for Single-Molecule SERS Detection", *RSC Adv.* 6, 2882 (2016)

[52] L. Scarabelli, M. Coronado-Puchau, J. J. Giner-Casares, J. Langer and L. M. Liz-Marzán: "Monodisperse Gold Nanotriangles: Size Control, Large-Scale Self-Assembly, and Performance in Surface-Enhanced Raman Scattering", *ACS Nano* 8, 5833 (2014)

[53] R. M. Stöckle, Y. D. Suh, V. Deckert and R. Zenobi: "Nanoscale Chemical Analysis by Tip-Enhanced Raman Spectroscopy", *Chem. Phys. Lett.* 318, 131 (2000)

[54] K. Santhosh, O. Bitton, L. Chuntonov and G. Haran: "Vacuum Rabi Splitting in a Plasmonic Cavity at the Single Quantum Emitter Limit", *Nat. Commun.* 7, ncomms11823 (2016)

[55] F. Benz et al.: "Single-Molecule Optomechanics in "Picocavities"", *Science* 354, 726 (2016)

[56] R. Chikkaraddy et al.: "Mapping Nanoscale Hotspots with Single-Molecule Emitters Assembled into Plasmonic Nanocavities Using DNA Origami", *Nano Lett.* 18, 405 (2018)

[57] U. Kreibig and M. Vollmer: *Optical Properties of Metal Clusters*, volume 25 (Springer, Heidelberg, 1995)

[58] K. L. Kelly, E. Coronado, L. L. Zhao and G. C. Schatz: "The Optical Properties of Metal Nanoparticles: The Influence of Size, Shape, and Dielectric Environment", *J. Phys. Chem. B* 107, 668 (2003)

[59] M. Meier and A. Wokaun: "Enhanced Fields on Large Metal Particles: Dynamic Depolarization", *Opt. Lett.* 8, 581 (1983)

[60] A. Wokaun, J. P. Gordon and P. F. Liao: "Radiation Damping in Surface-Enhanced Raman Scattering", *Phys. Rev. Lett.* 48, 957 (1982)

[61] G. Zengin, G. Johansson, P. Johansson, T. J. Antosiewicz, M. Käll and T. Shegai: "Approaching the Strong Coupling Limit in Single Plasmonic Nanorods Interacting with J-Aggregates", *Sci. Rep.* 3, 3074 (2013)

[62] D. G. Baranov, M. Wersäll, J. Cuadra, T. J. Antosiewicz and T. Shegai: "Novel Nanostructures and Materials for Strong Light–Matter Interactions", *ACS Photonics* 5, 24 (2018)

[63] V. V. Egorov and M. V. Alfimov: "Theory of the J-Band: From the Frenkel Exciton to Charge Transfer", *Phys.-Usp.* 50, 985 (2007)

[64] F. C. Spano: "The Spectral Signatures of Frenkel Polarons in H-and J-aggregates", *Acc. Chem. Res.* 43, 429 (2009)

[65] E. I. Mal'tsev et al.: "Electroluminescence of Polymer/J-Aggregate Composites", *Appl. Phys. Lett.* 75, 1896 (1999)

[66] T. Tani: *Photographic Sensitivity: Theory and Mechanisms* 8 (Oxford University Press, Oxford, 1995)

[67] J. L. Bricks, Y. L. Slominskii, I. D. Panas and A. P. Demchenko: "Fluorescent J-Aggregates of Cyanine Dyes: Basic Research and Applications Review", *Methods Appl. Fluoresc.* 6, 012001 (2017)

[68] E. E. Jelley: "Spectral Absorption and Fluorescence of Dyes in the Molecular State", *Nature* 138, 1009 (1936)

[69] E. E. Jelley: "Molecular, Nematic and Crystal States of I:I'–Diethyl-ψ-Cyanine Chloride", *Nature* 139, 631 (1937)

[70] G. Sheibe: "Variability of the Absorption Spectra of Some Sensitizing Dyes and its Cause", *Angew. Chem.* 49, 563 (1936)

[71] G. Scheibe: "Über die Veränderlichkeit der Absorptionsspektren in Lösungen und die Nebenvalenzen als ihre Ursache", *Angew. Chem.* 50, 212 (1937)

[72] D. Möbius: "Scheibe Aggregates", *Adv. Mater.* 7, 437 (1995)

[73] S. Kirstein and S. Daehne: "J-aggregates of Amphiphilic Cyanine Dyes: Self-Organization of Artificial Light Harvesting Complexes", *Int. J. Photoenergy* 2006 (2006)

[74] H. von Berlepsch, C. Böttcher, A. Ouart, C. Burger, S. Dähne and S. Kirstein: "Supramolecular Structures of J-Aggregates of Carbocyanine Dyes in Solution", *J. Phys. Chem. B* 104, 5255 (2000)

[75] S. Makio, N. Kanamaru and J. Tanaka: "The J-aggregate 5, 5', 6, 6'-tetrachloro-1, 1'-diethyl-3, 3'-bis (4-sulfobutyl) benzimidazolocarbocyanine Sodium Salt in Aqueous Solution", *Bull. Chem. Soc. Jpn.* 53, 3120 (1980)

[76] J. Frenkel: "On the Transformation of Light into Heat in Solids. I", *Phys. Rev.* 37, 17 (1931)

[77] M. Kasha, H. Rawls and M. A. El-Bayoumi: "The Exciton Model in Molecular Spectroscopy", *Pure Appl. Chem.* 11, 371 (1965)

[78] E. McRae and M. Kasha: "The Molecular Exciton Model" In L. Augenstein, R. Mason and B. Rosenberg (Editors), *Physical Pocesses in Radiation Biology* (Academic Press, New York, 1964)

[79] G. Lanzani: *The Photophysics Behind Photovoltaics and Photonics* (Wiley-VCH, Weinheim, 2012)

[80] F. Würthner, T. E. Kaiser and C. R. Saha-Möller: "J-aggregates: From Serendipitous Discovery to Supramolecular Engineering of Functional Dye Materials", *Angew. Chem., Int. Ed.* 50, 3376 (2011)

[81] T. Kobayashi: *J-Aggregates* (World Scientific, Singapore, 1996)

[82] S. Strickler and R. A. Berg: "Relationship Between Absorption Intensity and Fluorescence Lifetime of Molecules", *J. Chem. Phys.* 37, 814 (1962)

[83] A. Eisfeld and J. S. Briggs: "The J-band of Organic Dyes: Lineshape and Coherence Length", *Chem. Phys.* 281, 61 (2002)

[84] J. Moll, S. Daehne, J. R. Durrant and D. A. Wiersma: "Optical Dynamics of Excitons in *J* Aggregates of a Carbocyanine Dye", *J. Chem. Phys.* 102, 6362 (1995)

[85] M. van Burgel, D. A. Wiersma and K. Duppen: "The Dynamics of One-Dimensional Excitons in Liquids", *J. Chem. Phys.* 102, 20 (1995)

[86] B. L. Darby, B. Auguié, M. Meyer, A. E. Pantoja and E. C. Le Ru: "Modified Optical Absorption of Molecules on Metallic Nanoparticles at Sub-Monolayer Coverage", *Nat. Photonics* 10, 40 (2016)

[87] R. Rosei: "Temperature Modulation of the Optical Transitions Involving the Fermi Surface in Ag: Theory", *Phys. Rev. B* 10, 474 (1974)

[88] R. Rosei, F. Antonangeli and U. Grassano: "D Bands Position and Width in Gold from Very Low Temperature Thermomodulation Measurements", *Surf. Sci.* 37, 689 (1973)

[89] M. Guerrisi, R. Rosei and P. Winsemius: "Splitting of the Interband Absorption Edge in Au", *Phys. Rev. B* 12, 557 (1975)

[90] P. Winsemius, M. Guerrisi and R. Rosei: "Splitting of the Interband Absorption Edge in Au: Temperature Dependence", *Phys. Rev. B* 12, 4570 (1975)

[91] N. W. Ashcroft and N. D. Mermin: *Solid State Physics* (Holt-Saunders, Philadelphia, 1976)

[92] R. L. Olmon, B. Slovick, T. W. Johnson, D. Shelton, S.-H. Oh, G. D. Boreman and M. B. Raschke: "Optical Dielectric Function of Gold", *Phys. Rev. B* 86, 235147 (2012)

[93] T. J. Antosiewicz, S. P. Apell and T. Shegai: "Plasmon–Exciton Interactions in a Core–Shell Geometry: From Enhanced Absorption to Strong Coupling", *ACS Photonics* 1, 454 (2014)

[94] S. Zou, N. Janel and G. C. Schatz: "Silver Nanoparticle Array Structures that Produce Remarkably Narrow Plasmon Lineshapes", *J. Chem. Phys.* 120, 10871 (2004)

[95] A. Vial, A.-S. Grimault, D. Macías, D. Barchiesi and M. L. de la Chapelle: "Improved Analytical Fit of Gold Dispersion: Application to the Modeling of Extinction Spectra with a Finite-Difference Time-Domain Method", *Phys. Rev. B* 71, 085416 (2005)

[96] T. Stoll, P. Maioli, A. Crut, N. Del Fatti and F. Vallée: "Advances in Femto-Nano-Optics: Ultrafast Nonlinearity of Metal Nanoparticles", *Eur. Phys. J. B* 87, 260 (2014)

[97] N. E. Christensen and B. O. Seraphin: "Relativistic Band Calculation and the Optical Properties of Gold", *Phys Rev. B* 4, 3321 (1971)

[98] N. V. Smith: "Photoelectron Energy Spectra and the Band Structures of the Noble Metals", *Phys. Rev. B* 3, 1862 (1971)

[99] D. Brust: "Band-Theoretic Model for the Photoelectric Effect in Silicon", *Phys. Rev.* 139, A489 (1965)

[100] J. H. Hodak, I. Martini and G. V. Hartland: "Spectroscopy and Dynamics of Nanometer-Sized Noble Metal Particles", *J. Phys. Chem. B* 102, 6958 (1998)

[101] B. Rethfeld, D. S. Ivanov, M. E. Garcia and S. I. Anisimov: "Modelling Ultrafast Laser Ablation", *J. Phys. D: Appl. Phys.* 50, 193001 (2017)

[102] C. Voisin, N. Del Fatti, D. Christofilos and F. Vallée: "Ultrafast Electron Dynamics and Optical Nonlinearities in Metal Nanoparticles", *J. Phys. Chem. B* 105, 2264 (2001)

[103] P. Vasa and C. Lienau: "Strong Light–Matter Interaction in Quantum Emitter/Metal Hybrid Nanostructures", *ACS Photonics* 5, 2 (2018)

[104] G. Grynberg, A. Aspect and C. Fabre: *Introduction to Quantum Optics: From the Semi-Classical Approach to Quantized Light* (Cambridge University Press, Cambridge, 2010)

[105] E. M. Purcell: "Spontaneous Emission Probabilities at Radio Frequencies", *Phys. Rev.* 69, 681 (1946)

[106] P. Meystre and M. Sargent III: *Elements of Quantum Optics* (Springer, New York, 1999)

[107] P. W. Milonni: *The Quantum Vacuum: An Introduction to Quantum Electrodynamics* (Academic Press, Boston, 1993)

[108] T. Yoshie, A. Scherer, J. Hendrickson, G. Khitrova, H. M. Gibbs, G. Rupper, C. Ell, O. B. Shchekin and D. G. Deppe: "Vacuum Rabi Splitting with a Single Quantum Dot in a Photonic Crystal Nanocavity", *Nature* 432, 200 (2004)

[109] A. F. Koenderink: "On the Use of Purcell Factors for Plasmon Antennas", *Opt. Lett.* 35, 4208 (2010)

[110] P. Lalanne, W. Yan, K. Vynck, C. Sauvan and J.-P. Hugonin: "Light Interaction with Photonic and Plasmonic Resonances", *Laser Photonics Rev.* 12, 1700113 (2018)

[111] C. Sauvan, J. P. Hugonin, I. S. Maksymov and P. Lalanne: "Theory of the Spontaneous Optical Emission of Nanosize Photonic and Plasmon Resonators", *Phys. Rev. Lett.* 110, 237401 (2013)

[112] L. Novotny: "Strong Coupling, Energy Splitting, and Level Crossings: A Classical Perspective", *Am. J. Phys.* 78, 1199 (2010)

[113] G. Khitrova, H. Gibbs, M. Kira, S. W. Koch and A. Scherer: "Vacuum Rabi Splitting in Semiconductors", *Nat. Phys.* 2, 81 (2006)

[114] B. M. Garraway: "The Dicke model in Quantum Optics: Dicke Model Revisited", *Philos. Trans. R. Soc., A* 369, 1137 (2011)

[115] G. S. Agarwal: "Vacuum-Field Rabi Splittings in Microwave Absorption by Rydberg Atoms in a Cavity", *Phys. Rev. Lett.* 53, 1732 (1984)

[116] H. Groß, J. M. Hamm, T. Tufarelli, O. Hess and B. Hecht: "Near-Field Strong Coupling of Single Quantum Dots", *Sci. Adv.* 4 (2018)

[117] G. Zengin, M. Wersäll, S. Nilsson, T. J. Antosiewicz, M. Käll and T. Shegai: "Realizing Strong Light–Matter Interactions between Single-Nanoparticle Plasmons and Molecular Excitons at Ambient Conditions", *Phys. Rev. Lett.* 114, 157401 (2015)

[118] D. Melnikau, R. Esteban, D. Savateeva, A. Sánchez-Iglesias, M. Grzelczak, M. K. Schmidt, L. M. Liz-Marzán, J. Aizpurua and Y. P. Rakovich: "Rabi Splitting in Photoluminescence Spectra of Hybrid Systems of Gold Nanorods and J-Aggregates", *J. Phys. Chem. Lett.* 7, 354 (2016)

[119] A. E. Schlather, N. Large, A. S. Urban, P. Nordlander and N. J. Halas: "Near-Field Mediated Plexcitonic Coupling and Giant Rabi Splitting in Individual Metallic Dimers", *Nano Lett.* 13, 3281 (2013)

[120] S. Rudin and T. L. Reinecke: "Oscillator Model for Vacuum Rabi Splitting in Microcavities", *Phys. Rev. B* 59, 10227 (1999)

[121] F. C. Spano and S. Mukamel: "Cooperative Nonlinear Optical Response of Molecular Aggregates: Crossover to Bulk Behavior", *Phys. Rev. Lett.* 66, 1197 (1991)

[122] L. D. Bakalis and J. Knoester: "Pump–Probe Spectroscopy and the Exciton Delocalization Length in Molecular Aggregates", *J. Phys. Chem. B* 103, 6620 (1999)

[123] H. Fidder, J. Knoester and D. A. Wiersma: "Observation of the One-Exciton to Two-Exciton Transition in a J Aggregate", *J. Chem. Phys.* 98, 6564 (1993)

[124] N. T. Fofang, N. K. Grady, Z. Fan, A. O. Govorov and N. J. Halas: "Plexciton Dynamics: Exciton–Plasmon Coupling in a J-Aggregate–Au Nanoshell Complex Provides a Mechanism for Nonlinearity", *Nano Lett.* 11, 1556 (2011)

[125] J. Bellessa, C. Bonnand, J. C. Plenet and J. Mugnier: "Strong Coupling between Surface Plasmons and Excitons in an Organic Semiconductor", *Phys. Rev. Lett.* 93, 36404 (2004)

[126] P. Vasa et al.: "Ultrafast Manipulation of Strong Coupling in Metal–Molecular Aggregate Hybrid Nanostructures", *ACS Nano* 4, 7559 (2010)

[127] S. R. K. Rodriguez, J. Feist, M. A. Verschuuren, F. J. Garcia Vidal and J. Gómez Rivas: "Thermalization and Cooling of Plasmon–Exciton Polaritons: Towards Quantum Condensation", *Phys. Rev. Lett.* 111, 166802 (2013)

[128] A. I. Väkeväinen, R. J. Moerland, H. T. Rekola, A.-P. Eskelinen, J.-P. Martikainen, D.-H. Kim and P. Törmä: "Plasmonic Surface Lattice Resonances at the Strong Coupling Regime", *Nano Lett.* 14, 1721 (2014)

[129] N. Zhou, M. Yuan, Y. Gao, D. Li and D. Yang: "Silver Nanoshell Plasmonically Controlled Emission of Semiconductor Quantum Dots in the Strong Coupling Regime", *ACS Nano* 10, 4154 (2016)

[130] J. Wen et al.: "Room-Temperature Strong Light–Matter Interaction with Active Control in Single Plasmonic Nanorod Coupled with Two-Dimensional Atomic Crystals", *Nano Lett.* 17, 4689 (2017)

[131] D. Zheng, S. Zhang, Q. Deng, M. Kang, P. Nordlander and H. Xu: "Manipulating Coherent Plasmon–Exciton Interaction in a Single Silver Nanorod on Monolayer WSe_2", *Nano Lett.* 17, 3809 (2017)

[132] R. Chikkaraddy et al.: "Single-Molecule Strong Coupling at Room Temperature in Plasmonic Nanocavities", *Nature* 535, 127 (2016)

[133] E. Eizner, O. Avayu, R. Ditcovski and T. Ellenbogen: "Aluminum Nanoantenna Complexes for Strong Coupling between Excitons and Localized Surface Plasmons", *Nano Lett.* 15, 6215 (2015)

[134] G. P. Wiederrecht, G. A. Wurtz and J. Hranisavljevic: "Coherent Coupling of Molecular Excitons to Electronic Polarizations of Noble Metal Nanoparticles", *Nano Lett.* 4, 2121 (2004)

[135] Q. Cui, A. Yashchenok, L. Zhang, L. Li, A. Masic, G. Wienskol, H. Möhwald and M. Bargheer: "Fabrication of Bifunctional Gold/Gelatin Hybrid Nanocomposites and Their Application", *ACS Appl. Mater. Interfaces* 6, 1999 (2014)

[136] J. Xie, Q. Zhang, J. Y. Lee and D. I. C. Wang: "The Synthesis of SERS-Active Gold Nanoflower Tags for In Vivo Applications", *ACS Nano* 2, 2473 (2008)

[137] D. Djoumessi Lekeufack, A. Brioude, A. W. Coleman, P. Miele, J. Bellessa, L. de Zeng and P. Stadelmann: "Core–Shell Gold J-Aggregate Nanoparticles for Highly Efficient Strong Coupling Applications", *Appl. Phys. Lett.* 96, 253107 (2010)

[138] Y. Zhang, B. Walkenfort, J. H. Yoon, S. Schlücker and W. Xie: "Gold and Silver Nanoparticle Monomers are non-SERS-Active: A Negative Experimental Study with Silica-Encapsulated Raman-Reporter-Coated Metal Colloids", *Phys. Chem. Chem. Phys.* 17, 21120 (2015)

[139] Y.-F. Zhang, D.-J. Yang, J.-H. Wang, Y.-L. Wang, S.-J. Ding, L. Zhou, Z.-H. Hao and Q.-Q. Wang: "Multiple Hybridized Resonances of IR-806 Chromonic Molecules Strongly Coupled to Au Nanorods", *Nanoscale* 7, 8503 (2015)

[140] F. Todisco et al.: "Ultrastrong Plasmon–Exciton Coupling by Dynamic Molecular Aggregation", *ACS Photonics* 5, 143 (2018)

[141] H. v. Berlepsch and C. Böttcher: "Tubular J-aggregates of a new Thiacarbocyanine Cy5 Dye for the Far-Red Spectral Region – a Spectroscopic and Cryo-Transmission Electron Microscopy Study", *Phys. Chem. Chem. Phys.* 20, 18969 (2018)

[142] M. Kiel: "Static and Ultrafast Optical Properties of Nanolayered Composites" Ph.D. thesis, Universität Potsdam (2012)

[143] K. Aslan and V. H. Pérez-Luna: "Surface Modification of Colloidal Gold by Chemisorption of Alkanethiols in the Presence of a Nonionic Surfactant", *Langmuir* 18, 6059 (2002)

[144] P. Buffat and J.-P. Borel: "Size Effect on the Melting Temperature of Gold Particles", *Phys. Rev. A* 13, 2287 (1976)

[145] S. Link, C. Burda, B. Nikoobakht and M. El-Sayed: "How Long Does It Take to Melt a Gold Nanorod?: A Femtosecond Pump–Probe Absorption Spectroscopic Study", *Chem. Phys. Lett.* 315, 12 (1999)

[146] S. Link, C. Burda, M. B. Mohamed, B. Nikoobakht and M. A. El-Sayed: "Laser Photothermal Melting and Fragmentation of Gold Nanorods: Energy and Laser Pulse-Width Dependence", *J. Phys. Chem. A* 103, 1165 (1999)

[147] N. T. Fofang, T.-H. Park, O. Neumann, N. A. Mirin, P. Nordlander and N. J. Halas: "Plexcitonic Nanoparticles: Plasmon–Exciton Coupling in Nanoshell–J-Aggregate Complexes", *Nano Lett.* 8, 3481 (2008)

[148] A. Brodeur and S. Chin: "Ultrafast White-Light Continuum Generation and Self-Focusing in Transparent Condensed Media", *J. Opt. Soc. Am. B* 16, 637 (1999)

[149] R. Trebino, K. W. DeLong, D. N. Fittinghoff, J. N. Sweetser, M. A. Krumbügel, B. A. Richman and D. J. Kane: "Measuring Ultrashort Laser Pulses in the Time-Frequency Domain Using Frequency-Resolved Optical Gating", *Rev. Sci. Instrum.* 68, 3277 (1997)

[150] D. Schick, A. Bojahr, M. Herzog, C. v. K. Schmising, R. Shayduk, W. Leitenberger, P. Gaal and M. Bargheer: "Normalization Schemes for Ultrafast X-Ray Diffraction Using a Table-Top Laser-Driven Plasma Source", *Rev. Sci. Instrum.* 83, 025104 (2012)

[151] F. Zamponi et al.: "Femtosecond Hard X-Ray Plasma Sources with a Kilohertz Repetition Rate", *Appl. Phys. A* 96, 51 (2009)

[152] C. V. Raman and K. S. Krishnan: "A New Type of Secondary Radiation", *Nature* 121, 501 (1928)

[153] K. Kneipp, M. Moskovits and H. Kneipp: *Surface-Enhanced Raman Scattering: Physics and Applications*, volume 103 (Springer, Heidelberg, 2006)

[154] S. Schücker: "Surface-Enhanced Raman Spectroscopy: Concepts and Chemical Applications", *Angew. Chem., Int. Ed.* 53, 4756 (2014)

[155] S. Nie and S. R. Emory: "Probing Single Molecules and Single Nanoparticles by Surface-Enhanced Raman Scattering", *Science* 275, 1102 (1997)

[156] K. Kneipp, Y. Wang, H. Kneipp, L. T. Perelman, I. Itzkan, R. R. Dasari and M. S. Feld: "Single Molecule Detection Using Surface-Enhanced Raman Scattering (SERS)", *Phys. Rev. Lett.* 78, 1667 (1997)

[157] Y. Sugawara, T. Kelf, J. Baumberg, M. Abdelsalam and P. Bartlett: "Strong Coupling between Localized Plasmons and Organic Excitons in Metal Nanovoids", *Phys. Rev. Lett.* 97, 266808 (2006)

[158] G. A. Wurtz, P. R. Evans, W. Hendren, R. Atkinson, W. Dickson, R. J. Pollard, A. V. Zayats, W. Harrison and C. Bower: "Molecular Plasmonics with Tunable Exciton–Plasmon Coupling Strength in J-Aggregate Hybridized Au Nanorod Assemblies", *Nano Lett.* 7, 1297 (2007)

[159] A. Yoshida, N. Uchida and N. Kometani: "Synthesis and Spectroscopic Studies of Composite Gold Nanorods with a Double-Shell Structure Composed of Spacer and Cyanine Dye J-Aggregate Layers", *Langmuir* 25, 11802 (2009)

[160] M. Wersäll, J. Cuadra, T. J. Antosiewicz, S. Balci and T. Shegai: "Observation of Mode Splitting in Photoluminescence of Individual Plasmonic Nanoparticles Strongly Coupled to Molecular Excitons", *Nano Lett.* 17, 551 (2017)

[161] F. Kato, H. Minamimoto, F. Nagasawa, Y. S. Yamamoto, T. Itoh and K. Murakoshi: "Active Tuning of Strong Coupling States between Dye Excitons and Localized Surface Plasmons via Electrochemical Potential Control", *ACS Photonics* 5, 788 (2018)

[162] J. Cuadra, D. G. Baranov, M. Wersäll, R. Verre, T. J. Antosiewicz and T. Shegai: "Observation of Tunable Charged Exciton Polaritons in Hybrid Monolayer WS_2–Plasmonic Nanoantenna System", *Nano Lett.* 18, 1777 (2018)

[163] S. Balci, B. Kucukoz, O. Balci, A. Karatay, C. Kocabas and G. Yaglioglu: "Tunable Plexcitonic Nanoparticles: A Model System for Studying Plasmon–Exciton Interaction from the Weak to the Ultrastrong Coupling Regime", *ACS Photonics* 3, 2010 (2016)

[164] X. Liu, T. Galfsky, Z. Sun, F. Xia, E.-c. Lin, Y.-H. Lee, S. Kéna-Cohen and V. M. Menon: "Strong Light–Matter Coupling in Two-Dimensional Atomic Crystals", *Nat. Photonics* 9, 30 (2015)

[165] Z.-J. Yang, T. J. Antosiewicz and T. Shegai: "Role of Material Loss and Mode Volume of Plasmonic Nanocavities for Strong Plasmon–Exciton Interactions", *Opt. Express* 24, 20373 (2016)

[166] R. Liu, Z.-K. Zhou, Y.-C. Yu, T. Zhang, H. Wang, G. Liu, Y. Wei, H. Chen and X.-H. Wang: "Strong Light-Matter Interactions in Single Open Plasmonic Nanocavities at the Quantum Optics Limit", *Phys. Rev. Lett.* 118, 237401 (2017)

[167] H. J. Kimble: "Strong Interactions of Single Atoms and Photons in Cavity QED", *Phys. Scr.* T76, 127 (1998)

[168] M. Sukharev and A. Nitzan: "Numerical Studies of the Interaction of an Atomic Sample with the Electromagnetic Field in Two Dimensions", *Phys. Rev. A* 84, 043802 (2011)

[169] Y.-W. Hao, H.-Y. Wang, Y. Jiang, Q.-D. Chen, K. Ueno, W.-Q. Wang, H. Misawa and H.-B. Sun: "Hybrid-State Dynamics of Gold Nanorods/Dye J-Aggregates under Strong Coupling", *Angew. Chem. Int. Ed.* 123, 7970 (2011)

[170] T. Simon, D. Melnikau, A. Sánchez-Iglesias, M. Grzelczak, L. M. Liz-Marzán, Y. Rakovich, J. Feldmann and A. S. Urban: "Exploring the Optical Nonlinearities of Plasmon-Exciton Hybrid Resonances in Coupled Colloidal Nanostructures", *J. Phys. Chem. C* 120, 12226 (2016)

[171] E. Eizner, K. Akulov, T. Schwartz and T. Ellenbogen: "Temporal Dynamics of Localized Exciton–Polaritons in Composite Organic–Plasmonic Metasurfaces", *Nano Lett.* 17, 7675 (2017)

[172] S. Balci, C. Kocabas, B. Küçüköz, A. Karatay, E. Akhüseyin, H. Gul Yaglioglu and A. Elmali: "Probing Ultrafast Energy Transfer between Excitons and Plasmons in the Ultrastrong Coupling Regime", *Appl. Phys. Lett.* 105, 051105 (2014)

[173] S. Park, M. Pelton, M. Liu, P. Guyot-Sionnest and N. F. Scherer: "Ultrafast Resonant Dynamics of Surface Plasmons in Gold Nanorods", *J. Phys. Chem. C* 111, 116 (2007)

[174] G. V. Hartland: "Coherent Excitation of Vibrational Modes in Metallic Nanoparticles", *Annu. Rev. Phys. Chem.* 57, 403 (2006)

[175] X.-J. Chen, G. Cabello, D.-Y. Wu and Z.-Q. Tian: "Surface-Enhanced Raman Spectroscopy Toward Application in Plasmonic Photocatalysis on Metal Nanostructures", *J. Photochem. Photobiol., C* 21, 54 (2014)

[176] G. Cerullo and S. De Silvestri: "Ultrafast Optical Parametric Amplifiers", *Rev. Sci. Instrum.* 74, 1 (2003)

[177] L. Zhou et al.: "Quantifying Hot Carrier and Thermal Contributions in Plasmonic Photocatalysis", *Science* 362, 69 (2018)

[178] Y. Sivan, J. Baraban, I. W. Un and Y. Dubi: "Comment on “Quantifying Hot Carrier and Thermal Contributions in Plasmonic Photocatalysis”", *Science* 364 (2019)

[179] L. Zhou, D. F. Swearer, H. Robatjazi, A. Alabastri, P. Christopher, E. A. Carter, P. Nordlander and N. J. Halas: "Response to Comment on “Quantifying Hot Carrier and Thermal Contributions in Plasmonic Photocatalysis”", *Science* 364 (2019)

[180] R. M. Sarhan, W. Koopman, R. Schuetz, T. Schmid, F. Liebig, J. Koetz and M. Bargheer: "The Importance of Plasmonic Heating for the Plasmon-Driven Photodimerization of 4-Nitrothiophenol", *Scientific reports* 9, 1 (2019)

Acknowledgements

I could not have realised this work without the help and contributions of many people. At this point I would like to express my gratitude to them. First of all to Matias Bargheer who gave me the opportunity to work in his group and who supported me with advice, money and the liberty to develop and pursue my own ideas. Just as much I want to thank Wouter Koopman for his time, patience and effort. He was for sure irreplaceable for me and for the work. I would like to express my gratitude to all authors of the articles of this work. All members of the group of UDKM are to be thanked for a fantaistic working atmosphere on both a professional and private level. I would like to thank the graduate school SALSA, not only for the financial support, but also for the opportunity to attend various workshops an the insight into scientific areas beyond physics and plasmonics.

And of course, thank you Sophie, thank you Frida.